Unveiling the nature of intermediate polars through multi-wavelength observations and computer modelling

Oliver Butters

M.Sci. (Hons) ARCS (Imperial College London) 2005

Submitted for the degree of Doctor of Philosophy

Faculty of Science, The Open University

Supervised by Dr. Andrew Norton

Submitted September 2009

Abstract

This thesis explores the nature of the class of stars known as intermediate polars, a sub-class of cataclysmic variables. Both observational and theoretical computer modelling approaches are employed in this exploration.

The first science chapter gives the results of a campaign to determine the credentials of six candidate intermediate polars. These candidates were picked based upon their hard X-ray detection with the *INTEGRAL* or *Swift* satellites. Three were confirmed as intermediate polars, two as likely intermediate polars, and one as a likely polar.

The initial results of an ambitious campaign to measure the degree of circular polarization in all intermediate polars are then reported. Since circular polarization can only be generated by a large magnetic field, this is the only reliable way to unambiguously detect its presence. This work discovered two very highly polarized sources, and draws a possible correlation between the presence of significant circular polarization and the detection of hard X-rays.

In a complementary study, results of a numerical simulation of the accretion flow structure in intermediate polars using *HyDisc* are then given. This forms part of a larger ongoing project which aims to understand intermediate polars by modelling their accretion flow topology. The main result here was the characterization of the variation of the accretion flow topologies as a function of the mass ratio of a given system.

The final science chapter introduces a nascent synthetic light curve modelling program. This generates time dependent emission profiles of intermediate polars using the *HyDisc* program as the basis of the accretion flow topology. A key result from this, is that the unabsorbed emission from intermediate polars can vary at the spin and orbital period. This is due to the accretion flow only accreting onto the surface of the WD from locations fixed in the orbital frame.

Acknowledgements

I would like to thank my main supervisor, Andrew Norton, for all his guidance and support throughout my Ph.D. He has presented me with many opportunities to do things and go to interesting places. He may not admit it, but he has taught me a lot over these last few years.

Academically speaking I am also very grateful to the collaborators that Andrew introduced me to, particularly Seppo Katajainen, and Koji Mukai whom I have enjoyed working with during my Ph.D. Not to mention the folk in P&A, who have inspired me over many a coffee break. Then there is Pip. A special thanks should go to Geoff for keeping the computers ticking over and working the rather unsociable hours that I have tended to need help at.

A thank you should also go to Peter Twining and the Schome team for distracting me from my work (and paying for the privilege!) during most of Ph.D. too.

Outside of academia I am grateful for the help, support and encouragement offered to me by my parents and sister, even if they never *really* understood what it is I do. Then of course there is Bint, it was her influence that made me move to the wonderful Milton Keynes, and has generally made life tolerable since.

Finally I wish to acknowledge Neil, Becca (again), and Sean for acknowledging me in their theses :)

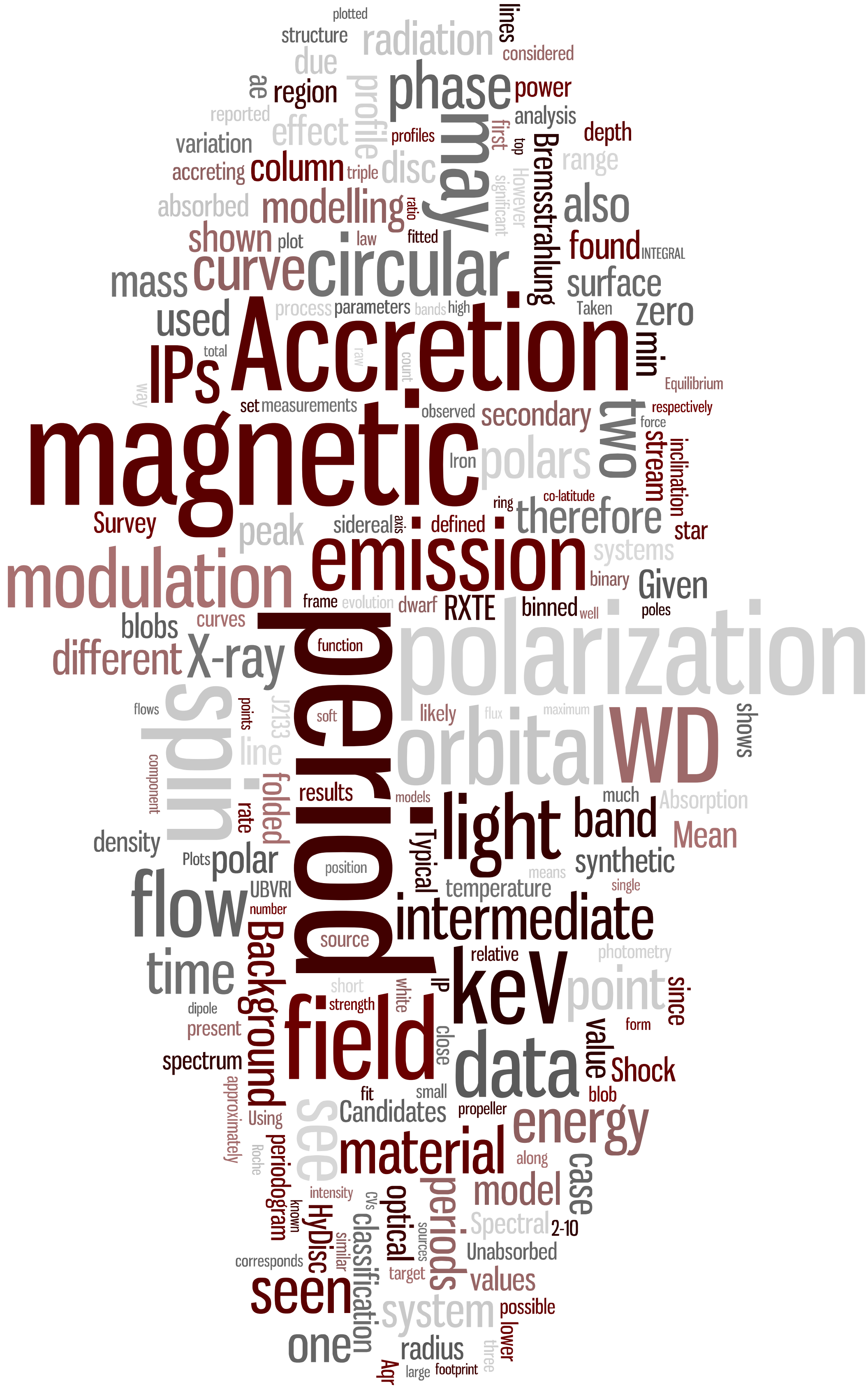
plotted
structure
radiation
lines
considered
due
phase
power
region
profile
analysis
reported
effect
may
first
depth
variation
profiles
top
Bremsstrahlung
accreting
column
triple
disc
range
However
absorbed
modelling
ratio
significant
also
shown
plot
law
fitted
found
INTEGRAL
mass
curve
circular
surface
process
parameters
bands
high
Taken
used
zero
IPs
Accretion
min
total
raw
count
Equilibrium
way
set
measurements
observed
secondary
respectively
magnetic
two
force
stream
inclination
Iron
polars
ring
co-latitude
Survey
peak
sidereal
axis
defined
therefore
star
systems
modulation
emission
binary
Given
frame
evolution
dwarf
RXTE
binned
well
poles
blobs
curves
function
different
X-ray
period
polarization
spin
flows
points
J2133
soft
likely
flux
maximum
shows
line
orbital
WD
component
folded
results
models
much
Absorption
rate
light
band
Mean
density
Typical
means
synthetic
Plots
polar
position
temperature
single
flow
UBVRI
number
intermediate
Background
source
relative
photometry
time
short
IP
keV
point
since
dipole
strength
white
present
field
close
value
form
spectrum
data
Shock
approximately
fit
small
blob
Using
see
Candidates
propeller
energy
Roche
material
along
case
periodogram
intensity
known
CVs
optical
periods
model
HyDisc
similar
classification
sources
Spectral
2-10
corresponds
target
Unabsorbed
seen
values
system
possible
one
radius
three
lower
Aqr
large
footprint

Contents

List of Figures

List of Tables

Chapter 1

Introduction

This chapter introduces the class of stars known as cataclysmic variables, giving the background knowledge needed for the subsequent chapters in this thesis. It begins with a general introduction, then concentrates on the intermediate polars, focusing on specific aspects covered in later chapters.

1.1 Context

Accretion physics is an important area of research in astrophysics since it is a process present in many different systems across the Universe. For example, it is a critical mechanism in the evolution of binary stars, it is the driving force in the creation of the planets around their stars and it is now thought to be a very important process in active galactic nuclei (where material is accreting onto a super massive black hole). With this in mind, a better understanding of accretion physics in general would benefit many areas of astrophysics.

Binary stars are an ideal laboratory to study accretion physics, partly because the properties of the systems may be calculated via direct observation. For instance, the mass and rotation rates may be found. This is not currently possible for the other examples of accreting objects, because the very long timescales required to study them, make their properties inaccessible to observation. Binary systems are also abundant enough that there is a wealth of information available to scrutinise.

Some binary stars are the progenitors to SNIa, one of the 'standard candles' used in cosmology to gauge distances. A better understanding of the evolution of the progenitor into a supernova would therefore help constrain all of cosmology.

1.2 Binary systems

The occurrence of two objects in a stable orbit around a common centre of mass is known as a binary system. Other systems do exist, for example, hierarchical binary systems in which two stars orbit each other, and their common centre of mass forms a binary with another star. In this way many-body systems may be built, e.g. the quadruple system AO Velorum (Gonzalez et al. 2005). Systems with three or more bodies orbiting a common centre of mass, unlike the hierarchical systems, are inherently unstable, and will either eventually collide or eject members until a stable binary orbit is left.

Stars may be at any stage of their stellar evolution when in a binary system. However, the evolutionary status of the individual stars greatly affects the conditions of the system as a whole.

Binary systems may be divided into two groups; non-interacting and interacting. In the former, no mass transfer takes place and both stars evolve almost as if they were single isolated stars, except for a slight gravitational perturbation. In the latter, mass transfer takes place which greatly affects the evolution of both the stars. There are two means by which this mass transfer may take place; wind accretion and accretion via the inner Lagrange point, L_1. Wind accretion takes a form similar to that seen in the Solar wind, and accretion via the L_1 point is a stream of material which flows from one star to the other.

Within the interacting binary systems are two subsets; that of compact binaries and normal binaries. Compact binaries have at least one of a white dwarf, a neutron star or a black hole as a member. Normal binaries just have normal (i.e. non-compact) stars which follow their slightly modified evolution due to the mass transfer. The fact that at least one of the stars in a compact binary is compact means that the mass to radius ratio is large. If the accreting star is compact then the accreting material may become very hot as is falls into the potential well; values of 100,000K for a white dwarf are not uncommon. This high temperature means that the accreting material is almost certainly ionised, i.e. it can be treated as a plasma.

1.3 Cataclysmic variables

When an interacting binary system is comprised of a white dwarf (WD) and a main sequence star (typically a red dwarf), the system is classified as a cataclysmic variable (CV). This configuration occurs because the binary pair had one member sufficiently massive, that it formed a WD at the end of its stellar evolution. The more massive star will always reach the end of its life first, since larger stars move through the phases of stellar evolution at a higher rate than smaller stars (Kolb 2002).

CVs are a useful tool in astrophysics due to their systemic properties - their dynamics are such that they radiate in accessible wavebands and vary on accessible timescales.

1.3.1 Evolution into CVs

CVs are thought to go through a common envelope (CE) phase. This arises because the star which will become a WD will first become a red giant when it moves off the main sequence. This means it expands and may overflow its Roche lobe (see Section 1.4.1 for an explanation of Roche lobes), resulting in accretion from the primary (the red giant) to the secondary (the red dwarf). The rate at which matter is transferred to the main sequence star may be such that the Eddington limit is reached. This is the point when the radiation pressure from the accreting object balances the gravitational attraction of the accreting material, therefore any further material cannot accrete and begins to form a common envelope. Alternatively the secondary star may expand to fill its Roche lobe, and therefore begin to form a common envelope around both stars by Roche lobe overflow. In both processes a CE will form with its inner radius being approximately equal to the radius of the outer Lagrange point (Warner 1995).

It is during this CE stage that most of the conditions of the binary are set, leading to it being considered a kind of 'nursery' for CVs (Paczynski 1976). Given the evolutionary sequence of WDs, it is necessary to have an initial mass of 0.95 $\lesssim M_1 \lesssim$ 10 Solar masses to ensure a WD (and not a neutron star) is formed.

Once the CE has been formed the members of the binary may transfer momentum to the envelope via a drag force, D, (see Equation 1.1) and thus spiral in.

$$D \sim R^2_{\text{secondary}} v^2_{\text{orb}} \rho_{\text{CE}} \tag{1.1}$$

Where $R_{\text{secondary}}$ is the radius of the secondary star, v_{orb} is the orbital velocity, and ρ_{CE} is the density of the CE. This transfer of momentum to the CE causes it to be slowly expelled from the system. The time scale of the spiralling in process is typically of the order of a few thousand years, and once it is over the properties of the system (the masses, radii, separation, spin and orbital periods) are largely fixed.

1.3.2 Orbital period

If the primary and secondary are treated as point sources then Kepler's third law may be used to estimate their separation (see Equation 1.2).

$$a = \left(\frac{GM_{\text{tot}}P_{\text{orb}}^2}{4\pi^2}\right)^{\frac{1}{3}} \tag{1.2}$$

Where a is the separation, M_{tot} is the total mass of the system, and P_{orb} is the orbital period. Or, in more natural units

$$a = 2.296 \times 10^7 M_{\text{tot}}^{1/3}(M_\odot)P_{\text{orb}}^{2/3}(\text{mins}) \ \ \text{m} \tag{1.3}$$

In non-magnetic CVs there is a wide range of orbital periods, generally ranging from approximately 77 minutes to about 12 hours (Ritter & Kolb 2003). For a total mass of 1 $M_\odot$ this corresponds to separation range of $4.2 \ \times 10^8 - 1.8 \times 10^9$ m.

The distribution of these periods is subject to a great deal of research as a 'period gap' between two and three hours is evident (see Figure 1.1). The current consensus for the origin of the period gap is due to the proposed evolution of CVs. As a CV evolves the system loses angular momentum via gravitational radiation and magnetic braking, this causes the orbital period to decrease.

Initially the secondary fills its Roche lobe and overflowing material is accreted onto the primary. This process is thought to drive the secondary out of equilibrium. This is the case as the thermal timescale is longer than the timescale on which material is accreted. Therefore as the secondary loses its mass the weight on the core decreases, this reduces the rate of nuclear reactions in the core, and so the pressure on the outer layers decreases. This reduced pressure causes the star to shrink, but the star transfers more matter to the primary at a faster rate, and so it is cannot shrink fast enough and is driven out of equilibrium. For much of the orbital period evolution the secondary is therefore larger than the nuclear burning at its core can sustain.

When the orbital period reaches $\sim$3 hrs the magnetic braking is thought to switch off due to the star becoming fully convective. Any dynamo effects that sustain the magnetic field will be halted by this. This greatly reduces the rate of angular momentum loss and so the binary detaches. The secondary is then allowed to continue shrinking until it is again in equilibrium.

The system continues to evolve to a shorter orbital period via gravitational radiation. During this stage of evolution no significant radiation is given off since there is no Roche lobe overflow and hence no accretion. Once the orbit has reduced enough that the Roche lobe has shrunk to the size of the secondary, Roche lobe overflow may begin again. This stage is maintained until the secondary reaches a minimum mass (approximately $0.06M_{\odot}$) at which point it is degenerate. The secondary then expands as it loses material to the primary, this causes the orbital period to increase.

While this is the widely accepted view of the evolution of the orbital period, there is no observational evidence to show it happening, due to the large time scales of evolution, only the current state of systems (see Figure 1.1). This distribution of CVs is subject to several selection effects however, since different discovery techniques may preferentially detect CVs in specific parts of the orbital period range. This can be illustrated by the recent paper of Gänsicke et al. (2009) where a population of CVs was studied based upon their detection in the Sloan Digital Sky Survey (SDSS) spectroscopic data base alone. The distribution exhibits a much greater proportion of CVs in the 80–86 min range than that shown in Figure 1.1. The relatively large number of CVs in that sample makes it one of the more reliable population studies. The interpretation Gänsicke et al. (2009) give for this peak is that it is the long sought after period minimum spike that should occur when CVs reverse their orbital period evolution to longer periods.

1.3.3 Stellar components

WDs are typically relatively small and dense since they no longer undergo fusion, and are therefore not sustained by thermal pressure but electron degeneracy. Broadly speaking they can be split into three groups based upon their composition; He, C/O and O/Ne/Mg. The He WDs are likely the result of a binary pair in which material has been ripped from the surface of the star as it evolved, and thus pegging the evolution to He as the end point. The majority of WDs are the result of the more massive stars, which will be hot enough to fuse He into C and O in their cores, leaving a H and He layer. More massive stars undergo a further fusion in their cores and produce O/Ne/Mg. As long as this is where the fusion stops (i.e. the star is not massive enough to fuse neon) then a O/Ne/Mg WD may be formed. The upper limit the mass a WD can take is the Chandrasekhar limit, above this the WD would become degenerate and form a neutron star. WD masses therefore typically fall in the range $0.3 - 1.3M_{\odot}$. This in turn implies that the radii of WDs are $\sim\ 10^{7}$m.

As noted above, the heavier star in a binary will evolve faster, this places the constraint that the secondary is less massive than the primary for a CV to form. This is also the condition for stable mass transfer to occur,

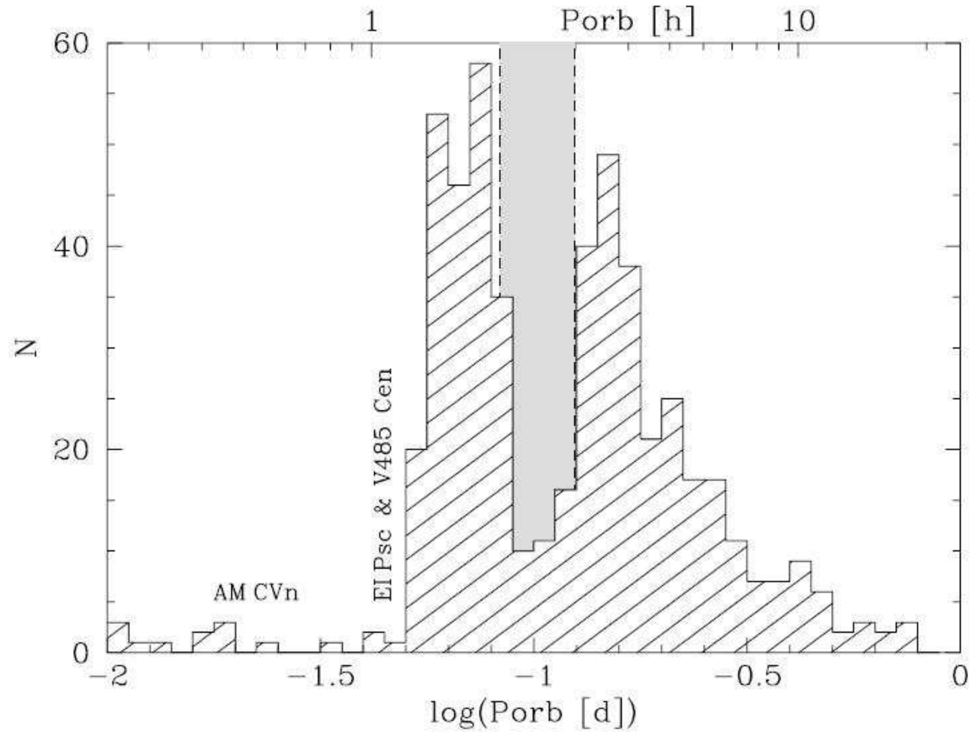

Figure 1.1: Period distribution of CVs, the 2–3h period gap is indicated in grey. The short period systems labelled AM CVn are double degenerate systems. (Taken from Gänsicke (2005))

if matter were to accrete from the primary to the secondary then the mass transfer would become unstable. This places a constraint on the upper limit of the orbital period. For a CV to be visible the secondary must be filling its roche lobe, and since the roche lobe gets larger as the orbital period increases, the upper mass places an effective upper limit on the orbital period. If the secondary is evolved, and therefore expanded, then it can overcome this upper orbital period limit. Assuming the secondary is not evolved and fills its roche lobe it follows the relation

$$\frac{\rho_2}{\rho_\odot} = 75.5 P_{\mathrm{orb}}^{-2}(hr) \tag{1.4}$$

where ρ_2 is the density of the secondary (Smith & Dhillon 1998). For orbital periods of approximately 80 min to 9 hr this corresponds to a density range of $50\rho_\odot - 1\rho_\odot$. Smith & Dhillon (1998) also present fits to model data for the mass-period relationship in CVs, they find $M_2/M_\odot = 0.065 P_{\mathrm{orb}}^{5/4}$. For a range of orbital periods of 80 min to 9 hr this implies a mass range of $0.09 - 1.0 M_\odot$.

1.4 Non-magnetic accretion

Accretion is the process by which material falls into a potential well, or in the case of a CV, on to the surface of a white dwarf. As the material falls in, it can heat up and thus radiate away energy. It is often this radiation that is seen when interacting binary systems are observed, since it can outshine the members of the system (i.e. the WD and the red dwarf) by many magnitudes.

1.4.1 Roche lobe

In a CV the gravitational potential and the centrifugal potential are important factors in the dynamics of accretion. These may be combined to form the Roche potential in a rotating system, $\Phi_{\rm R}(\mathbf{r})$, (see Equation 1.5).

$$\Phi_{\rm R}(\mathbf{r}) = -\frac{GM_1}{|\mathbf{r}-\mathbf{r_1}|} - \frac{GM_2}{|\mathbf{r}-\mathbf{r_2}|} - \frac{1}{2}\left(\mathbf{\Omega}\wedge\mathbf{r}\right)^2 \tag{1.5}$$

Where G is the gravitational constant, M_1 is the mass of the primary star (the WD), M_2 is the mass of the secondary star (the donor star), $\mathbf{r_1}$ and $\mathbf{r_2}$ are the position vectors of the primary and secondary respectively and $\mathbf{\Omega}$ is the angular velocity relative to the inertial frame. The first two terms then correspond to the gravitational potential of the two stars, and the third term is the centrifugal term. The Roche lobe may then be defined as the equipotential which passes through the inner Lagrange point (see e.g. Frank et al. (2002)). This is illustrated in Figure 1.2.

A binary system is defined as detached if both members lie within their respective Roche lobes, this means no matter flows between them. The system is semi-detached if only one member fills its Roche lobe, in this case accretion occurs. If both members fill their Roche lobes, the system is considered a contact binary and the stars are essentially touching each other.

When Roche lobe overflow occurs, a geometrically thin, highly supersonic, gas stream follows a ballistic trajectory toward the accretor. This stream will intersect itself after one orbit of the accretor and form a torus and, eventually, a disc. This process can be seen in Figure 1.3.

1.4.2 Equation of motion

Taking the Roche potential in to account, the equation of motion for a point source in a non-magnetic CV, is the Euler equation as given in Equation 1.6 (Frank et al. 2002).

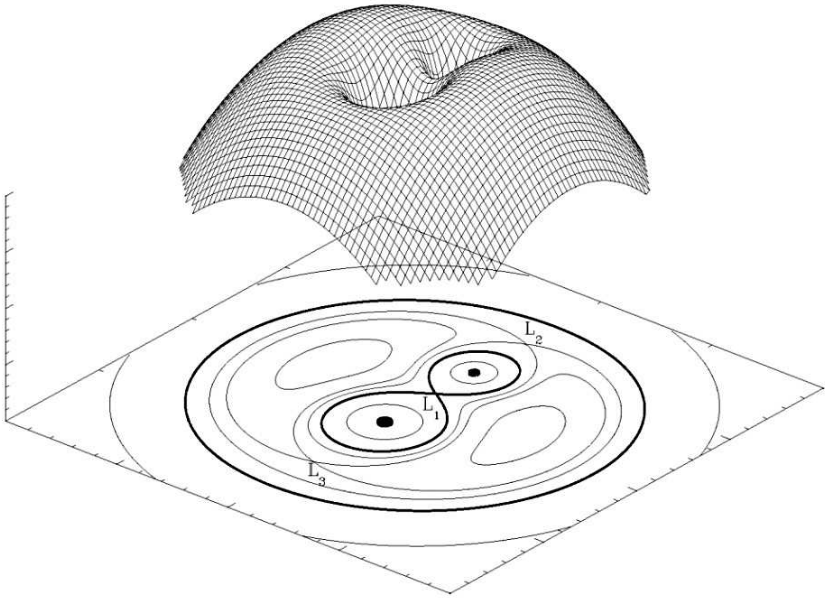

Figure 1.2: Illustration of the Roche potential around a binary star with a mass ratio of two. (van der Sluys 2006).

$$\frac{\partial \mathbf{v}}{\partial t} + (\mathbf{v}.\nabla)\mathbf{v} = -\nabla\Phi_{\mathrm{R}} - 2\mathbf{\Omega} \wedge \mathbf{v} - \frac{1}{\rho}\nabla P \tag{1.6}$$

Where the motion of a specific point source is described by the Roche potential, the Coriolis force (per unit mass due to the rotation of the binary pair with an orbital frequency $\mathbf{\Omega}$), and the pressure gradient that the point sources experience due to the neighbouring material.

A handle on the dynamics of the torus may be grasped if single particle trajectories are considered. Assuming angular momentum is conserved and the particles follow a Keplarian orbit, then an approximation of the radius of the torus (r_{circ}) relative to the binary separation, as a function of the ratio q (secondary mass / primary mass), may be given by Equation 1.7 (Frank et al. 2002).

$$\frac{r_{\mathrm{circ}}}{a} = (1+q)(0.500 - 0.227\mathrm{log}q)^4 \tag{1.7}$$

This is, of course, an approximation since other effects will be present in the ring when more than one particle is considered. Viscous processes, for example, will cause energy to be radiated away in the form of heat, causing particles to move closer to the primary as they fall further into the potential well. To conserve angular momentum, some particles will have to move outward, spreading the ring into a disc, as in Figure 1.3.

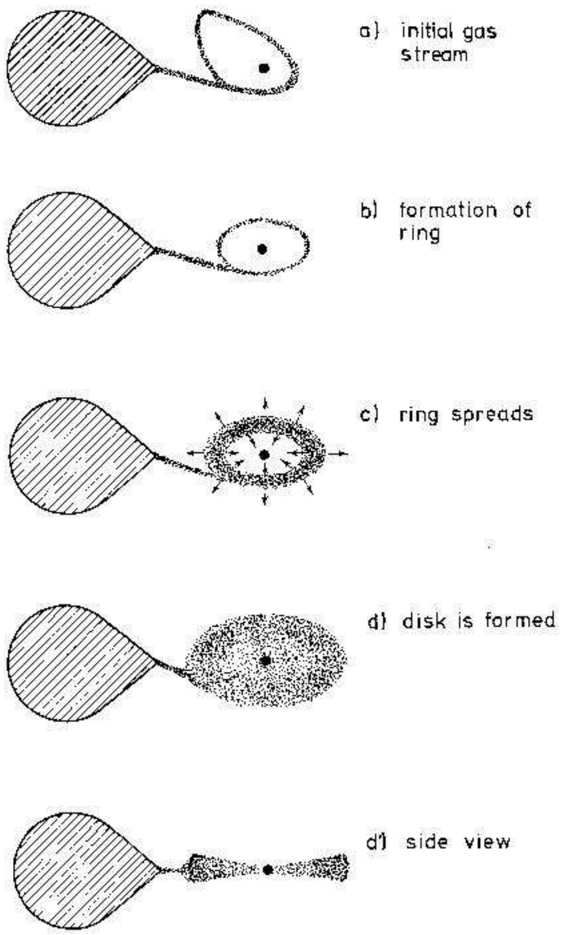

Figure 1.3: Schematic illustrations of the initial formation of a ring and its evolution into a disc Verbunt (1982).

Taking this into account, $r_{\rm circ}$ is therefore the minimum outer radius an accretion disc can have. The maximum outer radius the disc can have has an upper boundary of the Roche lobe, since anything which goes past this has effectively 'escaped' the pull of the WD. Typical values of $r_{\rm circ}$ are of the order of 10^8 m.

1.4.3 Bright spot

In the region where the accretion flow impacts on the accretion disc, a hot spot is formed (see Figure 1.4). It is here that much of the kinetic energy from the accretion flow is converted into heat and thus radiation. This can be seen best observationally in eclipsing systems where the secondary obscures the accreting WD. Before the eclipse, the bright spot moves more into the line of sight of the observer, causing an increase in brightness. The WD then gets eclipsed leaving the bright spot clearly visible, which subsequently gets eclipsed and emerges on the other side of the red dwarf.

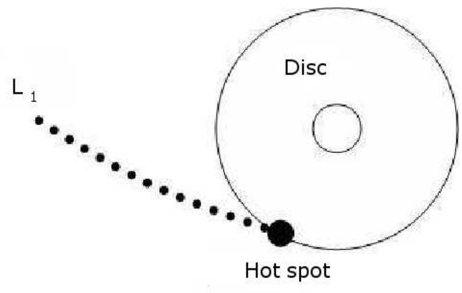

Figure 1.4: Illustration of an accretion stream impacting on an accretion disc forming a hot spot (not to scale).

1.4.4 Boundary layer

The boundary layer (Figure 1.5) is the region where the accretion disc, which is obeying Keplarian motion, is decelerated to match the spin of the WD. This deceleration gives rise to the accreting material being supported by the pressure gradient instead of the centrifugal force previously, i.e. the last term in Equation 1.6 begins to dominate over the earlier ones (Warner 1995). The properties of the boundary layer greatly affects the nature of the radiation as seen from Earth. An optically thick boundary layer will absorb a great deal of the radiation and re-emit it as a blackbody, while an optically thin boundary layer will not.

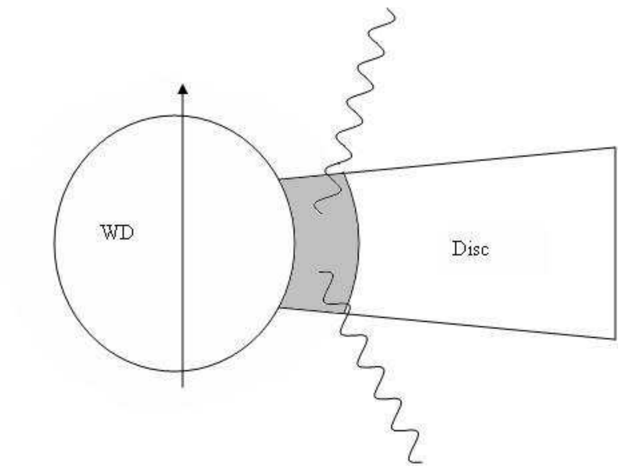

Figure 1.5: Illustration of the boundary layer in an accretion disc. The boundary layer (shaded area) is where much of the emitted radiation comes from (not to scale).

1.4.5 Viscosity

On its most basic level viscosity is a proportionality between stress and strain in an accretion disc, or stress = $\nu\times$ strain, where ν is the viscosity. Using this definition of viscosity, a formal description of the torque it produces, G, may be derived (see Equation 1.8 (Kolb 2002)).

$$G = 2\pi R\nu\Sigma R^2 \frac{\partial\Omega}{\partial R} \tag{1.8}$$

Here Σ is the surface mass density, R is the distance from the WD, and Ω is the angular velocity. It is this equation which describes the process causing a ring, which may have formed at the circularization radius, to spread out to form a disc (as in Figure 1.3). This is illustrated in the Keplarian case (where $G < 0$) showing that the slower moving outer region tries to slow the faster moving inner region, and vice versa. Once the inner ring has been slowed, it falls further into the potential well and the faster moving outer region moves further out, i.e. a disc is formed.

Once a disc has been formed, the rate of energy loss due to viscosity, $D(R)$, may be deduced. If the disc is thought of as a series of concentric rings then it is clear that any particular ring (not one at the boundary) will have one ring inside it trying to spin it up, and one outside of it trying to spin it down. The difference in the energy deposited and taken away by these two process is converted into heat and radiated away (Equation 1.9).

$$D(R) = \frac{1}{2}\nu\Sigma\left(R\frac{\partial\Omega}{\partial R}\right)^2 \tag{1.9}$$

The true nature of the viscosity is not understood. For this reason a phenomenological approach was taken and $\alpha-$viscosity was created, where α is a dimensionless constant less than unity (Shakura & Sunyaev 1973). The nature of α is such that it is likely to be a function of many variables and so is very difficult to quantify. Observations of non-steady state discs have found that $\alpha \sim 0.01 - 1$, which differs significantly from the molecular viscosity of $\sim 10^{-11}$ (Warner 1995). It is hoped that this phenomenological approach can be superseded in the near future with a full implementation of magneto-hydro-dynamics (MHD) in the treatment of viscosity.

1.5 Magnetic cataclysmic variables

The magnetic field strength of an isolated WD is dependent on its evolution history, it may take a value of anything between a few Gauss to 10^9 G (Cumming 2004). A small magnetic field strength on the WD in a CV indicates the system is a *normal* CV while a large one means it may be classed as a magnetic cataclysmic variable (mCV). It is likely that there exists a continuum of field strengths between the 'non-magnetic' and the 'magnetic' CVs. Instead of setting an arbitrary cut-off between the two sub-classes, a CV is generally thought of as being magnetic when the accretion process is *dominated* by the magnetic field.

In terms of the CV population as a whole, mCVs make up approximately 25% of the known population, the uncertainty in this arises due to the inconsistencies in classification (Ritter & Kolb 2003). Other factors may affect this value, for instance mCVs may be subject to selection effects. mCVs generally emit X-rays (see Section 1.8), surveys that find unclassified X-ray sources (e.g. the recent *INTEGRAL* mission) can therefore give a list of candidates that may be mCVs on further inspection. The relative abundance of mCVs to the non-magnetic CVs is then strongly dependent on the wave-band that is surveyed. The characteristic time scales in mCVs tend to be shorter too (in the intermediate polars a spin period is present - see below, and the polars tend to be at the shorter end of the orbital period distribution). This has the effect that less time is needed to observe the candidate to decide its classification, hence it is more likely to classify an mCV for a given amount of observing time.

Within the mCV class, a further division may be made with regards to the relative spin and orbital periods. Polars, also known as AM Her stars, have the characteristic that the spin period of the WD is equal to the orbital period ($P_{\text{spin}} = P_{\text{orb}}$). This relationship occurs because the magnetic field of the WD is so large that it extends to the secondary star and the two interact. The nature of the interaction depends on whether the secondary has a magnetic field or not. If it does not then the primary's magnetic field will thread the secondary, then as the primary rotates the field will become distorted and cause a braking effect. If the secondary has a magnetic field then the two fields will connect and generate large currents as plasma flows along the field lines thus causing another braking effect.

Intermediate polars (IP), also known as DQ Her stars, have the characteristic that the spin period of the WD and the orbital period are not equal ($P_{\text{spin}} \neq P_{\text{orb}}$), moreover the orbital period is greater than the spin period ($P_{\text{orb}} > P_{\text{spin}}$). This is a consequence of the apparent weaker magnetic field strength of the WD (when compared to the polars), and so the synchronisation does not occur.

A schematic of where mCVs lie in relation to all other star systems can be found in Figure 1.6.

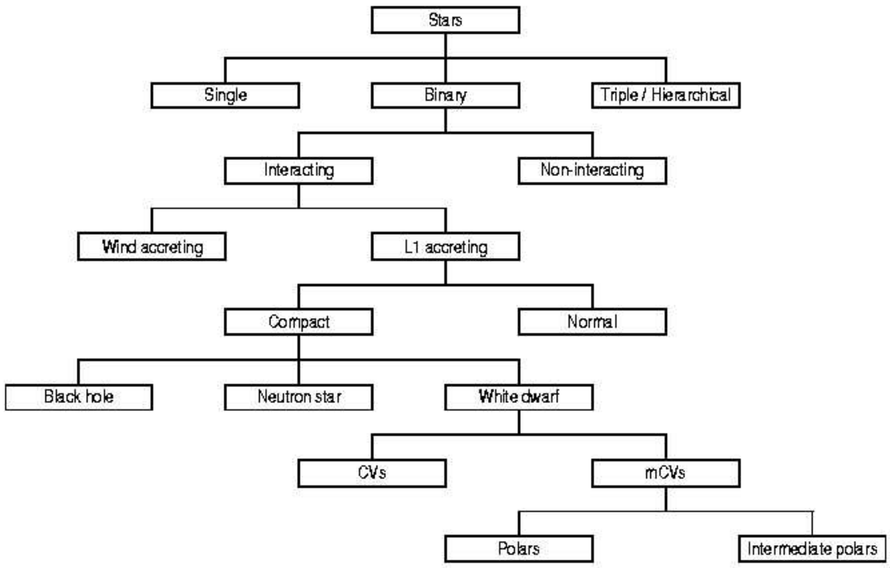

Figure 1.6: Schematic showing the relation between different classes of binaries.

The precise nature and origin of the magnetic field on the WD in a mCV is unknown. Stellar evolution models suggest that the magnetic flux through the surface of a star ($\propto BR^2$) is approximately conserved during the lifetime of the star (see e.g. (Kolb 2002)). This has the effect that when a main sequence star reaches the end of its evolution and its radius reduces, the magnetic field at the surface is dramatically increased. The Sun, for instance, has a surface magnetic field of one Gauss and a radius of $7{\times}10^8$m. If it were to end its evolution as a WD, of radius 10^7m, then it would have a surface magnetic field of 5 MG. For mCVs with surface field strengths in the range 10–100 MG, this requires the progenitor star to have a surface magnetic field of 2 MG. A comparison between the field strengths of isolated WDs and those in accreting systems is shown in Table 1.1. The two populations show a different distribution of field strengths, and so the magnetic field origin cannot be as simple as suggested above. It should be noted however that selection effects may play a role here, and so the validity of this comparison is not clear. One theory that tries to address the relative field strengths is that the magnetic field in an isolated WD is a consequence of the currents caused by the bulk movement in its core. As the WD cools the core solidifies, this has the effect of increasing the magnetic field strength. In a mCV the WD has material accreted on to it and so is heated, this means that the core will not solidify and the larger

Table 1.1: Magnetic white dwarf properties

	Isolated	Accreting
Number	> 200	≈ 90
Magnetic Field	$10^3 - 10^9$ G	$7 \times 10^6 - 3 \times 10^8$ G (AM Hers)
		$\sim 10^5 - 10^7$ G (IPs)

magnetic field strengths seen in the isolated cases may not be produced (Cumming 2004). This then allows a regime where the polars and IPs may be from the same population, and that the IPs may evolve into polars since IPs typically have a longer orbital period than polars. The higher mass accretion rates typically found in IPs may be suppressing the magnetic field of the WD. As the system evolves, the orbital period decreases and the mass accretion rate will drop, consequently the magnetic field on the WD is no longer suppressed and the system emerges as a polar (Cumming 2004).

An alternative theory for the origin of the magnetic field comes from Tout et al. (2008) who suggests that *all* magnetic WDs evolve from the common envelope phase outlined above. They suggest that in the common envelope, a dynamo effect causes a magnetic field to form on the WD. Moreover, the closer the binary pair are together the larger the resultant magnetic field, with the extreme of this being when two WDs merge. This then implies an origin for the high magnetic isolated WDs, as well as describing the apparent magnetic field strength of the polars and intermediate polars respectively.

1.6 Magnetic accretion

1.6.1 Background

Magnetic accretion is the accretion process which occurs in systems where the primary star (the WD in this case) has a large magnetic field. Due to the amplitude and topology of the magnetic fields, the accretion process differs from that of a non-magnetic CV significantly.

Plasma

Since accretion, in this case, is the process of stellar material collecting around a companion, it is important to take into account the nature of the accreting material i.e. it is a plasma. The material has this excited state, since it is flowing directly from a main sequence stellar companion with a temperature of approximately 3000 K near the L_1 point. As it travels toward the WD surface, the typical temperatures can be of the order of 100 000 K.

This complication means that the accretion process cannot be treated as a simple hydro-dynamics problem, it must be treated as a magneto-hydro-dynamics problem.

Diamagnetic blobs

The accreting material was originally thought to be of a homogeneous nature, hence it could be thought of as a smooth flow of material. This idea has been superseded by the notion of inhomogeneous diamagnetic blobs (Kuijpers & Pringle 1982; King 1993). This arises by considering the magnetic field in the region of the accretion stream, the magnetic pressure increases faster than the gas can adjust sub-sonically, so the stream is fragmented into blobs. A variety of processes then act upon these blobs as they travel toward the WD, the dominant effect being to fragment the blobs further. It is thought that by the time the blobs reach the magnetospheric radius that they are very small ($< 10^6$m) (Warner 1995).

Magnetospheric radius

An indication of the importance of the magnetic field to the accretion process is the magnetospheric radius, R_{M}. This is defined as the distance from the WD where the magnetic pressure is equal to the ram pressure i.e. equating Equations 1.10 and 1.11 (where B is the magnitude of the magnetic field at a given point, ρ is the density of the in-falling material, and v is the velocity of the material).

$$P_{\mathrm{mag}} = \frac{4\pi}{\mu_0}\frac{B^2}{8\pi} \tag{1.10}$$

$$P_{\mathrm{ram}} = \rho v^2 \tag{1.11}$$

The location of R_{M} governs the dynamics of the system, if is close to the L_1 point then the plasma will couple straight to the magnetic field and be channelled along it directly to the surface of the WD, so no accretion disc is formed. If the converse is true and R_{M} is much smaller than the distance to the L_1 point then a truncated accretion disc will form outside of R_{M} and the plasma will couple to the field at R_{M}, and be channelled to the surface from there. The two scenarios are called an accretion column and an accretion curtain respectively. For a typical IP with a surface magnetic field of 1 MG, a primary mass of $0.5M_{\odot}$, and a mass accretion rate of $10^{-10}M_{\odot}yr^{-1}$, the magnetospheric radius would be of the order of 10^{8}m.

Spin and orbital periods

In mCVs there is not as strong evidence for an orbital period gap as seen in the non-magnetic CVs (see Figure 1.7). This is particularly true for the polars where clearly no period gap is present. The accretion rate in the polars is generally a lot less than the IPs, and is consistent with being driven by gravitational radiation only. The secondary in polars is therefore allowed to evolve in thermal equilibrium during the entirety of the orbital period evolution. When the orbital period reaches three hours and the star becomes fully convective it doesn't shrink further, and so a period gap does not form. It is likely that the magnetic field of the secondary is suppressed by the field of the primary in polars, and this stops magnetic braking affecting the orbital period evolution. There are no IPs in the period gap in Figure 1.7, but the total number of IPs is much less than the polars, so this may be coincidence. The accretion rate of IPs is greater than the polars and is consistent with magnetic braking. It is therefore likely that when IPs get to three hours and the secondary becomes fully convective that a period gap will start. A much higher population is needed before this idea can be tested however.

The spin period is linked to the orbital period in a way not seen in non-magnetic CVs, as noted earlier. The spin period is always less than or equal to the orbital period. The shortest orbital period in an mCVs is a polar with 1.30 hr in CY Hyi, the shortest in the IPs is 1.35 hr in HT Cam. The longest polar orbital period is 7.98 hr in V1309 Ori, and the longest in an IP is 48 hr in GK Per (Ritter & Kolb 2003).

1.6.2 Field-plasma interaction

The field

The magnetic field in a WD is usually considered as a dipole, this allows relatively simple models to be formulated. In reality the magnetic field topology is likely to be much more complex. Beuermann et al. (2007) present models of the surface magnetic field structure of three polars. They find that a dipole approximation is far from an ideal fit to their spectro-polarimetry data, and that rather complex multi-pole approximations are needed. This multi-pole magnetic field structure would lead to a much more complex accretion structure, with likely multiple accretion columns. This technique has only been applied to a handful of mCVs over a limited part of parameter space (Beuermann et al. (2007) only look at short period polars), so the occurrence

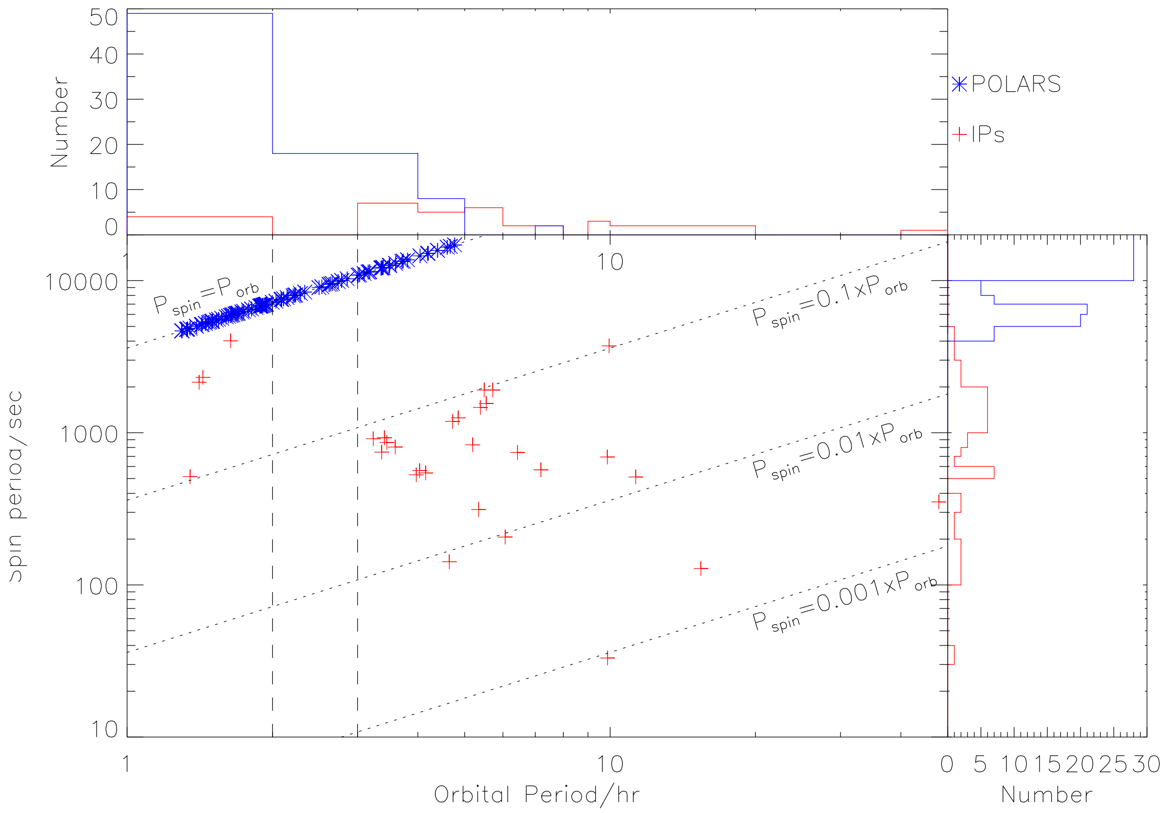

Figure 1.7: Spin and orbit distribution of all confirmed IPs and polars.

of multi-pole fields among mCVs in general is unknown. For this reason (and to simplify the models used in this thesis) the fields considered here are dipole only.

The magnetic moment of a WD with a dipole field can be given as $\mu = Br^3$ where B is the field strength at r. For $\mu = 10^{34}$G cm^3, B at the surface of the WD is of order 30MG.

Coupling to the field

As the blobs approach the field they are increasingly influenced by it. The actual process by which the blobs thread themselves onto the field lines is unknown. Various ideas have been proposed, most of which involve some kind of MHD, but none have so far been proven.

Moving along the field

For typical WD conditions the electron mean free path, $\lambda_{\rm e}$, is much greater than the Lamour radius, $r_{\rm L_e}$, of the blobs.

$$r_{\rm L_e} \sim 10^{-7}{\rm m} \qquad \lambda_{\rm e} \sim 10^{2}{\rm m} \tag{1.12}$$

This has the effect of channelling the electrons along the field lines, since any other process, e.g. thermal conduction will be suppressed orthogonal to the field lines (Frank et al. 2002).

Once the material is attached to the field lines it is channelled along them to the magnetic poles. This leads to a roughly radial accretion flow near the poles. The geometry of this accretion near the poles is dictated by how the blobs attach themselves to the field lines. In an idealised symmetric case, it is possible to have an accretion column that is a hollow cylinder structure (Frank et al. 2002). The majority of systems do not fall into this category since they may have e.g. an offset between the orbital and magnetic axes, this leads to an accretion curtain being formed (see Figure 1.8). Most systems will also have the blobs attach themselves to the magnetic field at a range of distances, this will have the effect of causing a more ‘filled’ cylinder accretion column structure.

Material channelled into a small fraction of the surface

The size of the magnetosphere dictates where the in falling material is ‘captured’ by the magnetic field. Once attached to the field it is channelled to the two magnetic poles of the WD, this has the effect that only a small

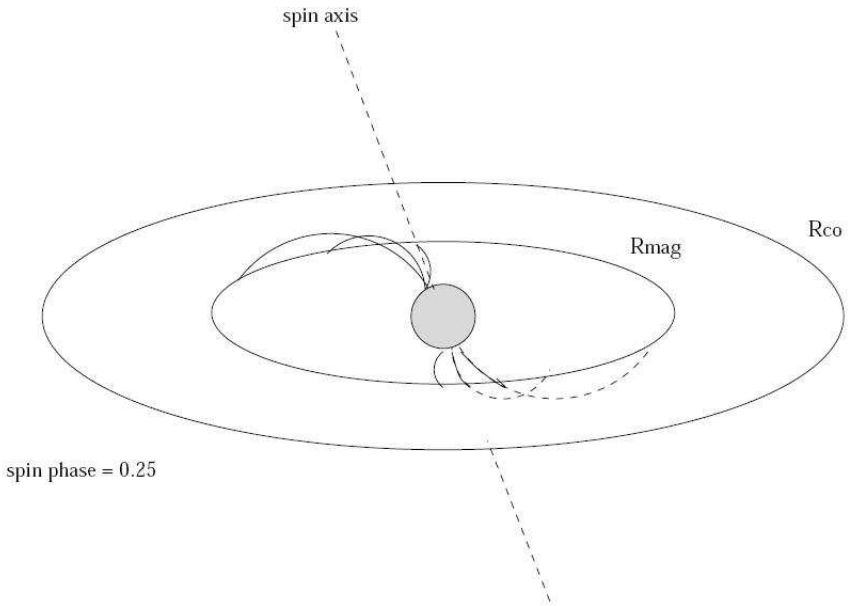

Figure 1.8: An accretion curtain. (Harlaftis & Horne 1999)

fraction of the surface will have material accreting on to it. Using geometrical arguments it can be shown that the fraction of the surface accreted on, $f_{\rm disc}$, goes as that shown in Equation 1.13 (Frank et al. 2002).

$$f_{\rm disc} \sim \frac{R_1}{2R_{\rm M}} \tag{1.13}$$

Where R_1 is the radius of the WD and $R_{\rm M}$ is the magnetospheric radius.

Many factors, such as plasma instabilities, contribute to a significant margin of error in calculating $f_{\rm disc}$. There is mounting evidence, from hard X-ray light curves, that the value for $f_{\rm disc}$ is underestimated in IPs using this method (Frank et al. 2002).

One specific study has measured a value of $f_{\rm disc}$ on XY Ari (Hellier 1997). XY Ari is an eclipsing IP with a WD radius of 4.3–7.0$\times 10^6$m, the value of $f_{\rm disc}$ obtained was <0.002, and this was found to wander over a region on the WD of <0.01.

1.6.3 Magnetic drag force

A consequence of having the material described as diamagnetic blobs, and the field described as previously, is that a drag force is present. If the magnetic field is rotating faster than the material in the accretion disc is, then the diamagnetic blobs will experience a net force speeding them up. The opposite is true also. If the

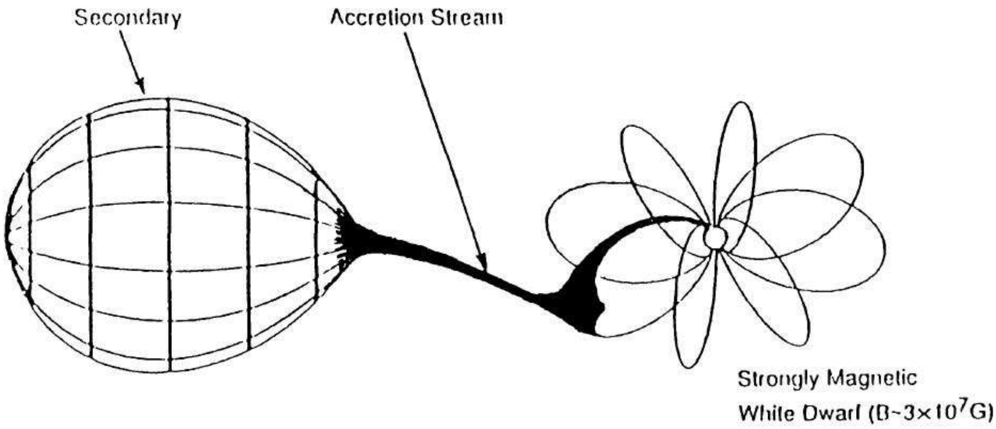

Figure 1.9: Illustration of the accretion geometry in a polar. (Cropper 1990)

magnetic field is rotating slower than the accretion disc material then the material will give up some of its angular momentum and speed the WD up. This process may be modelled by treating this effect as a drag term proportional to the relative velocities of the accretion disc material and the magnetic field (King 1993; Wynn & King 1995).

1.6.4 Polars

The magnetic accretion process is different in polars and IPs. In polars the influence of the magnetic field is such that it can stretch all the way to the L_1 point and beyond. This enables the various mechanisms which synchronise the spin and orbital periods of the system. The knock on effect of this is that the accretion process is greatly affected. The in falling material almost inevitably attaches itself to the magnetic field lines in the vicinity of the L_1 point, so all the material is channelled to the surface of the WD before any kind of accretion disc can form (see Figure 1.9) (Warner 1995; Frank et al. 2002).

1.6.5 Intermediate polars

The magnetospheric radius of IPs may be small enough that an accretion disc may form outside of it in much the same way as in non-magnetic CVs, and the magnetic field may only become relevant in the accretion process close to the surface of the WD, as depicted in Figure 1.10.

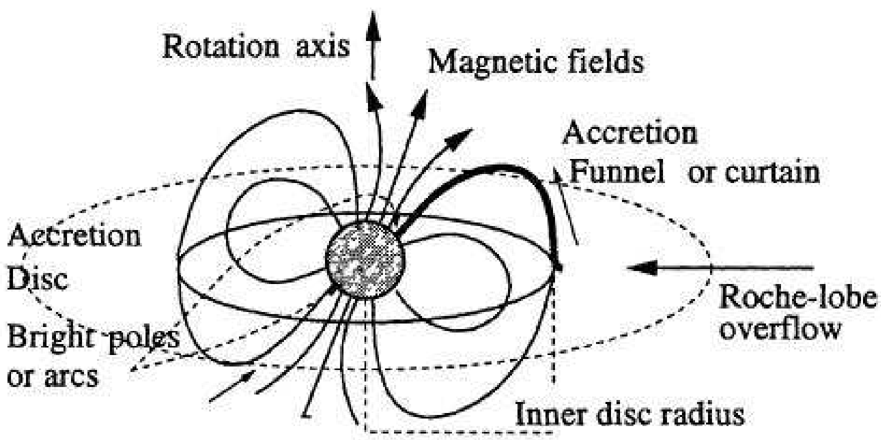

Figure 1.10: Illustration of the accretion geometry in an intermediate polar (Li 1999).

Spin Equilibrium

Taking the idea of the magnetic drag force a stage further and applying it fully to the spin evolution of IPs allows a critical orbital energy, E_{E}, to be found such that any blobs above this value will be ejected from the system, while any below will be accreted (Equation 1.14).

$$E_{\mathrm{E}} \simeq -\frac{1}{2}\Omega J \tag{1.14}$$

Where Ω is the angular velocity and J is the specific angular momentum of the blobs (Frank et al. 2002). The accretion of the blobs will transfer angular momentum to the WD and thus decrease its period, while the ejection of blobs will take angular momentum away from the WD and thus increase its period.

This spin equilibrium process is one which may be observed directly. AE Aquarii is believed to be centrifugally ejecting material, and so spinning down. The time scale of this spin down has been calculated at $\sim 10^7$ years, so what is being observed is a short (when compared to the average WD lifetime) transition to an equilibrium period (Frank et al. 2002). By considering the mass accretion rate onto AE Aqr needed to spin it up to such a short period, Schenker et al. (2002) conclude that AE Aqr may belong to a class of IPs that have evolved from super soft sources. Other systems are known to be evolving in a similar way (see Table 1.2). Taking this into account, it is fair to assume that a vast majority of IPs are in spin equilibrium.

Table 1.2: $\dot{\mathrm{P}}_{\mathrm{spin}}$ evolution in the IPs. (Patterson 1994)(and references therein)

Star	P_{spin}(s)	$\dot{P}_{\mathrm{spin}}(10^{-11})$
AE Aqr	33.0767	<0.004
V533 Her	63.6330	<0.04
DQ Her	71.0654	–0.05
GK Per	351.341	–2.7
YY Dra	529.22	<21
V1223 Sgr	745.506	+2.3
AO Psc	805.203	–6.0
BG CMi	913.496	–7.0
FO Aqr	1254.451	<2.2
EX Hya	4021.62	–3.5

The sidereal effect

Many IPs show an optical signal at various combinations of the spin and orbital frequencies. One common optical signal is at $\omega - \Omega$, this arises from the reprocessing of X-rays from the accretion column (which is varying at the spin period). If there is a structure fixed in the orbital frame (such as a hot spot) then this can absorb the X-rays and re-emit them in the optical at this $\omega - \Omega$ period.

If both magnetic poles can be seen then often a 2ω pulse can be observed in both the optical and the X-ray.

An X-ray signal is also present in stream fed accretion cases at $\omega - \Omega$, this arises due to the accretion region on the WD migrating around the magnetic pole as the system rotates. If there is an offset between the magnetic and spin axes then the stream will flip to the opposite pole at half of this beat period.

Other, more complex periodicities are sometimes seen in IPs. If the amplitude of the spin modulation varies over the orbital cycle (due to e.g. the disc structure obscuring the WD), then this gives rise to the two sidebands $\omega - \Omega$ and $\omega + \Omega$. If the disc was such that it varied at twice the orbital frequency then $\omega - 2\Omega$ and $\omega + 2\Omega$ would exist. If the disc topology is complex and cannot be described by a simple sinusoid, but instead a series of sinusoids at various multiples of the orbital period, then each of these would appear as a sideband.

A similar argument can be used for the beat period instead of the spin period. The sidebands of $\omega - \Omega$

would then be ω and $\omega - 2\Omega$. Again, if the disc topology is complex then various other sidebands may be seen (Hellier 2001).

Coupling time

Using the diamagnetic blob approach outlined earlier, and applying the work of Arons & Lea (1980), it may be shown that the blobs are not instantly forced to follow the field lines, but orbit the WD $\gtrsim$ 10 times before they do so. The reason behind this being that the time scale the blobs lose energy due to the magnetic field is as in Equation 1.15 and the dynamical timescale is as in Equation 1.16. Where c_{A} is the Alfven speed, m is the mass of a blob, B is the magnetic field, and l is the length scale of a blob. Realising these two time scales with typical IP parameters yields the $\sim$10 rotation period value, since $t_{\mathrm{drag}} \sim 10 t_{\mathrm{dyn}}$. The flow will, therefore, not have a sudden transition from gravitational flow to magnetic, but a gradual change where the magnetic field takes on an ever increasing importance until it is the dominant force. During this transition period the material may orbit the WD $\sim$ 10 times (Wynn & King 1995).

$$t_{\mathrm{drag}} = \frac{c_{\mathrm{A}} m}{B^2 l^2} \tag{1.15}$$

$$t_{\mathrm{dyn}} = \left(\frac{r^3}{G M_1} \right)^{1/2} \tag{1.16}$$

1.7 Shock

1.7.1 Background

In mCVs the magnetic field is strong enough to funnel the accreting plasma to the poles. In this polar region, the velocity of the radially in-falling material is close to the free fall velocity, which for typical mCVs, is in the range 3,000–10,000 km s^{-1}. When compared to the sound speed ($\sim$ 100 km s^{-1}) this velocity is very large so a shock therefore develops (Figure 1.11) (Patterson 1994). The shock may formally be defined as the region where the gas pressure is equal to the ram pressure.

In the region between the shock and the WD surface, the material is cooled as it descends and so a temperature and density stratification occurs. This is where most of the energy is released in the form of X-rays.

Typically, the range of energy of the radiation is in the 10–40keV region, sufficient to ensure all of the in-falling material is ionised (Wu 2000).

The height of the shock is an important factor, since if it occurs below an optically thick region then it will not be directly visible. The radiation will be seen as a blackbody emission from the region it was absorbed by. If the shock is above an optically thick or below an optically thin region then it may be seen directly. It has been shown that the shock is usually at a height above the photosphere that allows it to be seen directly (Frank et al. 2002).

An equilibrium shock height will exist, since if the post shock material cannot radiate the energy away faster than it is being deposited, then it will heat up and expand, rising the height of the shock and increasing the emission area. Conversely the opposite it true, if energy is being radiated away faster than it is being supplied then the emission region will shrink and a new equilibrium position achieved (Warner 1995). This idea is contradicted by the notion of giving the shock a small radial velocity. If the shock has a small velocity in the direction away from the surface then in the shock rest frame, the in-falling material will be arriving faster and the shock temperature will rise. If this process leads to a longer cooling path then material will aggregate on the surface of the WD. This extra material will increase the pressure of the post shock region and thus raise the height of the shock above the surface by imparting to it a further radial velocity up wards, and so a positive feedback loop is formed (Wu 2000). With these two opposing ideas it is clear that there are many aspects of the shock that are not completely understood.

1.7.2 The standard model

When describing the shock region the standard model gives a good first approximation of the processes involved. The key approximation is that the electron and ion temperatures are equal during the entire accretion process.

Pre-shock

This is the region the accreting material passes through on its way to the shock. The material will typically be approximately radially falling towards the WD at close to the free fall velocity. The exact path taken is dependent on the magnetic field topology. The radiation given off below the pre-shock will ensure that the material is fully ionised.

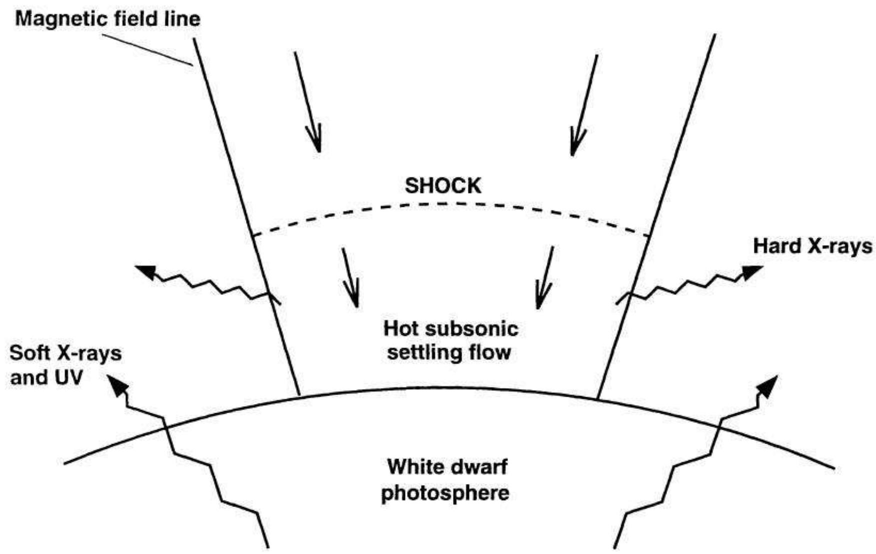

Figure 1.11: Illustration of the geometry of the shock region with radially in falling material.(King 1995)

Post-shock

The post shock is the region the material falls through after emerging from the shock all the way down to the WD surface. It is in this region that a vast majority of the radiation is emitted.

Jump conditions

In the standard model the pre and post shock conditions may be related by the use of the Rankine-Hugoniot strong-shock jump conditions (Equations 1.17, 1.18 & 1.19) (Wu 2000).

$$v_{\text{post}} = \frac{1}{4} v_{\text{pre}} \approx \frac{1}{4} v_{\text{ff}} \tag{1.17}$$

$$\rho_{\text{post}} = 4\rho_{\text{pre}} = \frac{4\dot{m}}{v_{\text{pre}}} \approx \frac{4\dot{m}}{v_{\text{ff}}} \tag{1.18}$$

$$kT_{\text{post}} \equiv kT_{\text{s}} \approx \frac{3}{32} m_{\text{H}} v_{\text{ff}}^2 \tag{1.19}$$

Where subscripts *pre* and *post* refer to the pre-shock and post-shock regions respectively, v is velocity, v_{ff} is the free fall velocity, ρ refers to the density, $\dot{m}$ is the specific accretion rate along the flow (kg m^{-2}s^{-1}), T is the temperature, T_{s} is the temperature immediately after the shock, and m_{H} is the atomic mass of hydrogen.

This assumes an adiabatic index of 5/3.

For typical WD parameters (i.e. about a Solar mass, radius of 10^7m, and an accretion rate of $\lesssim 10$ kg m^{-2}s^{-1}), $v_{\rm post} \sim 10^6$m s^{-1}, $\rho_{\rm post} \sim 10^{-2}$kg m^{-3}, and $kT_{\rm s} \sim$ few keV.

Shock conditions

The shock is the region where the pre and post shock conditions must be equal. This is achieved by a very rapid change in the conditions over a relatively short distance. In the standard model the electrons and ions are assumed to be able to exchange energy efficiently enough that this shock is the same for both species.

The temperature of the shock is that given by Equation 1.20, this varies from Equation 1.19 slightly by introducing the mean molecular weight.

$$kT_{\rm s} \approx \frac{3}{8}\frac{\mu G M_{\rm wd} m_{\rm H}}{R_{\rm wd}} \tag{1.20}$$

where μ is the mean molecular weight (Wu et al. 2003). Taking Nauenberg's mass-radius relation and using the mean molecular weight of solar abundances gives a relation which may then be used to calculate the mass of the WD given the temperature of the shock directly (Fujimoto & Ishida 1997). Alternatively, the temperature of the shock may be calculated from a given mass.

The shock height is determined approximately by the free fall velocity and the cooling time. The cooling time depends on the efficiency of the different cooling mechanisms, for instance, the cooling time for Bremsstrahlung radiation is given by Equation 1.21.

$$t_{\rm br} \sim \frac{3 n_{\rm e} k T}{\Lambda_{\rm br}} \tag{1.21}$$

where $\Lambda_{\rm br}$ is the Bremsstrahlung cooling function (see e.g. Rybicki & Lightman (1986)) and $n_{\rm e}$ is the electron number density. If Bremsstrahlung cooling is the dominant cooling effect, then the cooling time will be close to that of Equation 1.21, a typical value of this would be $\sim$0.1 s. Other cooling effects will be present, such as cyclotron emission etc, but the cooling time, and thus the shock height, will only become dependant on these when they are significantly efficient.

Hydrodynamics of the shock

The equations which concisely describe the flow at the shock are the continuity equation, the momentum conservation equation, ion-energy and electron energy Equations (Equations 1.22, 1.23, 1.24 and 1.25)(Wu 2000).

$$\frac{d}{dt}\rho + \rho(\nabla \cdot \mathbf{v}) = 0 \tag{1.22}$$

$$\frac{d}{dt}\mathbf{v} + \frac{1}{\rho}\nabla(P_{\mathrm{e}} + P_{\mathrm{i}}) = \mathbf{g} + \mathbf{f}_{\mathrm{rad}} \tag{1.23}$$

$$\frac{d}{dt}P_{\mathrm{i}} - \gamma\frac{P_{\mathrm{i}}}{\rho}\frac{d}{dt}\rho = -(\gamma - 1)\Gamma_{\mathrm{ei}} \tag{1.24}$$

$$\frac{d}{dt}P_{\mathrm{e}} - \gamma\frac{P_{\mathrm{e}}}{\rho}\frac{d}{dt}\rho = -(\gamma - 1)\left[\nabla \cdot (\mathbf{q} + \mathbf{F}_{\mathrm{rad}}) - \Lambda_{\mathrm{h}} - \Gamma_{\mathrm{ei}}\right] \tag{1.25}$$

Where $P_{\mathrm{e,i}}$ refers to the electron and ion pressures respectively, $\mathbf{g}$ is the gravitational force, $\mathbf{f}_{\mathrm{rad}}$ is the radiative force, γ is the adiabatic index of the gas, Γ_{ei} is the volume exchange, $\mathbf{q}$ is the heat flux, $\mathbf{F}_{\mathrm{rad}}$ is the radiative flux, and Λ_{h} is the heating function.

If the radiation is assumed to be optically thick then the hydrodynamics equations are coupled to the radiative-transfer equation (Equation 1.26)(Wu 2000).

$$(\mathbf{n} \cdot \nabla)I(\mathbf{r}, \mathbf{n}, \nu) = -\chi(\mathbf{r}, \mathbf{n}, \nu)I(\mathbf{r}, \mathbf{n}, \nu) + \eta(\mathbf{r}, \mathbf{n}, \nu) \tag{1.26}$$

Where I is the intensity of the radiation, χ is the extinction coefficient, η is the emissivity, and $\mathbf{n}$ is the normal vector of the radiation propagation. Solving the hydrodynamics equations and the radiative-transfer equation simultaneously is non-trivial, various simplifications have been made to make this feasible.

Settling material on the surface

As noted earlier, the material is slowed down as it enters the shock so that the condition that it is stationary at the WD surface is met, this is known as the stationary wall condition. This appears to be a physically correct boundary condition, but the application of it affects models greatly. Hypothesising that all the material lands in exactly the same spot on the surface will inevitably lead to an infinitely dense region. The nature of simulations will mean that this artificially skews any results. With this in mind, any results from simulations must, as always, be given a full dose of cynicism.

It is thought that some material may settle on the surface by avoiding the shock and then burrowing into the WDs photosphere (Patterson 1994). This will have the effect that radiation is given off by the surface of the WD directly, as a blackbody at a temperature of about 10^6K (Wu et al. 2003). This process will mean that the energy going into the shock will be lowered since some of the gravitational potential energy is given off directly at the WD surface, as a consequence the shock temperature may be lowered.

Models of the standard model

Using the ideas put forward for the standard model, leads to a scenario where as material flows from the inner edge of a truncated accretion disc to the WD surface, it goes through a shock and is then cooled by various cooling mechanisms (each of varying importance at different areas of the flow). To solve all these simultaneous effects, or even to simulate them, is non-trivial. A simple power law was therefore proposed in which the total cooling, Λ, is given by $\Lambda \propto \rho^2 T^\alpha$ where α is the temperature power law index and can take a range of values, but corresponds to pure Bremsstrahlung when equal to 1/2 (Chevalier & Imamura 1982). This power law idea has been developed extensively with a more sophisticated model now available, where the in-falling material is allowed to diffuse away near to the bottom of the post-shock flow and so merge smoothly with the WD atmosphere (Wu & Cropper 2001).

1.7.3 The not so standard model

The electrons and ions serve different processes in pre and post shock regions, the ions are carriers of kinetic energy and momentum, while the electrons are responsible for much of the radiation. This means that if the two species cannot efficiently transfer energy between one another then they will become thermally decoupled, and the flow considered two temperature. The equipartition timescale for electron-ion collisions, t_{ei}, is given in Equation 1.27.

$$t_{\mathrm{ei}} \sim \frac{3}{2}\frac{n_{\mathrm{e}}k(T_{\mathrm{i}} - T_{\mathrm{e}})}{\Gamma_{\mathrm{ei}}} \tag{1.27}$$

where Γ_{ei} is the rate of energy exchange due to electron-ion collisions (Saxton et al. 2005). This then gives an inequality from which the validity of the one temperature (standard) model can be seen. If the flow

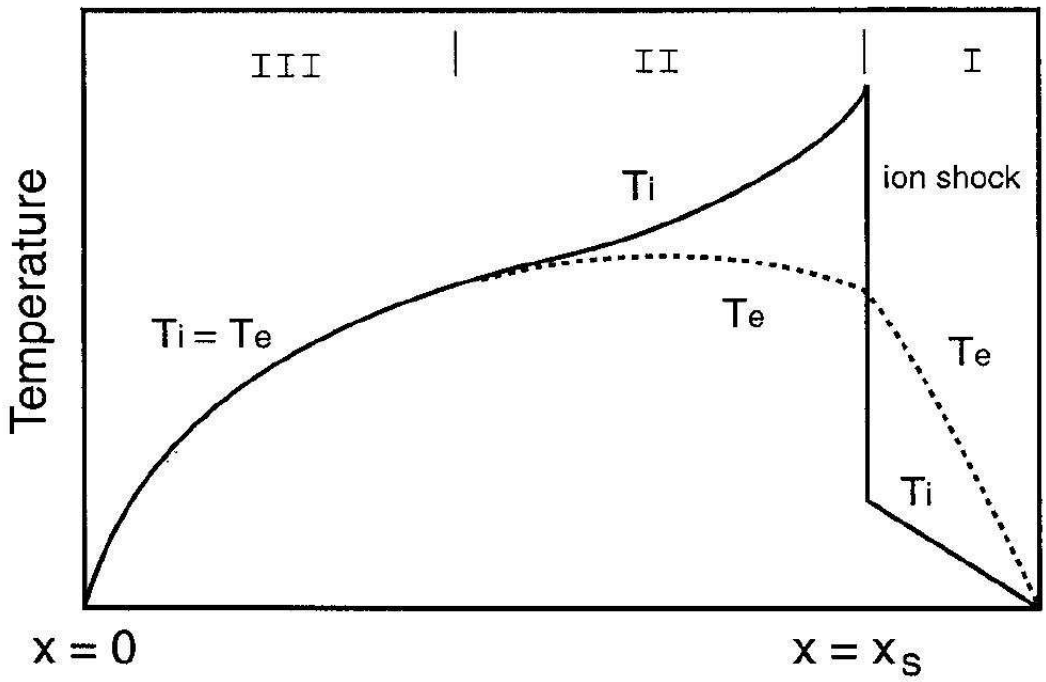

Figure 1.12: Schematic illustration of the ion and electron temperature profiles in the two temperature regime. The horizontal axis represents the height above the WD surface, with x_s being the height of the shock (Wu 2000).

considered is dominated by Bremsstrahlung cooling then $t_{\rm ei} << t_{\rm cool} \sim t_{\rm br}$ (since Bremsstrahlung occurs due to particle interaction) and therefore two temperature effects are unimportant. If cyclotron cooling is dominant then the electrons and ions are not interacting frequently, therefore $t_{\rm ei} >> t_{\rm cool} \sim t_{\rm cyc}$ and two temperature effects are important. Typical values of $t_{\rm ei}$ may therefore be $\sim$ few sec. If the electrons and ions are thermally decoupled and electron conduction of energy is efficient, then energy may be conducted through the ion shock by the electrons, leading to a pre-heating of the in falling material (see Figure 1.12).

This scheme complicates the description further and leads to a set of transcendental equations (Wu 2000).

1.7.4 Numerical models

While both the one temperature and two temperature models may describe the dynamics of the shock region impeccably well, they are incredibly difficult to implement into a numerical simulation. Due to this difficulty, only regimes where time dependence has been neglected, or the dimensionality reduced to just one dimension have been modelled. An example of one of these models is Fischer & Beuermann (2001) who have a one-dimensional stationary radiation hydrodynamic model of polars for a short accretion column. They derive the temperature and density profile for a range of $\dot{m}$ and B typical for polars. They then go on to use these values to calculate the emission spectra they would expect Bremsstrahlung and cyclotron emission to produce. Once a trend has been found in their model a further scaling has to be made to take account of the one-dimensionality of their model. While this gives an insight into the processes it is not a full description, what is needed is a full three dimensional, time dependant, two temperature model to really test the validity of the models.

Other factors may be missing from the simulations too, for instance the boundary conditions have an important effect, as noted earlier, and other mechanisms, such as the material accreting directly onto the surface have been suggested but not incorporated into any of the models in a consistent way.

Then there is the fundamental problem of the discretisation of time and space, this is the basis of many discrepancies in numerical models (Rapaport 2004). This can be illustrated in modelling the shock, where two different groups have obtained different answers to the same problem by using different discretisation schemes (Langer et al. 1982; Imamura et al. 1984).

1.8 Radiation

A simple, yet naive, description of the luminosity, L, of radiation given off by an accreting WD is given in Equation 1.28.

$$L \approx GM\dot{M}/R \approx 10^{34}\dot{M}_{17} \quad \text{erg s}^{-1} \tag{1.28}$$

where all the variables relate to the WD conditions and $\dot{M}_{17}$ is the accretion rate in units of 10^{17} g s^{-1}. This gives a value for the luminosity which is larger than those observed by approximately two orders of magnitude. A more accurate description can be achieved when the nature and position of the radiation sources are considered.

Magnetic CVs emit radiation in X-ray, UV, optical and sometimes radio bands, the strength of the emission is different for the polars and the IPs. The polars are typically strong soft X-ray sources ($\lesssim 0.1$keV), and the IPs hard X-ray sources, (few 10s keV).

In general, the dominant radiation processes are Bremsstrahlung and cyclotron emission, the former being heavily dependant on temperature and density, and the latter strongly dependant on the geometry of the system.

An increasing number of IPs are being found that also emit blackbody radiation.

1.8.1 X-ray

Most cataclysmic variables emit X-ray radiation to some degree. The source of the X-rays in the non-magnetic systems is the boundary layer between the disc and the WD (see e.g. the dwarf nova HT Cas (Mukai et al. 1997)). The magnetic CVs emit much more X-ray radiation. This is due to the funnelling of the same amount of accreting material into accretion columns (which have a smaller volume), which then give rise to a shock. It is below this shock that the X-rays are given off from the plasma which often has a temperature in excess of 10 keV. At these temperatures the plasma will radiate Bremsstrahlung radiation.

Bremsstrahlung radiation

Bremsstrahlung radiation (or free-free radiation) is a result of the acceleration of charged particles. This acceleration occurs due to the Coulomb interaction of approaching charged particles. The acceleration may act as to slow the particles or to deflect them. In either case an acceleration is involved and thus radiation is given off. The radiation may be caused by electrons or protons, but due to the small rest mass of electrons, and thus relative ease of acceleration, electrons are the particle species usually considered.

The formal definition of the emission, $\varepsilon_\nu^{\rm ff}$, from Bremsstrahlung radiation is that given in Equation 1.29.

$$\varepsilon_\nu^{\rm ff} = 6.8 \times 10^{-51} Z^2 n_{\rm e} n_{\rm i} T^{-1/2} e^{-h\nu/kT} \bar{g}_{\rm ff} \quad \text{W m}^{-3}\ \text{Hz}^{-1} \tag{1.29}$$

Where Z is the ion charge, $n_{\rm e,i}$ are electron and ion densities, T is the temperature, ν is the frequency of radiation, and $\bar{g}_{\rm ff}$ is the velocity averaged Gaunt factor (Rybicki & Lightman 1986). Gaunt factors are a correction to a classical approach of modelling to achieve an answer more consistent with quantum mechanics. A suitable value for the Gaunt factor, for typical mCV conditions, is that outlined in equation 1.30 (Paradijs & Bleeker 1997). Figure 1.13 (dashed line) shows a plot of Bremsstrahlung emission for typical mCV parameters.

$$\bar{g}_{ff}(\nu, T) = \frac{\sqrt{3}}{\pi} \ln\left(\frac{kT}{h\nu}\right) \tag{1.30}$$

As material falls toward the surface of the WD it cools and the density of material increases (see section 1.7), this means that different strata will be emitting different amounts of Bremsstrahlung due to the temperature and

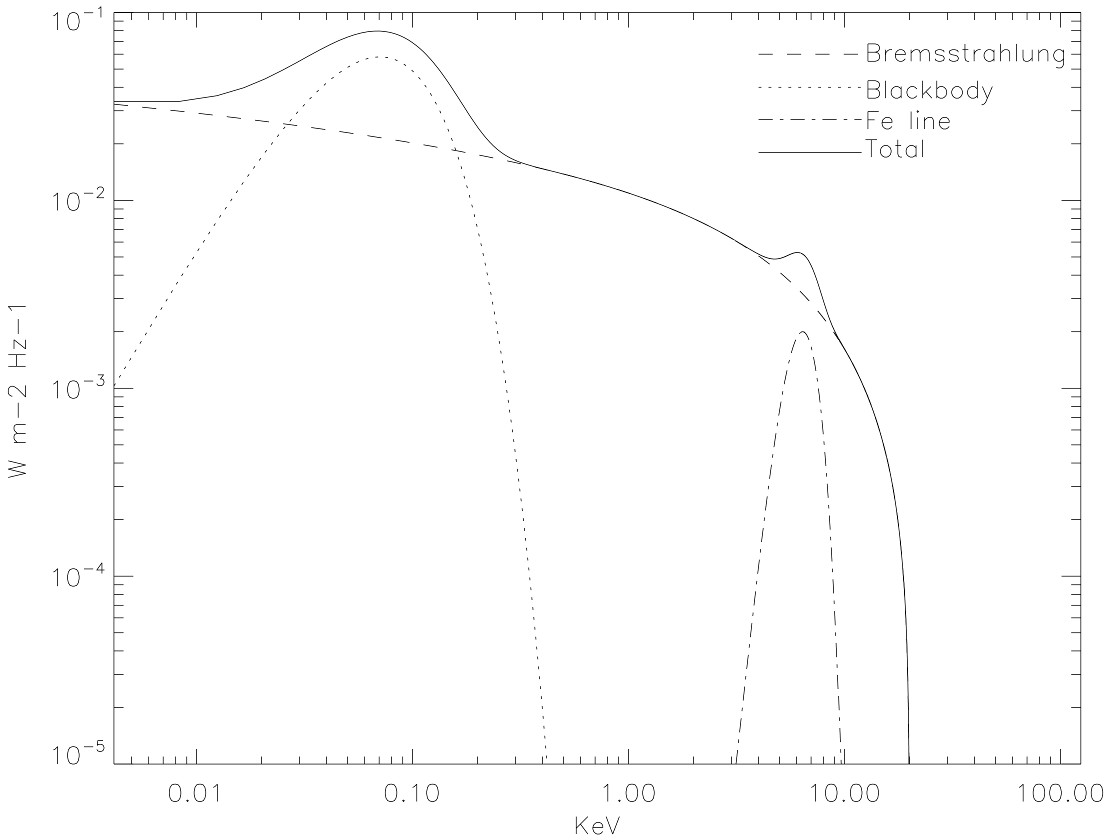

Figure 1.13: Simulated X-ray emission spectrum of an accretion column. The dashed line corresponds to a 20 keV thermal Bremsstrahlung emission, the dotted line a 25 eV blackbody emission, and the dash-dot line a Gaussian centred at 6.4 keV to represent the Fe features. The solid line is the summed emission.

density dependencies. An ideal representation of the Bremsstrahlung radiation would be a multi-temperature multi-density plot, this is non-trivial, and as such often single-temperature single-density models are used.

Blackbody radiation

A soft X-ray blackbody component has been found in an increasing number of IPs. Typically this is seen to be emitting with a temperature of a few tens of eV. There is no consensus on the origin of this component, most believe it comes from the WD surface, but there is no agreement on whether it comes from reprocessed hard X-rays or from blobs avoiding the shock and heating the surface directly. The equation describing blackbody radiation is

$$I_\nu(T) = \frac{8\pi h\nu^3}{c^2}\frac{1}{e^{\frac{h\nu}{kT}}-1} \quad \mathrm{W\ m^{-2}\ Hz^{-1}} \tag{1.31}$$

where the symbols have the same definitions as before. A plot of a blackbody is shown in Figure 1.13 (dotted line).

Iron features

Iron features are ubiquitous in IPs between six and seven keV. Sometimes three iron emission features can be seen, but they are often blended into one as a result of the poor energy resolution of most X-ray detectors. The three lines are: the fluorescent (Fe Kα) at 6.4 keV and the thermal plasma features at 6.7 keV (He-like Fe) and 7.0 keV (H-like Fe) (Ezuka & Ishida 1999).

The fluorescent line emission occurs as high energy X-rays hit the iron atoms and expel electrons from inner orbits. Electrons from outer orbits then ‘fall’ into the inner orbits and emit radiation. For the iron atoms the transition from the L shell to then K shell is called Fe Kα, and it emits at 6.40 keV. This is thought to come mostly from material around the shock region and as such is related to the column density of line of sight material. As well as this some of this emission comes from reflected radiation from the WD surface (see e.g. Beardmore et al. (1995)).

The H-like Fe line at 7.0 keV occurs when electrons are captured by completely ionized iron ions (Fe XXVI). This gives rise to Balmer-like emission. The 6.7 keV (He-like Fe) line is from the Fe XXV ions.

Emission from various different transitions in the H-like and He-like ions and the bulk motion of the accretion stream will have the effect of broadening the emission lines. Typically each of the iron lines may have an equivalent width of approximately 0.1 keV (see e.g. Ezuka & Ishida (1999)). A plot of an iron line is shown in Figure 1.13 (dash-dot line).

Absorption

At the high temperatures seen in IPs the emission region is generally assumed to be optical thin. This means that there will be no self absorption of the emission by the emitting region.

There are several different absorption processes and locations in an IP. Each will affect different wavelength radiation differently. Here only the absorption applicable to the X-ray radiation is considered.

White dwarf

Approximately half of the radiation given off by Bremsstrahlung emission will be directed toward the WD. The WD is thought to have a small reflectivity (less than 0.3 at 10 keV (Ezuka & Ishida 1999)), therefore a relatively small amount will be reflected. The rest of the radiation will be absorbed by the photosphere and, presumably, re-emitted as blackbody radiation.

Accretion column

Close to the surface of the WD the accretion column is sufficiently ionized for it to scatter the emitted radiation. This effect, electron scattering, is small and hence is usually ignored by the optically thin approximation. Rosen (1992) showed that this effect may contribute a few percent towards the modulation depth of a typical IP. However, the line of sight along which this effect would be most prevalent coincides with the largest expected effect from photoelectric absorption (see below), and therefore would be virtually unnoticeable.

Disc

The matter accreting around the WD originates from the donor star and will be mostly hydrogen. Taking this into account a description of the optical depth for photoelectric absorption, $\tau_{\rm pe}$, for energies, E, and number density, $N_{\rm H}$ (atoms cm^{-3}), can be formulated (as in Equations 1.32 & 1.33) (Norton 1988).

$$\tau_{\rm pe} \simeq 10^{-21.8} E^{-2.7} N_{\rm H} \quad \text{for} \quad 0.53 \leq E \leq 10\text{keV} \tag{1.32}$$

$$\tau_{\rm pe} \simeq 10^{-22.0} E^{-2.9} N_{\rm H} \quad \text{for} \quad 0.10 \leq E \leq 0.53 \text{keV} \tag{1.33}$$

Interstellar material

Interstellar space is abundant in neutral hydrogen, opaque to energies of 13.6 – 100eV. This covers the soft X-ray part of the electro-magnetic spectrum, and therefore absorbs much of the radiation given off by mCVs.

Modulation depth

Norton & Watson (1989) studied the modulation depth of the variation associated with the spin period of the WD. They found that the modulation depth varied with energy, the largest modulation being present at lower energies. This was in agreement with the accretion curtain model where the variation is due to the photoelectric absorption in the accretion column. This is also in contrast to the occultation model where modulation occurs due to emitting regions being obscured by the body of the WD.

Spectral profile

Given the expected radiation processes, a typical IP spectrum may be expected to have a photoelectrically absorbed Bremsstrahlung profile (at a temperature of a few keV) with iron features close to 6.4 keV, and a low temperature blackbody component. Figure 1.13 shows what a typical emission spectrum may look like, but when absorption processes are considered a typical observed spectrum is rather different.

1.8.2 Optical cyclotron emission

In an accretion column in a mCV there will be material accreting onto the magnetic poles of the WD. The charged particles in this material will spiral along the magnetic field lines as they fall to the surface (due to the Lorentz force), emitting circularly polarized radiation. This process is known as cyclotron radiation.

The viewing angle, with respect to the magnetic field lines, dictates the kind of radiation observed. When viewed perpendicular to the the field lines linearly polarized radiation is seen, when viewed along the field lines circularly polarized radiation is seen, as shown in Figure 1.14.

The fundamental cyclotron frequency, ν, an electron in a uniform magnetic field emits at is

$$\nu = \frac{eB}{2\pi m_{\rm e}} = 2.8 \times 10^{13} B_7 \text{ Hz} \tag{1.34}$$

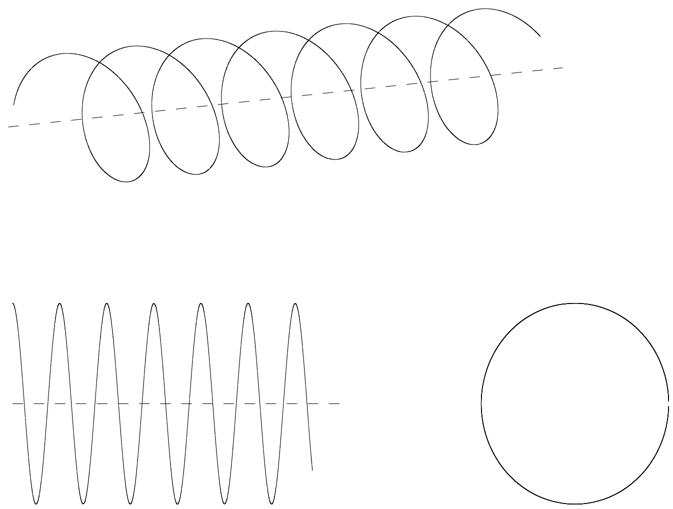

Figure 1.14: Plot of the kind and direction of polarized radiation given off from a charge spiralling along a field line. The upper plot shows a 3D view (dashed line represents the magnetic field), the lower left plot shows shows the projection of the path along the field line, and the lower right plot shows the projection in the direction of the field line.

where B_7 is the magnetic field strength in units of 10^7 G. Or equivalently in terms of the wavelength of the emitted radiation, λ

$$\lambda = \frac{2\pi mc}{eB} = 10.7B_7^{-1}\ \mu\mathrm{m} \tag{1.35}$$

Integer multiples of ν represent the various harmonics of the emission. In terms of the wavelength this is then

$$\lambda = \frac{10.7\mu\mathrm{m}}{n}B_7^{-1} \tag{1.36}$$

Where *n* is the harmonic number.

It may be expected to see the strongest emission at the fundamental frequency, but in fact the optical depth of the plasma is such that it is opaque to the fundamental and low harmonics, so this radiation is reprocessed and eventually emerges as blackbody radiation. It is not until higher harmonics that the plasma becomes optically thin, at this *n*th harmonic the emitted radiation has the wavelength, λ, as given by Equation 1.36. This suggests that in a uniform field if the magnetic field is approximately 10 MG, the radiation lies predominately in the optical or IR.

The magnetic field structure is not uniform in mCVs, but likely a dipole (or similar) topology. This means the field strength will be a function of position above the WD surface. The observed circular polarization will then be strongly dependent on the orientation of the field and the location of the emitter with respect to the observer. This 'beaming' effect, the range of velocities of the electrons, and their varying temperature will have the effect of causing the electrons to emit a broad harmonic structure. By modelling the polarized radiation given off (i.e. simulating the harmonic structure) it is possible to estimate the magnetic field strength of the WD. Wickramasinghe & Meggitt (1985) did this for a range of magnetic field strengths in polars. Their models take into account the magnetic field strength, the temperature, the plasma parameter, and the viewing angle. These four variables cause the modelling to give non-unique solutions for the fitting of the harmonic curve. This can be illustrated in Figure 1.15 where it can be seen that increasing just the optical depth of the T_{e}=10 keV model and decreasing the optical depth in the T_{e}=5 keV model will give very similar results. Variation in B and position angle will complicate things further. As such, without further information (such as the position angle or the electron temperature) it is very difficult to estimate the magnetic field using this method. Despite this, their model has been used extensively in estimating the magnetic field strength in polars by measuring the

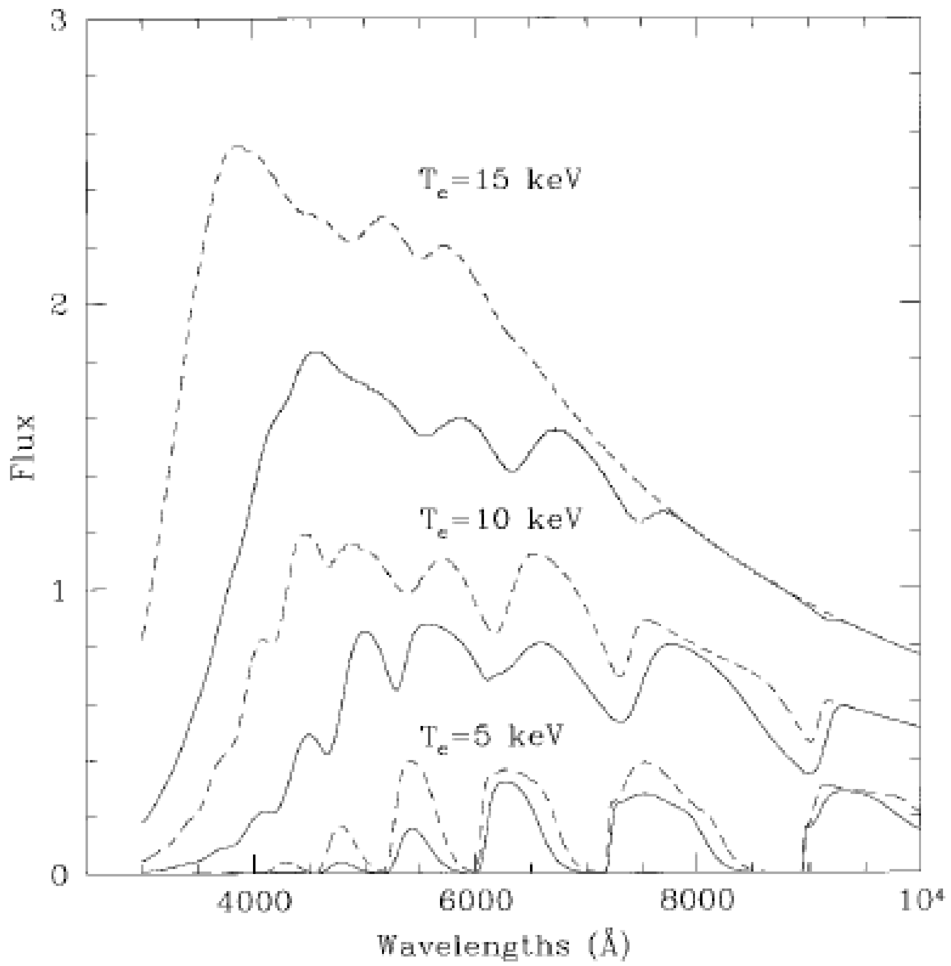

Figure 1.15: Theoretical cyclotron spectra as a function of electron temperature T_e for a viewing angle θ=90°. The solid and dashed curves are for optical depth parameter $\Lambda = 2 \times 10^5$ and $\Lambda = 10^6$ respectively. The magnetic field $B = 30$ MG. Taken from Wickramasinghe & Ferrario (2000).

level of circular polarization in different discrete wave-bands (see e.g. Piirola et al. (1987a,b); Katajainen et al. (2003)) and has also been used in IPs (see e.g. Piirola et al. (1993)). A similar method employed in polars (where there is a generally more cyclotron emission) looks for cyclotron humps in their unpolarized spectra. Subtracting a model of the light form the WD and secondary leaves light primarily from the cyclotron emitting accretion column, this can then be compared to models such as that shown in Figure 1.15.

The polarized light measured in mCVs is generally quoted as a fraction of the total incoming radiation. In polars the source of the unpolarized and polarized radiation should vary at the same period - the orbital period. In IPs however, the situation is more complex. The presence of an accretion disc, that emits at optical frequencies, will dilute the measured polarization. If the flux from the accretion disc varies at any period other than the spin period then this will dilute the signal in a complex fashion. Added to this are the possible presence of a hot spot and the emission from the secondary which will vary at the orbital period.

The geometry of the accretion column is also an issue, since it will affect the visibility of the circular polarization. A very tall and thin accretion column will look different to a short fat one as the location of the circular polarization emitting region will be different. This is the case as these two extremes will have very different densities and temperatures. If the accretion flow topology is such that the accretion column has a much denser region on one side, then the circular polarization will preferentially be produced on the other, less dense, side (Wickramasinghe & Meggitt 1985).

Norton & Watson (1989) validated the accretion curtain model using X-ray variability measurements. This accretion curtain will obscure the column (and therefore the circular polarization emission region) at different spin phases. The geometry of accretion curtain is highly dependent on the topology of the accretion flow - a curtain in a disc flow will look very different to a that in a stream flow. The absorption of the circular polarization is therefore heavily dependent on the accretion flow topology too.

Another likely complexity is that the magnetic field structure of the WD may not be dipole-like (see e.g. Beuermann et al. (2007)). This could lead to multiple accretion columns at multiple magnetic poles. If the magnetic field is close to being a dipole it is also possible that it could be offset from the centre, leading to one pole appearing to be stronger than the other and not at diametrically opposed poles. This complexity is further confounded by the very fact that the accreting material does not come from infinity, in which case even an ideal dipole would not form an accretion column at exactly the position of the magnetic poles.

Given all these complications, it is not possible to be certain what the average magnetic field strength *really* is in IPs. It is possible that estimates of the field strength are over an order of magnitude understated. What is assumed to be low number harmonics of a low magnetic field, may in fact be high number harmonics of a much larger field.

Method of circular polarization detections

Assuming circular polarization in IPs can be measured in a similar way to polars and that IPs are of a comparable field strength, implies that harmonics will be present in the UV-IR. The optimal method to reveal these harmonics would be spin phase resolved circular spectro-polarimetry. This requires very large telescopes with very specialized instrumentation allowing high time resolution data collection. This method has yet to be fully exploited for IPs, therefore the rest of this section concentrates on the more readily available technique of circular photo-polarimetry.

The general principle of circular photo-polarimetry is to measure the fraction of polarized radiation after a $\lambda/4$ wave plate, which converts circular polarization into linear polarization. This process introduces biases however, for example, incomplete $\lambda/4$ retardation by the wave plate. These biases may cause so called 'Stokes parameters cross talks', particularly in the case of targets with non-negligible linear polarization. These cross talks can effectively be eliminated by rotating the wave plate to at least two different wave plate angles and then calculating a single measurement of the circular polarization by using flux values from both positions. This process has an important effect on the temporal resolution of the data, since enough time must be spent integrating on the target to get a good signal to noise value, and if this has to be done multiple times then the temporal resolution will suffer.

By taking simultaneous circular polarization measurements in different pass-bands a clearer understanding of the harmonic structure may be gained. If the pass-bands are defined to have a range comparable to the expected width of the harmonics then comparison of the circular polarization in each band may give an indication of the magnetic field strength. In reality it is unlikely that a harmonic will fall just within a single pass-band, and also be the only one in that pass-band.

1.9 Known intermediate polars

The incidence of long spin period IPs is almost certainly underestimated due a temporal selection effect across all wavelengths. The typical length of observational time on telescopes is such that long spin period systems may not be identified due to the lack of complete periods observed. This will be exacerbated if the spin pulse profile is complex due to a non-uniform accretion disc, or if the magnetic field produces a multi-pole accretion column situation. Even if a relatively long base line is available for observations, a varying accretion rate could still mask a long period coherent modulation from the WD.

The occurrence of short spin period IPs is also probably underestimated, but for a different reason. The short period systems may be accreting at a higher rate than the long period systems, this leads to a much greater volume of absorption material near the accreting region, and therefore a possible under counting (Patterson 1994)

This chapter has so far introduced different features observed in some intermediate polars. Not all of these features are ubiquitous amongst the IPs, this makes a formal definition of the class troublesome. As such different authors tend to have different definitions and therefore different members of the class.

A popular, and reasonably up to date, list of IPs is that of Mukai (2008), in which the absence of certain characteristics is treated at the discretion of the author and therefore not an absolute reason to not be included in the class.

Typically the features required to be considered an IP include some combination of:

1. X-ray spin period modulation - Generally seen as the most important characteristic, since this confirms the accretion column structure/magnetic nature/WD rotational period.
2. Iron features in the X-ray spectrum.
3. Possible orbital X-ray modulation.
4. Energy dependent spin modulation depth.
5. Bremsstrahlung spectrum.
6. Optical circular polarization.

Recently some of these features have been called in to question as a means to classify an IP. Ramsay et al. (2008) argue that since X-ray spin modulation will only be present when the magnetic axis and the spin axis are significantly misaligned, that there exist a whole population where this is not the case.

For the purpose of the rest of this thesis the list of Mukai (2008) is used (see Table 1.3).

Table 1.3: Confirmed IPs, adapted from *The Catalog of IPs and IP Candidates by Right Ascension, Version 2008a* with updated periods. Sorted according to R.A.

Variable name	Alternative name	R.A.	Dec	$P_{\rm orb}$/hr	$P_{\rm spin}$/s
	IGR J00234+6141	00 22 57.63	+61 41 07.8	4.033	563.5
	1RXS J002258.3+614111				

Continued on the next page ...

Continued from the previous page

Variable name	Alternative name	R.A.	Dec	$P_{\rm orb}$/hr	$P_{\rm spin}$/s
V709 Cas	RX J0028.8+5917	00 28 48.9	+59 17 21.6	5.341	312.78
	XSS J00564+4548	00 55 20.0	+46 12 57	?	465.68
	1RXS J005528.0+461143				
XY Ari	H0253+193	02 56 08.15	+19 26 33.8	6.0648	206.3
GK Per	Nova Persei 1901	03 31 12.0	+43 54 17	47.9233	351.
V1062 Tau	H0459+246	05 02 27.59	+24 45 22.1	9.952	3780.
UU Col	RX J0512.2−3241	05 12 13.22	−32 41 39.8	3.45	863.5
TV Col	A0526−328	05 29 25.53	−32 49 05.3	5.4864	1911.
TX Col	1H0542−407	05 43 20.27	−41 01 56.1	5.718	1911.
V405 Aur	RX J0558.0+5353	05 57 59.27	+53 53 45.1	4.16	545.456
MU Cam	1RXS J062518.2+733433	06 25 16.23	+73 34 38.9	4.7186	1187.25
	1RXS J070407.9+262501	07 04 08.67	+26 25 10.9	∼4.0	480.
BG CMi	3A0729+103	07 31 29.04	+09 56 21.8	3.2349	913.5
	Swift J0732.5−1331	07 32 37.64	−13 31 09.0	5.604	512.42
PQ Gem	RE0751+14	07 51 17.33	+14 44 23.9	5.1926	833.41
HT Cam	RX J0757.0+6306	07 57 01.33	+63 06 01.4	1.4331	515.06
DW Cnc		07 58 53.07	+16 16 45.4	1.4350	2314.66
WX Pyx	1E 0830.9−2238	08 33 5.75	−22 48 32.6	6-9?	1560.
EI UMa	PG 0834+488	08 38 21.99	+48 38 02.1	6.43	741.6
	1H0832+488				
YY Dra	(DO Dra)	11 43 38.51	+71 41 19.2	3.96	530.
	3A1148+719				
	PG1140+72				
V1025 Cen	RX J1238−38	12 38 16.38	−38 42 46.0	1.41	2147.
EX Hya	4U1228−29	12 52 24.47	−29 14 57.5	1.6376	4021.62

Continued on the next page ...

Continued from the previous page

Variable name	Alternative name	R.A.	Dec	$P_{\rm orb}$/hr	$P_{\rm spin}$/s
NY Lup	1RXS J154814.5−452845	15 48 14.5	−45 28 39.0	9.87	693.01
V2400 Oph	RX J1712.6−2414	17 12 36.43	−24 14 44.7	3.43	927.66
	IGR J17303−0601	17 30 21.50	−05 59 33.5	15.42	128.0
	1RXS J173021.5−055933				
	1RXS J180340.0+401214	18 03 39.67	+40 12 20.6	4.402	1520.
DQ Her	Nova Herculis 1934	18 07 30.12	+45 51 32.7	4.65	142.
V1223 Sgr	4U1851−31	18 55 02.0	−31 09 48	3.366	745.63
V2306 Cyg	WGA J1958.2+3232	19 58 14.48	+32 32 42.2	4.35	1466.66
AE Aqr		20 40 09.7	−00 52 16.3	9.88	33.062
	1RXS J213344.1+510725	21 33 43.65	+51 07 24.5	7.19	570.82
	RX J2133.7+5107				
FO Aqr	H2215−086	22 17 55.49	−08 21 05.4	4.85	1254.
AO Psc	H2252−035	22 55 17.99	−03 10 40.0	3.591	805.2

Chapter 2

RXTE classification of intermediate polar candidates

The results of a campaign to observe six hard X-ray emitting intermediate polar candidates with the Rossi X-ray timing explorer satellite are presented here. By searching for X-ray temporal variations and analysing their spectral features this campaign aimed to determine the candidates' credentials as intermediate polars and decide if they should be included into the class.

This chapter begins with a brief introduction which gives the motivation for this project (Section 2.1), Section 2.2 outlines the aims, Section 2.3 outlines the methodology, Section 2.4 gives the results, discussion and conclusion for each individual target, then Section 2.5 conclude the chapter.

A majority of this work has been published, see Butters et al. (2007, 2008, 2009b) and also Appendix C.

2.1 Introduction

Section 1.9 discussed the defining characteristics of IPs, for the purpose of this survey the main feature required to be considered a bone fide IP was X-ray modulation at a period commensurate with a spin period. Other features were also be considered as additional evidence in support of this classification, but the spin modulation was key here. Currently the range of spin periods in IPs is between 33 s (AE Aqr) and 4022 s (EX Hya) (see Figure 2.1), so any spin periods found here are expected to be in or close to this range.

Some IPs also exhibit X-ray modulation at the orbital period. Parker et al. (2005) showed that this effect is widespread, but not ubiquitous, in their sample of 16 IPs. The orbital periods seen in IPs (in either X-ray or optical) range from 1.4 hr (V1025 Cen) to 48 hr (GK Per) (see Figure 2.1).

Several X-ray telescopes have been utilised to search for X-ray modulation, notably the Advanced Satellite for Cosmology and Astrophysics (*ASCA*) and the Rossi X-ray Timing Explorer (*RXTE*) as well as EXOSAT and GINGA. An important common feature of these telescopes is the range of energies they survey; all are relatively soft. This may have had the effect of skewing the the population of known mCVs toward the softer members.

Recently the hard X-ray telescopes *Swift* and *INTEGRAL* have been unexpectedly finding many existing IPs in their surveys. This allows candidate mCVs to be selected on the basis of being hard X-ray emitters, and therefore may highlight any biases in the identification process.

INTEGRAL has found the confirmed IPs (see Mukai (2008) for confirmed IPs) 1RXS J173021.5–055933, V709 Cas, GK Per, IGR J000234+6141, RXJ2133.7+5107, NY Lup, V1223 Sgr, V2400 Oph, MU Cam and FO Aqr in the 20–100 keV band in its ongoing IBIS survey (Barlow et al. 2006; Bird et al. 2007).

Given the defining characteristic above, here this chapter presents a search for X-ray periodicities in hard X-ray selected candidate IPs using data from pointed *RXTE* observations. Spectral properties are also included in this study.

2.2 Aim

The aim of this study was to determine the credentials of six hard X-ray selected candidate IPs. Period searching of the X-ray light curve showed any modulation that was associated with the spin period, the orbital period, the beat period, or any harmonics thereof. The depth of any modulation seen, as a function of energy, gave an indication as to the absorption processes occurring. Spectral analysis yielded properties of the emission region including temperature and column density.

The candidates picked for this study were suspected IPs which have been observed in the optical, and also in the hard X-ray with either *Swift* or *INTEGRAL*. The candidates are those in Table 2.1.

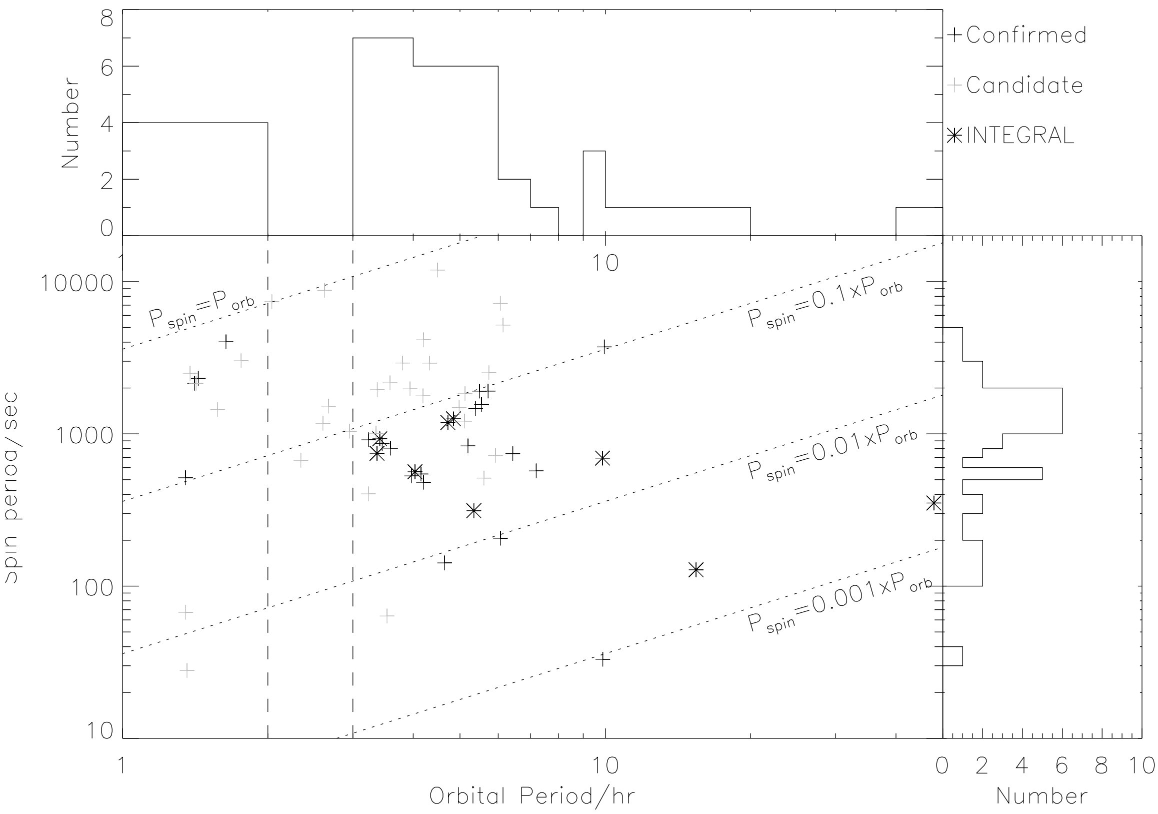

Figure 2.1: Spin and orbit distribution of all confirmed and candidate IPs (as given in Mukai (2008)).

Table 2.1: Targets awarded observing time. The abbreviated name is used henceforth in this chapter. Sorted by R.A.

Target	Abbreviated name[a]	R.A.	Dec
XSS J00564+4548	J0056	00 55 28.1	+46 11 43
SWIFT J0732.5–1331	J0732	07 32 37.5	–13 31 04
XSS J12270–4859	J1227	12 27 58.9	–48 53 44
IGR J14536–5522	J1453	14 53 41.1	–55 21 39
IGR J15094–6649	J1509	15 09 26.0	–66 49 23
IGR J17195–4100	J1719	17 19 35.6	–41 00 55

[a] Used henceforth.

Table 2.2: *RXTE* observing log.

Target	Start time (UTC)	End time (UTC)	Time on target (s)	Good time[a] (s)
J0732	19:12 13/07/07	06:24 15/07/07	56 172	36 240
J1453	03:47 24/11/07	03:59 25/11/07	60 555	31 320
J1227	16:13 28/11/07	16:20 29/11/07	58 183	26 814
J0056	05:27 20/12/07	00:31 22/12/07	84 672	37 800
J1719	18:45 07/01/08	11:16 09/01/08	69 636	35 936
J1509	06:33 30/12/08	14:46 31/12/08	55 702	42 856

[a] Good time is defined as the time that met our selection criteria (see text).

2.3 Method

Data were obtained from the *RXTE* satellite (Bradt et al. 1993) with the Proportional Counter Array (PCA) instrument during cycle 12 (proposal 93009). See Table 2.2 for the observing log.

2.3.1 Data reduction

In each case initial data reduction was done with the standard FTOOLS (version 6.02). This involved:

1. Combining the data sets,
2. Defining a good time interval (GTI) (see below),
3. Selecting the desired columns and the top layer of the detector,
4. Picking a temporal resolution,
5. Selecting the desired energy range,
6. Extracting the data as either a light curve or spectrum,
7. Doing the same for the background,
8. Subtracting the background.

The selection criteria for the GTIs were:

1. An *elevation* greater than 10 degrees (ensures pointing well away from Earth),
2. An *offset* of less than 0.02 degrees (ensures pointing in the right direction),
3. An *electron2* of less than 0.1 (this is a measure of the background noise),
4. A *time_since_saa* of greater than 30 mins (makes sure sufficiently far from the South Atlantic Anomaly),
5. The desired Proportional Counter Unit (PCU) is turned on.

2.3.2 Light curve analysis

Due to the age of *RXTE*, not all of the five PCUs in the PCA are still functional; PCU2 always works with PCUs 3 and 4 working intermittently. So if PCUs 3 and/or 4 were on for a sufficiently long time they were included in the light curve analysis, otherwise just PCU2 was used.

Background subtracted light curves were constructed in each of four energy bands: 2 – 4 keV, 4 – 6 keV, 6 – 10 keV and 10 – 20 keV, as well as a combined 2 – 10 keV band, the temporal resolution on these being 16 s. These were then subjected to period searching algorithms. Two different algorithms were used; initially a variable gain implementation of the CLEAN algorithm and later on in the campaign a red-noise model. A background subtracted light curve was also constructed with a temporal resolution of 128 s for each target so a plot of the unfolded data could be plotted concisely.

CLEAN

The variable gain implementation of CLEAN (Lehto 1997) is a period search algorithm which iteratively deconvolves the window function from a raw data set. It achieves this by following this procedure:

1. Calculate the window function,
2. Calculate the power spectrum,
3. Find the highest peak in the power spectrum,
4. Convolve the window function with a delta function centred on the highest peak,
5. Subtract the convolved window function from the power spectrum,
6. Repeat steps 2–5 approximately 1000 times,

7. Add the remaining noise to the delta functions produced above to create the CLEANed power spectrum.

This method was chosen as the data sets are typically split up into many smaller non-contiguous chunks, and their power spectra therefore display many aliases.

To estimate an error in the calculated periods a Gaussian was fitted to each peak in the CLEANed power spectrum. The width of the Gaussian was taken to be an indication of the error. This method will likely have the effect of overestimating the true error on the period.

Generally CLEAN finds any periodicities in the data, however, sometimes the signal to noise of the resultant CLEAN plot is low. To address this a second period searching method was used in these cases to assess the significance of the periods (see below). This method is very CPU intensive (and therefore time consuming) to run, and so is only used for the low signal to noise cases.

Red noise

In the presence of white noise in the data, the power values in the power spectrum are expected to follow an exponential distribution. However, any correlated noise e.g. red noise, will mean the distribution becomes frequency dependent. This makes estimating the significance limits in the power spectra non-trivial. As accreting systems usually show flickering in their light curves, it is feasible to believe that there may be a significant red noise component in the data. In order to take this into account in the analysis, the technique introduced in Hakala et al. (2004) was used. The data were equally spaced (apart from the large gaps in between different orbits), so the red noise component was modelled by fitting a second order auto-regressive process model to the light curves. This model was then used to generate 50 000 synthetic light curves with similar red and white noise properties, as well as observing window, to the original data sets. The 95.2%, 99.72% and 99.954% (2, 3 and 4σ respectively) significance limits (as a function of frequency) were then calculated.

To estimate the error on the measured periods the raw data was folded at the period found from the period analysis. A curve was then fitted to this folded data. This curve (repeated over the whole data set) was then subtracted from the raw data leaving residual values. These were then shuffled and added to the fitted curve, yielding a new synthetic raw data set. This synthetic data was then analysed as before. This whole process was repeated ~ 200 times and the resulting periods were then used to calculate a standard deviation of periods, which was then used as the error estimate.

This particular analysis was carried out by Pasi Hakala.

Folding and modulation depths

The data were then folded at any candidate periods and phase binned at each energy range using the Starlink period software package. Each folded data set then had a sinusoid fitted to it, this allowed an estimate of the modulation depth to be made by dividing the semi-amplitude by the mean count rate.

2.3.3 Spectral analysis

A mean X-ray spectrum was extracted for each source, and two spectral models applied to find the best fit, using the XSPEC (version 12.2.0) package. The models considered were a photoelectrically absorbed single temperature Bremsstrahlung with a Gaussian at the iron line emission energy, and a photoelectrically absorbed power law with a similar Gaussian. In both cases the column density used for fitting had a lower limit of the Galactic column density (as given by the HEASARC n_{H} tool[1]).

To keep the spectral analysis consistent only PCU 2 was used for each target.

2.4 Individual targets

Individual targets are now presented in order of R.A. Each sub-section begins with a short summary of the history of the object, the data is then considered, and then it finishes with a short discussion and conclusion.

2.4.1 XSS J00564+4548

Background

J0056 was associated with the *ROSAT* source 1RXS J005528.0+461143, and catalogued as an unidentified object in the *RXTE* all sky survey (Revnivtsev et al. 2004). It was found to have a count rate of 0.71$\pm$0.04 ct s^{-1} PCU^{-1} in the 3–8 keV energy band and a photon index of 1.77$\pm$0.23. Analysis by Bikmaev et al. (2006) using *Swift*/XRT archive data revealed two X-ray sources in the *ROSAT* error circle. One source was present at low energy, which they presumed to be a chromospherically active star. The other source showed a typical spectrum of a CV, with an emission feature close to 6.7 keV. Bikmaev et al. (2006) also carried out optical observations with the 1.5 m Russian-Turkish Telescope. Their photometric data indicated a period of approximately 480 s to be present.

[1]http://heasarc.nasa.gov/cgi-bin/Tools/w3nh/w3nh.pl

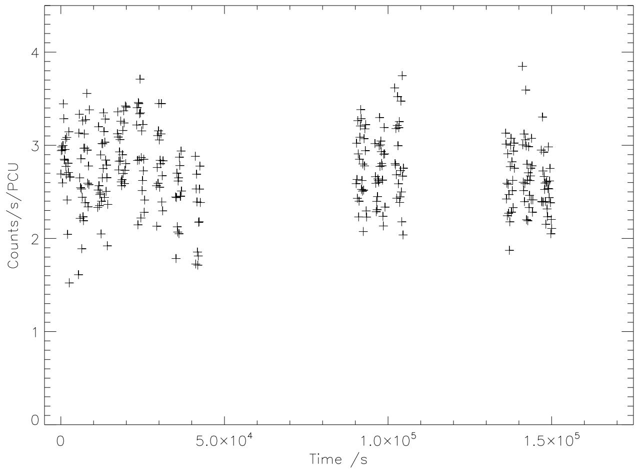

Figure 2.2: 2 – 10 keV background subtracted light curve of J0056. The zero point corresponds to the start of the observations at JD=2454473.283724. The data is binned into 128 s bins. The typical error on each point is ±0.26.

Data

J0056 was observed over two consecutive days (see Table 2.2). The total good time on target (37 800 s) comprised fourteen approximately equal segments of one satellite orbit each. In the 2–10 keV energy band the raw count rate varied between 3.9 and 9.1 ct s^{-1} PCU^{-1}. The background count rate, generated from the calibration files, varied between 2.9 and 4.1 ct s^{-1} PCU^{-1}. Figure 2.2 shows the 2–10 keV background subtracted light curve with a 128 s resolution.

Light curve analysis

A significant ($>4\sigma$) peak was present in the periodogram at ~185 cycles day^{-1} in the 2–10 keV energy band (see Figure 2.3). Analysis of the peak gave a pulsation period of 465.68±0.07 s. The data were then folded in each energy band at this period, Figure 2.4 shows the result of the 2–10 keV energy band (Appendix A shows each energy band folded at this period). There is a clear decreasing trend in the modulation depth with increasing energy (see Table 2.3). Clustered around the 185 cycles day^{-1} peak were a series of smaller peaks, spaced apart by ~8 cycles day^{-1}, the largest of which was at 489.0±0.7 s. There was also one other peak detected at above the 4σ level at ~41 cycles day^{-1} (2 109 s).

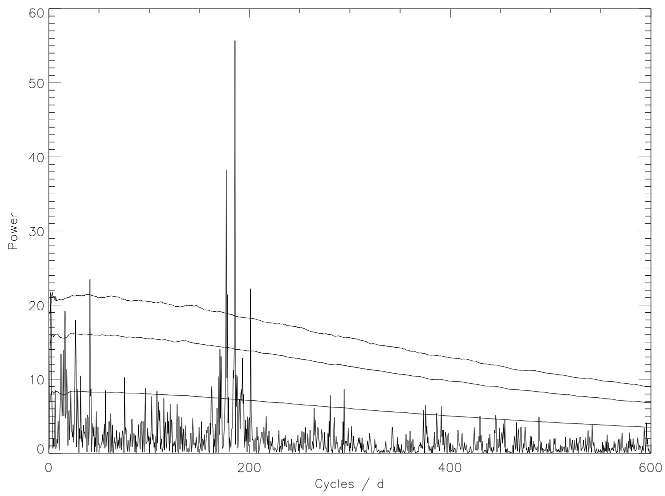

Figure 2.3: 2 – 10 keV periodogram of J0056. Three significance levels, 95.2, 99.7 and 99.954% (2, 3 and 4σ respectively), are superimposed.

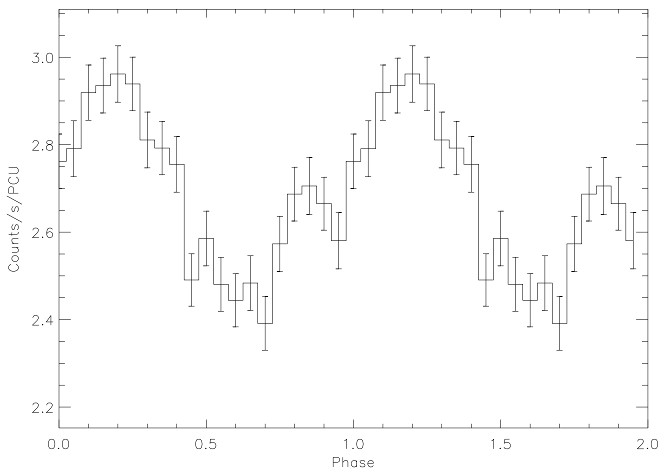

Figure 2.4: 2–10 keV light curve of J0056 folded at the 465.68 s pulse period with an arbitrary zero point. Two cycles are shown for clarity.

Table 2.3: Light curve modulation depth of the pulse profile (folded at the 465.68 s period) of J0056 in different energy bands.

Energy band (keV)	Modulation depth (%)	Fitted mean (ct s^{-1} PCU^{-1})
2–10	8±1	2.69
2–4	14±2	0.59
4–6	9±1	0.93
6–10	5±1	1.17
10–20	8±3	0.60

Table 2.4: Bremsstrahlung (top) and power law (bottom) spectral fitting parameters of J0056. $n_{\rm H}$(Galactic)=0.1×10^{22} cm^{-2}

$n_{\rm H}$ 10^{22} cm^{-2}	kT keV	Γ	Fe keV	$\sigma_{\rm Fe}$ keV	EW keV	$\chi^2_{\rm reduced}$	Flux (2–10keV) 10^{-11} ergs cm^{-2} s^{-1}
0.6±0.3	22±3	–	6.5±0.1	0.3±0.1	0.8	0.8	2.8
1.9±0.7	–	1.7±0.1	6.5±0.1	0.3±0.1	0.9	1.1	2.9

Spectral analysis

The best spectral fit was a simple photoelectrically absorbed Bremsstrahlung model with a Gaussian added (see Figures 2.5 & 2.6, and Table 2.4).

Discussion

The period found here (465.68 ± 0.07 s) was interpreted as the spin period of the WD in J0056. Bikmaev et al. (2006) gave an approximate value of 480 s from their analysis. To obtain an estimate of the error in their period the approximate FWHM of their Lomb-Scargle plot was calculated, which gave 480 ± 20 s. This X-ray period determination therefore is in agreement with their optical data. If the second strongest peak in the periodogram is interpreted as a beat period, then this implies the orbital period must be $\sim$ 2.7 hrs. This places it in the 2–3 hr CV period gap, but we note that there are now several CVs in this range and some mCVs too. This interpretation would also explain the cluster of peaks around the spin period as being various harmonics of the

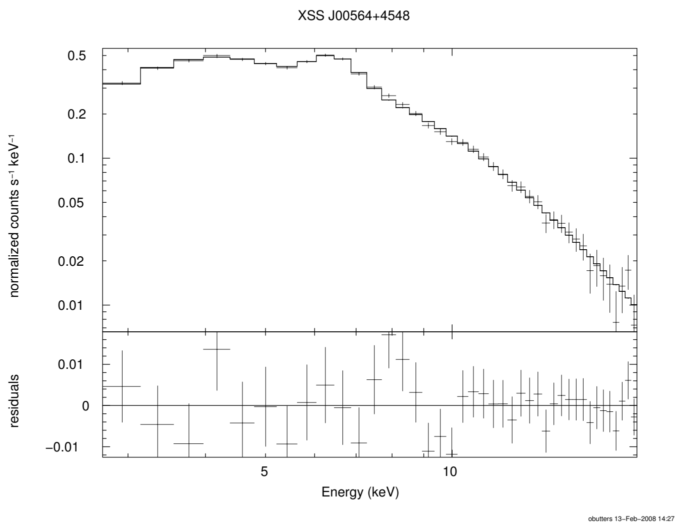

Figure 2.5: 2.5–20 keV mean spectrum of J0056 fitted with a photoelectrically absorbed Bremsstrahlung plus iron line profile.

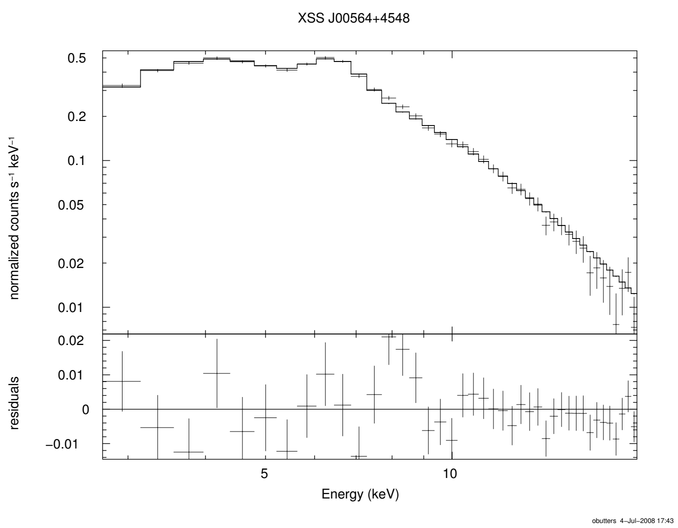

Figure 2.6: 2.5–20 keV mean spectrum of J0056 fitted with a photoelectrically absorbed power law plus iron line profile.

beat period. The origin of the 41 cycles day^{-1} peak is uncertain as it is too short to be interpreted as an orbital period of a typical IP. The energy dependant modulation depth of the folded light curves is common among IPs and indicates an accretion column absorbing structure (Norton & Watson 1989). We also note that the pulse profile of J0056 is very similar in shape to that of FO Aqr (Beardmore et al. 1998).

The spectral fits indicate that the emission process is more likely to be a photoelectrically absorbed single temperature Bremsstrahlung process than one which can be fit with a power law, as is common in IPs. The power law spectral fit is however in agreement with Revnivtsev et al. (2004). The Gaussian at 6.5 keV is identifiable with an iron feature which is also a common aspect of IPs, and agrees with the feature found by Bikmaev et al. (2006).

The *ROSAT* bright source catalogue has no other sources in the *RXTE* PCA field of view of J0056. Bikmaev et al. (2006) showed that there was a source in the error circle of *ROSAT* but it was only present at low energies, and so will not affect this measurement. There is therefore very little contamination from other near by sources. We note that J0056 is significantly brighter now than was reported in the *RXTE* all sky survey (Revnivtsev et al. 2004).

Conclusion

The unambiguous detection of an X-ray spin period of 465.68 $\pm$ 0.07 s in J0056 and its decreasing modulation depth with increasing energy, along with its spectral properties, confirm its inclusion into the IP class.

2.4.2 Swift J0732.5–1331

Background

Prior to our paper (Butters et al. 2007), there was no peer-reviewed analysis of J0732 published in the literature. There were however several mentions of it in Astronomical Telegrams, which are summarised below. These were all published in early 2006.

J0732 was first detected by Ajello et al. (2006) with the *Swift* Burst Alert Telescope and *Swift* X-ray telescope (XRT). With the XRT 600 counts in 3400 s were recorded, coincident with the *ROSAT* source 1RXS J073237.6–133113. This is also coincident with the 2MASS source J073237.64–133109.4, a proposed K main-sequence star 400 pc away. Based on its X-ray luminosity and colours, Ajello et al. (2006) suggested a CV identification for the object.

Masetti et al. (2006a) used the BFOSC instrument on the G.D. Cassini 1.5 m telescope to obtain the optical spectrum of the counterpart to J0732. Two objects were found close to the reported position, a normal G/K type Galactic star (the 2MASS source) and a fainter one deemed to be the true optical counterpart. The spectral signature of the system was concluded to be that of an accretion disc in a low mass X-ray binary.

Patterson et al. (2006) also obtained low resolution spectra, this time on the MDM 2.4 m telescope, of the 2MASS optical counterpart proposed by Ajello et al. (2006) (i.e. the field star), concluding that it was indeed a normal G star. In the same telegram Patterson et al. (2006) also reported optical photometry of the true counterpart (obtained by the small telescope network of the Center for Backyard Astrophysics[2]) which revealed a stable pulsation period of 512.42±0.03 s with most of the power in the first harmonic. This was deemed to be the spin period of a rotating white dwarf and Patterson et al. (2006) consequently suggested an IP classification for the object. A possible 11.3 hour orbital signal was also suggested, but owing to its low amplitude, this required the binary to be close to face on, as any variation in brightness due to the projected Roche lobe filling secondary was small.

Marsh et al. (2006) subsequently used *ULTRACAM* mounted on the William Herschel Telescope to observe the optical counterpart of J0732. The spin pulsation detected by Patterson et al. (2006) was seen. The counterpart and the non-associated field star were found to be approximately $1.8''$ apart.

Torres et al. (2006) performed spectral analysis of the optical counterpart at the Mt. Hopkins 1.5 m telescope. Balmer emission lines from Hα to at least Hγ were found. This reinforced its classification as a probable IP. However, despite seeing a variation in the radial velocities of the various emission lines, they were unable to determine an orbital period.

Wheatley et al. (2006) later reanalysed the original *Swift* data reported in Ajello et al. (2006) and found an X-ray pulsation at the proposed spin period. The modulation was found to be single peaked and only present below 2 keV. Reanalysis of the spectral data suggested a temperature typical of intermediate polars (kT ~20 keV). This data set is, however, short and suffers from severe aliasing effects.

Thorstensen et al. (2006) carried out time series spectroscopy at the MDM Observatory on the optical counterpart. The radial velocities of the Hα emission lines were found to vary periodically with a period of 0.2335±0.0008 days (5.60±0.02 h), which was interpreted as the orbital period of the system. This is close to half the photometric period suggested by Patterson et al. (2006).

[2]http://cba.phys.columbia.edu/

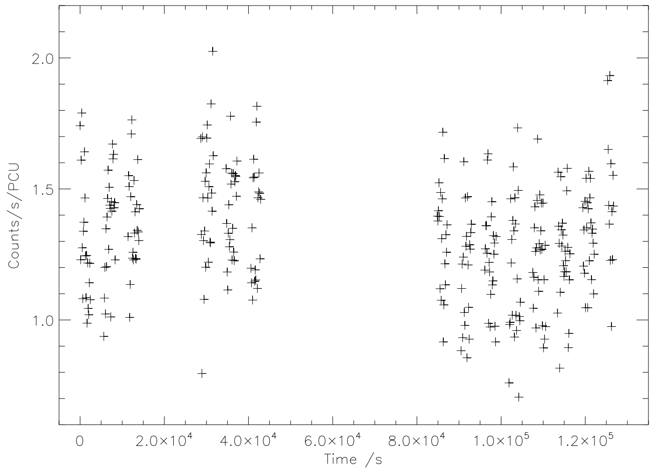

Figure 2.7: 2 – 10 keV background subtracted light curve of J0732. The zero time corresponds to the start of the observations at JD 2454295.30035. The data is binned into bins of 128 s width. The typical error on each point is ± 0.2

Data

Data were obtained over two consecutive days, from 13th July 2007 (see Table 2.2). The total time on target was 36 240 s, comprising fourteen approximately equal segments of one satellite orbit each. The raw count rate varied between 3.9 and 5.4 count s^{-1} PCU^{-1}. The background count rate, generated from the calibration files, varied between 2.9 and 3.8 count s^{-1} PCU^{-1}.

Light curve analysis

The background subtracted 2 – 10 keV light curve is shown in Figure 2.7. The data were subsequently analysed with the CLEAN algorithm. The results of this are shown in Figure 2.8

Spin Period

Strong peaks are evident in the CLEANed periodogram at 168 cycles day^{-1} (512 s) and at its first harmonic, in the 2 – 10 keV energy band. Similar signals are seen in each energy band. Analysis of the peaks yields a pulsation period of 512.4 ± 0.3 s. The data in each of the energy resolved light curves were then folded at the 512.4 s period, Figure 2.9 shows the result in the 2 – 10 keV energy band (each individual band is shown in Appendix A). The modulation depths of the pulse profiles of each energy band are shown in Table 2.5.

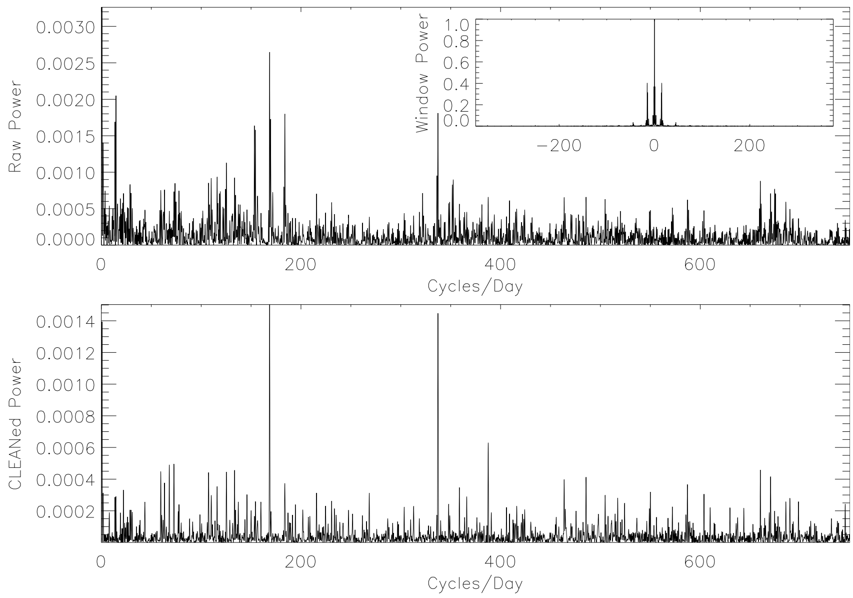

Figure 2.8: 2 – 10 keV CLEANed periodogram of J0732. The upper plot shows the raw periodogram, with the window function inset; the lower plot shows the deconvolved (CLEANed) periodogram.

Orbital Period

The windowing of the data is such that no reliable signal can be extracted for periods of a few hours from the periodogram, therefore no reliable orbital period can be found. Folding the X-ray data at the 5.6 h spectroscopic period (Thorstensen et al. 2006) yields no coherent modulation (see Figure 2.10), but folding it at the 11.3 h photometric period (Patterson et al. 2006) does give a single peaked sinusoid-like structure (see Figure 2.11).

Table 2.5: Light curve modulation depths of the pulse profile of J0732 in different energy bands.

Energy band (keV)	Modulation depth (%)	Fitted mean (ct s^{-1} PCU^{-1})
2–10	8±1	1.31
2–4	16±3	0.25
4–6	7±2	0.46
6–10	7±2	0.56
10–20	10±4	0.28

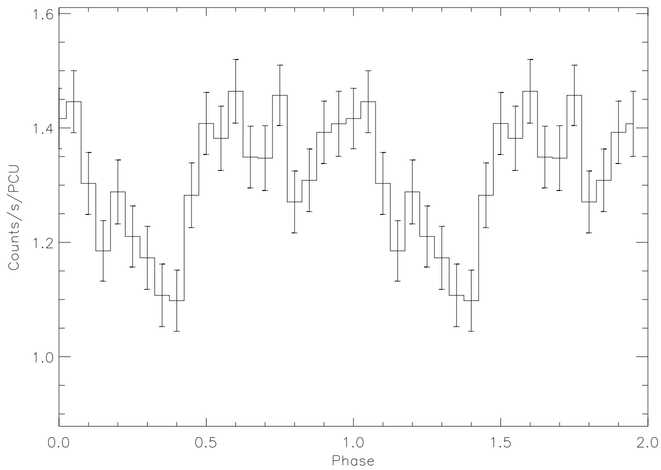

Figure 2.9: 2 – 10 keV light curve of J0732 folded at the 512.4 s pulse period with an arbitrary zero point. Two cycles are shown for clarity.

Table 2.6: Bremsstrahlung (top) and power law (bottom) spectral fitting parameters of J0732. $n_{\rm H}$(Galactic)=0.4 $\times$ 10^{22} cm^{-2}

$n_{\rm H}$	kT	Γ	Fe	$\sigma_{\rm Fe}$	EW	$\chi^2_{\rm reduced}$	Flux (2–10keV)
10^{22} cm^{-2}	keV		keV	keV	keV		10^{-11} ergs cm^{-2} s^{-1}
2.0±0.5	37±7	–	6.4±0.1	0.3±0.1	0.3	1.0	1.4
2.1±0.5	–	1.5±0.1	6.4±0.1	0.4±0.2	0.5	0.9	1.4

Spectral analysis

Both the photoelectrically absorbed Bremsstrahlung plus Gaussian and the photoelectrically absorbed power-law plus Gaussian gave good fits to the data (see Figures 2.12 & 2.13 and Table 2.6).

Discussion

The strong X-ray signal at the 512.4 ± 0.3 s pulse period seen at all energies is characteristic of IPs and confirms the nature of the object. Patterson et al. (2006) found a much stronger peak at the first harmonic in their frequency analysis of the optical photometry data. This is characteristic of a double-peaked pulse profile and indicates that two emission regions can be seen. The X-ray data reported here exhibit the same periodicity,

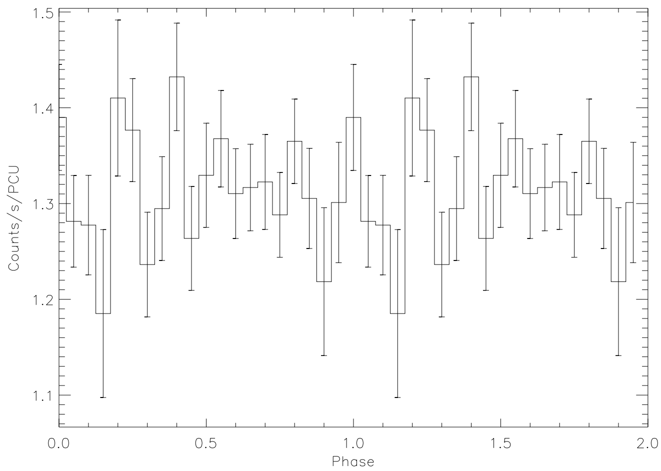

Figure 2.10: 2 – 10 keV light curve of J0732 folded at the 5.6 h spectroscopic period suggested by Thorstensen et al. (2006) with an arbitrary zero point. Two cycles are shown for clarity.

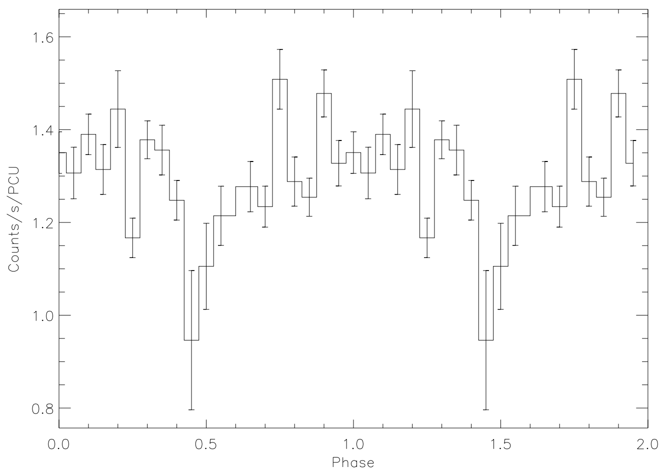

Figure 2.11: 2 – 10 keV light curve of J0732 folded at the 11.3 h photometric period suggested by Patterson et al. (2006) with an arbitrary zero point. Two cycles are shown for clarity.

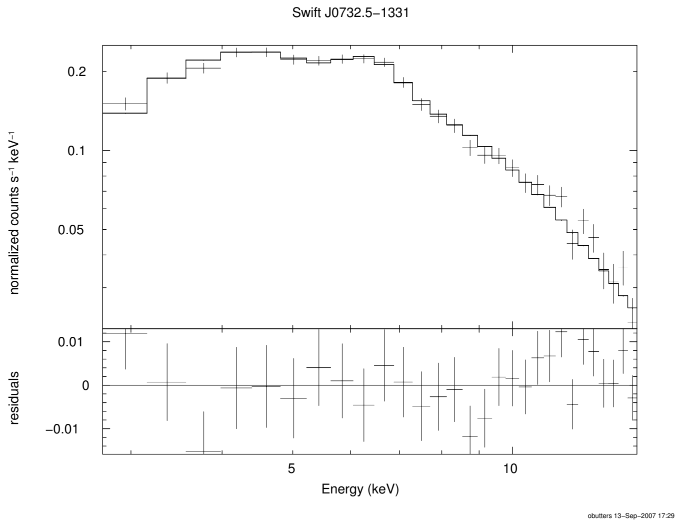

Figure 2.12: 2.5 – 15 keV mean spectrum of J0732 fitted with a photoelectrically absorbed Bremsstrahlung plus iron line profile.

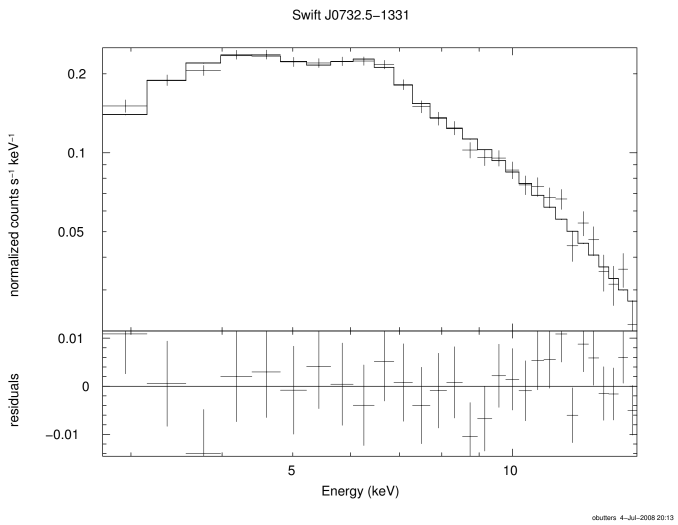

Figure 2.13: 2.5 – 15 keV mean spectrum of J0732 fitted with a photoelectrically absorbed power law plus iron line profile.

but a somewhat different profile. The first harmonic in the X-ray data is still present, and the pulse profile consequently shows a second minimum superimposed on the pulse maximum, but the overall profile is only marginally double-peaked. The most likely geometry of this system is therefore one where one magnetic pole can always be seen, the other being behind the WD for most of the cycle. If the heights of the accretion columns are such that a fraction of the hidden pole's column can be seen at certain phases, then the X-ray profile may be explained. If the optical emission arises from reprocessed X-rays (i.e. further up the accretion column) then it may be seen from both poles and this would explain the optical signal of Patterson et al. (2006).

The modulation depth of the X-ray pulse profile is approximately constant above 4 keV, implying that the dominant effect shaping the profile is geometric, probably self-occultation by the white dwarf. At the lowest energies (2 – 4 keV) the modulation depth is higher, which implies that phase-varying photoelectric absorption (as well as occultation) is the process which causes the modulation. The spectral fitting also indicates the presence of a significant local absorbing column, and has parameters that are typical of other IPs.

There is still some ambiguity about the orbital period of this system. The likelihood of it being the 11.3 h period suggested by Patterson et al. (2006) is now increased, given the X-ray signal seen here. The possibility of aliasing in this data set, means that it cannot be definitively said to be so and we cannot rule out the 5.6 h spectroscopic period found by Thorstensen et al. (2006). The absence of a beat period in the frequency analysis of the optical data does suggest that the true orbital period may be long, since no reprocessed radiation is seen from the face of the secondary star and therefore the bodies are likely to be far apart.

The lack of an X-ray beat signal in these *RXTE* data indicates that there is no significant stream-fed component to the flow. This suggests a relatively weak magnetic field strength and is consistent with the small $P_{\rm spin}/P_{\rm orb}$ ratio of the system (Norton et al. 2004), namely 0.025 or 0.013 depending on which is the correct orbital period.

The presence of an iron line at 6.4 keV in both spectral models reinforce the case for J0732 to be an IP since it is a feature often seen in other IPs (Hellier & Mukai (2004)). Both spectral models are a good fit to the data, but if the Bremsstrahlung fit is the correct one then the high temperature is also consistent with other IPs.

Finally, we note that the average *RXTE* count rate (1.3 ct s^{-1} PCU^{-1} in the 2 – 10 keV band) is consistent[3] with the value obtained with the *Swift* satellite, indicating that the system has not changed significantly in brightness since its discovery.

[3]Using webPIMMS: http://heasarc.gsfc.nasa.gov/Tools/w3pimms.html

Conclusion

The unambiguous X-ray spin period detection at 512.4 $\pm$ 0.3 s, along with the spectral fit, confirm the intermediate polar status of J0732. We are unable to determine the orbital period from these *RXTE* data although there is some indication of modulation at the previously suggested photometric period of 11.3 h and none at the spectroscopic period of 5.6 h. To conclude, we note that this system is similar in terms of its small $P_{\rm spin}/P_{\rm orb}$ value, to the IPs RX J2133.7+5107 and NY Lup (IGR J15479–4529). Both of these are *INTEGRAL* hard X-ray sources and both also have soft X-ray components. We might therefore expect that Swift J0732.5–1331 would also display such characteristics upon further study.

2.4.3 XSS J12270–4859

Background

J1227 was found in the *RXTE* all sky survey (Revnivtsev et al. 2004). It was classified as a CV and suggested to be an IP by Masetti et al. (2006b), using optical spectroscopy. Bird et al. (2007) later found J1227 to be an *INTEGRAL* source.

Data

Data were collected over the course of just over one day (see Table 2.2). Total good time on target (26 814 s) was split over nine segments. The raw target count rate varied between 2.4–10.9 ct s^{-1} PCU^{-1}, the generated background count rate varied between 2.8–3.9 ct s^{-1} PCU^{-1}. The background subtracted 2–10 keV is shown in Figure 2.14.

Light curve analysis

Analysis of the light curve showed significant (>4σ) structure at $\sim$100 cycles day^{-1} (see Figure 2.15). The peak of this structure was at 859.57$\pm$0.64 s. Folding the data at this period showed a clear modulation in the 2–10 keV energy band (see Figure 2.16), with approximately the same percentage depth in each energy band (see Table 2.7 and Appendix A). There was also a peak at approximately one cycle day^{-1} in the periodogram; this peak was discounted as it was of the order of the length of the observing run, and was probably a feature of the window function.

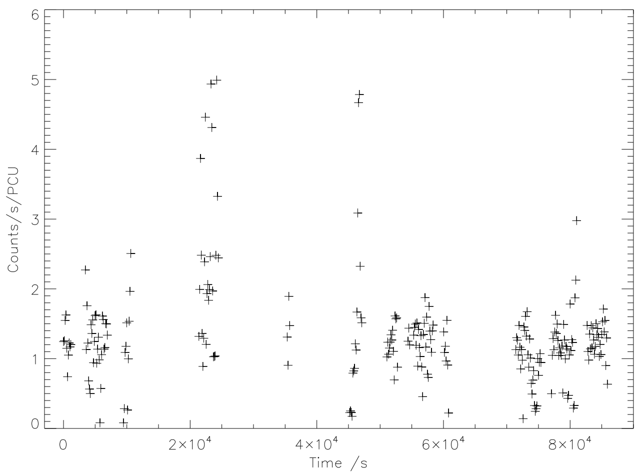

Figure 2.14: 2–10 keV background subtracted unfolded light curve of J1227. The temporal resolution is 128 s. The zero point corresponds to the first measurement of the night at JD=2454433.17557589. The typical error on each point is ±0.26.

Table 2.7: Light curve modulation depths of J1227, in different energy bands.

Energy band (keV)	Modulation depth (%)	Fitted mean (ct s^{-1} PCU^{-1})
2–10	26±2	1.29
2–4	27±3	0.37
4–6	25±3	0.45
6–10	27±3	0.47
10–20	28±7	0.22

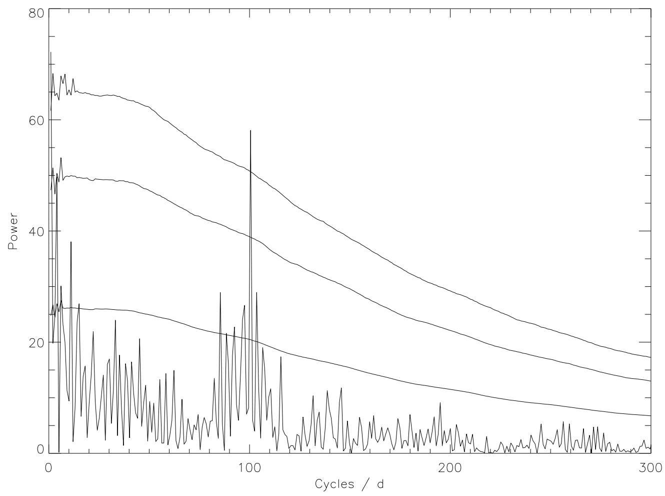

Figure 2.15: 2–10 keV periodogram of J1227. Three significance levels, 95.2, 99.7 and 99.954% (2, 3 and 4σ respectively), are superimposed.

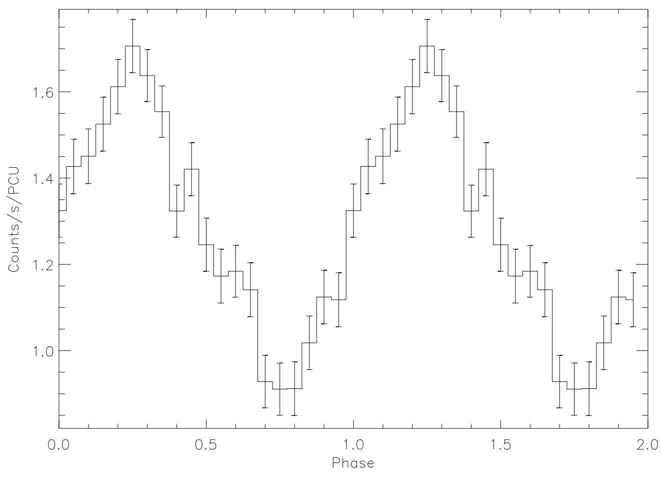

Figure 2.16: 2–10 keV light curve of J1227 folded at the 859.57 s pulse period with an arbitrary zero point. Two cycles are shown for clarity.

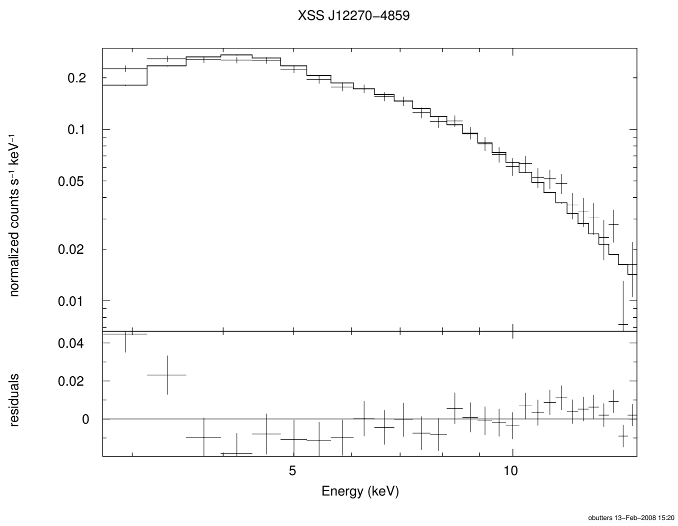

Figure 2.17: 2–15 keV mean spectrum of J1227 fitted with a photoelectrically absorbed Bremsstrahlung plus Gaussian.

Table 2.8: Bremsstrahlung (top) and power law (bottom) spectral fitting parameters of J1227. n_{H}(Galactic)=0.1 $\times\, 10^{22}$ cm^{-2}

n_{H}	kT	Γ	Fe	σ_{Fe}	EW	$\chi^2_{\mathrm{reduced}}$	Flux (2–10keV)
10^{22} cm^{-2}	keV		keV	keV	keV		10^{-11} ergs cm^{-2} s^{-1}
0.1[a]	14±1	–	6.5[b]	0.1[b]	<0.08	1.3	1.5
0.1[a]	–	1.8±0.1	6.5[b]	0.1[b]	<0.17	0.8	1.5

[a] Pegged to a lower limit of this value to reflect the Galactic column density,

[b] No error as this value was imposed. See notes in the text.

Spectral analysis

In fitting the spectrum, the column density was pegged to the lower limit of the Galactic column density for both the models. The best fit was the power law model, giving $\chi^2_{\mathrm{reduced}}$ =0.8 (see Table 2.8). There is no significant sign of an excess at the iron line energy (see Figures 2.17 & 2.18). A Gaussian was fitted to the expected position of the iron emission feature, but in each case only a small upper limit to the equivalent width was found (<0.08 and <0.17 keV for the Bremsstrahlung and power law models respectively).

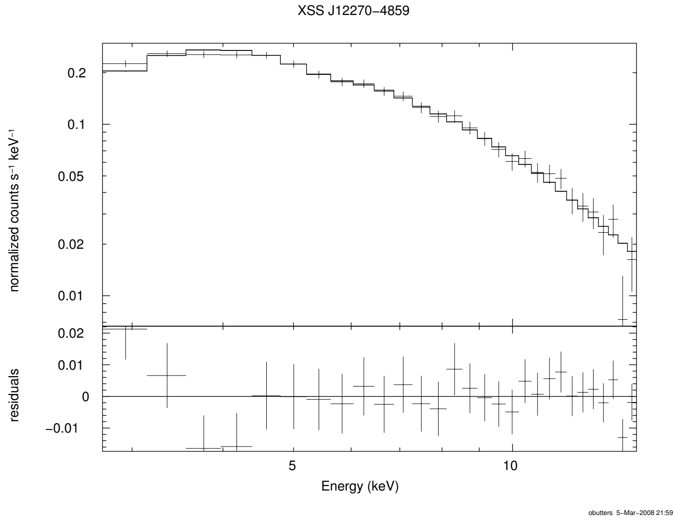

Figure 2.18: 2–15 keV mean spectrum of J1227 fitted with a photoelectrically absorbed power law plus Gaussian.

Discussion

J1227 exhibits a structure in the periodogram that indicates it has a period close to 100 cycles day^{-1}. This is consistent with being interpreted as a spin period. It shows an approximately constant modulation in each energy band at the 859.57$\pm$0.64 s period, which implies that the process causing this effect must be a geometrical effect causing obscuration instead of absorption.

Recently (subsequent to the publication of these results (Butters et al. 2008)), Pretorius (2009) conducted high speed photometry of J1227. She found no evidence in the optical of a period commensurate with the X-ray one found here.

The upper limit placed on the equivalent width of a potential iron line is small, and goes against the classification of this as an IP, since all IPs exhibit some kind of iron emission features. We do note however that Masetti et al. (2006b) did see significant iron features in their optical spectra. The best spectral fit is obtained from a power law profile, the parameters of which are in good agreement with Revnivtsev et al. (2004). We note that a multi-temperature Bremsstrahlung fit may be more accurate, but beyond the scope of this study. The count rate has not changed significantly since the measurements of Revnivtsev et al. (2004).

There are several X-ray sources nearby in the PCA field of view which may contribute to the count rate. We used the *ROSAT* count rate of each source to estimate an *RXTE* count rate using the on line tool webPIMMS[4]

[4]http://heasarc.nasa.gov/Tools/w3pimms.html

(for each source we assume a power law with a photon index of 1.7), we then scaled this value by the response of the PCUs based upon the distance from the source. These extra sources will have the effect of decreasing the percentage modulation depth. Moreover, since it is likely that these sources are softer than the target, the contamination will have a greater effect at lower energies. The modulation depth will therefore be reduced more at lower energies. This could make a decreasing modulation depth with energy look like a constant modulation depth with energy. The spectral fitting is likely to be affected by these other sources and they may be the cause of the poor Bremsstrahlung model fit. We estimate that they may have contributed up to 0.26 ct s^{-1} PCU^{-1} in the 2–20 keV energy band, i.e $\lesssim$20% of the total count rate.

Conclusion

J1227 clearly exhibits some properties seen in IPs, but not to an extent for us to definitively classify it as such. If J1227 does turn out to be an IP, then the presence of an X-ray iron feature will have to be reconsidered as a defining characteristic of IPs, since it is not present here. [5]

2.4.4 IGR J14536–5522

Background

J1453 was discovered as a hard X-ray source with *INTEGRAL* (Kuiper et al. 2006). Soon afterwards it was observed with *Swift*/BAT, and found to be a relatively soft source with $kT \sim 30 - 40$keV for a single temperature Bremsstrahlung fit, exhibiting variability (Mukai et al. 2006). Pointed *Swift*/XRT observations gave a flux of 3.3×10^{-11} ergs cm^{-2} s^{-1} at 0.4–10 keV, and a complex spectrum requiring at least two components to fit the data (Mukai et al. 2006). Masetti et al. (2006c) used the CTIO 1.5 m telescope to get optical spectroscopy of J1453, on the basis of the Balmer and HeI lines they classified it as a CV. Mukai et al. (private communication 2008) have optical spectroscopy obtained from the SALT in 2006 which exhibits a clear modulation at 3.1565(1) hr, as well as S.A.A.O. 1.9 m optical photometry which does not.

[5] Since the submission of this thesis this data set has been reanalysed along with some Suzaku data by Saitou et al. (2009). They conclude that J1227 is in fact a low mass X-ray binary with many flaring events, and that the period seen here can be accounted for by these flares.

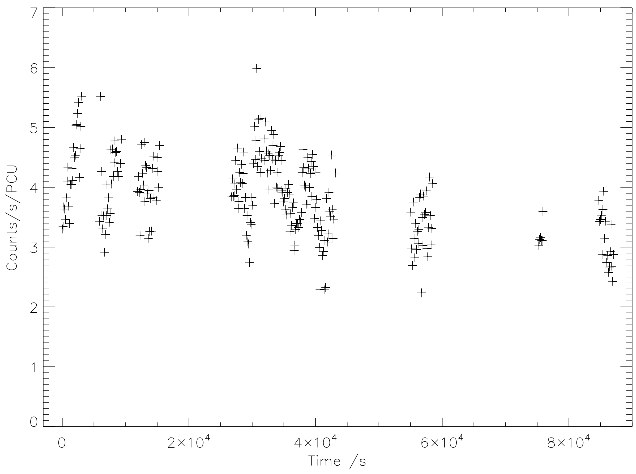

Figure 2.19: 2–10 keV background subtracted unfolded light curve of J1453 with a 128 s resolution. The zero point corresponds to the first observation at JD=2454428.6574277. Typical errors are ± 0.30 on each data point.

Data

Data was collected over the course of just over one day (see Table 2.2). The total good time on target (31 320 s) was split into 13 segments. PCUs 3 and 4 were functioning so intermittently that they were not included in the analysis of this target. The raw target count rate varied between 4.3 and 11.2 counts s^{-1} PCU^{-1} and the raw background (generated from the calibration files) between 2.7 and 4.1 counts s^{-1} PCU^{-1}.

Light curve analysis

The background subtracted 2–10 keV light curve is shown in Figure 2.19. When analysed with the CLEAN algorithm three periods are evident; 3746 ± 110 s, 7202 ± 220 s and $15\,594 \pm 1123$ s (see Figure 2.20). These values are potentially a period and its first and third harmonic (within errors). Plots of the data folded at these values are shown in Figures 2.21, 2.22 & 2.23 and Appendix A. The CLEAN analysis shows no evidence of any periodicity at the 3.1 hr (11 363 s) spectroscopic period, the data folded at this period is shown in Figure 2.24.

There is some indication of a trend in the modulation depth of the light curves of each potential period to decrease with increasing energy (see Table 2.9).

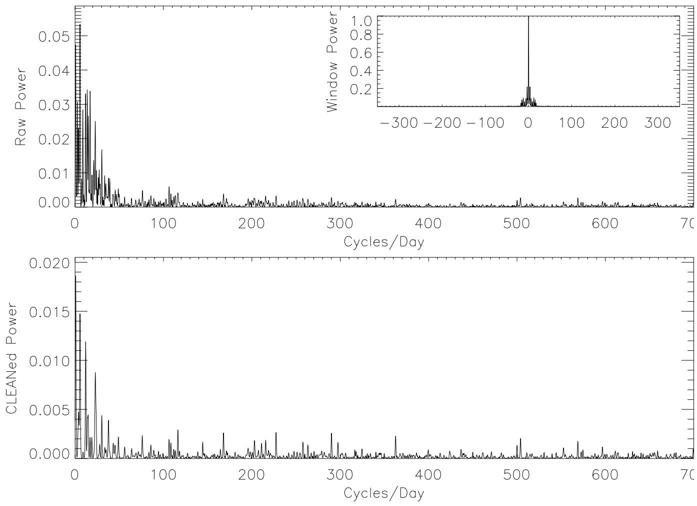

Figure 2.20: 2–10 keV CLEANed periodogram of J1453. The upper plot shows the raw periodogram, with the window function inset; the lower plot shows the deconvolved (CLEANed) periodogram.

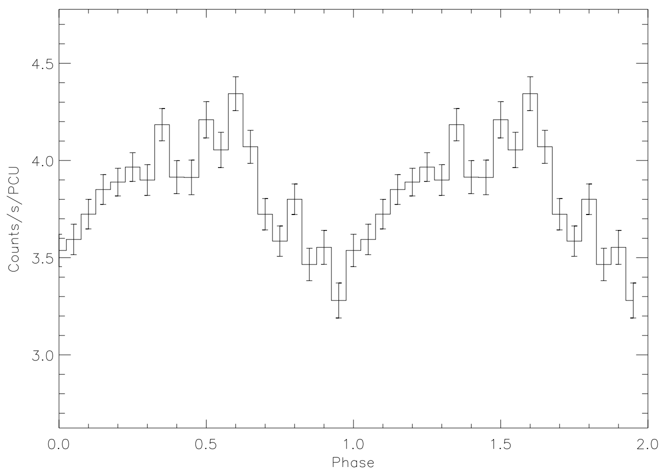

Figure 2.21: 2–10 keV folded light curve of J1453. Folded at 3746 s with an arbitrary zero point. Two periods are shown for clarity.

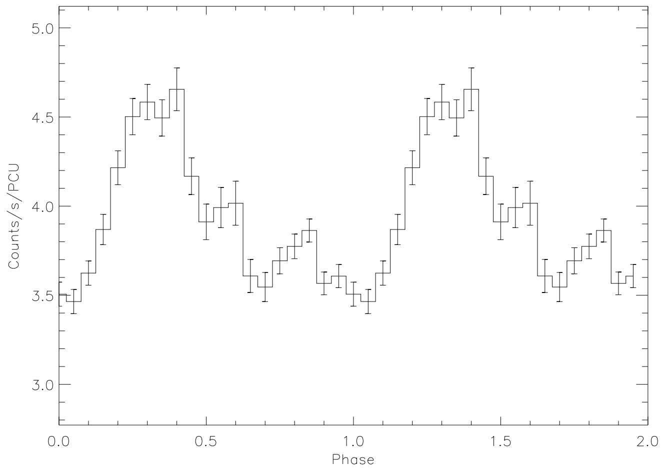

Figure 2.22: 2–10 keV folded light curve of J1453. Folded at 7202 s with an arbitrary zero point. Two periods are shown for clarity.

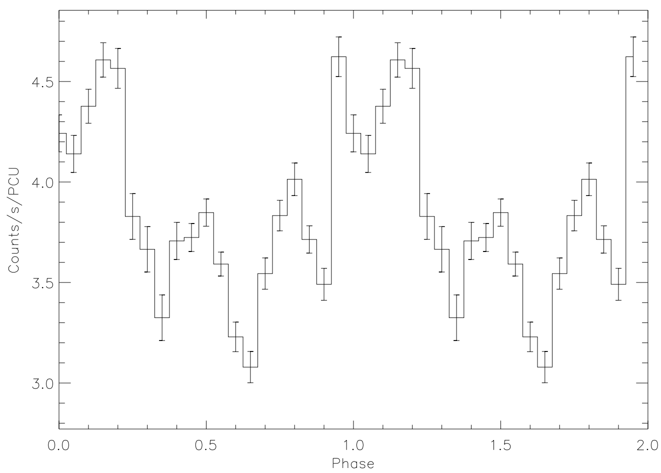

Figure 2.23: 2–10 keV folded light curve of J1453. Folded at 15 594 s with an arbitrary zero point. Two periods are shown for clarity.

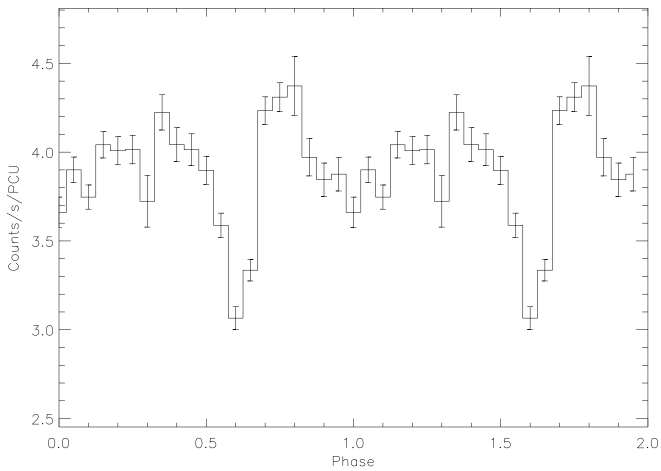

Figure 2.24: 2–10 keV folded light curve of J1453. Folded at 11 363 s with an arbitrary zero point. Two periods are shown for clarity.

Table 2.9: Light curve modulation depths of J1453, in different energy bands and folded at each of the potential periods.

Energy band	Modulation depth				Fitted mean
(keV)	(%)	(%)	(%)	(%)	(ct s^{-1} PCU^{-1})
	3746	7202	15 594	11 363	
2–10	8 ± 1	10 ± 1	12 ± 1	4 ± 1	3.8
2–4	11 ± 1	11 ± 1	14 ± 1	7 ± 1	0.9
4–6	6 ± 1	11 ± 1	12 ± 1	4 ± 1	1.4
6–10	8 ± 1	9 ± 1	9 ± 1	3 ± 1	1.6
10–20	6 ± 3	7 ± 3	7 ± 1	1 ± 3	0.7

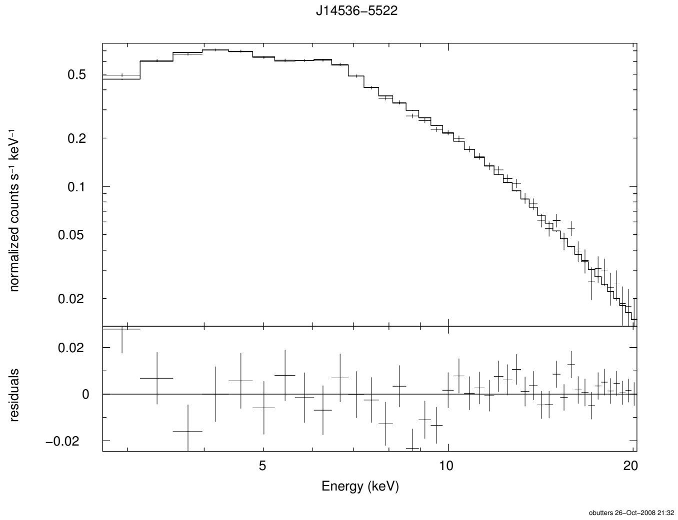

Figure 2.25: 2.5–20 keV mean spectrum of J1453 fitted with a photoelectrically absorbed Bremsstrahlung plus iron line profile.

Table 2.10: Bremsstrahlung (top) and power law (bottom) spectral fitting parameters of J1453.$n_{\rm H}$(Galactic)=$0.5\ \times 10^{22}$ cm^{-2}.

$n_{\rm H}$	kT	Γ	Fe	$\sigma_{\rm Fe}$	EW	$\chi^2_{\rm reduced}$	Flux (2–10keV)
10^{22} cm^{-2}	keV		keV	keV	keV		10^{-11} ergs cm^{-2} s^{-1}
0.5[a]	25±1	–	6.4±0.1	0.3±0.1	0.4	1.2	4.1
0.7±0.4	–	1.6±0.1	6.4±0.1	0.5±0.1	0.5	0.9	4.1

[a] Pegged to a lower limit of this value to reflect the Galactic column density.

Spectral analysis

Fitting spectral models required the column density be pegged to a lower limit if the Galactic column density for the Bremsstrahlung fit. The best fit was the power law fit, yielding a $\chi^2_{\rm reduced} = 0.9$ (see Figures 2.25 & 2.26 and also Table 2.10). In both cases a Gaussian was fitted to model the iron line emission as there was an excess at ~ 6.4keV.

Discussion

The peaks in the periodogram of J1453 are not typical of spin periods of IPs. The shortest of these is 3746±110 s, this would make it one of the longest spin periods of the IPs. This period is also not seen in

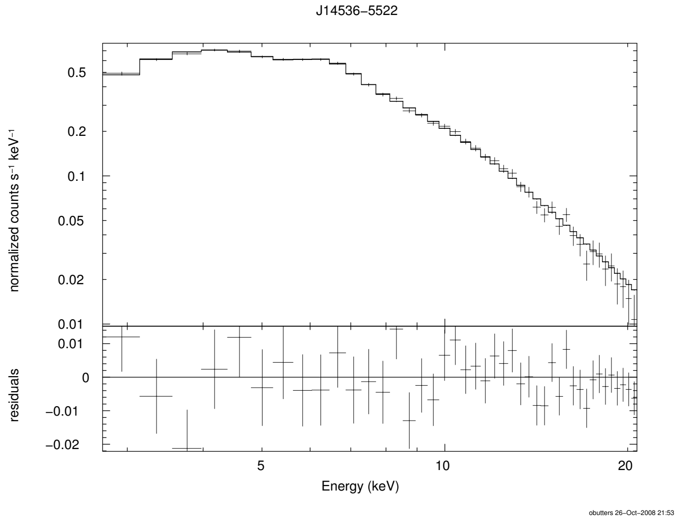

Figure 2.26: 2.5–20 keV mean spectrum of J1453 fitted with a photoelectrically absorbed power law plus iron line profile.

the optical data. As such the evidence for this as a spin period is weak. The same is true for the 7202 and 15 594 s peaks. The lack of any strong spin period candidates implies that J1453 is probably not an IP.

These periods are potential candidates for the orbital period of the system. In fact the reported orbital period is equal to what would be the second harmonic of 3746 s, with the two longer periods being further harmonics. The error on this is relatively large however, and the correspondence may jut be a coincidence. A longer base line in the X-ray data would constrain this period further and conclusively show if this was real.

The modulation depth of the of the folded light curve at each candidate energy decreases with increasing energy. This is a common feature of IPs, and indicates photoelectric absorption from an accretion curtain (Norton & Watson 1989).

The spectral profiles indicated a photoelectrically absorbed power law plus iron line was the preferred fit. The Bremsstrahlung was acceptable, with a slightly higher $\chi^2_{\rm reduced}$. This slightly worse fit probably arose from the lowest energy value as this was where the residuals were highest. This would be expected if there was a soft X-ray component (as concluded in Mukai et al. (2006)), that has not been taken into account in the modelling. Clearly one low energy data point is not enough for us to attempt to characterise this here.

The flux seen here is significantly higher than previously measured – 4.1 ct s^{-1} PCU^{-1} in the 2–10 keV energy band as opposed to 3.3 ct s^{-1} PCU^{-1} at 0.4–10 keV. According to the *ROSAT* All Sky Survey bright source catalogue there is one other X-ray source in the field of view of J1453. Estimating an *RXTE* count rate using webPIMMS[6] and scaling according to the position on the detector gives an estimated count rate of 0.96 ct s^{-1} PCU^{-1}. This other source has also been detected with *INTEGRAL* and therefore is a hard X-ray source also. This may affect the spectrum in a complex way that we cannot characterise here.

One possible classification of this is object is a polar. The lack of detection of the spectroscopic period in the X-ray data, and it's absence in the S.A.A.O. photometric data, go against the classification of J1453 as a *synchronous* polar. However, one possible classification is an *asynchronous* polar. This is a polar which has been forced from synchronism by a classical nova eruption. Such a system would have a spin period that is different from the orbital period by only a few percent, as such the accretion flow would vary on a very long beat period. This could be the cause of the differing light curves on different nights, while still maintaining the spectral properties of a synchronous polar. The periodic signals seen here could then be explained as QPOs. In fact, Potter et al. (2008) report significant circular polarization in J1453, so a polar classification is very likely.

Conclusion

J1453 exhibits the spectral properties seen in IPs, but not the temporal characteristics. This may be because it is an asynchronous polar. If this is the case then of the four *INTEGRAL* sources classed as polars three of them are asynchronous.

2.4.5 IGR J15094–6649

Background

In the *INTEGRAL*/IBIS survey, J1509 was detected as an unclassified object in the 20–100 keV energy range (Barlow et al. 2006). Both a Bremsstrahlung and a power law were fitted to the data in order to determine an identification. In both cases a good fit was found; Bremsstrahlung with kT=13.8±5.1 keV and power law with Γ=3.6±0.8. The flux was given as 1.38×10^{-11} ergs s^{-1} cm^{-2} in the 20–100 keV band.

Masetti et al. (2006b) classified J1509 as an IP based upon optical spectra taken at the 1.5 m Cerro Tololo Interamerican Observatory (CTIO) in Chile.

Very recently Pretorius (2009) published optical photometry and spectroscopy of J1509, along with four other candidate IPs from the *INTEGRAL* sample. A clear radial velocity signal was detected at a period of 5.89 ± 0.01 h which was identified as the orbital period of the system, as well as a photometric modulation at

[6] http://heasarc.nasa.gov/Tools/w3pimms.html

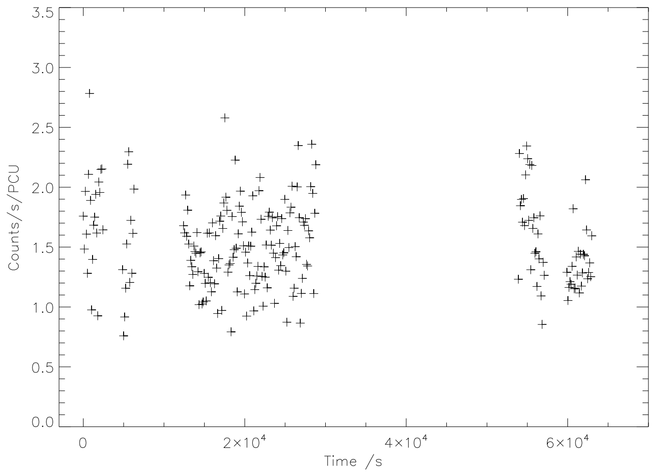

Figure 2.27: 2 – 10 keV background subtracted light curve of J1509. The zero time corresponds to the start of the observations at JD2454830.77312937984. The data is binned into bins of 128 s width. The typical error on each point is 0.26 counts s^{-1} PCU^{-1}.

809.42 ± 0.02 s which was taken to be the spin period of the magnetic white dwarf. These results provided very strong indications that J1509 is an IP, and detection of a commensurate pulse period in X-ray data would absolutely confirm its classification.

Data

Data were obtained over two consecutive days, from 30th – 31st December 2008 (see Table 2.2). The total time on target was 42 856 s. Only the top layer of PCU2 was included in the measurements.

In the 2 – 10 keV energy band the raw count rate varied between 2.5 and 6.9 count s^{-1} PCU^{-1}. The background count rate, generated using the faint source background model, varied between 2.9 and 4.1 count s^{-1} PCU^{-1}. The background subtracted 2 – 10 keV light curve is shown in Figure 2.27.

Light curve analysis

A strong peak is evident in the CLEANed periodogram at approximately 107 cycles day^{-1}, in the 2 – 10 keV energy band (see Figure 2.28). Also present are its first and second harmonics at $\sim$ 214 and $\sim$ 321 cycles day^{-1} respectively. Analysis of the second harmonic peak yields a fundamental pulsation period of 809.7 ± 0.6 s (based on a Gaussian fit to the periodogram). This is in excellent agreement with the optical photometric pe-

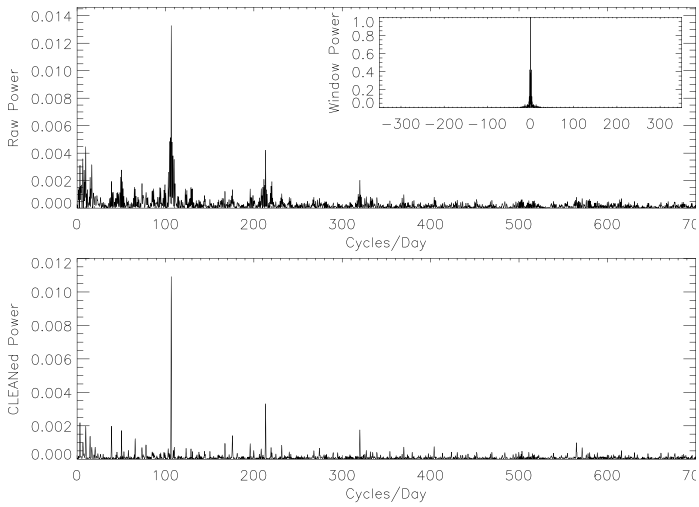

Figure 2.28: 2-10 keV CLEANed periodogram of J1509. The upper plot shows the raw periodogram, with the window function inset; the lower plot shows the deconvolved (CLEANed) periodogram.

riod detected by Pretorius (2009). Each of the energy resolved light curves were folded at the 809.7 s period, and Figure 2.29 shows the result in the 2 – 10 keV energy band (Appendix A shows the other energy bands). The modulation depths of the pulse profile are shown in Table 2.11.

There is no indication in the power spectrum of the spectroscopic orbital period previously reported by Pretorius (2009). Folding the X-ray light curve at the proposed orbital period yields a profile with no significant coherent modulation (see Figure 2.30).

Spectral analysis

Both models had an excess at approximately 6.4 keV, so a Gaussian was added to account for the iron line emission. Both models gave a good fit to the data (see Figures 2.31 & 2.32 and Table 2.12).

Discussion

The X-ray period found here (809.7 s) is in agreement with the photometric pulsation period found by Pretorius (2009) and is typical of a white dwarf spin period in an IP. Furthermore, the increasing modulation depth with decreasing energy in the folded pulse profiles is an indication that an accretion column absorbing structure is present (Norton & Watson 1989). The complex pulse profile and presence of strong harmonics in the power spectrum are reminiscent of the canonical IP FO Aqr (Beardmore et al. 1998), although unlike that system,

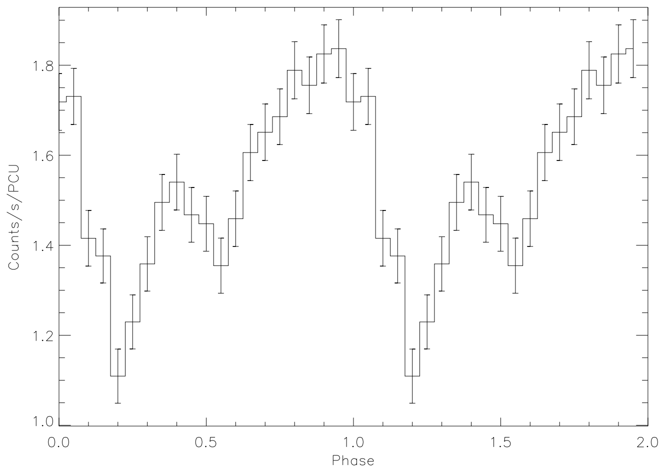

Figure 2.29: 2 – 10 keV light curve of J1509 folded at the 809.7 s period with an arbitrary zero point. Two cycles are shown for clarity.

Table 2.11: Modulation depths of the pulse profile of J1509 in different energy bands. Modulation depth is defined here as the semi-amplitude of a fitted sinusoid divided by the fitted mean.

Energy band (keV)	Modulation depth (%)	Fitted mean (ct s^{-1} PCU^{-1})
2–10	15±1	1.54
2–4	27±3	0.33
4–6	16±2	0.54
6–10	9±2	0.67
10–20	7±4	0.34

Table 2.12: Bremsstrahlung (top) and power law(bottom) spectral fitting parameters of J1509. $n_{\rm H}$(Galactic)=0.2 $\times 10^{22}$ cm^{-2}.

$n_{\rm H}$ 10^{22} cm^{-2}	kT keV	Γ	Fe keV	$\sigma_{\rm Fe}$ keV	EW keV	$\chi^2_{\rm reduced}$	Flux (2–10keV) 10^{-11} ergs cm^{-2} s^{-1}
1.2±1.0	19±4	–	6.3±0.1	0.4±0.2	0.9	0.6	1.6
3.0±1.3	–	1.8±0.1	6.4±0.1	0.4±0.2	0.9	0.6	1.5

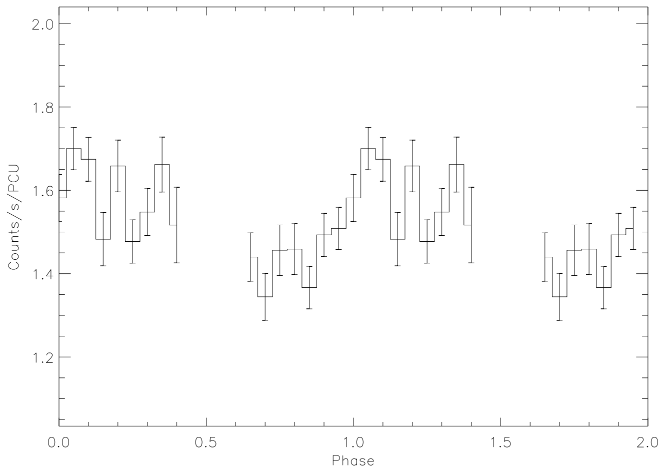

Figure 2.30: 2 – 10 keV light curve of J1509 folded at the 21 204 s period of Pretorius (2009) with an arbitrary zero point. Two cycles are shown for clarity.

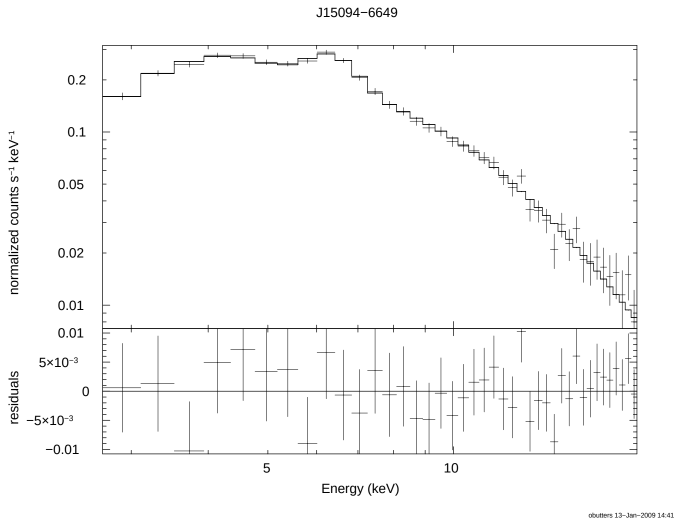

Figure 2.31: 2.5 – 20 keV mean spectrum of J1509 fitted with a photoelectrically absorbed Bremsstrahlung plus iron line profile.

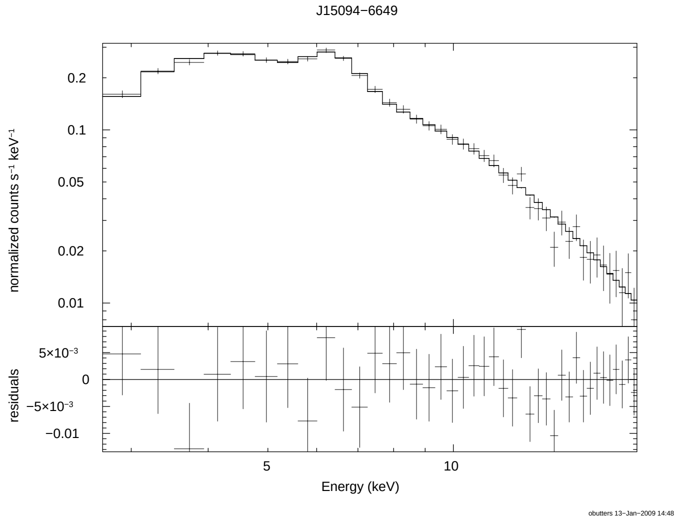

Figure 2.32: 2.5 – 20 keV mean spectrum of J1509 fitted with a photoelectrically absorbed power law plus iron line profile.

there is here no evidence for an additional X-ray modulation at the beat period (841.5 s), which would be indicative of a stream-fed component to the accretion. We note that whilst some IPs exhibit the white dwarf spin period in their X-ray flux, they may show the beat period in optical photometry (for example, AO Psc). This arises due to reprocessing of the X-ray signal, probably from the face of the donor star. In the case of J1509, we can be confident that we are seeing the spin period of the white dwarf in both the optical and X-ray light curves. The length of the X-ray data set probably precludes the detection of the orbital period, or may indicate that the system is seen at relatively low inclination angle (Parker et al. 2005), so no such modulation is present.

Both spectral fits are good, and the Bremsstrahlung model in particular is in agreement with that seen in the *INTEGRAL* data at higher energies (Barlow et al. 2006). The fit parameters are typical of those seen in other IPs. The column density is greater than the Galactic column density (as given by the HEASARC $n_{\rm H}$ estimator). This too is typical of IPs and is likely due to absorption by material within the accretion flow. The *ROSAT* Bright Source Catalogue has one other source in the *RXTE* field of view. A count rate for it was estimated using the webPIMMS[7] tool and scaled according to the response of the detector. The count rate of this additional source was small ($\sim\ 0.04$ counts s^{-1} PCU^{-1}) and therefore does not affect our result.

[7]http://www.ledas.ac.uk/pimms/w3p/w3pimms.html

Conclusion

IGR J15094–6649 is confirmed as an IP and adds to the growing list of hard X-ray selected magnetic CVs discovered by *INTEGRAL*.

2.4.6 IGR J17195–4100

Background

J1719 was detected as an *INTEGRAL* object by Bird et al. (2004). Pandey et al. (2006) found radio galaxies coincident with its error circle and suggested it was extragalactic. Tomsick et al. (2006) confirmed a tentative association of J1719 with the softer X-ray target 1RXS J171935.6–410054 using pointed *Chandra* data. They also reported variability of J1719 in the 0.3–10 keV band and a flux of $2.5^{+0.9}_{-0.4}\times10^{-11}$ ergs cm^{-2} s^{-1}. In calculating this flux they used a power law model and a galactic column density of 0.77×10^{22} cm^{-2} (derived from Dickey & Lockman (1990)). Tomsick et al. (2006) also reported the spectral properties of J1719 using public *INTEGRAL* data, finding a flux of 1.9×10^{-11} ergs cm^{-2} s^{-1} in the 20–50 keV energy band. Masetti et al. (2006b) classified J1719 as a CV based upon its optical spectrum and speculated that it may be an IP.

Data

Data were taken over two consecutive days (see Table 2.2). The total good time on target (35 936 s) was split over twelve approximately equal segments. The raw target flux varied from 5.4–11.3 ct s^{-1} PCU^{-1} and the generated background varied from 2.8–3.9 ct s^{-1} PCU^{-1}. Figure 2.33 shows the background subtracted 2–10 keV light curve.

Light curve analysis

The periodogram of J1719 had six potential periods that were over 4σ (see Figure 2.34). To discount any artifacts arising from the windowing of the raw data the CLEAN algorithm was also used (see Figure 2.35). This was a necessary step as the raw data was rather fragmented. The four peaks between 8 and 22 cycles day^{-1} were found to have a much lower significance in the CLEANed analysis and were thus discounted as an artifact of the windowing. Both remaining peaks above the 4σ level (1842.4$\pm$1.5 s and 2645.0$\pm$4.0 s) were equally viable periods. The 1842.4 s period was selected to fold the data at, but we stress that the other period was

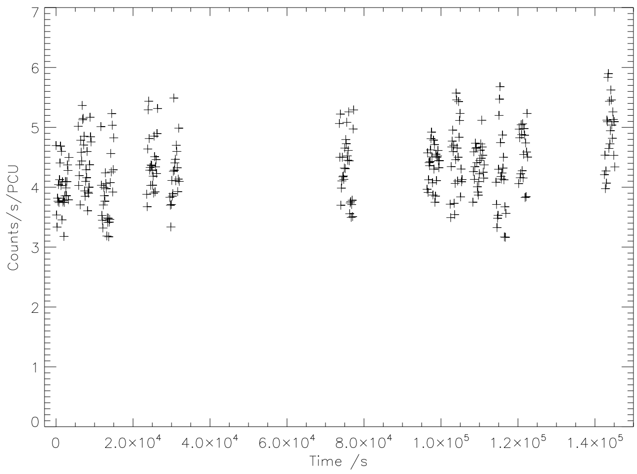

Figure 2.33: 2–10 keV background subtracted unfolded light curve of J1719 with a 128 resolution. The zero point corresponds to the first observation at JD=2454473.2837240. Typical errors are ± 0.30 on each data point.

an equally likely candidate period (see Figure 2.36 and Appendix A). Folding the data in each energy band at this period showed that the modulation depth is constant across them all (see Table 2.13). We also note that there is a further peak (at just below 3σ significance) at 941 s, whose period is close to half that of the 1842.4 s candidate period, and may therefore represent a first harmonic.

Spectral analysis

Spectral analysis showed the presence of an iron line in a photoelectrically absorbed Bremsstrahlung profile, however the fit was poor with $\chi^2_{\mathrm{reduced}}$ =3.0 (see Figure 2.37). A better fit was achieved with a power law model as shown in Figure 2.38 and Table 2.14, however this fit had the column density pegged to a lower limit of 0.7 $\times 10^{22}$ cm^{-2} to reflect the Galactic column density.

Discussion

The peaks in the periodogram of J1719 (1842.4±1.5 s and 2645.0±4.0 s) are typical for a spin period length in IPs. The small peak at 941 s is close to being half the 1842.4 period, and therefore may be a first harmonic, however, the significance of this peak is below 3σ. If the two longer periods above correspond to the spin and beat periods respectively then this implies an orbital period of approximately 1.7 hrs. The small, almost constant, modulation depth seen in the light curves in each energy band is not present among any other confirmed

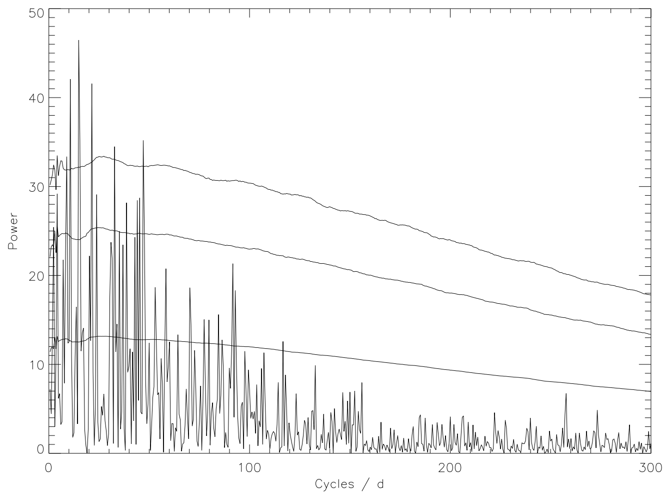

Figure 2.34: 2–10 keV periodogram of J1719. Three significance levels, 95.2, 99.7 and 99.954% (2, 3 and 4σ respectively), are superimposed.

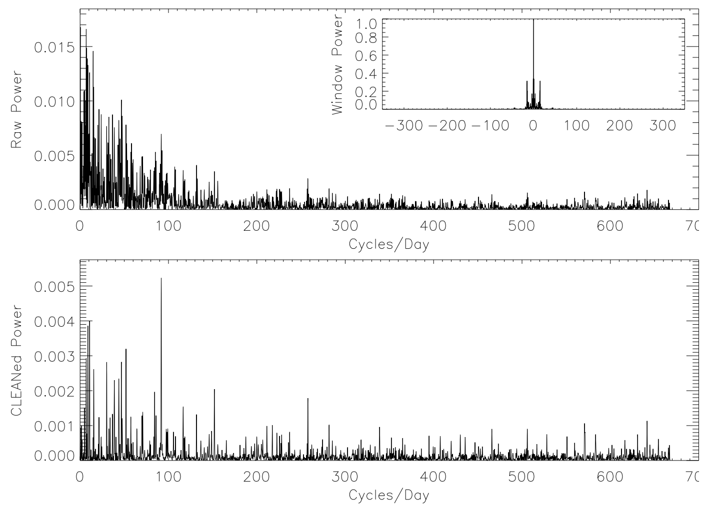

Figure 2.35: 2–10 keV CLEANed periodogram of J1719. The upper plot shows the raw periodogram, with the window function inset; the lower plot shows the deconvolved (CLEANed) periodogram.

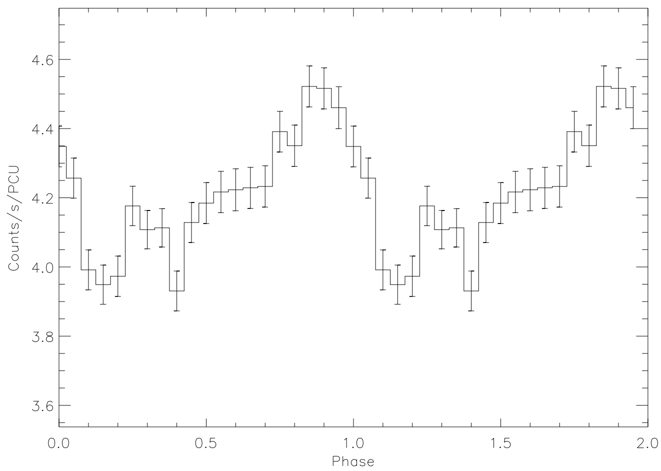

Figure 2.36: 2–10 keV folded light curve of J1719. Folded at 1842.4 s with an arbitrary zero point. Two periods are shown for clarity.

Table 2.13: Light curve modulation depths of J1719, folded at the possible period of 1842.4 s, in different energy bands.

Energy band (keV)	Modulation depth (%)	Fitted mean (ct s^{-1} PCU^{-1})
2–10	5±1	4.22
2–4	4±1	1.01
4–6	4±1	1.45
6–10	6±1	1.75
10–20	5±2	0.72

Table 2.14: Bremsstrahlung (top) and power law (bottom) spectral fitting parameters of J1719. $n_{\rm H}$(Galactic)=0.7 $\times 10^{22}$ cm^{-2}.

$n_{\rm H}$	kT	Γ	Fe	$\sigma_{\rm Fe}$	EW	$\chi^2_{\rm reduced}$	Flux (2–10keV)
10^{22} cm^{-2}	keV		keV	keV	keV		10^{-11} ergs cm^{-2} s^{-1}
0.7±0.1	17±1	–	6.5±0.1	0.1±0.1	0.5	3.0	4.4
0.7[a]	–	1.8±0.1	6.5±0.1	0.3±0.1	0.7	1.1	4.7

[a] Pegged to a lower limit of this value to reflect the Galactic column density.

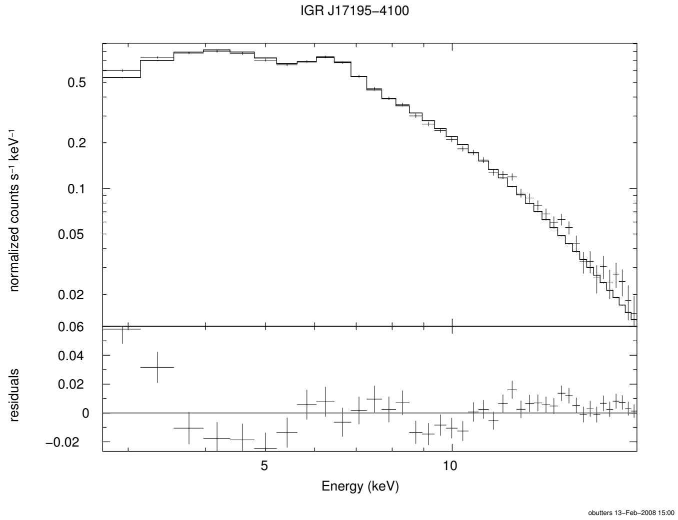

Figure 2.37: 2.5–20 keV mean spectrum of J1719 fitted with a photoelectrically absorbed Bremsstrahlung law plus iron line profile.

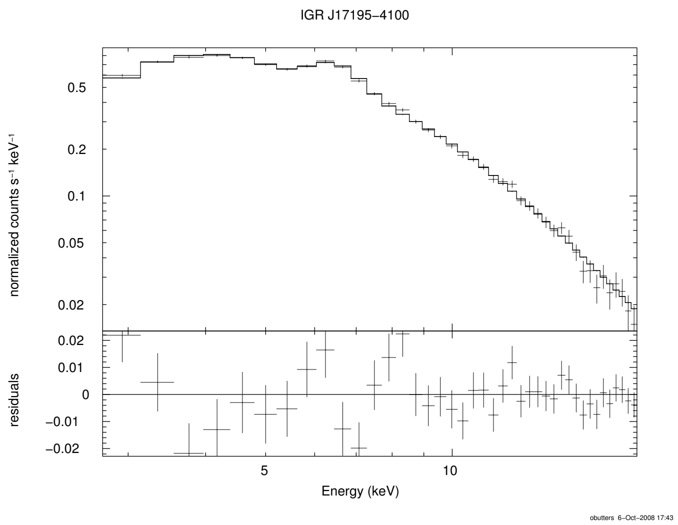

Figure 2.38: 2.5–20 keV mean spectrum of J1719 fitted with a photoelectrically absorbed power law plus iron line profile.

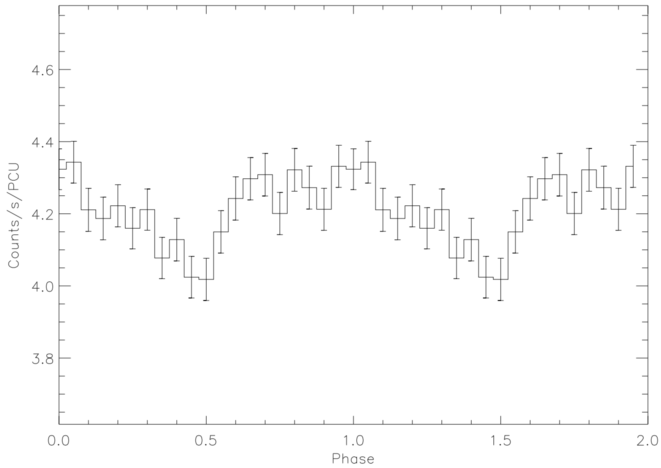

Figure 2.39: 2–10 keV folded light curve of J1719. Folded at the optical spin period of 1139.55 s proposed by Pretorius (2009).

IPs and implies that the modulation is caused by obscuration as opposed to absorption.

Again, after the publication of this data in Butters et al. (2008), Pretorius (2009) published optical photometry and spectroscopy of this source. She did not find either of the periods noted here, moreover she found a period of 1139.55±0.4 s which she interpreted as the spin period. Inspection of the periodograms presented here (Figures 2.34 & 2.35) shows that this period is not prominent in the X-ray. Folding the data at this period gives the plot in Figure 2.39, the modulation depth of this plot is less than that of Figure 2.36. This reinforces that the optical period seen by Pretorius (2009) is not present in the X-ray. The energy resolved modulation depths also show a constant modulation depth at this period. Similarly, the orbital period suggested by optical spectroscopy is also not seen in the X-ray (see Figure 2.40).

The presence of an iron feature at 6.5 keV is a strong indicator of an IP classification. A significantly better spectral fit is obtained from a power law instead of a Bremsstrahlung model. The 2–10 keV fluxes obtained from each of the spectral models are also considerably larger than the value reported by Tomsick et al. (2006) in the 0.3–10 keV energy band. This may be indicative of the simplistic single temperature Bremsstrahlung model used here; multi-temperature fits are often needed to model the post-shock flow (see e.g. Ezuka & Ishida (1999)). However, the signal to noise and the spectral resolution of the data is such that a complex model may yield non-unique or degenerate results.

This target also has other sources in the field of view. Using the same technique as for J1227, outlined

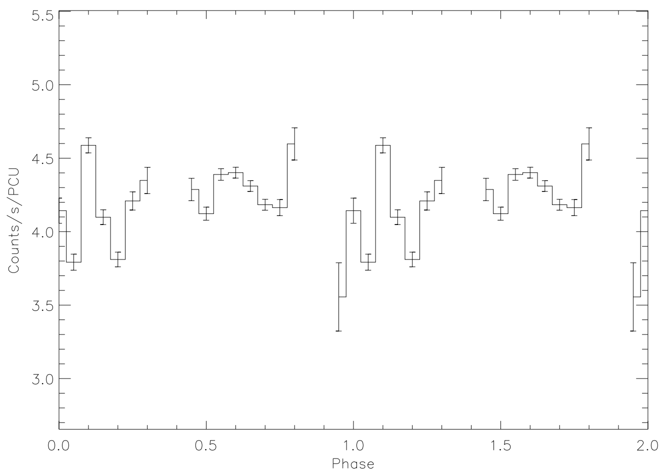

Figure 2.40: 2–10 keV folded light curve of J1719. Folded at the optical orbital period of 14418 s proposed by Pretorius (2009).

in section 2.4.3, these may contribute up to 1.1 ct s^{-1} PCU^{-1} in the 2–20 keV energy band, i.e. $\lesssim 20\%$ of the measured count rate. As was suggested for J1227, it is likely that these other sources in the field of view are softer than the target. If this is the case then the modulation of the target will be reduced the most at lower energies. Therefore the modulation depth may appear constant across the different energies instead of increasing at lower energies.

It is also possible these other sources may skew the model fit in such a way that the calculated flux is then overestimated, this may explain why the flux reported here is larger than the Tomsick et al. (2006) value. We emphasise that this is only an estimate of the contamination; the other sources may differ markedly from the assumed spectral shape.

Conclusion

J1719 clearly exhibits some properties seen in IPs, but not to an extent for it to be definitively classified it as such. We do note that it is likely J1719 is an IPs, and that its true nature is being masked by the presence of contamination from other sources.

2.5 Chapter Conclusion

One of the biggest surprises of the *INTEGRAL* mission is the detection of mCVs. In its ongoing IBIS survey it has detected ten confirmed IPs (Barlow et al. 2006; Bird et al. 2007). *Swift* has also detected six of these ten. Each of the targets selected here was chosen as it was a hard X-ray emitting source, detected with either *INTEGRAL* or *Swift*. Of the six targets observed in this campaign three have been confirmed as IPs, two as possible IPs and the sixth as a likely polar. This indicates that hard X-ray selected mCV targets are ideal objects to try to classify.

The characteristics of the IPs found here are typical of other (usually soft X-ray selected) IPs. Therefore there is no evidence that the hard X-ray selected and the soft X-ray selected populations are physically different. Further to this; *INTEGRAL* has not surveyed the whole sky to an equal extent, therefore it is likely that as more of the existing IPs have a greater exposure time that they will be found to emit hard X-rays also.

In each of the spectra presented here the lowest energy data point is typically the one which is the worst fit to the model, particularly in the Bremsstrahlung fits. This may be caused by the presence of a soft X-ray component, as has been seen in an increasing number of IPs. Clearly the data range and resolution is such that this component cannot be modelled here, since this would lead to non-unique models of this component.

If J1453 is confirmed as an asynchronous polar (AP) then this brings the total number of APs detected by *INTEGRAL* to three (BY Cam and V1432 Aql being the other two). Compared to the synchronous polars they are then hugely over represented (only one synchronous polar has been found as an *INTEGRAL* source). One possible explanation for this is that the APs have an accretion footprint that will 'wander' around the surface of the WD. This will have the effect of making the accretion column less dense, and more like the stream-fed IPs.

Chapter 3

Circular polarization survey of intermediate polars

The results of a survey of circular polarization emission from intermediate polars are presented here. This chapter begins with a short introduction to put the survey in context (Section 3.1), and then summarizes all the previous circular polarization measurements in the field (Section 3.3). The method used and the style of reporting the data is then outlined (Section 3.5). Then the results of each of the targets is reported, along with a discussion of each (Section 3.7). All of this work has been reported in Katajainen et al. (2007) and Butters et al. (2009a).

3.1 Introduction

Non-magnetic CVs evolve from long orbital periods (a few hours) to short orbital periods (just over an hour). The proposed explanation for this evolution is magnetic braking and gravitational radiation (King 1988). Gravitational radiation is expected to be an important factor in mCVs, but the presence of magnetic braking is currently under some debate (see e.g. Webbink & Wickramasinghe (2002)). This means that mCVs will evolve from long orbital periods to short orbital periods too (even if magnetic braking is not present). Since IPs generally have a longer orbital period than the polars it was suggested that IPs evolve into polars (Chanmugam & Ray 1984). This hypothesis has not been widely accepted as there is little evidence of large magnetic fields in IPs. There are however *some* IPs with similar magnetic field strength to the polars, possibly up to 30 MG in the case of V405 Aur (Piirola et al. 2008).

Cumming (2004) suggested that the relatively high accretion rate in IPs may suppress the magnetic field by overcoming ohmic diffusion, such that magnetic flux is advected into the interior of the WD. This would cause the surface magnetic field to appear less than it really is. The evolution of non-magnetic CVs is one where the orbital period decreases until $\sim$ 3 hr when the accretion effectively 'turns off' then it resumes at $\sim$ 2 hr. Applying this to mCVs allows a regime where an IP may have its 'true' magnetic field resurface when the accretion turns off, allow synchronisation, then reappear as a polar when the accretion resumes at a lower rate. This theory also ties in with studies of isolated WDs, where peak magnetic fields of $\sim 10^9$ G are seen. In binaries however, the field strength is typically an order of magnitude smaller (the maximum seen is 230 MG in AR UMa (Schmidt et al. 1996)) (Wickramasinghe & Ferrario 2000).

This is not the only theory of the origin and evolution of the magnetic field in mCVs. As noted in Section 1.5, Tout et al. (2008) suggest that *all* magnetic WDs evolve from a binary common envelope phase. Moreover the closer the binary pair are together the stronger the resultant magnetic field, with the isolated magnetic WDs being the end point of a merger.

In order to test any evolutionary hypotheses, an accurate determination of the magnetic fields present in IPs is needed. The best way of doing this is via circular polarization measurements, however, the method of reporting the level of circular polarization is rather ambiguous. Some authors quote the average level throughout their observing run, some give orbitally binned data, but most report data phase binned at the spin period. Each method may have the effect of giving a different interpretation of the magnetic field (see e.g. Uslenghi et al. (2001) where the data is presented in mean, spin binned and orbitally binned format). The average value approach could potentially smooth a sinusoidal-like variation, with an arbitrary amplitude and zero offset, to an average of zero. Phase binning at the orbital period may be severely affected by the variation in orbitally varying unpolarized light. Phase binning over the spin period can reduce both these effects, and since the circular polarization is thought to originate from the accretion column (emission from which varies at the spin period), this is the most desirable approach. The base line chosen needs to be sympathetic to the orbital variation, i.e. either be short in relation to the orbital period, or considered in chunks, and the integration time short compared to the spin period.

3.2 Expected circular polarization signature

Section 1.8.2 outlined how circularly polarized radiation is emitted in IPs and some of the theoretical modelling that has been done to characterize it. By considering this work the circular polarization signature expected to be seen in observations of IPs can be deduced.

An ideal dipole would give off equal levels of positive circular polarization from one pole and negative from the other when accreting from a uniform accretion flow. If the dipole were centred at the centre of the white dwarf and both poles could be seen, then the circular polarization would cancel out.

If the geometry of the system is such that only one pole can be seen then either positive or negative polarization will be seen at all wavelengths. By looking at different colour pass bands the harmonic structure may be deduced, and therefore the magnetic field strength.

If both poles can be seen but are accreting at different rates then they will be at different temperatures. This will allow a different harmonic structure to be emitted at each pole. If the harmonics are such that a peak from one pole is at the same wavelength as a trough from the other, then by looking simultaneously at different colour pass bands the two poles may be resolved. This would result in positive polarization being seen in one band and negative in another.

Obviously the situation where the magnetic field structure is non-dipole like significantly complicates this analysis.

3.3 Previous circular polarization detections in IPs

DQ Her was the first IP (although not classified as an IP at the time) to have circular polarization detected (Swedlund et al. 1974). This white light detection was carried out over the course of three months allowing many measurements over the entire 4.6 hr orbital period. The level of circular polarization was found to vary periodically over the spin period (142 s), and to be both positive and negative. This variation was also found to have a different profile over the orbital period. The maximum amplitude of variation was found to be approximately 0.6%. Stockman et al. (1992) also measured the level of circular polarization on DQ Her, they found a mean level of $+0.01 \pm 0.01\%$, however, they remark that short period systems will have their levels of reported circular polarization reduced due to the long measurement times.

The next detection of circular polarization in an IP was BG CMi (Penning et al. 1986; West et al. 1987).

Measurements were taken in five different pass bands at various times over four months. This allowed the measurements to be plotted over the orbital period (3.75 hr). In the $1.10-1.38\mu$m band the data were distributed randomly about the mean of $-1.74 \pm 0.26\%$ indicating no orbital modulation. Phase binning the data at the spin period (15.9 min) showed a coherent modulation, however the variation was within two sigma of being zero. West et al. (1987) also considered the variation of the circular polarization with the pass band, they found that the amplitude detected increased with wavelength, ranging from $-0.053 \pm 0.051\%$ at $0.32 - 0.86\mu$m to $-4.24 \pm 1.78\%$ at $1.40 - 1.65\mu$m.

PQ Gem (RE 0751+14) was found in the early 1990's to exhibit significant circular polarization which was modulated at the spin period (Rosen et al. 1993; Piirola et al. 1993; Potter et al. 1997).

Since then, several IPs have been found to exhibit similar behaviour, or have had upper limits placed on their level of circular polarization (see Table 3.1 for a summary of all measurements taken to date).

Table 3.1: Summary of previously measured circular polarization in IPs. (a) numbers in parentheses indicate the effective wavelength of the filter. (b) estimated from plots. (c) I corresponds to an unspecified time between 0.5–1 mins. (d) Constant polarimeter position. Names in bold represent objects with significant measured circular polarization.

Name	Wavelength range[a] (nm)	Mean (%)	Min (%)	Max (%)	Integration time (s)	Total time	Ref
AE Aqr	350–920	-0.03 ± 0.02			15	140 min	1
	I	-0.06 ± 0.03			15	150 min	1
	350–570	-0.06 ± 0.02			5	390 min	1
	320–860	$+0.01 \pm 0.02$			$8{\times}I^c$	$\times 2$	2
	590–860	-0.01 ± 0.01			1^d	34 min	2
	320–860	-0.13 ± 0.03			$8{\times}I^c$	$\times 5$	2
	320–860	$+0.01 \pm 0.01$			$8{\times}I^c$	$\times 3$	2
	1150–1350	$+0.06 \pm 0.08$				4 min	2

Continued on the next page...

Continued from the previous page.

Name	Wavelength range[a]	Mean	Min	Max	Integration time	Total time	Ref
	(nm)	(%)	(%)	(%)	(s)		
	1450–1650	-0.80 ± 0.60				7 min	2
	500–750	$+0.07 \pm 0.02$			5	255 min	3
	(550)	$+0.06 \pm 0.01$			5	323 min	3
AO Psc	570–920	$+0.03 \pm 0.03$			240	180 min	1
	I				240	180 min	1
	320–860	-0.05 ± 0.06			$8\times I^c$	$\times 1$	2
	660–860	$+0.00 \pm 0.07$			$8\times I^c$	$\times 3$	2
	320–860	$+0.03 \pm 0.03$			$8\times I^c$	$\times 2$	2
BG CMi	640–860	-0.24 ± 0.03			$2\times \sim 30$		4
	320–860	-0.05 ± 0.05					5
	720–860	-0.25 ± 0.06					5
	1110–1380(1250)	-1.74 ± 0.26					5
	1400–1650(1500)	-4.24 ± 1.78					5
DQ Her	370–580		-0.6^b	$+0.6^b$	14.2	$\sim$1980 min	6

Continued on the next page...

Continued from the previous page.

Name	Wavelength range[a] (nm)	Mean (%)	Min (%)	Max (%)	Integration time (s)	Total time	Ref
	320–860	$+0.01 \pm 0.01$				250 min	2
EX Hya	570–920	-0.02 ± 0.04			240	200 min	1
	590–860	$+0.01 \pm 0.02$			2^d	68 min	2
FO Aqr	640–860	$+0.06 \pm 0.02$					4
	330–920	-0.01 ± 0.02			120	200 min	1
	I	$+0.11 \pm 0.07$			240	200 min	1
	320–860	-0.06 ± 0.04			$8{\times}I^c$	$\times 2$	2
	320–860	$+0.01 \pm 0.04$			$8{\times}I^c$	$\times 6$	2
	720–860	-0.01 ± 0.17			$8{\times}I^c$	$\times 5$	2
	1150–1350	$+0.19 \pm 0.13$				51 min	2
	1150–1350	$+1.09 \pm 0.31$				141 min	2
	Visual	$+0.11 \pm 0.13$	-0.2^b	$+0.3^b$	28	270 min	7
	IR	-0.01 ± 0.55	-1.3^b	$+0.8^b$	28	270 min	7
GK Per	1150–1350	$+0.03 \pm 0.10$				45 min	2

Continued on the next page...

Continued from the previous page.

Name	Wavelength range[a] (nm)	Mean (%)	Min (%)	Max (%)	Integration time (s)	Total time	Ref
PQ Gem	*U*	$+0.0 \pm 0.6$				80 min	8
	B	$+0.0 \pm 0.6$				80 min	8
	V	$+0.0 \pm 0.9$				80 min	8
	R		-1.1	$+0.6$		80 min	8
	U		-0.4^b	$+0.3^b$	$8{\times}5$	162 min	9
	B		-0.3^b	$+0.4^b$	$8{\times}5$	162 min	9
	V		-0.7^b	$+0.7^b$	$8{\times}5$	162 min	9
	R		-1.5^b	$+0.7^b$	$8{\times}5$	162 min	9
	I		-2.7	$+1.5$	$8{\times}5$	162 min	9
	U		-0.5^b	$+0.3^b$		~730 min	10
	B		-0.2^b	$+0.3^b$		~730 min	10
	V		-0.6^b	$+0.4^b$		~730 min	10
	R		-1.0^b	$+0.2^b$		~730 min	10
	I		-1.3^b	$+1.3^b$		~730 min	10

Continued on the next page...

Continued from the previous page.

Name	Wavelength range[a] (nm)	Mean (%)	Min (%)	Max (%)	Integration time (s)	Total time	Ref
	J		-1.2^b	$+1.0^b$		$\sim$270 min	10
	K		-2.0^b	$+1.3^b$		$\sim$460 min	10
TV Col	640–860	-0.03 ± 0.04					4
	320–860	-0.13 ± 0.09			$8{\times}I^c$	$\times 1$	2
	320–860	-0.07 ± 0.07			$8{\times}I^c$	$\times 3$	2
	320–860	-0.08 ± 0.10			$8{\times}I^c$	$\times 1$	2
V1223 Sgr	350–920	-0.06 ± 0.03			240	144 min	1
	I+ *R*	-0.04 ± 0.07			240	563 min	1
	V	-0.48 ± 0.62	$\gtrsim -2$	$\lesssim +2$	14		11
	R	$+0.03 \pm 0.13$	$\gtrsim -0.5$	$\lesssim +0.5$	14		11
	J	-0.36 ± 0.13	$\gtrsim -1$	$\lesssim +0.5$	14		11
	K	$+1.14 \pm 1.26$	$\gtrsim -8$	$\lesssim +8$	14		11
V2306 Cyg	(360)	$+0.04 \pm 0.06$			$8{\times}10$ (210)	872 min	12
	(440)	$+0.16 \pm 0.08$			$8{\times}10$ (210)	872 min	12

Continued on the next page...

Continued from the previous page.

Name	Wavelength range[a] (nm)	Mean (%)	Min (%)	Max (%)	Integration time (s)	Total time	Ref
	(530)	$+0.18 \pm 0.11$			8×10 (210)	872 min	12
	(690)	-0.55 ± 0.08	-1.3^{b}	$+1^{b}$	8×10 (210)	872 min	12
	(830)	-0.91 ± 0.14	-1.7^{b}	$+0.4^{b}$	8×10 (210)	872 min	12
	B	$+0.32 \pm 0.10$	-0.3^{b}	$+0.7^{b}$	58	52 min	13
	R	-1.99 ± 0.11	-5.2^{b}	-0.6^{b}	45	55 min	13
V2400 Oph	WL		-2.9^{b}	-1.0^{b}	120 & 180	~900 min	14
	V	$\sim -1.8^{b}$	-4.8^{b}	-1.0^{b}	120	~33 min	14
	R	$\sim -2.3^{b}$	-5.1^{b}	-0.5^{b}	120	~71 min	14
	I	$\sim -3.3^{b}$	-6.0^{b}	-1.0^{b}	120	~32 min	14
	320–700 (470)	-0.90 ± 0.03			50		15
	560–900 (700)	-2.82 ± 0.04			50		15
V405 Aur	500–750	1.8 (Semi-amp)					16
	U		-2	$+2$	8×12 (96)	1328 min	17
	B		-3	$+3$	8×12 (96)	1328 min	17

Continued on the next page...

Continued from the previous page.

Name	Wavelength range[a] (nm)	Mean (%)	Min (%)	Max (%)	Integration time (s)	Total time	Ref
	V		-3	$+3$	8×12 (96)	1328 min	17
	R		-2	$+2$	8×12 (96)	1328 min	17
	I		-1	$+1$	8×12 (96)	1328 min	17
YY Dra	320–860	$+0.09 \pm 0.10$			$8\times I^c$	$\times1$	2

References - (1) Cropper (1986); (2) Stockman et al. (1992); (3) Beskrovnaya et al. (1996); (4) Penning et al. (1986); (5) West et al. (1987); (6) Swedlund et al. (1974); (7) Berriman et al. (1986); (8) Rosen et al. (1993); (9) Piirola et al. (1993); (10) Potter et al. (1997); (11) Watts et al. (1985); (12) Uslenghi et al. (2001); (13) Norton et al. (2002); (14) Buckley et al. (1995); (15) Buckley et al. (1997); (16) Shakhovskoj & Kolesnikov (1997); (17) Piirola et al. (2008).

Table 3.2: Inferred magnetic field strengths from the measured circular polarization in IPs.

Name	Inferred magnetic field strength (MG)	Reference
BG CMi	5–10	West et al. (1987)
	2–10	Chanmugam et al. (1990)
PQ Gem	8–18	Piirola et al. (1993)
	9–21	Vaeth et al. (1996)
	9–21	Potter et al. (1997)
V2400 Oph	8	Buckley et al. (1995)
	9–27	Vaeth (1997)
V405 Aur	~ 30	Piirola et al. (2008)

V2306 Cyg is the only reported IP to show significant positive polarization in one band and negative in another (Norton et al. 2002). This requires two opposite poles to be seen and for them to be in different states (i.e. one or more of the temperature, geometry, accretion rate etc must be different at the two poles). In all the other cases the polarization has the same sign across the different wave bands.

Some of the significant (non-zero) measurements of circular polarization have had an estimate of the magnetic field present on the WD attributed to them. Each of these estimates are fundamentally based on fitting either narrow-band or broad-band photometry to a plot similar to that in Figure 1.15 (except V405 Aur which also had specto-polarimetry measurements taken). Estimates of which plot to use (i.e. what values of T_e etc) are based upon the data available and the general consensus of the accretion flow physics at the time. With over 20 years between the first and the most recent calculations it is possible that some of the numbers may be somewhat different now. It is therefore difficult to directly compare the magnetic field estimates that have been given (see Table 3.2).

3.4 Aim

The aim of this study was to systematically survey the IPs for circular polarization emission in a consistent way. Simultaneous photo-polarimetric measurements in multiple pass-bands helped to characterize the nature of the circular polarization. The analysis and method of reporting the data enabled as much information as possible about the circular polarization to be retained.

3.5 Observations

Observations were carried out at the 2.56m Nordic Optical Telescope (NOT) on the island of La Palma over three consecutive nights starting 2006 July 31. The telescope was fitted with the TurPol instrument. This is the double image chopping polarimeter (Piirola 1973, 1988; Korhonen et al. 1984), which is able to perform simultaneous photo-polarimetric measurements in all *UBVRI* bands, by using four dichroic filters (which split the light into five spectral pass-bands). The pass-bands are shown in Figure 3.1 and are defined as having an effective wavelength of 360, 440, 530, 690, and 830 nm for each of *UBVRI* respectively. By inserting a plane parallel calcite plate into the beam before the focal plane, polarization measurements are possible. The calcite splits the incoming light into two components, the ordinary and the extra-ordinary, which are orthogonally linearly polarized. A diaphragm in the instrument has two apertures, one passes the star's ordinary component, the other passes the extra-ordinary component. A chopper opens and closes the apertures alternately, illuminating the photo-cathode of the photomultiplier tube. By measuring the relative intensities of components after a wave-plate, (which may be rotated in 90° steps) the degree of circular polarization of the light entering from the star can be calculated. Both components of the sky background pass both diaphragms, and the polarization of the sky is thus directly eliminated. In addition, measurements of empty sky are also done at 10 minute intervals, as this sky value is needed in calibration of the photometry.

For one polarization data point, normally at least four multiples of the integration time plus mechanical dead-time (few seconds) generated from rotation of the wave plate is needed, assuming that the circular polarization is measured from two different wave plate positions. This will have the effect of 'smearing' out the data on some very short period objects, and therefore may under report their true polarization value. In this study, as some of the targets show remarkable variability within a short timescale, for these only one wave plate position measurement was used, instead of two (four in the case of J2133).

The targets chosen for this northern hemisphere survey are those in Table 3.3, and the observing log in Table 3.4. Note the very short period systems (AE Aqr (33 s), DQ Her (142 s), and J1730 (128 s)) had one orientation of the wave-plate per measurement, J2133 had four, and the other targets had two.

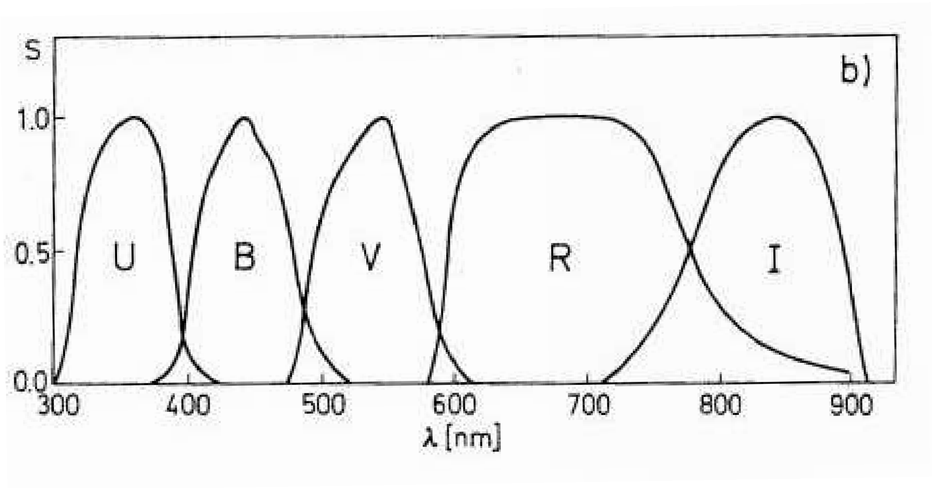

Figure 3.1: Normalized response curves of the *UBVRI* bands, with the effects of the additional glass filters and photocathode sensitivity taken into account. Taken from the NOT operating manual No.2, version 1.0.

Table 3.3: Target list.

Name	α2000	δ2000	V (mag)	$\mathrm{P_{spin}}$ (s)	$\mathrm{P_{orb}}$ (h)
J1730	17:30:21	−05:59:32	15.8	128.0	15.42
DQ Her	18:07:30	+45:51:32	13	142.1	4.65
V1223 Sgr	18:55:02	−31:09:48	13.2	745.6	3.37
V2306 Cyg	19:58:14	+32:32:42	16	1466.7	4.35
AE Aqr	20:40:09	−00:52:16	12	33.1	9.88
J2133	21:33:44	+51:07:24	15.3	570.8	7.19
FO Aqr	22:15:55	−08:21:05	13.5	1254.5	4.85
AO Psc	22:55:17	−03:10:39	13.3	805.2	3.59

J1730 = 1RXS J173021.5−055933,

J2133 = 1RXS J213344.1+510725.

Table 3.4: Observing log.

Name	Start time (HJD^a)	End time (HJD^a)	Duration (mins)	No. of P_{orb}	No. of P_{spin}	Filters	Exposure time^b (s)	Resolution^c (s)	V^d (mag)
DQ Her	13 948.4240	13 948.5349	159.7	0.57	67.4	*UBVRI*	1×10	~ 24	14.5
J2133	13 948.5732	13 948.6542	116.6	0.27	12.3	*UBVRI*	4×10	~ 96	15.3
FO Aqr	13 948.6933	13 948.7091	22.8	0.08	1.1^e	*UBVRI*	2×10	~ 48	13.9
AE Aqr	13 949.5103	13 949.5704	86.5	0.15	156.8	*UBVRI*	1×3	~ 8.5	11.4
V2306 Cyg	13 949.5794	13 949.6528	105.7	0.40	4.3	*UBVRI*	2×10	~ 48	14.7
AO Psc	13 949.7047	13 949.7194	21.2	0.10	1.6^e	*UBVRI*	2×10	~ 48	13.2
J1730	13 950.4112	13 950.5134	147.2	0.16	69.0	*UBVRI*	1×10	~ 24	16.3
V1223 Sgr	13 950.5298	13 950.5871	82.5	0.41	6.6	*UBVRI*	2×10	~ 48	13.7
AE Aqr	13 950.6224	13 950.6366	20.4	0.03	37.0	*UBVRI*	1×1	~ 4.5	11.6
J2133	13 950.6455	13 950.7187	105.4	0.24	11.1	*UBVRI*	4×10	~ 96	15.2

^{a} +2 440 000

^{b} The number of orientations of the wave plate, and the time spent at each orientation.

^{c} The resolution is roughly the number of orientations of the wave plate multiplied by the exposure time multiplied by two (to account for the ordinary and extraordinary measurements) plus some mechanical dead time.

^{d} Measured.

^{e} These data sets are short and therefore the reported uncertainties are probably underestimated.

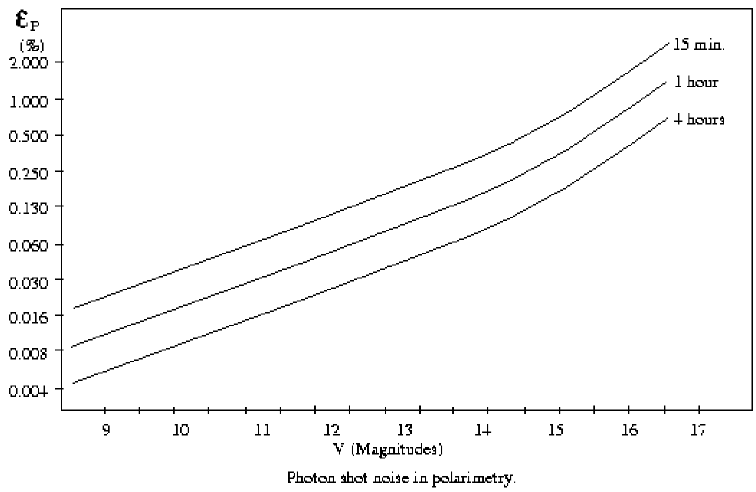

Figure 3.2: Measurement errors as a function of magnitude for TurPol. Taken from the NOT operating manual No. 2 version 1.0.

Figure 3.2 shows the estimated error in a measurement of the degree of circular polarization as a function of the magnitude of the target. The three lines show the approximate total time needed to reach a given accuracy. To reach a 0.2% accuracy for a 13th magnitude target takes approximately 15 minutes. To see any variation in the polarization ideally ten measurements were needed giving a typical total observing time of 150 mins.

The instrumental polarization was small in all bands (see Table 3.5). The circular polarization standard star GRW+70 8247 (West 1989) was used to check the calibration, the values reported here are consistent with previous measurements of the standard. The uncertainties quoted on each circular polarization measurement are based on photon noise and are one sigma.

The zero points of the *UBVRI* magnitude scale were determined by observations of Landolt standards (109 954, 111 250, 111 2093 and 114 637; Landolt (1992)) during each night.

3.6 Data reduction

Data reduction was carried out by Seppo Katajainen with the custom data reduction software developed for the instrument by Vilppu Piirola. This takes the raw data, carries out background subtraction then outputs absolute magnitude photometry derived from the Landolt standards. It compares the degree of polarization at each required angle of the wave plate to calculate the level of circular polarization. This aspect of the reduction software was modified to allow fewer wave plate positions for a single polarization measurement. As noted in

Table 3.5: Calibration data (taken on the first night).

	Instrumentational polarization		Measured standard polarization	
Band	Value (%)	uncertainty (%)	Value (%)	uncertainty (%)
U	−0.005	0.030	+0.126	0.103
B	−0.064	0.024	−3.607	0.112
V	−0.017	0.028	−3.959	0.166
R	−0.011	0.024	−4.064	0.156
I	−0.059	0.029	−2.647	0.226

Section 1.8.2 biases are introduced in circular polarization measurements by the retardation of the incoming wave. These are usually eliminated by rotating the wave plate to multiple orientations. By modifying the reduction software to use fewer orientations a better temporal resolution can be achieved, however this is at the cost of not eliminating these biases.

The variable gain implementation of the CLEAN algorithm (Lehto (1997) and also Section 2.3.2) was used to search for periodic variations in the photometry and polarization in each target. Only significant signals are reported in this chapter.

3.7 Results

Given the ambiguity in the previously reported results, the data is reported here in multiple formats. The average value over the run will show any large unmodulated polarization (like that in BG CMi) and allow comparison with most of the previous measurements. The peak amplitude (of the spin folded and phase binned data) gives an idea of how modulated the system is. The peak to peak value shows whether or not both magnetic poles can be seen, and gives the best indication of the presence of modulation. The results are given in order of increasing R.A.

3.7.1 1RXS J173021.5–055933

Background

1RXS J173021.5–055933 (J1730) is a recently classified IP. It has a reported orbital period of 15.42 hr and spin period of 128.0 s (Gänsicke et al. 2005). These parameters make it a close sibling of the enigmatic AE Aqr (spin and orbital periods of 33 s and 9.88 hr respectively). This short period (and therefore large number of completed spin cycles) has rendered the spin ephemeris of de Martino et al. (2008) out of date, and there is no published orbital ephemeris. Zero spin phase was therefore arbitrarily set to HJD 2 453 950.5, and a spin period of 0.001481481 d (Gänsicke et al. 2005) was used.

Photometry

Here the first simultaneous *UBVRI* photometry of this object is presented (see Figure 3.3). The photometry exhibits a double peak profile with equal maxima and unequal minima in each band. The photometric CLEANed periodograms of each individual band are shown in Figure 3.4. The spin period is seen at a value of 128.1±0.7 s and the first harmonic at 64.0±0.2 s (uncertainties based on a one sigma Gaussian fit to the periodogram). The spin peak is seen strongest in the *V* band.

de Martino et al. (2008) reported simultaneous optical Sloan filter data from the *u'*, *g'* and *r'* bands. The *u'* filter is approximately the same as the *U* band used here, *g'* covers the *B* and the upper half of *V*, and *r'* covers the lower half of *V* as well as *R*. In each of their *u'*, *g'* and *r'* band observations the fundamental and the first harmonic were seen, with the first harmonic, on average, being strongest. This is in contrast to what was seen here (see Figure 3.4), i.e. the fundamental being dominant. However, de Martino et al. (2008) show their *r'* band power spectra obtained on each of six consecutive nights. This shows a marked change in the relative strengths of the first harmonic and fundamental over time, with the last night exhibiting a similar structure to that reported here. de Martino et al. (2008) see the strongest signal in their *g'* and *u'* bands. The *U* band has very little power, however, the *V* band is the strongest, and since this contributes to what is their *g'* band this is consistent with their results.

Polarization

The wave plate was positioned in one orientation for each circular polarization measurement for 10 s. The data were binned into 15 bins over the spin cycle. In each band the mean circular polarization was within two

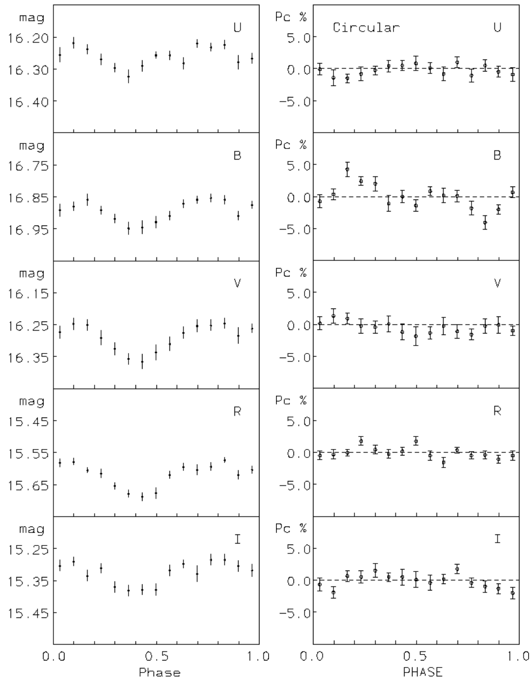

Figure 3.3: Spin folded and phase binned simultaneous *UBVRI* photometry (left) and circular polarization (right) plots of J1730. Zero phase corresponds to HJD 2 453 950.5. A spin period of 0.001481481 d was used.

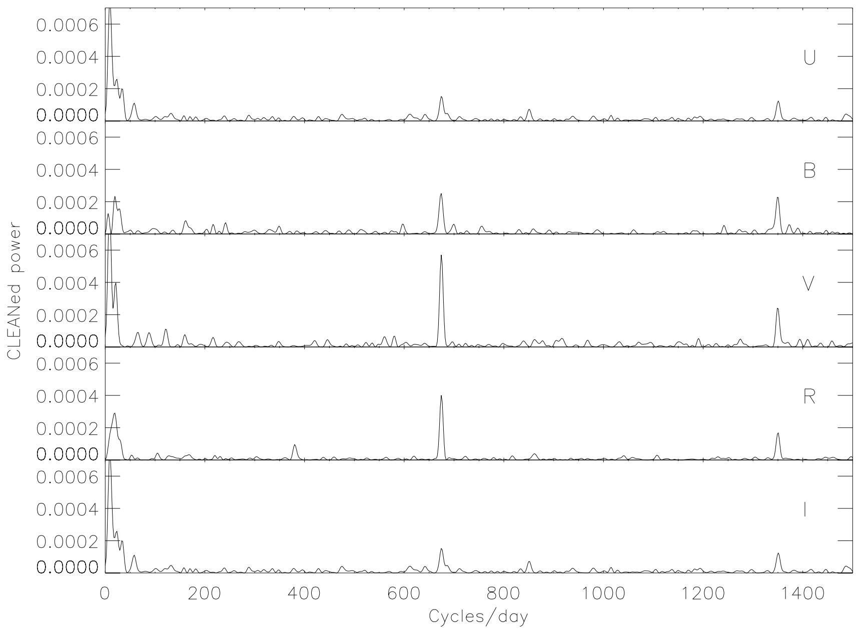

Figure 3.4: *UBVRI* CLEANed photometric periodograms of J1730.

sigma of being zero. The biggest amplitude modulation was $4.26 \pm 1.09\%$ and the greatest peak to peak value was $8.26 \pm 1.56\%$ (see Table 3.6). The spin period was recovered from a period search of the *B* band circular polarization also. The short spin period means that many spin cycles (69) were completed, leading to a high confidence in this data set.

Discussion

The level of polarization ($8.26 \pm 1.56\%$ peak to peak in the *B* band) makes this one of the most variable circularly polarized IPs, and therefore likely one of the most magnetic, measured to date. The uncertainty in the methods used to transform this level of polarization into a magnetic field estimate were outlined in Chapter 1. As a rough guide, V405 Aur may be considered; Piirola et al. (2008) found a peak to peak variation of ∼6% in the B-band as well as cyclotron humps in spectro-polarimetric measurements. They concluded that the WD probably has a magnetic field of ∼30 MG. By considering the data available here, i.e. just the photo-polarimetry, it is possible that J1730 has a magnetic field in excess of 30 MG.

The variation of the circular polarization in the *B* band, showing both positive and negative values, is indicative of both magnetic poles being visible (since each pole may only emit either positive or negative circular polarization). This is in good agreement with Gänsicke et al. (2005) who concluded that both poles could be seen. The raw circular polarization data is somewhat noisy, with individual measurements of over 15%. The origin of these values is uncertain, but it is possible that they may arise from short epochs when the diluting light is randomly lower due to flickering. In the *B* band the photometry and circular polarization are coincident; the peaks in the photometry align with the peak and trough in the circular polarization. This strengthens the assertion that both poles are seen and they are both emitting circular polarization. Like many of the other IPs for which circular polarization has been detected, J1730 is also an *INTEGRAL* source (Barlow et al. 2006).

The variable nature of this object over the course of several days (de Martino et al. 2008) makes this an ideal target for a long base line follow up. Monitoring how the circular polarization varies as the accretion column structure changes over time and linking this to the photometry may reveal more about the magnetic nature of this source and IPs in general. Phase resolved circular spectro-polarimetry would be the ideal tool in revealing the magnetic field strength of J1730, but taking into account the extremely short spin period (128 s), and relative faintness (V ∼17) there are very few telescope and instrument combinations available where these

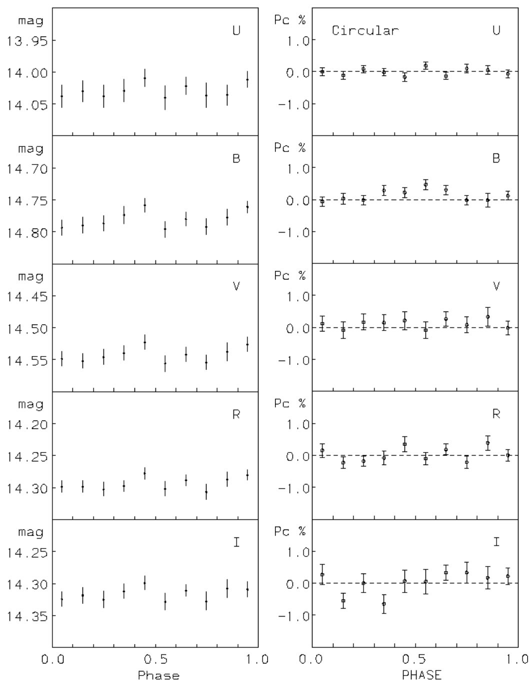

Figure 3.5: Spin folded and phase binned simultaneous *UBVRI* photometry (left) and circular polarization (right) plots of DQ Her. Zero phase corresponds to HJD 2 453 948.5. A spin value of 0.00164504 d was used.

kind of observations are possible.

3.7.2 DQ Her

Background

DQ Her has an orbital period of 4.65 h and a spin period of 142 s. Using the ephemeris of Zhang et al. (1995) DQ Her was at an orbital phase of 0.23 from the optical eclipse. An arbitrary zero point of HJD 2 453 948.5 was chosen for the spin phase, and a spin value of 0.00164504 d was used.

Polarization

Due to the short period, a single wave plate position was used for an integration time of 10 s. The data was binned into ten bins over the spin period. All of the mean polarization values are less than three sigma from zero. The maximum amplitude seen was $0.64 \pm 0.31\%$ and the maximum peak to peak value was $1.00 \pm 0.39\%$ (see Table 3.6), this is less than a three sigma detection of variation (see Figure 3.5).

Discussion

This is the first simultaneous *UBVRI* polarimetric observation of DQ Her. The maximum level of circular polarization seen here ($0.64 \pm 0.31\%$) is consistent with the plots of Swedlund et al. (1974) who illustrate a variation with a max/min of $\gtrsim 0.5\%$. They found that the polarization was also variable on the orbital period. The data in this study covered just under 0.6 of a complete orbital period and cannot be binned as theirs was. No overall trend in the data is seen. Their pass band was approximately equal to the *UBV* bands combined here.

The only other measurement of circular polarization in DQ Her was that of Stockman et al. (1992). They give a broadband integrated result close to zero, this is likely consistent with Swedlund et al. (1974) who see both positive and negative polarization values. As such, this is the first time-resolved *R* and *I* band (as well as the first simultaneous *UBVRI*) data. The largest departure from zero polarization was seen in the *I* band here, and the raw data showed up to $6 \pm 1\%$.

Although by itself this data cannot claim a significant circular polarization detection, when considered with the results of Swedlund et al. (1974), it seems likely that DQ Her does exhibit variable circular polarization. To make a definite conclusion, more measurements are needed, particularly in the *I* band.

3.7.3 V1223 Sgr

Background

V1223 Sgr has spin and orbital periods of 745.6 s and 3.37 h respectively. Using the orbital ephemeris of Jablonski & Steiner (1987), V1223 Sgr is at an orbital phase of 0.83 from the maximum light. The spin ephemeris has accumulated too much uncertainty to be useful here, so zero phase was arbitrarily set to HJD 2 453 950.5. A spin value of 0.00863 d from Osborne et al. (1985) was used.

Polarization

The polarization measurements consisted of two positions of the wave plate, each of 10 s. The data was binned into ten bins across the spin cycle. The mean values of the circular polarization were all within three sigma of being zero. The maximum amplitude variation was $1.30 \pm 1.12\%$ in the *U* band and the maximum peak to peak value was $2.16 \pm 1.22\%$ (see Figure 3.6). The peak to peak values were all within three sigma of being

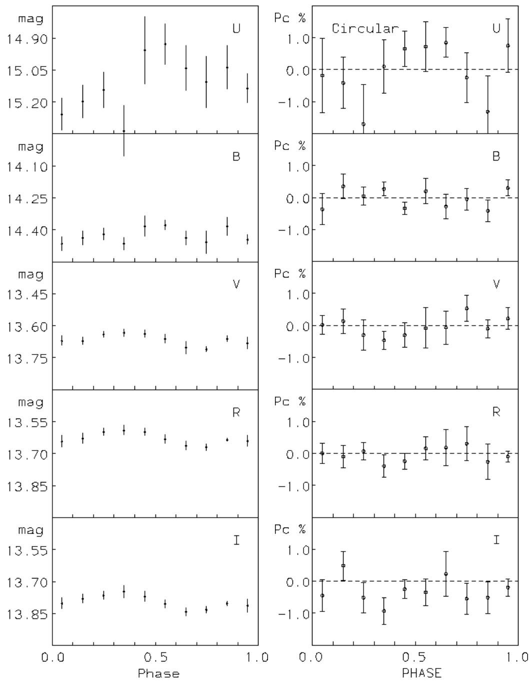

Figure 3.6: Spin folded and phase binned simultaneous *UBVRI* photometry (left) and circular polarization (right) plots of V1223 Sgr. Zero phase corresponds to HJD 2 453 950.5. A spin period of 0.00863 d was used.

zero (see Table 3.6).

Discussion

The mean circular polarization in V1223 Sgr was within four sigma of the previously reported values, and zero (see Tables 3.1 & 3.6). The maximum peak to peak variation of $2.16\% \pm 1.22\%$ in the *U* band is not constrained enough for this to be considered a definite detection, but when considered with the results of Watts et al. (1985) it is likely that V1223 Sgr is strongly polarized.

There is a clear hint of a double peaked structure in the *UVRI* circular polarization curves, indicating that two magnetic poles can be seen. This is an effect also seen in the photometry, with hints of a double peaked profile in each band. This is in contrast to previous results which show a single peaked structure.

The raw circular polarization measurements were stable in all bands at the start of the run, but the *U* band began to fluctuate as the run went on, sometimes, quite randomly, up to 20%.

V1223 Sgr has a similar spin and orbital period to V405 Aur which was recently found to be very magnetic (Piirola et al. 2008) and has its circular polarization peak in the blue part of the spectrum. If the level of polarization seen here is confirmed then V1223 Sgr would be a close twin of V405 Aur. V1223 Sgr is also an

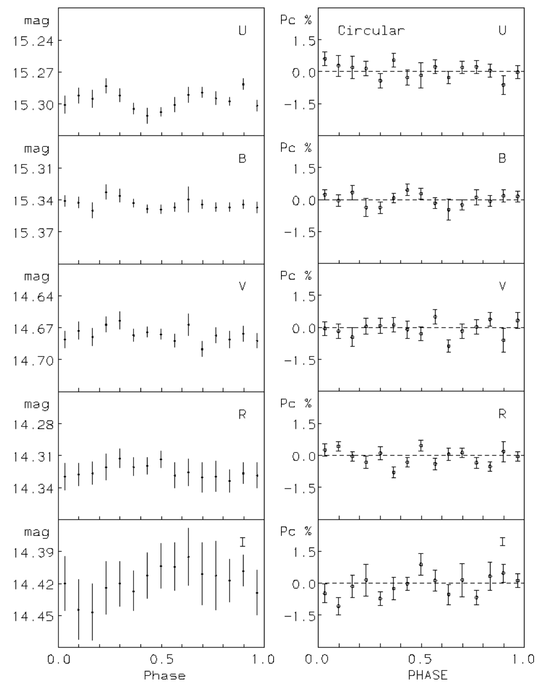

Figure 3.7: Spin folded and phase binned simultaneous *UBVRI* photometry (left) and circular polarization (right) plots of V2306 Cyg. The spin ephemeris of Norton et al. (2002) was used to phase the spin variations.

INTEGRAL source (Barlow et al. 2006).

3.7.4 V2306 Cyg

Background

V2306 Cyg has an orbital period of 4.35 h and a spin period of 1466.7 s (Norton et al. 2002; Zharikov et al. 2002). The spin ephemeris of Norton et al. (2002) was used to phase the spin variations here.

Polarization

Each polarization measurement consisted of two positions of the wave plate, each position being 10 s. The data were binned into 15 bins over the spin cycle. The maximum amplitude circular polarization was $1.06 \pm 0.41\%$ in the *I* band. The mean circular polarization in each band was consistent with zero (see Table 3.6). The maximum peak to peak value ($1.95 \pm 0.66\%$ in the *I* band) indicated that significant variation was present (see Figure 3.7 and Table 3.6).

Discussion

V2306 Cyg has had significant levels of circular polarization reported previously; Uslenghi et al. (2001) first reported it after using the TurPol instrument at the NOT (results summarised in Table 3.1). The mean results reported here are within the bounds given by uncertainties (two sigma) in their *UBV* bands, however in *R* and *I* Uslenghi et al. (2001) found a much higher amplitude mean value. Norton et al. (2002) also reported *B* and *R* band polarization at the NOT, this time using the ALFOSC instrument, they obtained mean values of $+0.32 \pm 0.10\%$ and $-1.99 \pm 0.11\%$ in each band respectively. Here, significantly lower values than theirs were seen.

The shape of the circular polarization variation seen here was one of two minima per spin cycle in the *B* and *I* bands (see Figure 3.7). The *B* band of Norton et al. (2002) had an indication of a two peaked profile, these results confirm this.

The discrepancy between these results and those reported previously can be explained in a variety of ways. The orbital phase may be different during each of the observations. Uslenghi et al. (2001) showed the circular polarization varied significantly over the orbital period, unfortunately the orbital ephemeris has accumulated too much uncertainty for this to be calculated. Another consideration is the brightness of the source. Uslenghi et al. (2001) did not quote a magnitude, but Norton et al. (2002) measured *UBVRI* magnitudes which are significantly fainter than seen here. Since circular polarization is calculated as a fraction of the total incoming light this may have had the effect of seriously diluting the result.

3.7.5 AE Aqr

Background

This is the first simultaneous *UBVRI* polarimetry measurement of AE Aqr. In most previous measurements a broad band filter and/or a much too long integration time has been used (see Table 3.1). This will have had the effect of smearing any polarization out to almost zero. In the cases where a short integration time has been used, only a mean value has been reported, except for Cropper (1986) where a maximum semi-amplitude of $\sim 0.1\%$ was given.

AE Aqr has the shortest spin period of all the known IPs ($\sim$33 s), and a relatively long orbital period of 9.88 h. Observed over two nights, it was at an orbital phase of 0.6 and 0.3 from superior conjunction of

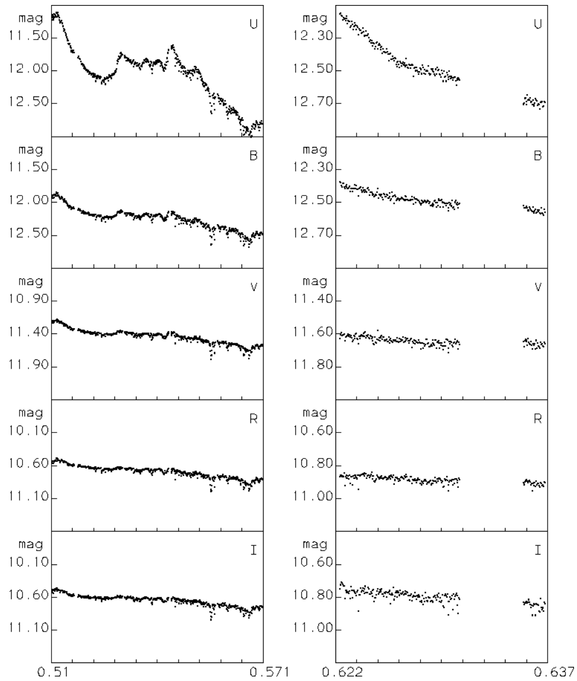

Figure 3.8: Raw *UBVRI* photometry of AE Aqr taken on the two nights. The abscissa is in left plot is HJD – 2 453 949, in the right plot it is HJD – 2 453 950.

the WD with respect to the secondary on the two nights respectively (Welsh et al. 1993). A spin period of 0.000382833 d, calculated for July/August 2006 from the ephemeris of de Jager et al. (1994) was used. The zero spin phase point used here is arbitrarily set to the midnight epoch at HJD 2 453 949.5.

Over the two nights this system showed a marked difference in its behaviour. During the first night, the *U* band exhibited significant flickering and a general trend of an increase in magnitude (see Figure 3.8). This was mirrored in the raw *U* band circular polarization, where the magnitude increased as the run went on. On the second night, the *U* band exhibited significantly less flickering. This was a trend that was seen in all bands to some extent (see Figure 3.8). This flickering is a well known feature of AE Aqr (see e.g. Beskrovnaya et al. (1996)). With this in mind the data from the two nights is presented separately.

Polarization

Only one position of the wave plate was used for each polarization measurement. On the first night, an integration time of $\sim$ 3 s was used, giving an overall temporal resolution of ~ 8.5 s. On the second night, an integration time of ~ 1 s was used giving a temporal resolution of ~ 4.5 s for a full polarization measurement. Even at this short time scale the measurements were smoothed to some extent. The data was folded and binned

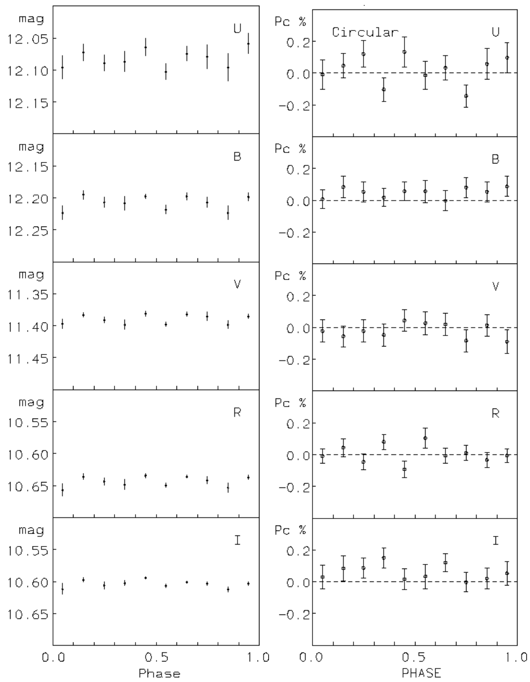

Figure 3.9: Spin folded and phase binned simultaneous *UBVRI* photometry (left) and circular polarization (right) plots of AE Aqr, taken on the first night (HJD 2 453 949). Zero phase corresponds to HJD 2 453 949.5. A spin period of 0.000382833 d was used.

into 10 bins over the spin cycle (see Figures 3.9 and 3.10). Both nights showed a very small amplitude circular polarization. However, in the raw data, values with an amplitude of over 2% (with a typical error of 0.6%) were not uncommon.

The mean values in each band (over each of the nights) were all within three sigma of zero. The peak amplitude was $0.80 \pm 0.39\%$ and the maximum peak to peak value was $1.22 \pm 0.48\%$ (see Table 3.6). The short spin period means that this data set covers many spin periods, and therefore the signal to noise is good.

Discussion

The data reported here broadly agrees with the previous mean measurements of close to zero. The small peak to peak values are also in agreement with this.

Given the generally accepted view that AE Aqr is a propeller system, it seems intuitive to assume that it would have a large magnetic field to power this regime. Norton et al. (2008) have shown, in their theoretical modelling, that propellers can exist at low magnetic field strengths when they are spinning sufficiently fast. So a large magnetic field in AE Aqr is not necessarily required.

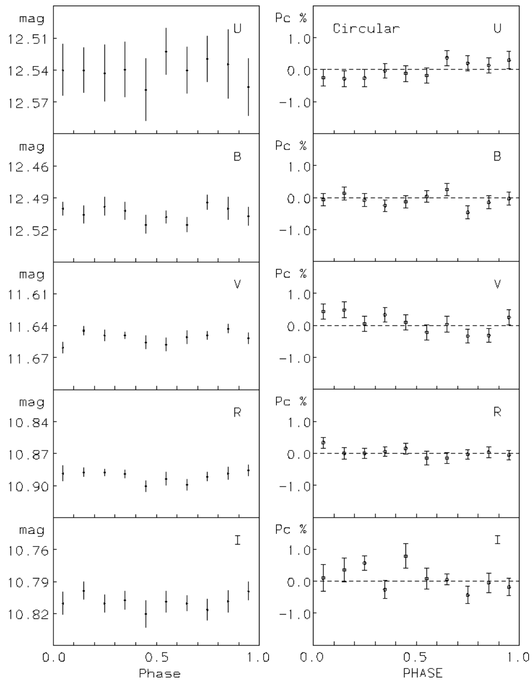

Figure 3.10: Spin folded and phase binned simultaneous *UBVRI* photometry (left) and circular polarization (right) plots of AE Aqr, taken on the second night (HJD 2 453 950). Zero phase corresponds to HJD 2 453 949.5. A spin period of 0.000382833 d was used.

3.7.6 1RXS J213344.1+510725

Background

This target was discovered from the *ROSAT* Galactic Plane survey by Motch et al. (1998), and identified as a B $\sim$ 16 mag star, which they classified as a CV. Recent observations with *XMM-Newton* showed that the X-ray data from J2133 require a multi-temperature Bremsstrahlung *and* a blackbody component with a temperature $kT_{\rm bb} \sim$ 100 eV in order to fit the detailed spectrum obtained (de Martino et al. 2006b). It is therefore similar to other IPs with a strong soft X-ray spectral component such as PQ Gem (Duck et al. 1994), V405 Aur (Haberl & Motch 1995), UU Col (Burwitz et al. 1996), NY Lup (Haberl et al. 2002) and MU Cam (Staude et al. 2003).

Like the soft intermediate polar NY Lup, but unlike most other IPs, J2133 has an unusually long orbital period, which in this case is $P_{\rm orb} = 7.193 \pm 0.016$ h (Bonnet-Bidaud et al. 2006). Only a few IPs are known to have a longer orbital period than this, and thus J2133 is among the widest IP binaries. The spin period of the WD in J2133 is relatively short, $P_{\rm spin} = 570.823 \pm 0.013$ s, and its $P_{\rm spin}/P_{\rm orb}$ ratio (a measure of the degree of asynchronism) is therefore 0.022, which is one of the smallest amongst all IPs. On this basis, the magnetic

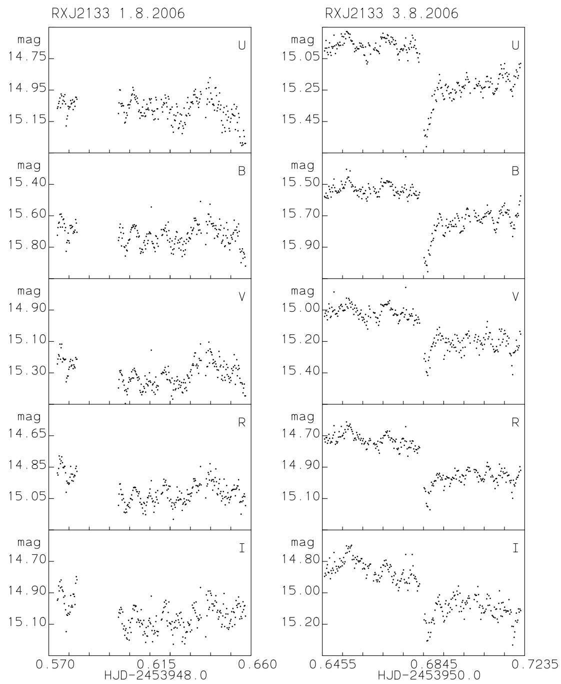

Figure 3.11: Raw *UBVRI* photometry of J2133, obtained on both nights. Each point represents a single photometric measurement, with 24 s time resolution.

field in J2133 is expected to be weak (Bonnet-Bidaud et al. 2006). J2133 was one of the intermediate polars detected by the *INTEGRAL*/IBIS survey Barlow et al. (2006) as a hard X-ray (20 – 100 keV) source.

Photometry

J2133 was observed for a total of 3.82 hours over the two nights (see the observing log in Table 3.4). Figure 3.11 shows the *UBVRI* photometry of J2133 from both of the observing nights. Each data point corresponds to a single measurement with 24 s time resolution. This consists of 10 s integration time on the target, 10 s integration time on the sky, and 4 s lost time due to the instrument mechanics. A "saw-tooth" shape with an amplitude of ~ 0.1 mag is seen in the light curves, which represents the pulsed modulation at the white dwarf spin period.

On the second night (HJD 2453950.0) a significant dip was observed in all *UBVRI* bands near the epoch HJD 2453950.685, when the brightness of the target dropped suddenly by approximately 0.5 in the U-band, and 0.4 in the $BVRI$-bands. Unfortunately observations of the sky background were being taken at the same time as the start of this dip, and therefore most of its ingress was missed. Later analysis showed that J2133 was observed at around same orbital phase as this dip on the first night, but unfortunately no data was taken exactly at the same phase. Bonnet-Bidaud et al. (2006) presented light curves from three separate nights (their Figure 1) covering almost the whole orbital period (7.2 h) in each. There is no such dip seen in any of their light curves, and thus the dip seen in this data from 2006 August 2/3, is unlikely to be an eclipse, and its cause still remains a puzzle.

The colours of J2133 for $U-B$, $B-V$ and $V-R$, show some small flickering, and these too exhibit the "saw tooth" profile reflecting the white dwarf pulse period. This is most apparent in the $U-B$ colour.

The average magnitudes in each of the *UBVRI* bands are 15.1, 15.7, 15.2, 14.9 and 15.0 respectively. This is consistent with the B band value of 15.8 reported by Motch et al. (1998), indicating that the brightness of the system has not changed significantly.

Period analysis

CLEAN period analysis shows that on July 31/Aug 1 a single consistent large peak occurred at a frequency of $\sim 152\ \mathrm{d}^{-1}$, which corresponds to the spin period of the white dwarf (Figure 3.12).A second spectral peak in the periodogram was also present at approximately 45 d^{-1}, corresponding to a period of roughly 0.0222 days or about 32 minutes. This is roughly the length of the brightening episode seen between 0.628 d and 0.660 d in Figure 3.11.The light curves do not cover the full orbital period, so no inference about that can be made from these data.

An identical analysis was performed for the raw polarization curves. The white dwarf spin frequency is detected clearly in the polarization curves of *VRI* and only marginally in *UB* (Figure 3.13).

Polarization

Figure 3.14 shows the circular polarimetry obtained on the two nights observing, folded at the previously known WD spin period of 570.823 s and then phase binned into 20 equal bins.

Significant circular polarization is seen in all *UBVRI* bands from J2133, and polarization variations are modulated at the WD spin period. Polarization is near to zero at phase $\Phi = 0.5$, and it increases smoothly until relative phase $\Phi = 0.0$. After that epoch there is a small dip in the polarization curves in the blue part of the spectrum, near phase $\Phi = 0.1 - 0.2$ (possibly due to cyclotron beaming effects), whilst from phase $\Phi = 0.2$ the polarization decreases until $\Phi\ \sim 0.5$. Polarization is positive over the whole WD spin period, and it has a colour dependence; the peak polarization values in the *UBVRI* bands are: +1.6, +2.3, +3.3, +2.8, and +2.6

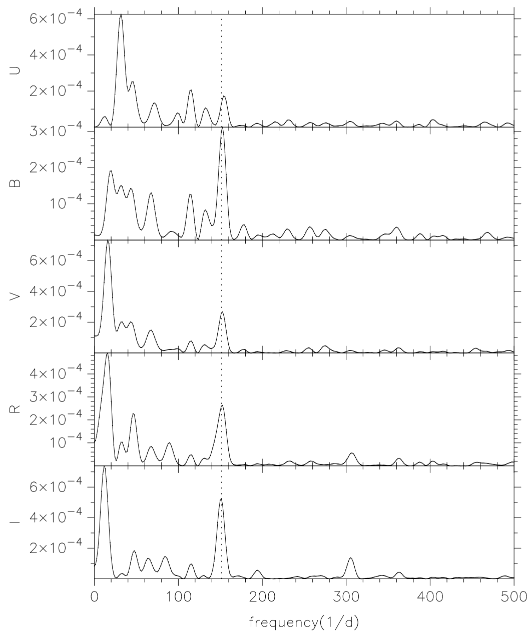

Figure 3.12: CLEANed periodogram of the light curves of J2133 observed during the night of 2006 July 31/August 1. The spin frequency of the white dwarf is ~ 152 cycles per day. The units of pseudo-power on the ordinate axis are mag^2 . A sinusoid with an amplitude of $A = 0.04\mathrm{mag}$ would produce a peak with power $\sim 4 \times 10^{-4}$.

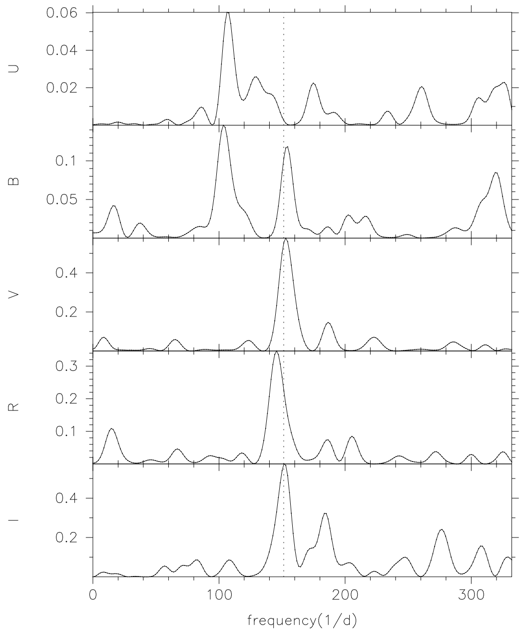

Figure 3.13: CLEANed periodogram of the polarization curves of J2133 observed during the night of 2006 July 31/August 1. The spin frequency of the white dwarf is ~ 152 cycles per day. The units of pseudo-power on the ordinate axis are $\%^2$. A sinusoid with an amplitude of $A = 1\%$ would produce a peak with power ~ 0.25. Note the scale on the ordinate axis - the peaks seen in the UB bands are of a comparable amplitude to noise seen in VRI.

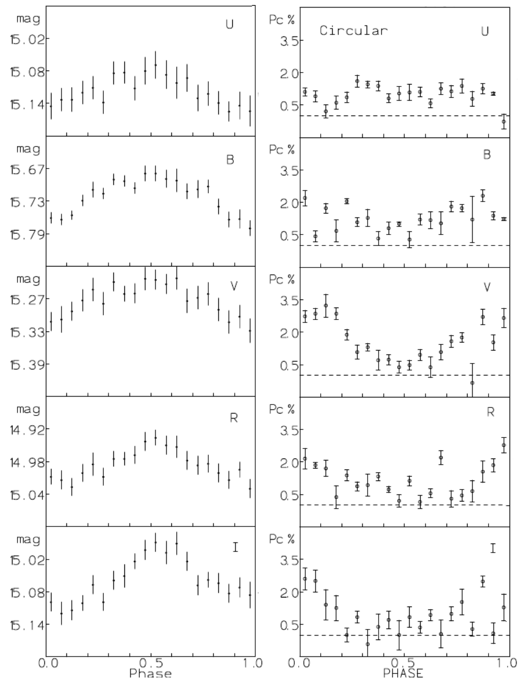

Figure 3.14: *UBVRI* photometry and polarization curves of J2133 observed at the NOT between 2006 July 31 and August 3, folded at the white dwarf spin period of 0.0066067d and averaged into 20 phase bins.

percent, respectively.

Discussion

Known polarized IPs so far have shown polarization predominantly in the red part of their spectrum, for example in PQ Gem, circular polarization is seen only in the R- and I-bands in the $UBVRI$ observations of Piirola et al. (1993). Similarly in BG CMi, polarization was found in the red part of the optical and particularly in the infrared region (Penning et al. 1986; West et al. 1987), whilst it was seen in the red part of the spectrum in V405 Aur (Shakhovskoj & Kolesnikov 1997). Norton et al. (2002) reported optical polarization found in V2306 Cyg, where circular polarization was seen to be negative at the several percent level in the R-band, but positive around one percent in the B-band. In V2400 Oph, Buckley et al. (1995) found optical polarization which was highest in the I-band. J2133 seems to be quite different in that sense, and this may be an indicator that the inferred magnetic field is stronger than found in other polarized IPs.

In J2133 circular polarization is positive throughout the spin cycle (Figure 3.14), which indicates that one pole is dominant. There is no sign of cyclotron emission from the other (negative) pole. Circular polarization is close to zero near phase 0.5, suggesting that the line of sight is nearly perpendicular to the magnetic field lines at that phase, i.e. the emission region is at the stellar limb. In terms of the co-latitude of the emission region, β, and the inclination of the WD spin axis, i, this can be written as $\beta \sim 90^\circ - i$. Circular polarization increases smoothly from phase 0.5 towards 0.0, when the emission region moves away from the limb to the position where the field lines point closest to us (phase 0.0).

At small viewing angles cyclotron emission *intensity* approaches zero (due to the cyclotron beaming effect), and the diluting effect of unpolarized thermal emission decreases the observed degree of polarization. The peak observed in the R band at phase 0.5 (Figure 3.14) becomes flatter in the V band, and a polarization dip is seen in the B and U bands, due to the cyclotron beaming effect, which is strongest at high harmonics (shorter wavelengths). The minimum in the light curves (Figure 3.14) takes place near phase 0.0, in accordance with the proposed cyclotron beaming geometry.

Circular polarization does not go to zero at phase 0.0, which means that viewing angles are $>> 0^\circ$ even when looking closest along the field lines. Simple geometric considerations then imply that either $i - \beta >> 0^\circ$ or $\beta - i >> 0^\circ$. For a high inclination system the emission region has to be closer to the rotation pole, and for a low inclination system it must be closer to the equator, to fulfil also the relation $\beta \sim 90^\circ - i$ (see above). However, without linear polarization measurements the value of i cannot be inferred. The absence of eclipses by the companion star requires that i is smaller than about 75°.

Circular polarization variations of J2133 can be compared with systems where the magnetic field strength is estimated to be about 25MG, such as the polars V834 Cen (Piirola 1995) and BY Cam (Piirola et al. 1994). The observed circular polarization variations in those stars resemble (in their colour dependence) those seen in J2133. Naturally the circular polarization level is higher in polars, for example in BY Cam or in V834 Cen the circular polarization peak values are almost 30 percent, as there is much less unpolarized light diluting the observed polarization in those systems. In IPs there is more unpolarized light due to their higher accretion rates and larger accretion stream compared to polars. More accurate estimates of the magnetic field of J2133 could be obtained in the future by using phase resolved circular spectro-polarimetry. Also, high signal-to-noise linear polarimetry of J2133 to find out the orbital inclination would be very useful.

The magnetic moment of J2133

Theoretical modelling of IPs by Norton et al. (2004) has begun to explain equilibrium values of the magnetic moment in these systems. They determined the equilibrium spin periods at which systems would lie, with a given orbital period and magnetic moment, assuming the white dwarf not to be spinning up or down on long

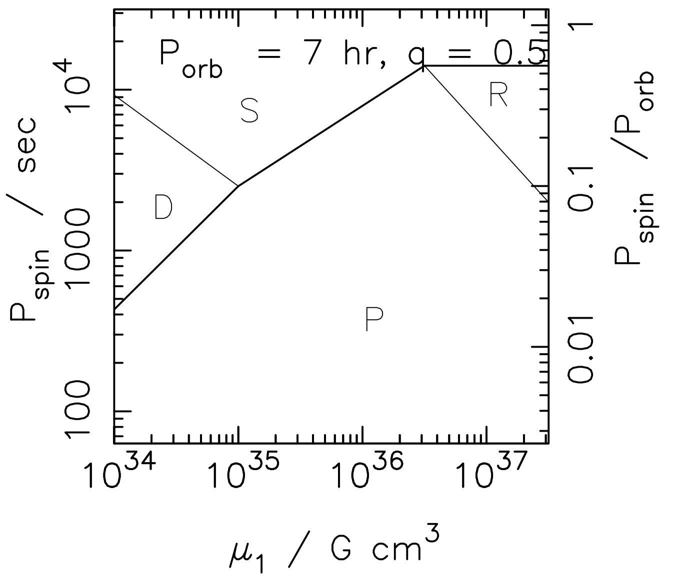

Figure 3.15: Spin period vs. magnetic moment diagram for a mass ratio of 0.5 and an orbital period of 7 h (adapted from Norton et al. (2008). The letters ‘S’, ‘P’, ‘D’ and ‘R’ indicate regions of parameter space in which a stream-like, propeller-like, disc-like and ring-like flow respectively may be seen. In spin equilibrium, systems tend toward the line which divides disc-like and stream-like flows from propeller-like and ring-like flows. Note that for a typical WD radius of $\sim 10^7$ m, $\mu = 10^{35}$ G cm^3 implies a B of $\sim$ 100MG. The upper part of this plot therefore shows an extreme which has not yet been observed in mCVs.

timescales. This theoretical work has since been extended so that the position of a system in the $P_{\rm spin}/P_{\rm orb}$ vs. magnetic moment plane can indicate the structure of the accretion flow in the system (Norton et al. (2008) and Chapter 4). The key result from this study is that the spin-to-orbital period ratio vs. magnetic moment plane can be divided into regions where the system will display either a disc-like, stream-like, propeller-like or ring-like accretion flow (Figure 3.15). Furthermore, the “triple point” positions (at which stream, disc and propeller or stream, ring and propeller flows can co-exist) on the $P_{\rm spin}/P_{\rm orb}$ axis are a function of mass ratio and not orbital period. The magnetic moments at which these transitions occur are, however, a function of orbital period.

The mass ratio of J2133 is uncertain, but likely to be in the range $q \sim 0.3 - 0.6$ (Bonnet-Bidaud et al. 2006). For a typical mass ratio of 0.5, the results of Norton et al. (2008) show that if J2133 is in equilibrium with $P_{\rm spin} = 571$ s and $P_{\rm orb} \sim 7$ h, its magnetic moment is of order $\sim 10^{34}$ G cm^3. A larger value of magnetic moment for a system with these periods and mass ratio would indicate a propeller-type flow subject to a spin-down of the white dwarf. A smaller value of the magnetic moment would indicate a disc-like flow which is spinning up the white dwarf (see Figure 3.15). For a smaller mass ratio, the magnetic moment corresponding to the equilibrium may be significantly smaller, and for a larger mass ratio, the magnetic moment may be somewhat higher. Hence, for a mass ratio in the range $q \sim 0.3 - 0.6$, if J2133 is accreting at close to its equilibrium spin rate, the magnetic moment is likely to be in the range $3 \times 10^{33} - 3 \times 10^{34}$ G cm^3. This magnetic moment is consistent with a relatively high magnetic field strength ($\sim 6 - 60$MG for a $R_{\rm wd} = 8 \times 10^6$m), as implied by the polarization results noted above.

The evolutionary status of J2133

J2133 is apparently a high magnetic field strength intermediate polar (possibly μ_1 is about 10^{34} G cm^3), yet it is a long way from synchronism ($P_{\rm spin}/P_{\rm orb} \sim 0.022$). A magnetic CV with a field this strong would be expected to synchronize on a relatively short timescale and emerge as a polar with a period of less than about 4 h. However, to become synchronized at the present orbital period it would require an even stronger magnetic field, and in fact very few polars have an orbital period this long: V1309 Ori has the longest known period amongst the polars at $P = 7.98$ h (Staude et al. 2001). So it is possible that J2133 is a relatively young system that has only recently come into contact and begun mass transfer, and has not yet had time to evolve to a shorter orbital period and approach synchronism. Nonetheless it is likely it will eventually synchronize and emerge as a polar.

3.7.7 AO Psc

Background

AO Psc is a typical IP with a spin and orbital period of 805.2 s and 3.59 h respectively. Using the orbital ephemeris of Kaluzny & Semeniuk (1988), AO Psc was at an orbital phase of 0.14. The error in the calculation of this phase is relatively small (0.2 of the orbital period), but the ephemeris is old (20 years) so it may be somewhat out of date. The spin ephemeris has an accumulated uncertainty of greater than one spin, so a zero point of HJD 2 453 949.5 was used. The spin period from Kaluzny & Semeniuk (1988) of 0.0009319484 d was used.

Polarization

Each polarization measurement consisted of two positions of the wave plate at 10 s each. The polarization data was then binned into eight bins across the spin cycle. The mean values in each band were within three sigma

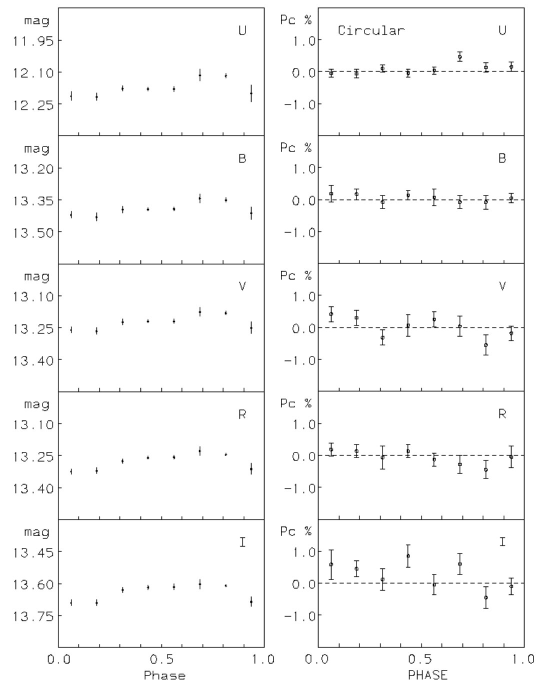

Figure 3.16: Spin folded and phase binned simultaneous *UBVRI* photometry (left) and circular polarization (right) plots of AO Psc. Circular polarization measurements have an 23 s resolution. Zero phase corresponds to HJD 2 453 949.5. A spin period of 0.009319484 d was used.

of being zero. The maximum amplitude in the binned data was $0.86 \pm 0.37\%$, with a maximum peak to peak variation of $1.30 \pm 0.50\%$, see Figure 3.16 and Table 3.6. This peak to peak variation is less than three sigma, so this cannot be claimed as a reliable detection of variable polarization.

Discussion

This is the first simultaneous *UBVRI* polarimetric observation of this target. All previous measurements have had a long integration time ($\gtrsim$ 240 s) when compared to the spin period (805.2 s) (see Table 3.1), so any variations shorter than this will have been smeared out effectively. The mean measured circular polarization values were consistent with previous measurements (all of which were within one sigma of zero) (see Table 3.1).

The peak to peak values showed hints of variation, $(1.30 \pm 0.50\%)$ in the *I* band, but the detection is not conclusive. The short data set (1.6 spin periods) means that the uncertainties in this observation are large. This, coupled with the non-zero peak to peak values and a tentative detection in the *I* band may warrant further investigation.

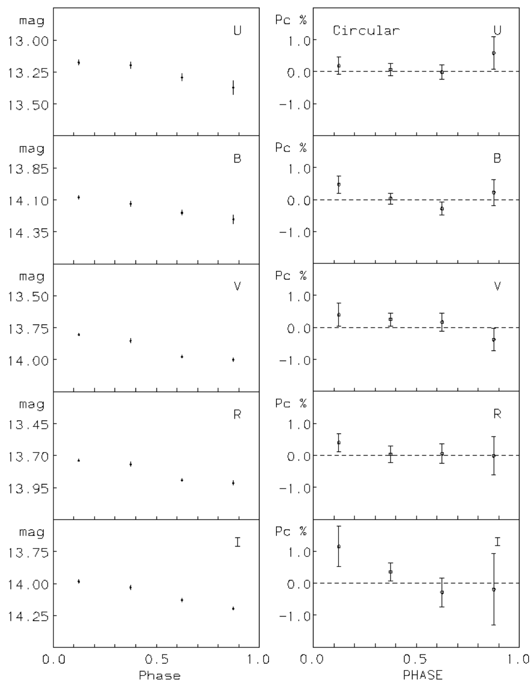

Figure 3.17: Spin folded and phase binned simultaneous *UBVRI* photometry (left) and circular polarization (right) plots of FO Aqr. Zero phase corresponds to HJD 2 453 948.5. A spin period of 0.0014519035 d was used.

3.7.8 FO Aqr

Background

FO Aqr has an orbital period of 4.85 h and a spin period of 1254.5 s. Using the ephemeris of Patterson et al. (1998), FO Aqr was at an orbital phase of 0.98 at the start of this observation. It was also at a spin phase of approximately 0.6 from pulse maximum, though FO Aqr is rather erratic and this value may be some way off now, so zero phase was arbitrarily set to HJD 2 453 948.5. Here a spin value of 0.014519035 d from Patterson et al. (1998) was used.

Polarization

Each polarization measurement was taken with two positions of the wave plate with an integration time of 10 s in each. The data was binned into four bins over the spin cycle. The mean circular polarization was within two sigma of being zero in each band. A peak amplitude of $1.15 \pm 0.65\%$ is present in the *I* band (see Figure 3.17). The peak to peak values had a maximum of $1.43 \pm 0.80\%$ (see Table 3.6).

Discussion

This is the first simultaneous *UBVRI* polarimetry of FO Aqr. All previous measurements report a mean value close to zero, except for in the $1.15 - 1.35\mu m$ range where $+1.1 \pm 0.3\%$ polarization has been detected (see Table 3.1). The mean circular polarization seen here is within two sigma of all the previous measurements where there is an overlap in pass band (see Table 3.1). Since the large value of the circular polarization in the *I* band has such a large uncertainty this cannot be claimed as a detection, although it is possible that circular polarization is present at the level of around 1%.

The short data set (1.1 spin periods) means that the uncertainties are probably much higher than quoted. This system also perhaps warrants further investigation, particularly in the *I* band.

3.7.9 Summary of results

Table 3.6 summarises the results obtained, this should now be used in conjunction with the results in Table 3.1.

Table 3.6: Summary of results. Minimum and maximum correspond to the phase binned data.

Target	Filter	Mean (%)	Minimum (%)	Maximum (%)	Peak-Peak (%)
J1730	*U*	-0.23 ± 0.18	-1.48 ± 0.72	$+1.02 \pm 0.84$	2.50 ± 1.11
	B	$+0.00 \pm 0.21$	-4.00 ± 1.11	$+4.26 \pm 1.09$	8.26 ± 1.56
	V	-0.39 ± 0.21	-1.79 ± 1.45	$+1.38 \pm 1.19$	3.17 ± 1.88
	R	-0.07 ± 0.13	-1.55 ± 0.79	$+1.80 \pm 0.67$	3.35 ± 1.07
	I	-0.12 ± 0.19	-1.95 ± 0.93	$+1.82 \pm 0.75$	3.77 ± 1.19
DQ Her	*U*	$+0.00 \pm 0.04$	-0.16 ± 0.14	$+0.19 \pm 0.13$	0.35 ± 0.19
	B	$+0.14 \pm 0.05$	-0.05 ± 0.17	$+0.47 \pm 0.16$	0.53 ± 0.23
	V	$+0.12 \pm 0.07$	-0.08 ± 0.25	$+0.35 \pm 0.29$	0.43 ± 0.39
	R	$+0.03 \pm 0.06$	-0.22 ± 0.20	$+0.40 \pm 0.23$	0.61 ± 0.31
	I	$+0.04 \pm 0.07$	-0.64 ± 0.31	$+0.35 \pm 0.25$	1.00 ± 0.39

V1223 Sgr	*U*	-0.01 ± 0.20	-1.30 ± 1.12	$+0.86 \pm 0.48$	2.16 ± 1.22
	B	-0.00 ± 0.08	-0.40 ± 0.34	$+0.36 \pm 0.38$	0.77 ± 0.51
	V	-0.04 ± 0.09	-0.45 ± 0.25	$+0.55 \pm 0.41$	1.00 ± 0.48
	R	-0.05 ± 0.09	-0.40 ± 0.36	$+0.32 \pm 0.55$	0.71 ± 0.65
	I	-0.27 ± 0.11	-0.92 ± 0.43	$+0.50 \pm 0.46$	1.42 ± 0.63
V2306 Cyg	*U*	$+0.06 \pm 0.08$	-0.61 ± 0.45	$+0.61 \pm 0.33$	1.23 ± 0.56
	B	-0.00 ± 0.07	-0.47 ± 0.51	$+0.46 \pm 0.29$	0.92 ± 0.59
	V	-0.07 ± 0.08	-0.86 ± 0.29	$+0.51 \pm 0.37$	1.36 ± 0.48
	R	-0.08 ± 0.06	-0.78 ± 0.26	$+0.45 \pm 0.26$	1.23 ± 0.37
	I	-0.11 ± 0.10	-1.06 ± 0.41	$+0.89 \pm 0.52$	1.95 ± 0.66
AE Aqr^a	*U*	$+0.02 \pm 0.02$	-0.14 ± 0.07	$+0.13 \pm 0.10$	0.27 ± 0.12
	B	$+0.05 \pm 0.02$	-0.00 ± 0.06	$+0.09 \pm 0.06$	0.09 ± 0.08
	V	-0.02 ± 0.02	-0.09 ± 0.08	$+0.04 \pm 0.07$	0.13 ± 0.11
	R	$+0.01 \pm 0.01$	-0.09 ± 0.05	$+0.11 \pm 0.06$	0.20 ± 0.08
	I	$+0.06 \pm 0.02$	-0.00 ± 0.06	$+0.15 \pm 0.07$	0.15 ± 0.09
AE Aqr^b	*U*	$+0.00 \pm 0.08$	-0.27 ± 0.26	$+0.38 \pm 0.23$	0.65 ± 0.35
	B	-0.07 ± 0.07	-0.46 ± 0.21	$+0.26 \pm 0.21$	0.72 ± 0.30
	V	$+0.08 \pm 0.07$	-0.33 ± 0.23	$+0.50 \pm 0.26$	0.83 ± 0.35
	R	$+0.02 \pm 0.04$	-0.14 ± 0.18	$+0.34 \pm 0.18$	0.48 ± 0.25
	I	$+0.10 \pm 0.07$	-0.42 ± 0.28	$+0.80 \pm 0.39$	1.22 ± 0.48
J2133	*U*	$+0.97 \pm 0.06$	-0.26 ± 0.36	$+1.62 \pm 0.28$	1.88 ± 0.46
	B	$+1.26 \pm 0.09$	$+0.29 \pm 0.38$	$+2.32 \pm 0.29$	2.03 ± 0.48
	V	$+1.54 \pm 0.09$	-0.33 ± 0.91	$+3.25 \pm 0.54$	3.58 ± 1.06
	R	$+1.17 \pm 0.08$	$+0.15 \pm 0.31$	$+2.79 \pm 0.36$	2.64 ± 0.48
	I	$+0.91 \pm 0.11$	-0.42 ± 0.70	$+2.62 \pm 0.52$	3.04 ± 0.87
FO Aqr	*U*	$+0.16 \pm 0.10$	-0.00 ± 0.24	$+0.56 \pm 0.53$	0.60 ± 0.58
	B	$+0.07 \pm 0.10$	-0.27 ± 0.20	$+0.47 \pm 0.28$	0.74 ± 0.34
	V	$+0.17 \pm 0.15$	-0.38 ± 0.36	$+0.40 \pm 0.36$	0.78 ± 0.51

	R	$+0.11 \pm 0.12$	-0.01 ± 0.60	$+0.42 \pm 0.30$	0.43 ± 0.67
	I	$+0.27 \pm 0.20$	-0.28 ± 0.47	$+1.15 \pm 0.65$	1.43 ± 0.80
AO Psc	*U*	$+0.07 \pm 0.05$	-0.06 ± 0.14	$+0.48 \pm 0.16$	0.54 ± 0.21
	B	$+0.07 \pm 0.06$	-0.08 ± 0.20	$+0.20 \pm 0.28$	0.28 ± 0.34
	V	$+0.05 \pm 0.09$	-0.55 ± 0.33	$+0.43 \pm 0.25$	0.98 ± 0.41
	R	-0.02 ± 0.08	-0.44 ± 0.29	$+0.19 \pm 0.21$	0.63 ± 0.36
	I	$+0.29 \pm 0.10$	-0.44 ± 0.35	$+0.86 \pm 0.37$	1.30 ± 0.50

[a] First night; [b] Second night.

3.8 Discussion

3.8.1 J1730 & J2122

The two systems showing the most circular polarization (J1730 and J2133) are similar in terms of their periodicities. Both have a long orbital period and thus have very wide orbits. This is coupled with a short spin period (and therefore a very small $P_{\text{spin}}/P_{\text{orb}}$). The other target looked at with a similarly small $P_{\text{spin}}/P_{\text{orb}}$ was AE Aqr. This showed no significant circular polarization. AE Aqr does however have a measurable $\dot{P}_{\text{spin}}$, whereas J1730 and J2133 do not (however these are both relatively newly discovered systems, so a long enough base line of observations may not exist yet). Perhaps this spin down in AE Aqr is a symptom of an accretion flow topology that some how masks the magnetic field strength. As was outlined in Chapter 1, AE Aqr may have evolved from a super soft source and so may belong to a different sub-group of IPs (Schenker et al. 2002). This could also be why no polarization is detected from it.

If the suspected large magnetic field in these systems are confirmed then both are likely to evolve into polars as their orbital periods decrease.

3.8.2 General

Generally each of the definite or potential circular polarization detections reported here have been most prominent towards the red end of the spectrum. This is in agreement with what has been seen before, and reinforces the notion of IPs being less magnetic than polars - as weaker fields will give rise to polarization appearing at longer wavelengths.

Amongst the IPs detected by *INTEGRAL* (Barlow et al. 2006; Bird et al. 2007) V2400 Oph has previously been found to display a large degree of circular polarization (Buckley et al. 1995, 1997), whilst J1730, J2133, V2306 Cyg, DQ Her, V1223 Sgr and FO Aqr are shown here to have some degree of circular polarization or at least strong hints of it. The only other *INTEGRAL*-detected IP to have its circular polarization measured is GK Per (Stockman et al. 1992). This was reported as having a mean value of $0.03 \pm 0.10\%$, but as noted earlier, the practice of reporting mean values may seriously under report the true magnetic nature. In light of this, it would be productive to look for circular polarization in the rest of the *INTEGRAL* IP sources, namely V709 Cas, IGR000234+6141, NY Lup, and MU Cam.

The presence of a soft X-ray component may be related to the presence of a large magnetic field. The circular polarization seen in J1730 and J2133 further adds to this trend as they are also soft X-ray sources (de Martino et al. 2008, 2006b). This brings the total of soft X-ray emitting, circularly polarized IPs to four, namely PQ Gem, V405 Aur, J2133 and J1730. Perhaps the same geometry which allows the soft X-ray component to be seen in some IPs but not others, as suggested by Evans & Hellier (2007), may also allow the efficient detection of circular polarization. Indeed Evans & Hellier (2007) suggested that the reason why some IPs show polarization and the others do not, is mostly due to different accretion geometry and hiding effects of the accretion curtains. This may tie in with the suggestion by Norton et al. (2002) with regard to V2306 Cyg, that cancellation of polarized emission between the two magnetic poles may hide significant polarization in some systems. Furthermore, it may be that only those systems which show an asymmetry between the poles (in terms of temperature etc or accretion curtain structure) or have an offset or non-dipole magnetic field structure, emit a detectable signal.

Beuermann & Schwope (1994) demonstrated an anti-correlation between magnetic field strength and the ratio of the strength of the hard X-ray emission to that of the soft X-ray emission in polars. Hence the polars, with stronger magnetic fields, have a stronger blackbody component and/or a weaker Bremsstrahlung component. In both polars and intermediate polars, a soft X-ray component may arise as accreting material impacts the white dwarf directly, resulting in blackbody radiation with a temperature of $kT_{\rm bb} \sim 50 - 100$ eV being emitted from the heated white dwarf surface. Although it is noted that that the visibility of a soft component in IPs may be a geometrical effect and arises from reprocessing of hard X-rays (Evans & Hellier 2007). In either case, it has a different origin to the multi-temperature X-ray Bremsstrahlung emission, whereas the cyclotron emission arises in the cooling plasma as it settles slowly onto the white dwarf surface below a shock.

Cumming (2004) suggested that the high accretion rates in intermediate polars might overcome ohmic diffusion and significantly affect the magnetic field structure. In this regime, magnetic flux is advected into the interior of the white dwarf, dramatically reducing the surface field. Hence, intermediate polars would appear to have a weaker field than they actually have. Now, it is apparent that in some intermediate polars, the accretion flow and magnetic field geometry are such that some of the accreting material directly, or indirectly, heats the white dwarf surface, giving rise to a soft X-ray component. If direct heating occurs, less of the accreting material interacts with the shock and may lead to a less significant ‘burying’ of the white dwarf magnetic field. Hence intermediate polars with soft X-ray spectral components, might be expected to preferentially exhibit signs of stronger magnetic fields, such as enhanced polarized emission.

The intermediate polars with polarized emission that have yet to show evidence for a soft X-ray component (e.g. BG CMi, V2306 Cyg, V2400 Oph), may simply suffer from less significant magnetic field burying for various reasons. Both BG CMi and V2400 Oph show evidence for stream-fed accretion (Norton et al. 1992; Buckley et al. 1997) and V2306 Cyg shows evidence for an asymmetric magnetic field at the two poles (Norton et al. 2002). Both of these differences could conceivably reduce the magnetic field burial, allowing detection of polarized emission from accretion under the influence of the inherent (stronger) magnetic field. The soft X-ray emitting intermediate polars, that are so far without detected polarized emission (e.g. UU Col, MU Cam, NY Lup), would make ideal targets to search for such a component. In particular, the system parameters of NY Lup ($P_{\rm spin}$ = 693 s, $P_{\rm orb}$ = 9.87 h) (Haberl et al. 2002; de Martino et al. 2006a) make it appear a close twin of J2133, and it too may be a young intermediate polar which will eventually evolve into a polar.

3.9 Conclusion

Temporal variation in the circular polarization emission of J1730 and J2133 have been detected with possible emission (and in some cases variation) in V2306 Cyg, DQ Her, V1223 Sgr, AO Psc and FO Aqr; AE Aqr had none detected at a significant level. Broadly speaking this is in agreement with previous results, and adds to the observational trend of IPs having less polarization than polars; and hence likely smaller effective magnetic field strength.

There are indications of a correlation between the detection of circular polarization in IPs and their detection as hard X-ray sources by *INTEGRAL*. We therefore suggest that other *INTEGRAL* sources should be tested for circular polarization. Where such objects also exhibit soft X-ray components (i.e. NY Lup and MU Cam), we predict there is a very good chance of detecting significant circular polarization.

We propose that there may be a link between the emission of a soft X-ray spectral component due to direct heating of the white dwarf surface and the detection of polarized emission in intermediate polars. Possibly the direct heating means that magnetic field burial below the accretion shock is less effective, so allowing the intrinsic field to produce a stronger polarization signal. If this link is confirmed it would argue that the soft X-ray component in IPs is indeed due to direct heating (as in polars) and not due to reprocessing of the hard X-rays.

Chapter 4

Accretion flow numerical modelling with *HyDisc*

The hydrodynamical code *HyDisc*, is a computer model of accretion flows in cataclysmic variables. In its original form it was written to model non-magnetic cataclysmic variables (Whitehurst 1988b). It was later developed to simulate the more complex magnetic cataclysmic variables (Wynn et al. 1995). In its current form it has been used extensively to explore the accretion topology of intermediate polars with varying spin periods, orbital periods, magnetic field strengths and magnetic-spin axis angle.

This chapter introduces *HyDisc*, and the theory behind it, before presenting a continuation of the study of accretion topology of intermediate polars. The latter part of this chapter presents work which has been published in Norton et al. (2008).

4.1 The Whitehurst years

4.1.1 The computational zone

HyDisc was originally written as a 2D non-magnetic code to simulate accretion discs in cataclysmic variables. In its most basic form *HyDisc* injected matter (in the form of point sources) into the full potential of an orbiting WD-main sequence pair. The point sources - representing matter, then evolved their positions in time by incremental amounts.

The system is considered in a frame co-rotating with the system, this gives rise to the centrifugal and Coriolis forces. The fundamental equation of motion *HyDisc* has to mimic is therefore

$$\frac{\partial \mathbf{v}}{\partial t} + (\mathbf{v}.\nabla)\mathbf{v} = -\nabla\Phi_{\mathrm{R}} - 2\mathbf{\Omega} \wedge \mathbf{v} - \frac{1}{\rho}\nabla P \tag{4.1}$$

Where the motion of a specific particle, $\mathbf{v}$ (in the rotating frame), is described by the Roche potential, Φ_{R} (which incorporates the the effect of both gravitational and the centrifugal force), the Coriolis force (per unit mass, due to the rotation of the binary pair with an orbital frequency $\mathbf{\Omega}$), and the pressure gradient that the particles experience due to the neighbouring material ∇P (ρ is the gas density).

Three boundaries are defined in the system,

1. The inner boundary at $r = R_{\mathrm{wd}}$ which defines the WD surface, any material crossing this is assumed to have been accreted.

2. The secondary surface, approximated by a circle centred on the secondary and passing through the L_1 point. Any material crossing this line is assumed to have been accreted by the secondary.

3. The outer boundary at $r = R_{\mathrm{esc}}$ (usually 10 binary radii), anything crossing this is assumed to have escaped to infinity.

4.1.2 Pressure

The pressure force is calculated as $\boldsymbol{\nabla} P$ where the gas pressure itself is calculated as that in Equation 4.2.

$$P = c_{\mathrm{s}}^2 \rho \tag{4.2}$$

Where ρ is the density and c_{s} is the local sound speed. The force due to the gas pressure, F_{gas}, between two particles a distance r apart, therefore has a magnitude as described by Equation 4.3.

$$F_{\mathrm{gas}} = \frac{c_{\mathrm{s}}^2 \rho}{r} \tag{4.3}$$

The sound speed used here (and throughout the rest of this thesis) is that appropriate for a typical $T \sim 3000$ K main sequence star, given by

$$c_{\rm s}^2 = \frac{kT}{m_{\rm H}} \tag{4.4}$$

Hence the sound speed is $c_{\rm s} \sim 5 \times 10^3$ m s^{-1}.

4.1.3 Viscosity

The force due to viscosity, $F_{\rm visc}$ is parametrized by the acceleration term Qu^2/r where Q is a constant which can take a value between 0.5 and 1, and u is the local velocity. The value used for Q is ~ 0.7 so that the viscosity is not too sticky or too ineffective. This parameterization can be thought of as analogous to the α parameterization of Shakura & Sunyaev (1973), whereby turbulent viscosity was mimicked without any real understanding of its cause. So the force due to gas viscosity has a magnitude

$$F_{\rm visc} = \frac{Qu^2\rho}{r} \tag{4.5}$$

The overall acceleration due to non-gravitational forces (i.e. gas pressure and viscosity) therefore has a magnitude

$$a_{\text{non-gravitational}} = \frac{c_{\rm s}^2}{r} + \frac{Qu^2}{r} \tag{4.6}$$

4.1.4 Normalization

In order to maintain a high accuracy the physical units in *HyDisc* are normalized according to typical values of the system. The specific normalization used for time, length and mass is that in Equations 4.7, 4.8 and 4.9, any further normalizations can then be derived from these.

$$\text{time} \quad \Omega = \frac{2\pi}{P_{\rm orb}} = 1 \tag{4.7}$$

$$\text{length} \quad a = \left(\frac{G(m_1 + m_2)P_{\rm orb}^2}{4\pi^2} \right)^{1/3} = 1 \tag{4.8}$$

$$\text{mass} \quad m_{\rm particle} = 10^{14}\text{kg} = 1 \tag{4.9}$$

4.1.5 Equations of motion

To describe the movement of the matter, the 2D restricted three-body equations of motion for co-planar orbits are used. In a co-rotating frame of reference with normalization carried out and a transformation of the origin to coincide with the primary these are Equations 4.10 and 4.11

$$\ddot{x} = 2\dot{y} + x + 1 - \mu - \frac{\mu x}{R_{\mathrm{wd}}^3} - \frac{(1+x)(1-\mu)}{R_{\mathrm{secondary}}^3} \tag{4.10}$$

$$\ddot{y} = -2\dot{x} + y\left(1 - \frac{\mu}{R_{\mathrm{wd}}^3} - \frac{1-\mu}{R_{\mathrm{secondary}}^3}\right) \tag{4.11}$$

And the Jacobi constant is that in Equation 4.12.

$$C = \mu R_{\mathrm{wd}}^3 + (1-\mu)R_{\mathrm{secondary}}^2 + \frac{2\mu}{R_{\mathrm{wd}}} + \frac{2(1-\mu)}{R_{\mathrm{secondary}}} - (\dot{x}^2 + \dot{y}^2) \tag{4.12}$$

Where μ is given by $\mu = M_1/(M_1 + M_2)$, R_{wd} is the radius of the primary and $R_{\mathrm{secondary}}$ is the radius of the secondary.

4.1.6 The time steps

In any simulation where various members have a different characteristic timescale, a fundamental problem arises. If each member is evolved by its characteristic time step then, all the members of the system will probably never synchronize again. e.g. if one member has a characteristic timescale of one second and another member 0.6 sec then the system will not be synchronized in 'real time' until 3 secs. In a many body system this problem is exacerbated and so there will probably never be a synchronization of all the members.

To solve this problem the smallest time step may be taken and the entire system evolved according to that. *HyDisc* takes a more efficient approach, where the time step for each individual member, δt_1, is as described in Equation 4.13.

$$\delta t_i = 2^{-i} t_0 \quad \text{where } i \ \exists \{0, 1, 2, \ldots\} \tag{4.13}$$

Where t_0 is the largest time step. Each time step is then assigned by first considering a value of zero for i, if this yields a time step smaller than the characteristic time scale of that member this is taken, if not, i is incremented until this is achieved. This means that all the members will be in phase and share the same time at multiples of t_0. In this way t_0 can be considered the temporal resolution of the system.

4.1.7 Evolution and energy conservation

The Jacobi constant is the integral of relative energy of a test particle moving in the non-inertial co-rotating frame. This is a fundamental constant of the system and must be conserved. For this reason the evolution scheme used is the rational extrapolation technique.The degree of relative energy conservation of a test particle is shown in Figure 4.1. The Jacobi constant is seen to be conserved to 1 part in 10^4.

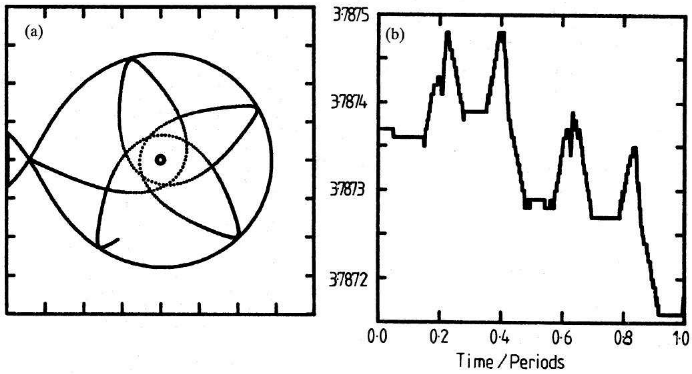

Figure 4.1: (a) A single particle trajectory. (b) The variation in the Jacobi constant for particle in (a). (Taken from Whitehurst (1988a).)

4.1.8 Inter-particle interaction

If the program were to run in such a way that each particle can interact with each other particle, then calculating the pressure and viscosity forces would have to be carried out $\sim N^2$ times, where N is the number of particles. This quickly becomes prohibitive in terms of processor time. To solve this problem a grid is placed over the computational zone with a cell size equal to the viscous scale length – which is the maximum range over which the particles can interact. Each temporal evolution then only needs to consider the members in one cell and its eight surrounding neighbours.

Each particle in a cell is then interacted not with every other particle, but the one which has the strongest interaction. The strongest interaction is defined as the one which is approaching the fastest, or if none are approaching the nearest neighbour.

4.1.9 Emission from the disc

In its original form the program simulated the emission from the disc. It assumed the disc was a collection of optically thick black body emitters. The typical outputs obtained were similar to those in Figure 4.2.

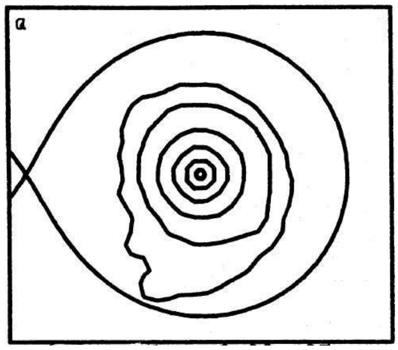

Figure 4.2: Simulated emission from an accretion disc. Each contour is scaled so that the contour levels fall at the relative values of 1,4,16,48 and 96. The highest contour lies at 75% of the maximum value. (Taken from Whitehurst (1988b))

4.1.10 The third dimension

Whitehurst (1994) then developed the model further and generalized it to take into account the third dimension (see Figure 4.3). This allowed a much more realistic simulation of accretion discs in super-humping systems, and paved the way for the model to be developed to simulate magnetic cataclysmic variables.

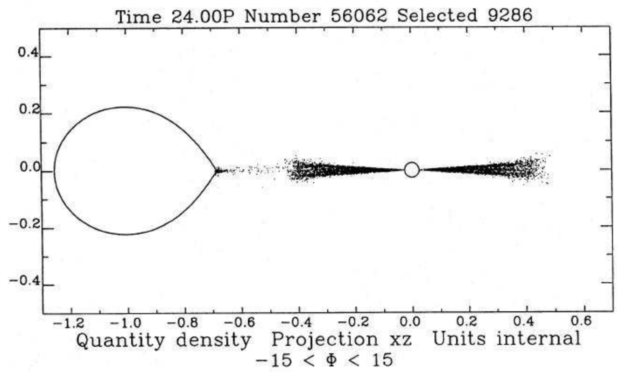

Figure 4.3: Simulated 3D accretion disc in a non-magnetic system. (Taken from Whitehurst (1994).)

4.2 The Wynn years

With a three dimensional non-magnetic model to work from, Wynn developed *HyDisc* to take into account magnetic field effects. This has allowed the modelling of magnetic CVs, more specifically IPs.

4.2.1 Magnetic theory

The accretion flow from the secondary in an IP is ionized as it is coming from a main sequence star, and collisions and X-rays from the shock region ensure that it stays ionized. This causes the accretion flow to be highly conductive, which in turn causes the motion relative to the WD magnetic field to cause magnetic stresses and thus alter the dynamics of the flow (Norton et al. 2004). The equation of motion of in falling ionized matter onto a WD can be given by Equation 4.14.

$$\frac{\partial \mathbf{v}}{\partial t} + (\mathbf{v}.\nabla)\mathbf{v} = -\nabla\Phi_{\mathrm{R}} - 2\mathbf{\Omega} \wedge \mathbf{v} - \frac{1}{\rho}\nabla P - \frac{1}{\rho}\nabla\left(\frac{B^2}{8\pi}\right) + \frac{1}{\rho R_{\mathrm{c}}}\left(\frac{B^2}{4\pi}\right)\hat{\mathbf{n}} \tag{4.14}$$

where B is the local magnetic field strength, R_{c} is the local radius of curvature of the magnetic lines of force and $\hat{\mathbf{n}}$ is the unit vector perpendicular to the magnetic field at a given position. The rest of the variables take on their previous meanings as in Equation 4.1. The extra terms on the right hand side are known as the magnetic pressure and magnetic tension forces.

The magnetic pressure term receives this nomenclature due to its similarities with the gas pressure term preceding it. It acts in much the same way as the gas pressure, in that it will try to spread the magnetic field lines out as far as possible. This means that a high degree of compression will cause a high pressure, and thus force, and a low degree will cause a small force.

The magnetic tension term acts in an analogous way to tension in a guitar string. Plucking the string will cause a force which acts as to bring the string back to its shortest length, i.e. straight. In much the same way magnetic field lines *prefer* to be straight.

4.2.2 Magnetic viscosity

When the magnetic tension is large the contortion of the field lines may be so great that magnetic breaking and reconnection will occur. This process is thought to be a possible explanation of viscosity in magnetic systems (Priest & Forbes 2000). This extra force can be 'absorbed' into the previous non-magnetic treatment

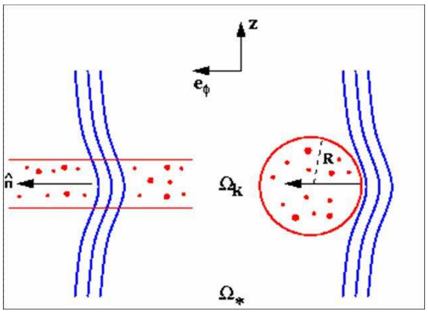

Figure 4.4: Illustration of plasma that has been frozen to the field lines contorting them as it moves, and diamagnetic blobs contorting the field lines in a similar way (not to scale)

of viscosity.

4.2.3 Magnetic drag force

HyDisc assumes that material from the donor star may be treated as diamagnetic blobs (King 1993). These blobs exclude the magnetic field as they travel through it. This has the effect of distorting the magnetic field as shown in the right hand panel of Figure 4.4. The alternative description of the material as a smooth flowing plasma which can be frozen to the field, also results in a distortion of the field similar to the diamagnetic case (see the left hand panel in Figure 4.4). In either case, the local radius of curvature, $R_c(r,t)$, will become small as the material flows at high velocity relative to the field lines. This effect means that the magnetic pressure term in Equation 4.14 may be considered negligible compared to the tension term. This assumption gives an acceleration, due to magnetic processes as in Equation 4.15.

$$\mathbf{a}_{\rm mag} \simeq \frac{1}{R_{\rm c}(r,t)} \frac{1}{\rho(r,t)} \left(\frac{B^2(r,t)}{4\pi} \right) \hat{\mathbf{n}} \tag{4.15}$$

If the assumption that Equation 4.15 can be set equal to some parameter $k(r,t)$ multiplied by the relative velocity (between the field lines and the accreting material) perpendicular to the field lines, $v_\perp$, is made then Equation 4.16 is evident.

$$\mathbf{a}_{\rm mag} \simeq -k(r,t)\mathbf{v}_\perp \tag{4.16}$$

If a further assumption that k, $R_{\rm c}$ and ρ are not time dependent is made then this gives

$$\frac{1}{\rho(r)R_{\rm c}(r)}\left(\frac{B(r)^2}{4\pi}\right)\hat{\mathbf{n}} = k(r)\mathbf{v}_{\perp} \tag{4.17}$$

4.2.4 Estimating parameters

Material is assumed to be flowing from the secondary to the primary via the L_1 point. The material in the secondary is assumed to have a velocity of order the sound speed. This means that material which is travelling toward the primary, in the vicinity of, but not necessarily at, the L_1 point, may have enough kinetic energy to overcome the potential 'hill'. In this way a nozzle may be defined which is centred on the L_1 point that has a finite width, w. Equating the kinetic energy of a blob to the potential energy needed to climb the potential hill close to the L_1 point leads to an expression for w (see Equation 4.18) (Pringle & Wade 1985).

$$w = \frac{c_{\rm s}P_{\rm orb}}{2\pi} \tag{4.18}$$

An estimate of the mass transfer rate, $\dot{M}$, at the nozzle (i.e. at $r = b$ where b is the distance from the WD to the L_1 point) can then be given by Equation 4.19.

$$\dot{M} \sim w^2 c_{\rm s}\rho(b) = \frac{c_{\rm s}^3 P_{\rm orb}^2 \rho(b)}{(2\pi)^2} \tag{4.19}$$

The typical density and size scales near the L_1 can then be given by Equations 4.20 and 4.21

$$\rho_{\rm gas}(b) \sim \frac{\dot{M}4\pi^2}{P_{\rm orb}^2 c_{\rm s}^3} \tag{4.20}$$

$$l_{\rm gas}(b) \sim w \sim \frac{c_{\rm s}P_{\rm orb}}{2\pi} \tag{4.21}$$

The assumption can then be made that the typical radius of curvature, $R_{\rm c}$ is approximately equal to the typical length scale of the gas, $l_{\rm gas}$ close to the L_1 point. Making the further assumption that ρ and $R_{\rm c}$ are essentially constant from the L_1 point (i.e. at $r = b$) down to the circularization radius (i.e. at $r = r_{\rm circ}$) leads to Equation 4.22.

$$\rho(b)R_{\rm c}(b) \sim \rho(r_{\rm circ})R_{\rm c}(r_{\rm circ}) \sim \frac{2\pi\dot{M}}{P_{\rm orb}c_{\rm s}^2} \tag{4.22}$$

The gas density and size scale will not be constant as a blob falls towards the surface of the WD. This may be expected to vary as $\rho(r) \propto r^{-2}$ and $l(r) \propto r^{-1}$ therefore

$$\rho(r)l(r) \propto r^{-3} \tag{4.23}$$

which implies that

$$\rho(r)R_{\rm c}(r) = \frac{2\pi\dot{M}}{P_{\rm orb}c_{\rm s}^2}\left(\frac{r}{r_{\rm circ}}\right)^{-3} \tag{4.24}$$

Given this scaling, k must scale as

$$k(r) \propto \frac{1}{r^{-3}}(r^{-3})^2 \propto r^{-3} \tag{4.25}$$

therefore

$$k(r) = k_0\left(\frac{r}{r_{\rm wd}}\right)^{-3} \tag{4.26}$$

Equations 4.17, 4.24 and 4.26 together imply that

$$\frac{P_{\rm orb}c_{\rm s}^2}{8\pi^2\dot{M}}B_{\rm wd}^2\left(\frac{r}{r_{\rm wd}}\right)^{-6}\left(\frac{r_{\rm circ}}{r}\right)^{-3} = k_0\left(\frac{r}{r_{\rm wd}}\right)^{-3}|v_\perp| \tag{4.27}$$

Or in a simplified form

$$B_{\rm wd}^2 = \frac{8\pi^2\dot{M}}{P_{\rm orb}c_{\rm s}^2}k_0\left(\frac{r_{\rm circ}}{r_{\rm wd}}\right)^3|v_\perp| \tag{4.28}$$

The relative perpendicular velocity between the accreting plasma and the magnetic field lines may be estimated as

$$|v_\perp| = \left|\left(\frac{GM_1}{r}\right)^{1/2} - \frac{2\pi r}{P_{\rm spin}}\right| \tag{4.29}$$

For an example typical set of values; $P_{\rm orb} = 4$ hr, $P_{\rm spin} = 1000$ s, $M_1 = 0.6M_\odot$, $M_2 = 0.3M_\odot$, $r_{\rm wd} \sim 10^7$ m, $k = 0.436$ (equivalent to a $k_{\rm input}$ =1000 after normalization); evaluated at the circularization radius this implies $a = 8.6 \times 10^8$ m, $r_{\rm circ} = 1.3 \times 10^8$ m, $v_\perp = 3.2 \times 10^4$ m s^{-1}, $\dot{M} = 2.1 \times 10^{14}$ kg s^{-1} (Warner 1995). Therefore

$$B_{\rm wd} = 1.1 \times 10^{6}{\rm G} \tag{4.30}$$

It should be noted that there may be some error in this conversion. Since multiple approximations have been made in this derivation it is prudent to consider B as an order of magnitude estimate.

The magnetic moment (μ) of the WD is used instead of magnetic field strength in the analysis done here. The relation between the two is $\mu = B_{\rm wd} r_{\rm wd}^{3}$.

The actual values of k for each blob of material is randomized about a mean value. This is to reflect the fact that each blob is not in fact uniform, and so size, shape and density perturbations may be treated in one go. This randomization has been found not to affect the overall dynamics of the system since the mean value of k is the important factor (Wynn & King 1995).

4.3 *HyDisc* configuration

4.3.1 Global options

For all of the work considered here, the magnetic field in *HyDisc* was configured to be a dipole (other options do exist). *HyDisc* has the functionality to have the WD spin period evolve based upon the angular momentum transferred to or taken away from the system. This feature was disabled such that the WD spin period was not permitted to change over time.

4.3.2 Free parameters

The user changeable free parameters along with the typical values used are then those in Table 4.1. Typically the ϕ_0, $burst_{\rm max}$, $k_{\rm var}$, and α parameters are kept constant for each run here and the rest are varied. The $burst_{\rm max}$ parameter is the number of particles inserted per orbit, this does not directly relate to the mass accretion rate. *HyDisc* treats mass in a completely arbitrary way, such that the true mass accretion rate is only factored in when converting k to B.

4.3.3 Accretion flows

Thus far in this thesis the term accretion disc has been used as a general description of the accretion topology in intermediate polars. In order to distinguish the different accretion structures in a consistent way, the term

Table 4.1: *HyDisc* free parameters.

HyDisc parameter	Description	Units	Typical values
$P_{\rm spin}$	Spin period	Seconds	100–10000
$P_{\rm orb}$	Orbital period	Hours	2–10
M_1	Primary mass	$M_\odot$	0.5–1.4
q	Secondary mass/Primary mass	–	0.2–0.9
$k_{\rm mean}$	k parameter	s^{-1}	1000
$k_{\rm var}$	Variance in k	%	10
θ_0	Magnetic co-latitude	Degrees	5
ϕ_0	Magnetic azimuth	Degrees	0
$burst_{\rm max}$	No. of particles injected	Particles/orbital period	50000
α	Viscosity	–	0.7

accretion flow is introduced as a general description of all accretion structures (in replacement of disc). This leaves the term accretion disc to describe a much more specific type of flow (see below).

Running the model for a given set of parameters leads to, broadly speaking, four different accretion geometries; a disc, a stream, a ring and a propeller (see Figure 4.5).

1. The disc has a majority of the accreting material form a circulating flattened structure around the WD. This is truncated at its inner edge by the WD magnetosphere, where material attaches to the the magnetic field lines before accreting on to the WD surface.

2. The stream has most of the material attach to the magnetic field lines almost immediately, following them on a direct path to the WD surface.

3. The ring has most of the material form a narrow annulus circulating the WD at the outer edge of its Roche lobe. The majority of this material is re-accreted on the secondary, but some is stripped away from its inner edge by the magnetic field lines before being channelled down to the WD surface.

4. The propeller has most of the material magnetically propelled away from the system by the rapidly rotating magnetosphere of the WD.

Whether each accretion flow is an equilibrium flow or not (i.e. whether the WD angular momentum would

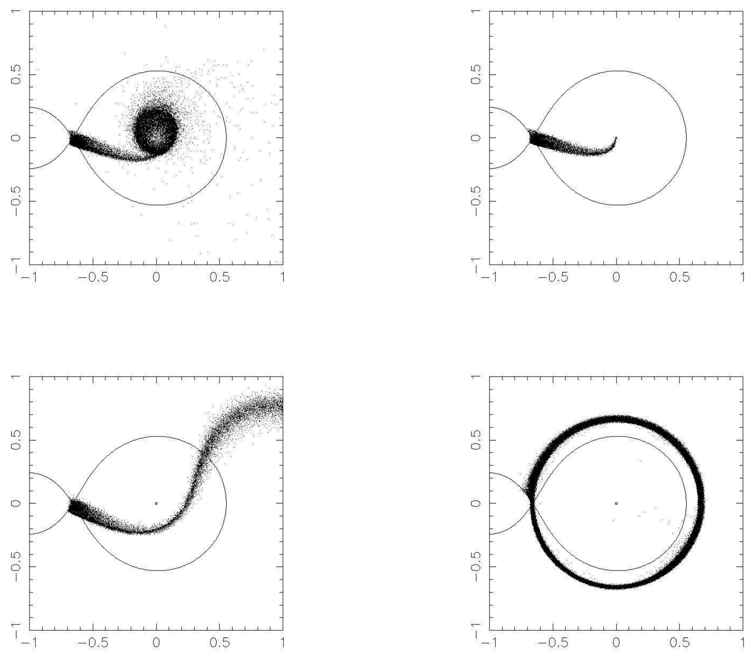

Figure 4.5: The four different simulated accretion pattern possibilities. From the top left going clockwise; a disc, a stream, a ring and a propeller. The solid line represents a line of equipotential that goes through the L_1 points. The WD is located at 0,0.

increase or decrease if the WD spin period were permitted to change) is governed by how much material is ejected or accreted. In general the propeller ejects angular momentum from the system and thus the spin period would increase. Similarly the stream flow transfers angular momentum to the WD and so would decrease the spin period. Both the disc and the ring systems can exist in equilibrium as they can balance the angular momentum flow by both accreting and ejecting matter simultaneously.

4.4 Previous work

4.4.1 Phase diagrams

Parker (2005) explored parameter space of mCVs with *HyDisc*, varying the spin period, the orbital period, and the magnetic moment. For each set of parameters the final flow type was classified as one of disc, stream, ring or propeller. By plotting the $P_{\rm spin}/P_{\rm orb}$ vs magnetic moment this was later converted to the representation of Norton et al. (2008) where parameter space was divided into regions of common flow type (see Figure 4.6).

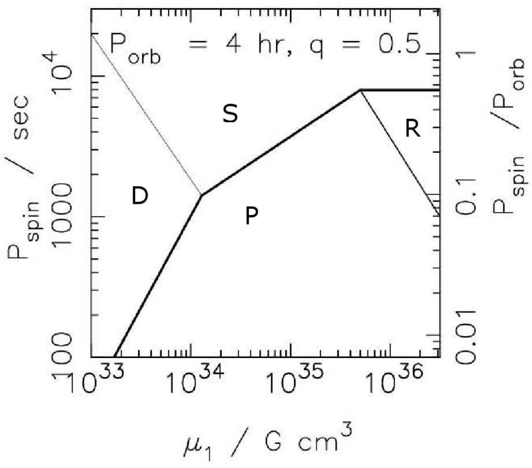

Figure 4.6: Different flow type regions in parameter space. D=Disc, S=Stream, P=Propeller and R=Ring. The orbital period is 4hrs.

This allowed a prediction of the expected flow type of the model from a given set of conditions. Because of the similarity with phase diagrams (of e.g. water) the intersections in the plots were dubbed *triple points*.

When considering the angular momentum change from the different flow regimes the equilibrium spin period can be deduced. The propeller flow will have the effect of spinning down the WD since material is ejected from the system by the magnetosphere of the WD. This will have the effect of moving the system vertically up in the phase diagrams. Similarly, the stream accretion will have the effect of moving the WD down in the plots. As such for a given orbital period and magnetic moment, the equilibrium spin period is indicated by the transition between the two. The disc and ring accretion regimes can maintain their spin periods as these tend to both accrete and eject material away, thus balancing the angular momentum transfer.

IPs are generally assumed to be in equilibrium, but at a given point they may be spinning up or down towards their equilibrium spin period. Moreover, Patterson (1994) predicted that the spin period derivative of an IP in equilibrium will not be steady. The spin-up and spin-down rates observed in IPs imply that they typically correspond to times scales $\sim\ 10^9$ years, this is in contrast to the time taken to reach equilibrium ($\sim\ 10^7$ years). Systems out of equilibrium are therefore likely just briefly put in this state – probably by fluctuations in the mass transfer rate.

Close to the triple points the flow becomes less well defined as there is a transition from one flow type to another (see Figure 4.7). The locations of the triple points were shown to stay at the same $P_{\rm spin}/P_{\rm orb}$ for the range of orbital period (for the $q = 0.5$ case), more precisely the lower triple point was at $P_{\rm spin}/P_{\rm orb} \sim 0.1$

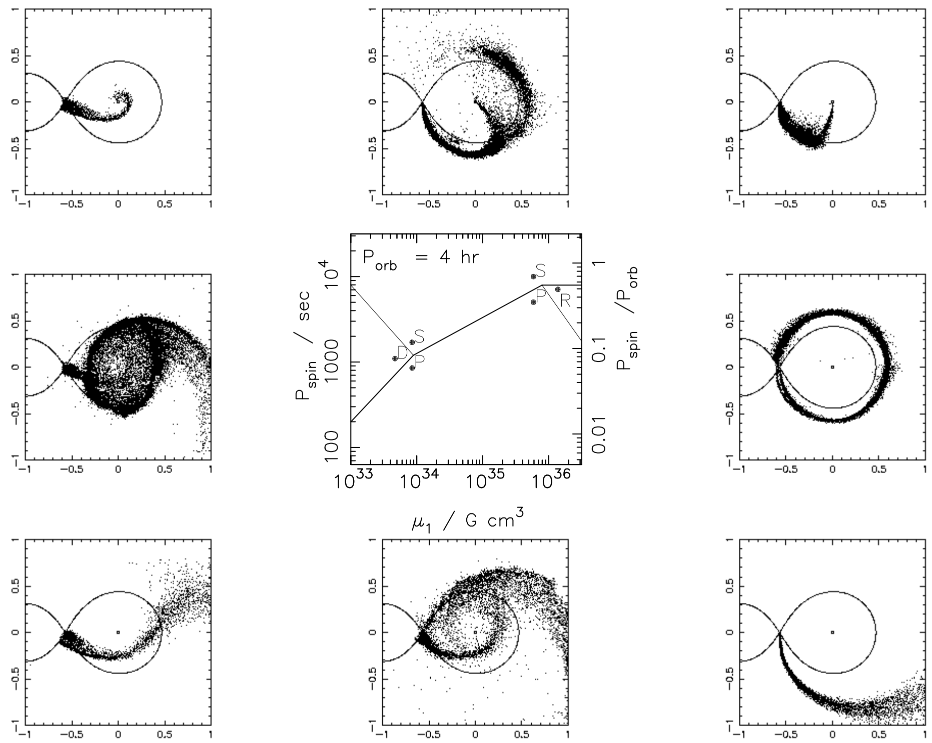

Figure 4.7: Plot of the different flow types around the triple points. The plots on the left hand column are the flow types in the vicinity of the lower triple point. The plots on the right are the flow types close to the upper triple point. The bottom central plot is the flow type *at* the lower triple point and the upper plot is the the flow type *at* the upper triple point.

and the upper triple point at $P_{\rm spin}/P_{\rm orb} \sim 0.6$ (see Figure 4.8).

It should be noted that some of the parameter space explored does not correspond with observed parameters. For example, $q = 0.5$ and $P_{\rm orb} = 80$ min in Figure 4.8 does not fit in with the current understanding of CV evolution (by 80 mins the mass accretion onto the primary would have reduced q significantly). These parameters are however included in the plots for completeness, and to help identify any trends.

4.5 Aims & Method

This work aimed to take the next logical step and investigate the effect of the mass ratio on the location of the triple points. In a similar way to Parker (2005), parameter space was explored by running *HyDisc* with many different initial conditions and classifying the final flow type as either a disc, a stream, a ring or a propeller. Regions of common flow type were then plotted in a similar way to the phase diagrams in Figure 4.7. Each

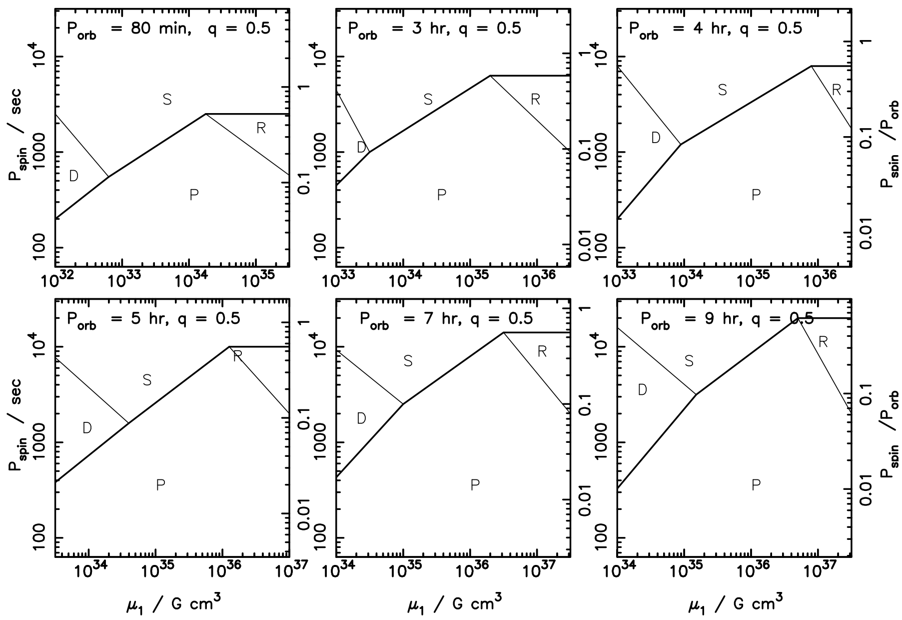

Figure 4.8: The variation of the triple points as a function of $P_{\rm orb}$ at $q = 0.5$. The upper triple point in each plot is at $P_{\rm spin}/P_{\rm orb} \sim 0.6$ and the lower at ~ 0.1.

HyDisc run had the same orbital period (4 hrs), but a different mass ratio, spin period and k parameter (which were kept constant for that run). This allowed the variation of the location of the triple points as a function of mass ratio to be explored.

4.6 Results & Discussion

Exploring parameter space for a fixed orbital period of four hours and with three different mass ratios (q = 0.2, 0.5 and 0.9), yielded the results in Figure 4.9. As can be seen from the plots, the triple points move to a larger $P_{\rm spin}/P_{\rm orb}$ and larger magnetic moment as the mass ratio is decreased. Reading the positions of the triple points off the plots gives the values in Table 4.2.

This result can be understood in the context of the work by King & Wynn (1999), who suggested that mCVs should have an equilibrium condition given by $R_{\rm co} \sim R_{\rm circ}$. That is to say the radius at which matter in a local Keplerian orbit co-rotates with the magnetic field ($R_{\rm co}$) is the same as the radius where it has an angular momentum equal to that of the matter at the L_1 point ($R_{\rm circ}$) (see Equations 4.31–4.34).

$$R_{\rm co} = \left(\frac{GM_1 P_{\rm spin}^2}{4\pi^2} \right)^{1/3} \tag{4.31}$$

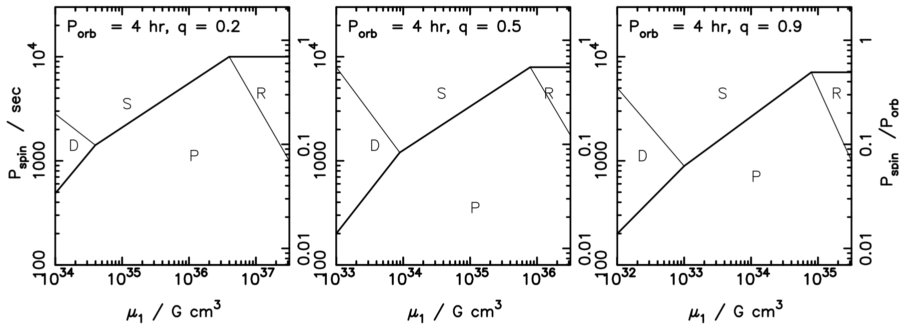

Figure 4.9: The variation of the triple points as a function of the mass ratio.

Table 4.2: Locations of the triple points

Mass ratio	$P_{\rm spin}/P_{\rm orb}$ (Lower triple point)	$P_{\rm spin}/P_{\rm orb}$ (Upper triple point)
0.2	0.097	0.69
0.5	0.083	0.56
0.9	0.063	0.49

Where M_1 is the mass of the primary.

$$R_{\rm circ} \simeq \frac{M}{M_1}\left(\frac{b}{a}\right)^4 \left(\frac{GMP_{\rm orb}^2}{4\pi^2}\right)^{1/3} \tag{4.32}$$

Where M is the total mass of the primary and secondary combined, b is the distance from the primary to the inner Lagrange point and a is the separation between the primary and the secondary. (b/a) has been shown to be approximated (Warner 1976) as

$$\frac{b}{a} = 0.500 - 0.227\log q \tag{4.33}$$

Where q is the mass ratio. Hence for the condition $R_{\rm co} = R_{\rm circ}$

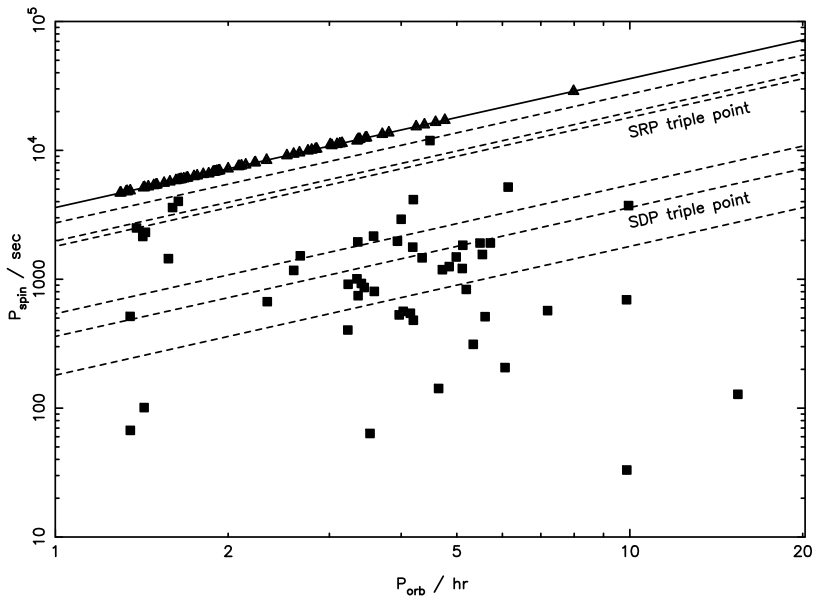

Figure 4.10: Known period distribution of IPs with the triple point locations overlaid. The lower three dashed lines correspond to the lower triple point, with the three lines representing mass ratios of 0.2, 0.5 and 0.9 (top to bottom). The top three dashed line equivalently correspond to the upper triple point.

$$\frac{P_{\rm spin}}{P_{\rm orb}} \sim (1+q)^2(0.500 - 0.227\log q)^6 \tag{4.34}$$

For an orbital period of four hours and the mass ratios of 0.2, 0.5 and 0.9, this predicts a $P_{\rm spin}/P_{\rm orb}$ of 0.118, 0.076 and 0.064 respectively. This is in fairly good agreement with the values of 0.097, 0.083 and 0.063 from Figure 4.9.

King & Wynn (1999) also suggested another possible equilibrium condition of $R_{\rm co} \sim b$, i.e. the distance to the L_1 point. This then gives rise to Equation 4.35.

$$\frac{P_{\rm spin}}{P_{\rm orb}} \sim (0.500 - 0.227\log q)^{3/2} \tag{4.35}$$

This can be identified with the upper triple point. For the three different mass ratios used earlier, this corresponds to a $P_{\rm spin}/P_{\rm orb}$ of 0.53, 0.43 and 0.36. The locations of the upper triple point in the plots above are $P_{\rm spin}/P_{\rm orb}$ of 0.69, 0.56 and 0.49. This is somewhat higher than the predicted values, this may be because the ring-like structures seen here are just outside of the Roche lobe surface. The radius the co-rotating material would have to be at for Equation 4.35 to correspond with the measured results is $1.2b$ from the WD.

By considering the period distribution of the known IPs, an indication of the likely flow types may be gained. Figure 4.10 plots the spin and orbital periods of the known IPs, as well as the location of the upper and lower triple points for the three mass ratios outlined above. Any IPs below the lower dashed lines are therefore likely to be disc accreting systems, any above the upper dashed lines are likely to be ring accreting systems and those in between likely stream fed/propeller accretors.

The plot shows that a majority of systems are close to the lower triple point (for mass ratios in the range 0.2–0.9). If these are all close to their equilibrium spin period then they will likely look like the flow seen in the lower centre plot of Figure 4.7. There is a cluster of systems at short orbital periods with large spin periods. These systems, often referred to as EX Hya like, have been suggested as likely ring-like accretion flow IPs (Norton et al. 2004). This suggestion has been given considerable support by the spectroscopic measurements of EX Hya (Mhlahlo et al. 2007), and further agrees with the model here. Some of the more 'extreme' systems, e.g. AE Aqr, lie a long way from the triple points for any reasonable mass ratio. This would imply, in the case of AE Aqr here, that it is likely to be a disc accreting system. AE Aqr is however a long way from equilibrium - it has a measurable $\dot{P}_{\rm spin}$ (de Jager et al. 1994), and so does not fit within the assumptions used here.

4.7 Conclusion

HyDisc has allowed the likely topology of the accretion flow structure in IPs to be explored. Here it has been demonstrated how the $P_{\rm spin}/P_{\rm orb}$ ratio of the upper and lower triple points varies with the mass ratio. Consideration of this variation allows a prediction of the accretion flow topology of IPs - if they are assumed to be in equilibrium. The next logical step in the development of *HyDisc* would be to extend it to simulate the light curves of IPs by considering the absorption of the accretion on the emitted radiation.

Chapter 5

Synthetic light curve modelling

This chapter introduces the synthetic light curve computer model written as an extension to *HyDisc* (introduced in Chapter 4). The fundamental idea behind the model is to take the output of *HyDisc* (which is a series of snapshot files taken at intervals which contain physical properties of the systems (such as periods and location of the accretion flow)), and turn that into a synthetic light curve.

5.1 Introduction

HyDisc has been very successful in modelling the accretion flow structure and evolution in intermediate polars (as outlined in Chapter 4). Its biggest drawback is that it makes no prediction of the observed light curves that the accretion flow would produce. This has made it difficult to draw firm conclusions over the validity of some of its results.

5.2 Aim

The main aim was to develop an extension to *HyDisc* that generates synthetic light curves based upon absorption along the line of sight through the accretion flow. Using this model to create synthetic light curves of typical accretion flow types (i.e. disc, stream, ring and propeller), characteristics in these light curves should be distinguishable. By considering these characteristics it may be possible to characterize the accretion flow topology of intermediate polars from their light curves. Moreover, by considering the known parameters of real intermediate polars and exploring the remaining free parameters it may be possible to constrain some of the unknowns.

5.3 The model

The model calculates the location of discrete emission points close to the WD, based upon the accretion structure. The line of sight from each emission point to an external observer is calculated, taking account of the inclinations, spin and orbital phases of the system. This line of sight then has its column density calculated based upon the density of material along its path. The emission profile is then absorbed accordingly for each individual emission point.

5.3.1 Free parameters

The main input to the model is the positions of the blobs and the physical parameters passed into *HyDisc*. Anything other than this is a further assumption that the model makes. As outlined in Chapter 4, *HyDisc* takes in the parameters in Table 4.1. So for the purpose of simulating light curves this leaves several free parameters.

Inclination

The inclination of the system, as defined by the angle between the angular momentum vector of the binary and the line of sight to the observer. In reality there is no significant bias towards any particular inclination, therefore this is variable between $0°$ and $180°$.

Distance

In many cases the distance to known IPs is uncertain, in the cases where a distance is known, it is often of the order of a few hundred parsecs. The model assumes that an observer at any given distance will have the emission profile they observe largely set by the parameters of the system, i.e. the emission profile at the edge of the accretion flow is what an observer would see no matter how far away they are. In reality some further processes will affect this, since interstellar space is generally fairly abundant with neutral hydrogen any wavelengths sensitive to this may be absorbed significantly.

Mass

HyDisc treats mass in a completely arbitrary way, with the real value of the mass of each blob of material undefined. In IPs, the mass accretion rate from the secondary is generally of the order of 10^{14}kg s^{-1} (see e.g. Warner (1995)). The individual blob mass is therefore just a function of the number of blobs *HyDisc* inserts to the system each orbit.

The emission profile

As *HyDisc* makes no inference about the emitted radiation this is essentially a completely free parameter. Generally IPs emit X-rays as Bremsstrahlung and blackbody emission (see Section 1.8). Assuming a Bremsstrahlung and blackbody like emission profile this leaves the temperatures and densities as free parameters. As Section 1.8 showed, Bremsstrahlung radiation generally occurs at a few tens of keV, and blackbody emission at a few tens of eV. All of the models run in this chapter have a blackbody temperature ($T_{\rm BB}$) of 50 eV, a Bremsstrahlung temperature ($T_{\rm Br}$) of 10 keV, and a column density of 10^{22} cm^{-2}. The combined emission profile used is that in Equation 5.1.

$$I(\nu) = \frac{8\pi h\nu^3}{c^2}\frac{1}{e^{\frac{h\nu}{kT_{\rm BB}}}-1} + 6.8\times10^{-51}Z^2 c n_{\rm e} n_{\rm i} T_{\rm Br}^{-1/2} e^{-h\nu/kT_{\rm Br}}\bar{g}_{\rm ff} \quad \mathrm{W\ m^{-2}\ Hz^{-1}} \tag{5.1}$$

where the symbols take on the same meanings as in Section 1.8.

The range of frequencies considered here is $2.4\times10^{16} < \nu < 2.4\times10^{18}$ Hz (0.1–10 keV), these are typical values for IPs.

The nature of computer simulations is such that an emission region has to be described as a set of discretized points in space, this has the effect that the emission profile is somewhat arbitrarily dependant on the discretization scheme used. As such the model does not attempt to give absolute intensity values.

5.3.2 Frames of reference

Periods

There is some degree of ambiguity in the literature as to what exactly the spin period and beat period *really* refer to. In this chapter the intrinsic spin period ($P_{\rm int}$) is defined to be the time it takes the WD to do one complete revolution in the *orbital frame*. The sidereal period ($P_{\rm sid}$) is what an observer outside of the orbital frame (with period P_{orb}) would see, and is defined in Equation 5.2.

$$\frac{1}{P_{\text{sid}}} = \frac{1}{P_{\text{int}}} + \frac{1}{P_{\text{orb}}} \tag{5.2}$$

The sidereal period is generally what is quoted as the spin period in the literature, and the the intrinsic spin period as the beat period. This slightly different nomenclature is used as *a priori* knowledge of the *real* spin period here renders the traditional relationship counter-intuitive.

WD-orbital frame

HyDisc uses a frame of reference centred on the WD with the x-axis running through the centre of the WD and secondary, such that zero is in the centre of the WD and the secondary is centred at x=-separation. The plane of the orbit is in the $x - y$ plane. This frame is referred to as the WD-orbital frame from here onwards.

The model mimics this, therefore the position data from *HyDisc* is in the correct frame. The model defines an observer at a given inclination and distance from the centre of mass (C.O.M.), in the $x - z$ axis, in the inertial frame centred on the C.O.M. Therefore a transformation to the WD-orbital frame is needed to gauge the position of the observer (see Equation 5.3). Here x, y and z correspond to positions in the WD-orbital frame (all non-primed x, y and z correspond to the WD-orbital frame), D is the distance to the observer from the C.O.M, Q is the distance from the centre of the WD to the C.O.M, ϕ is the inclination and Ω is the orbital frequency.

$$\begin{aligned} x &= +D \sin\phi \cos\Omega t - Q \\ y &= -D \sin\phi \sin\Omega t \\ z &= +D \cos\phi \end{aligned} \tag{5.3}$$

The initial angle of the magnetic field with respect to the inertial, the inclination (θ_0 in *HyDisc*), is the angle from the z-axis in the $x - z$ plane. The azimuth is with respect to the $x - z$ plane measured anti-clockwise i.e. towards the positive y-axis.

Dipole frame

The WD is always considered to be rotating with its spin axis aligned to the orbital axis of the system. The magnetic axis of the WD will generally be different from the spin axis, this angle is the magnetic co-latitude.

Many of the calculations carried out are easiest done when considered in the frame of the dipole magnetic field of the WD. This is defined as the dipole frame and identified with a prime ($'$) henceforth. The transformation from the WD-orbital frame to the dipole frame is that in Equation 5.4.

$$\begin{aligned} x' &= (x \cos \omega_{\text{int}} t + y \sin \omega_{\text{int}} t) \cos \alpha - z \sin \alpha \\ y' &= -x \sin \omega_{\text{int}} t + y \cos \omega_{\text{int}} t \\ z' &= (x \cos \omega_{\text{int}} t + y \sin \omega_{\text{int}} t) \sin \alpha + z \cos \alpha \end{aligned} \tag{5.4}$$

where α is the magnetic co-latitude and ω_{int} is the intrinsic spin frequency.

5.3.3 Blob size and shape

HyDisc treats all the blobs as point sources and only logs their position. In reality they will have a size and shape that affects the column density along the line of sight. To address this in the model the blobs are considered spherical when outside the magnetospheric radius and have their mass redistributed when inside. This redistribution is an approximation of how the blobs would be deformed, as they near the white dwarf, by the magnetic field.

The size of the magnetospheric radius can be estimated by considering the magnetic field strength felt by each individual blob, which is a function of k (see Equation 4.28). Each blob has a slightly different value of k, hence it will have a different magnetospheric radius. In reality the transition between being gravitational or magnetically dominated will be a continuous one close to the magnetospheric radius. To take this into account to some extent, a blob is considered to have its motion dominated by the magnetic field if it is inside the magnetospheric radius, or if it is significantly above or below the average height in the accretion flow.

Outside the magnetospheric radius

The length scale of the blobs (as discussed in Section 4.2.4) is:

$$l(b) \sim \frac{P_{\text{orb}} c_{\text{s}}}{2\pi} \tag{5.5}$$

where c_{s} is the speed of sound as given by:

$$c_{\text{s}}^2 = \frac{kT}{m_{\text{H}}} \tag{5.6}$$

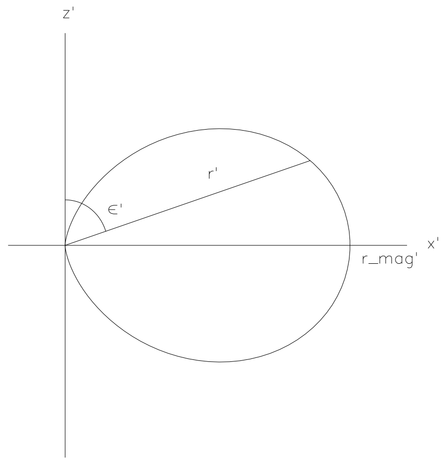

Figure 5.1: Dipole field showing relation between the distance to the field from the origin, r', the magnetospheric radius, $r'_{\rm mag}$, and the angle from the z'-axis, ϵ'.

For typical properties (e.g. $P_{\rm orb} \sim 15,000$ s and $c_{\rm s} \sim 5 \times 10^3 {\rm m\,s^{-1}}$) this gives a blob size of $\sim 10^7$ m. All blobs outside the magnetospheric radius are assumed to be spherical with the same radius as defined by Equation 5.5.

Inside the magnetospheric radius

As the blobs fall closer to the WD they are subject to ever greater magnetic forces that will distort them. The blobs are therefore redistributed along the field lines. This is achieved by considering the outline of the blobs at the magnetospheric radius and transforming this along a dipole field in such a way as to conserve volume. This transformation is carried out in the dipole frame. Firstly, this uses the equation of a dipole (Equation 5.7), shown in Figure 5.1, where r' is the distance to the field from the origin, ϵ' is the angle to the z'-axis, and $r'_{\rm mag}$ is the magnetospheric radius.

$$r' = r'_{\rm mag} \sin^2(\epsilon') \tag{5.7}$$

Given that the position of the blobs will not follow a dipole exactly as defined by the magnetic field of the

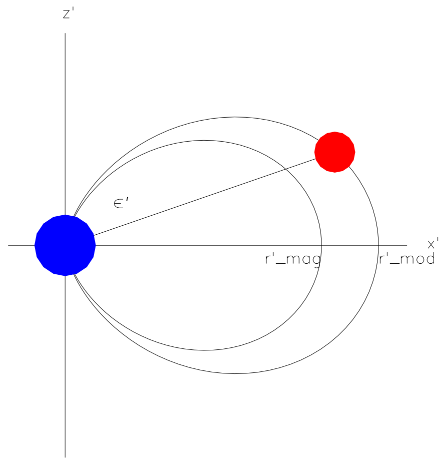

Figure 5.2: Modified dipole. The red circle corresponds to the position of a blob, r'_{mod} is then the magnetospheric radius that corresponds to the dipole that passes through the centre of this blob.

WD (due to all the other forces) an approximation is needed. A modified dipole is therefore introduced for each blob where this is defined as the dipole which corresponds to the location of the blob. Such that

$$r'_{\mathrm{blob}} = r'_{\mathrm{mod}} \sin^2(\epsilon'_{\mathrm{blob}}) \tag{5.8}$$

where r'_{mod} is the modified dipole radius, this is shown in Figure 5.2.

Each blob is then transformed along this field by first of all considering a sphere at r'_{mod} and $\epsilon' = 90°$ with a radius of rad_{blob}, the outline of this sphere is then transformed along the dipole where each point on the sphere is the corresponding r'_{mod}. This creates a cone-like structure with its base in the $x' - y'$ plane and the tip at the centre of the WD (see Figure 5.3). By approximating this structure as a cone (see Figure 5.4), the volume of transformed blob can be found with simple geometry such that

$$\frac{4}{3}\pi rad'^{3}_{\mathrm{blob}} = \frac{1}{3}\pi {r'_1}^2 l'_1 - \frac{1}{3}\pi {r'_2}^2 l'_2 \tag{5.9}$$

where the symbols are defined in Figure 5.4.

The gradient of the dipole is:

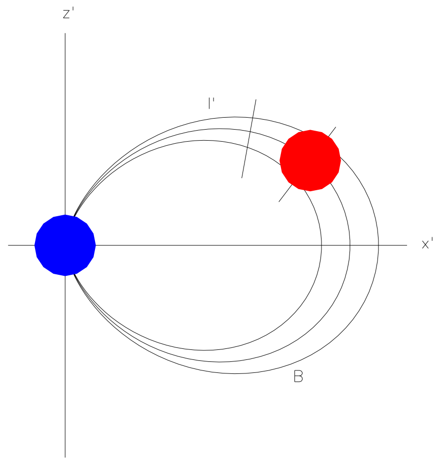

Figure 5.3: Outline of the redistributed volume that a blob is transformed to.

$$\left(\frac{dz'}{dx'}\right) = \frac{r'_{\text{mod}}\left(\frac{2}{3}\left(\frac{x'}{r'_{\text{mod}}}\right)^{\frac{1}{3}} - \left(\frac{x'}{r'_{\text{mod}}}\right)\right)}{\left(\left(\frac{x'}{r'_{\text{mod}}}\right)^{\frac{4}{3}} - \left(\frac{x'}{r'_{\text{mod}}}\right)^{2}\right)^{\frac{1}{2}}} \tag{5.10}$$

The tangent to the dipole describes the upper and lower bounds of the redistributed blob, and is defined as:

$$-\left(\frac{dz'}{dx'}\right)^{-1} = -\frac{\left(\left(\frac{x'}{r'_{\text{mod}}}\right)^{\frac{4}{3}} - \left(\frac{x'}{r'_{\text{mod}}}\right)^{2}\right)^{\frac{1}{2}}}{r'_{\text{mod}}\left(\frac{2}{3}\left(\frac{x'}{r'_{\text{mod}}}\right)^{\frac{1}{3}} - \left(\frac{x'}{r'_{\text{mod}}}\right)\right)} \tag{5.11}$$

The length along the field line to the WD is simply:

$$l'\Bigg|_{l'_{\text{wd}}}^{l'_{\epsilon}} = -\frac{r'_{\text{mod}}}{2}\cos(\epsilon')\left(1+3\cos^2(\epsilon)\right)^{1/2} + \frac{r'_{\text{mod}}}{4\sqrt{3}}\ln\left|\frac{\left(1+3\cos^2(\epsilon')\right)^{1/2} - \sqrt{3}\cos(\epsilon')}{\left(1+3\cos^2(\epsilon')\right)^{1/2} + \sqrt{3}\cos(\epsilon')}\right|\Bigg|_{\epsilon'_{\text{wd}}}^{\epsilon'} \tag{5.12}$$

The base of the redistributed blob is set to be the initial position of the blob, iterating along the dipole until Equation 5.9 is satisfied then gives the top of the redistributed blob. The transformed blob can then be completely described.

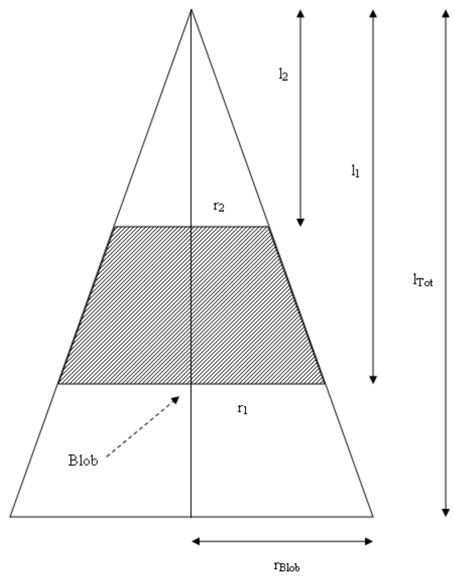

Figure 5.4: Approximate cone structure. The base of the cone corresponds to the size of a blob ($r_{\rm blob}$), the shaded area has an equivalent volume of a sphere with radius $r_{\rm blob}$

5.3.4 The footprint

HyDisc keeps track of how many blobs hit the surface of the WD during a given snapshot. Using the same dipole approach as before, and assuming that the closest blobs are the ones which hit the surface, allows an estimate of the size and location of the footprint. The emission is then defined as coming from a point $0.05r_{\rm wd}$ above the footprint.

5.3.5 Absorption

To carry out the absorption along the line of sight from the emission point to the observer the column density needs to be calculated. This is achieved by considering the position of the blobs in the WD-orbital frame. If a particular blob is considered to be outside the magnetospheric radius then it is treated as sphere, otherwise it is treated as a redistributed volume as outlined earlier.

Column density outside the magnetospheric radius

A spherical blob at position $x_{\rm o}, y_{\rm o}, z_{\rm o}$ (in the WD-orbital frame) with radius $r_{\rm o}$ is described by:

$$(x - x_{\rm o})^2 + (y - y_{\rm o})^2 + (z - z_{\rm o})^2 = r_{\rm o}^2 \tag{5.13}$$

The line of sight from an emission point to the observer can be described as:

$$\frac{x - x_1}{a} = \frac{y - y_1}{b} = \frac{z - z_1}{c} \tag{5.14}$$

Where x_1, y_1, z_1 is a point on the line and a, b, c are constants. Solving this pair of equations for x gives a quadratic

$$ix^2 + jx + k = 0 \tag{5.15}$$

Where

$$i = 1 + \left(\frac{b}{a}\right)^2 + \left(\frac{c}{a}\right)^2 \tag{5.16}$$

$$j = 2\left(\left(\frac{b}{a}\right)(y_1 - y_o) + \left(\frac{c}{a}\right)(z_1 - z_o) - \left(\left(\frac{b}{a}\right)^2 + \left(\frac{c}{a}\right)^2\right)x_1 - x_o\right) \tag{5.17}$$

$$k = x_o^2+y_o^2+z_o^2+y_1^2+z_1^2-2y_oy_1-2z_oz_1+\left(\left(\frac{b}{a}\right)^2 + \left(\frac{c}{a}\right)^2\right)x_1^2+2x_1\left(\frac{b}{a}\right)(y_o-y_1)+2x_1\left(\frac{c}{a}\right)(z_o-z_1)-r_o^2 \tag{5.18}$$

Therefore, if i, j, k give real roots to the quadratic equation (i.e. if $j^2 > 4ik$) then the line of sight and the blob intersect. Moreover, the intersects are those in Equation 5.19. This is however only the case if $b/a \neq \infty$ and $c/a \neq \infty$. When this is the case then Equations 5.13 & 5.14 can be solved for y or z and the intercepts found from the corresponding equations.

$$x_{\text{intersects}} = \frac{-j \pm \sqrt{j^2 - 4ik}}{2a} \tag{5.19}$$

Once the intersects are known the path length through the blob is calculated. The blobs are assumed to be uniformly dense, and thus the column density can be calculated.

Column density inside the magnetospheric radius

Inside the magnetospheric radius the blobs are redistributed along a dipole. This means that the simple test above cannot be used to find the intercepts of the line of sight and a blob. In order to calculate this, several inequalities are checked to see if the line of sight does pass through the redistributed blob. If it does then the intercepts are calculated. To calculate the column density the density of the redistributed blobs is assumed to be uniform.

Absorption

Once the total column density along a line of sight is known. absorption is then carried out as in Equation 5.20.

$$I[\nu] = I_0[\nu]e^{-\tau[\nu]} \tag{5.20}$$

where I_0 is the intensity given by the emission profile and τ is the optical depth for that specific frequency. Norton (1988) empirically found a relationship for the optical depth as a function of column density for high energies (see Equation 5.21). This is the method used in the model.

$$\begin{aligned} \tau &= 10^{-21.8}E^{-2.7}N_{\mathrm{H}} \quad \text{for } 0.53 < E \leq 10 \text{ keV} \\ \tau &= 10^{-22.0}E^{-2.9}N_{\mathrm{H}} \quad \text{for } 0.10 < E \leq 0.53 \text{ keV} \end{aligned} \tag{5.21}$$

Where E is in keV and N_{H}=column density in atoms cm^{-2}.

5.3.6 Model outputs

The model outputs data in a variety of formats, including the absorbed radiation from each emission point for each snapshot, the blob positions, and the initial emission profile. This allows a range of automatic data reduction and analysis to be carried out, which culminates in:

1. Plots of the summed absorbed radiation at a given frequency.
2. Plots of the summed absorbed radiation at a given frequency folded at the orbital period and binned.
3. Plots of the summed absorbed radiation at a given frequency folded at the sidereal period and binned.
4. Lomb-Scargle periodogram of the summed radiation.
5. Plots of the locations the blobs hit the surfaces of the WD.
6. A video of the blobs hitting the surface of the WD.

The data from *HyDisc* is in the form of discrete blobs of material, this means that the flow is non-uniform. Emission from the accretion column will therefore encounter an unpredictable number of blobs on its journey to the observer. This will introduce a ‘noise’ to the absorbed radiation, which is dependant on the number of blobs in the accretion flow (this is completely arbitrary). In some respects this is analogous to the flickering seen in the light curves of IPs. In order to reduce this effect the data is generated for a several spin and orbital periods and then folded and phase binned. This allows an average value to be calculated as well as an estimate of the error based on the different values.

In each of the plots the orbital phase is defined as being zero when the primary is *closest* to the observer (i.e. when the secondary would be eclipsed if the inclination was $90°$). The intrinsic spin phase (and therefore the sidereal phase) is defined as zero when the magnetic pole (assuming one pole) is pointing away from the secondary. Each plot is at an energy of 2 keV.

A more in depth summary of some of the technical aspects of the model is given in Appendix B.

5.4 Testing the model

In order to test the model a series of tests were carried out. Throughout the testing phase, and into the results phase, often an accretion flow from *HyDisc* is needed. As Parker (2005) showed there are a *vast* number of different accretion topologies possible. In order to study the different features of the accretion flows, four well defined flows were used; disc, stream, ring and propeller not near a transition to another flow type. As noted earlier, the *HyDisc* simulations have their periods fixed, this means they do not evolve over time as IPs would be expected to. The four flows used here being well away from a transition to another flow type indicate they are well away from what may become their final equilibrium state. The rate at which they would evolve to this equilibrium is not addressed here, and so the conditions presented may represent a very short-lived stage of IP evolution. Examples of the accretion flows for a magnetic co-latitude (m) of zero are shown in Figure 5.5, and their properties in Table 5.1. In each case the data taken from *HyDisc* was after the accretion flows had settled into equilibrium states, so Figure 5.5 represents the flows after 6.28 orbital periods - the time arbitrarily defined as t_0 in the model.

The ring flow in Figure 5.5 is typical of a low m, at high m there is a significant deviation from this flow structure and it becomes rather chaotic. The other flows look very similar overall at different m, with just the close in accretion differing.

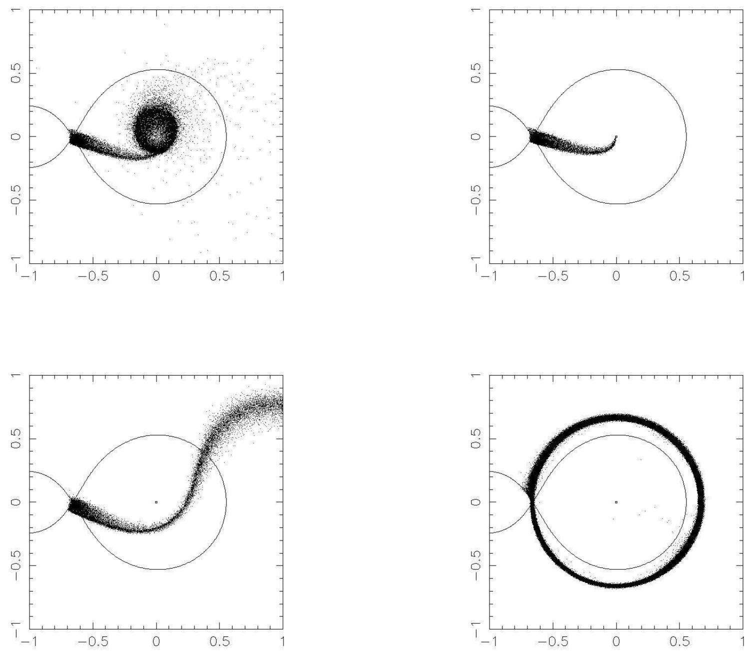

Figure 5.5: The four different simulated accretion pattern possibilities. From the top left going clockwise; a disc, a stream, a ring and a propeller. The solid line represents a line of equipotential that goes through the L_1 points. The WD is located at 0,0.

Table 5.1: Accretion flow properties as defined in *HyDisc*

	Disc	Stream	Propeller	Ring
P_{int} (s)	4000	10000	50	7000
P_{orb} (hr)	4	4	4	4
k	100	10000	100	10000000
B_{surface}[1] (MG)	2	18	9	560
M_{primary} ($M_\odot$)	0.6	0.6	0.6	0.6
q	0.5	0.5	0.5	0.5

[1] As derived from Equation 4.28.

5.4.1 Geometry tests

Intrinsic spin occultation

As a first test of the way geometry was treated in the model the orbital rotation of the system was effectively halted. This had the effect of making the WD-orbital frame coincident with the inertial frame of the observer. The mass of the blobs was also set to zero. This ensured that no absorption by the in-falling blobs occurred, any variation in the WD-orbital frame can then be apportioned to the occultation of the accretion region by the WD. To make this effect as obvious as possible the magnetic co-latitude (m) and the inclination (i) were set to 90°. The emission region was also defined as being a single point at the magnetic pole.

Figure 5.6 shows that the geometry of the system (in terms of the WD rotation) behaved as expected i.e. there was a strong modulation at the intrinsic spin period.

King & Shaviv (1984) carried out theoretical calculations of the emission profile of an accretion column with zero height from a rotating WD. Their models did not take into account of the orbital motion of the system and so tie in with the tests here. The geometry they used is that in Figure 5.7, a sample of their results is shown in Figure 5.8.

The model can define an accretion column (or columns) to reside at the magnetic poles with a cone-like structure. This consisted of a set of concentric circles centred on the magnetic poles. The number of circles, their angular extent, and the number of discrete emission points around the circles were defined as user variables. Layers of these concentric circles could be stacked on top of one another to give a cone like structure which mimics an accretion column. The model was run with a zero height accretion column with an angular extent of 11° for a variety of inclination and magnetic co-latitude angles. In each case ten concentric circles, each with eight emission points on them (plus one in the centre) at zero height (i.e. corresponding to being on the WD surface) were defined as the emission structure. The results from this are shown in Figure 5.9. The emission profiles match those predicted by King & Shaviv (1984) and thus demonstrate the intrinsic spin modulation caused by the occultation of the emission region by the WD worked as expected.

Orbital occultation

To test the orbital geometry of the system the spin variation of the WD was effectively halted by placing an emission point on the spin axis and the orbit of the binary allowed to continue. By having an inclination of 90°

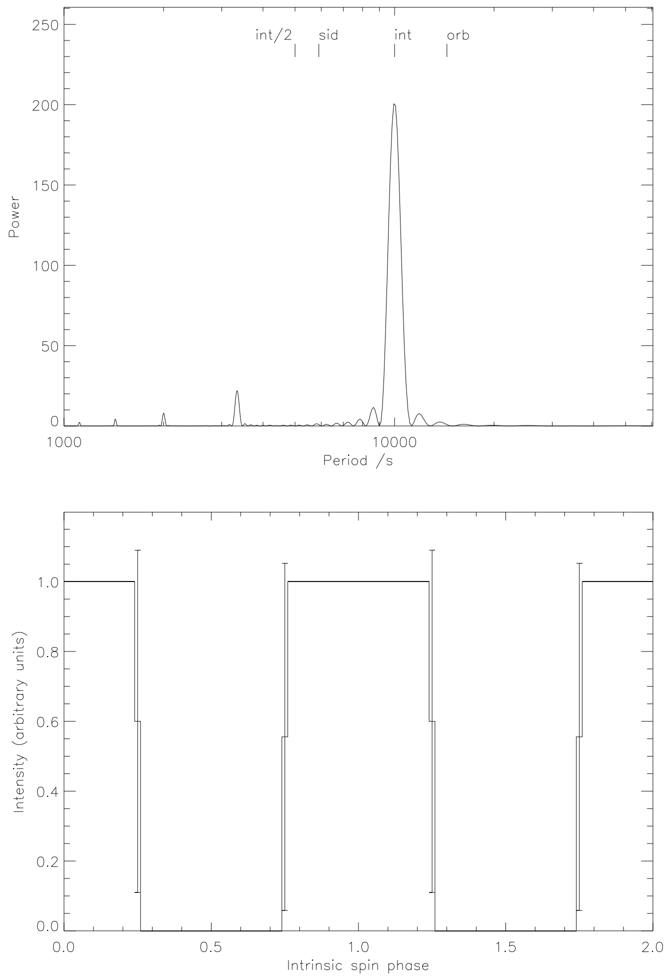

Figure 5.6: Periodogram (top) and intrinsic spin phase binned light curve (bottom) of a single emission point with no orbital modulation. Two periods are plotted.

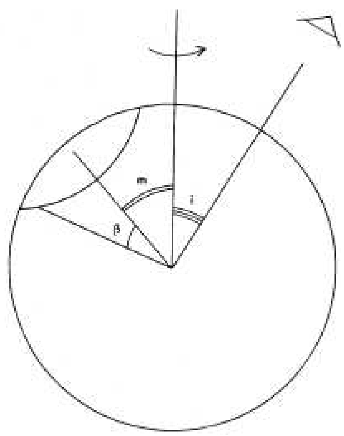

Figure 5.7: Accretion geometry used in King & Shaviv (1984).

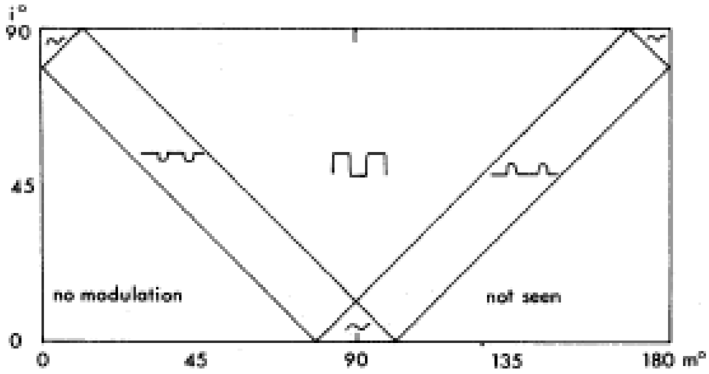

Figure 5.8: Predicted emission profiles for an accretion column with a height of zero and an angular extent (β) of 11.5° for a range of inclination and magnetic co-latitude. Taken from King & Shaviv (1984).

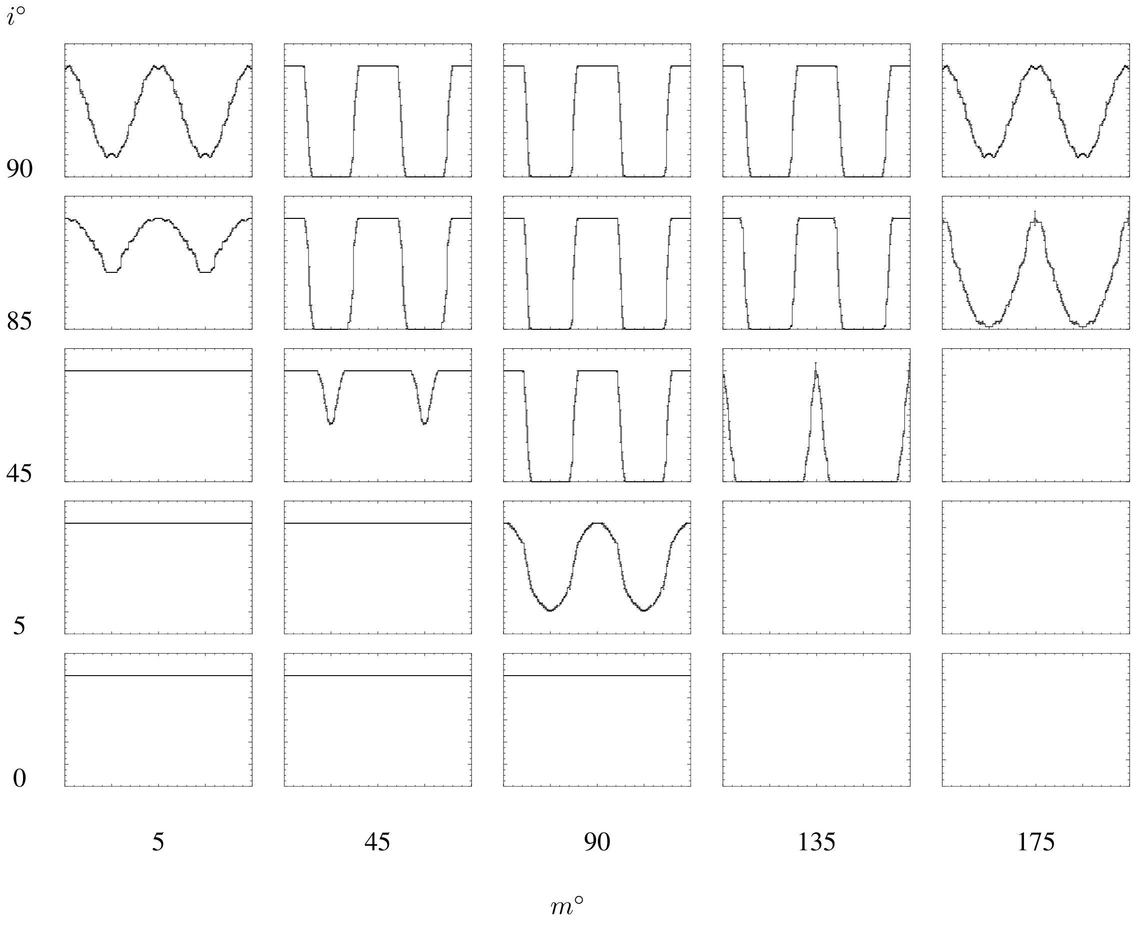

Figure 5.9: Modulation profiles of a range of magnetic co-latitude and inclination angles. The footprint was set to have a radial extent of 11°. The abscissa is the phase and the ordinate is the relative intensity. Two periods are shown for clarity.

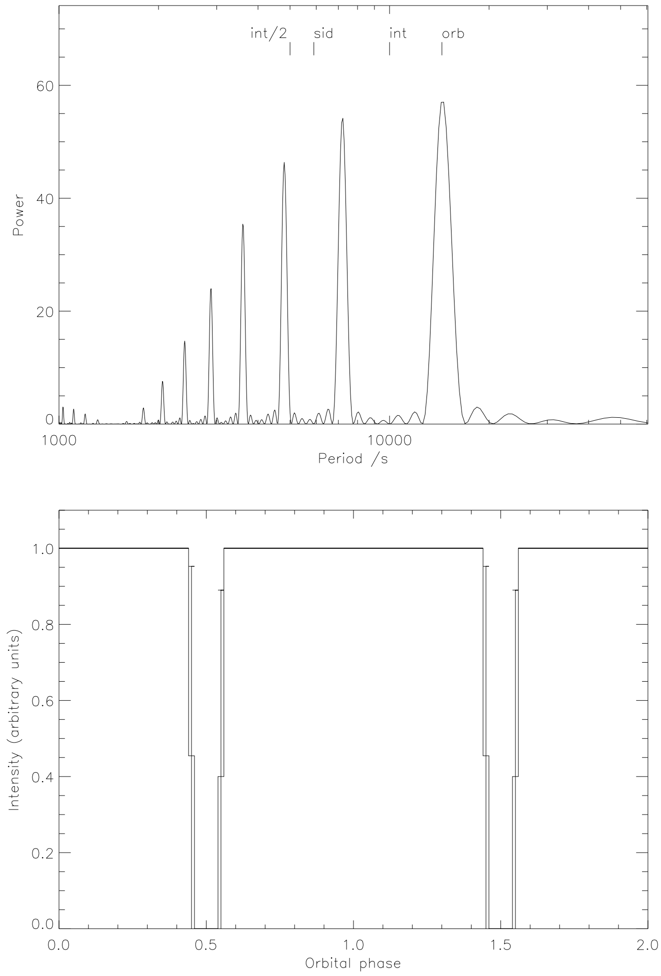

Figure 5.10: Periodogram (top) and orbital phase binned light curve (bottom) of a single emission point with no spin modulation. Two orbital periods are plotted.

the orbital geometry was tested by looking at the occultation by the secondary.

Figure 5.10 shows that geometry of the system (in terms of the orbital motion i.e. secondary occultation) behaved as expected, i.e. a coherent modulation at the orbital period. Several harmonics are seen in the periodogram, this is just a consequence of a square well being the sum of harmonics.

Combined intrinsic spin and orbital occultation

With both the WD allowed to spin and the system orbiting its common centre of mass the model was run again. This allowed a test of the combination of periods.

Figure 5.11 shows the sidereal period is present in the periodogram as expected. Note how the sidereal period is clearly present in the periodogram, but the orbital period is not. Figure 5.11 shows that variation is clearly evident in the orbitally folded data. This may be a indication that in circumstances such as the one shown here, the traditional period searching algorithms (such as the Lomb-Scargle periodogram) are inadequate for searching for orbital periods.

Combined intrinsic spin and orbital occultation with a structured emission region

Taking the single emission point a step further and using the flat emission region used earlier shows how the modulation (Figure 5.12) is very similar to the single emission point case in Figure 5.11. The only noticeable difference between the two sidereal plots is the single emission point has a much steeper ingress in egress. This is to be expected as the structured emission region will go through a phase of being partially occulted.

5.4.2 Footprint emission

To test the footprint emission points an accretion flow is needed as a starting point. Each flow type will have a different footprint as the region at which material starts to flow towards the WD is different. For illustration purposes a stream flow was used here (the different flow types are discussed later in this chapter).

A close-up of the blobs close to the WD surface is shown in Figure 5.13. Taking this a step further, the locations the blobs hit the WD surface is shown in Figure 5.14.

As a comparison with the single emission point shown above, the emission region generated from the footprint algorithm can be used with the geometry testing above (i.e. the intrinsic spin, orbital and combined plots) (see Figures 5.15, 5.16 and 5.17). It is obvious that the emission from the footprint is much more complex.

5.5 Results

5.5.1 Unabsorbed emission profiles

King & Shaviv (1984) showed how the emission profile of a WD varied due to the occultation of the emission region by the body of the WD. This work was carried out when it was thought that the emission profile could be explained solely by the occultation of the emission region. The work of Norton & Watson (1989) showed that the emission profile had a wavelength dependence, and therefore could not be due to occultation, and must

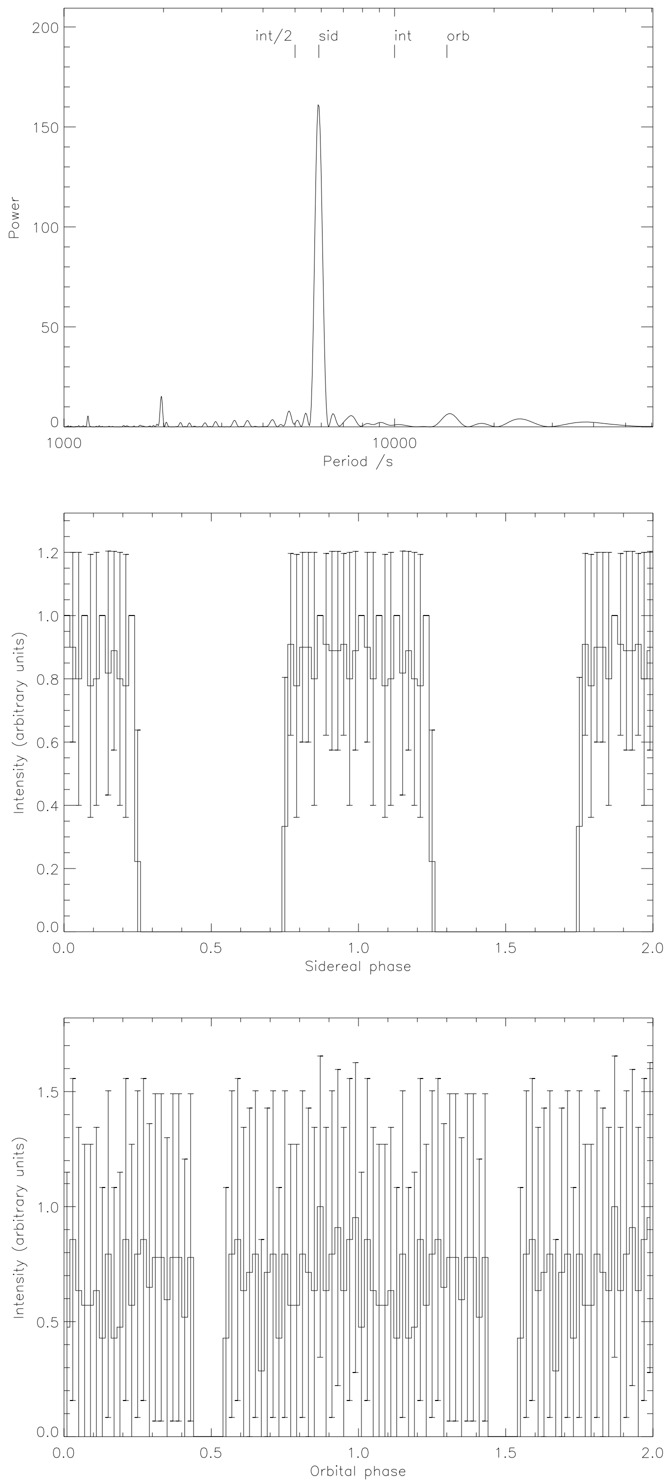

Figure 5.11: Periodogram (top), sidereal phase binned (middle) and orbital phase binned (bottom) light curves of a single emission point with spin and orbital modulation. Two periods are plotted.

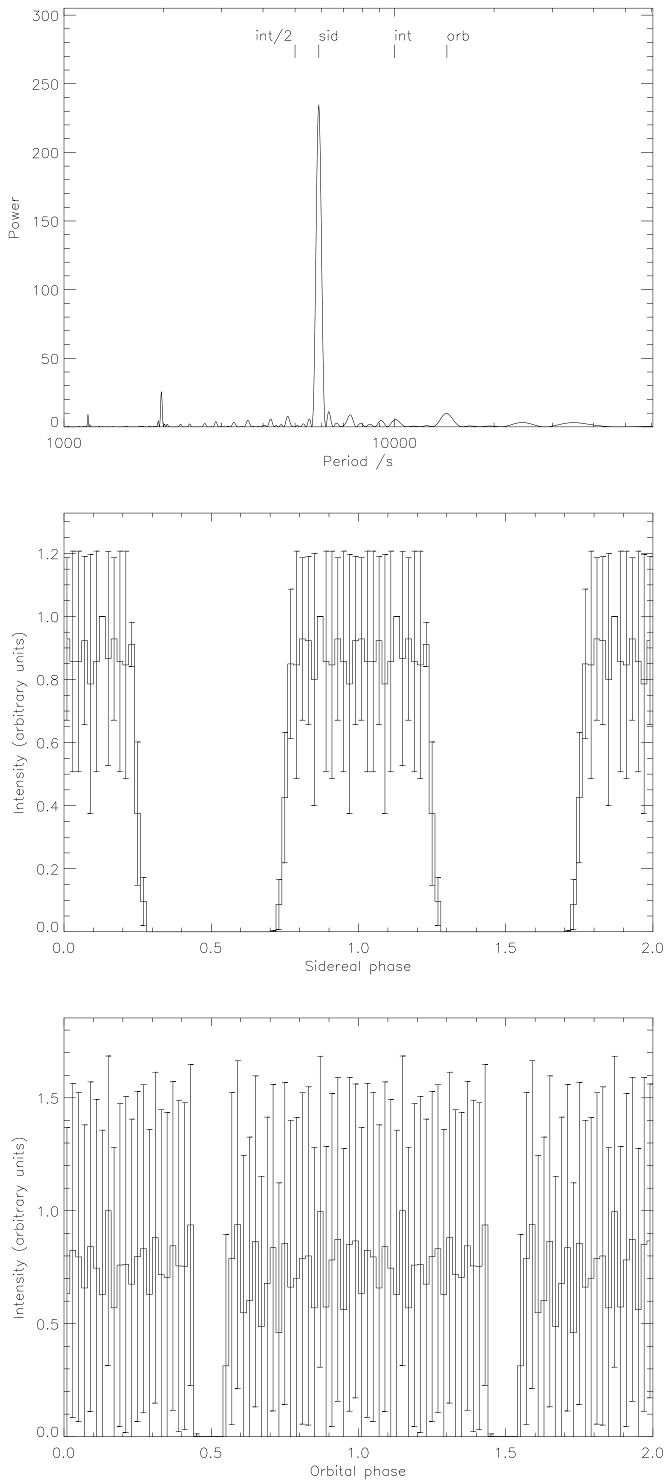

Figure 5.12: Periodogram (top), sidereal phase binned (middle) and orbital phase binned (bottom) light curves of a flat accretion column with a radial extent of 11° at an m of 90° and i of 90°. Two periods are plotted.

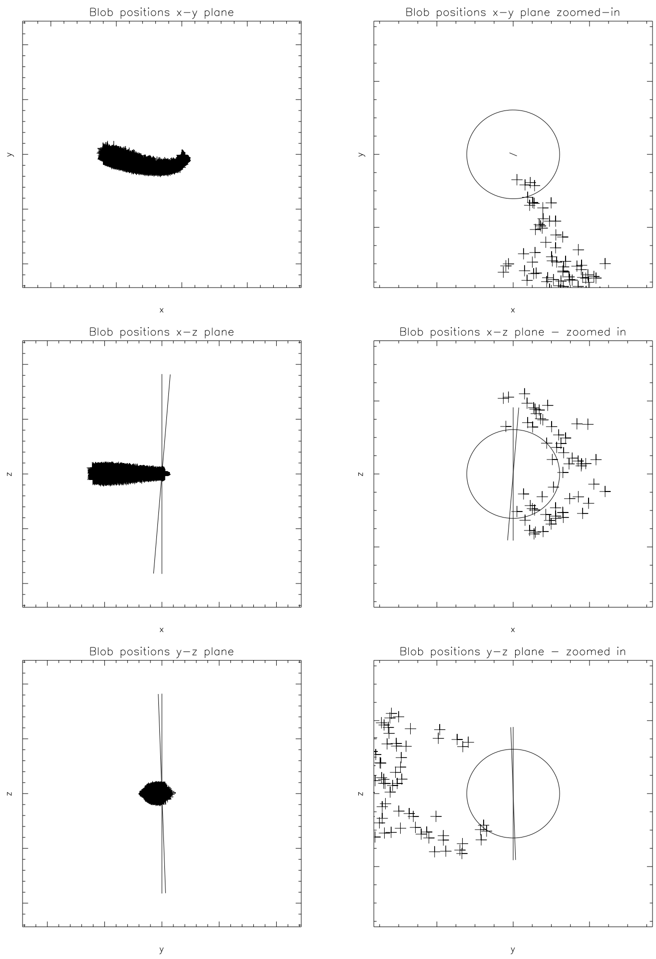

Figure 5.13: Zoomed-in plot of the positions of the blobs close to the WD, for an example snapshot of the stream flow. The vertical and near-vertical lines represent the spin and magnetic axis respectively.

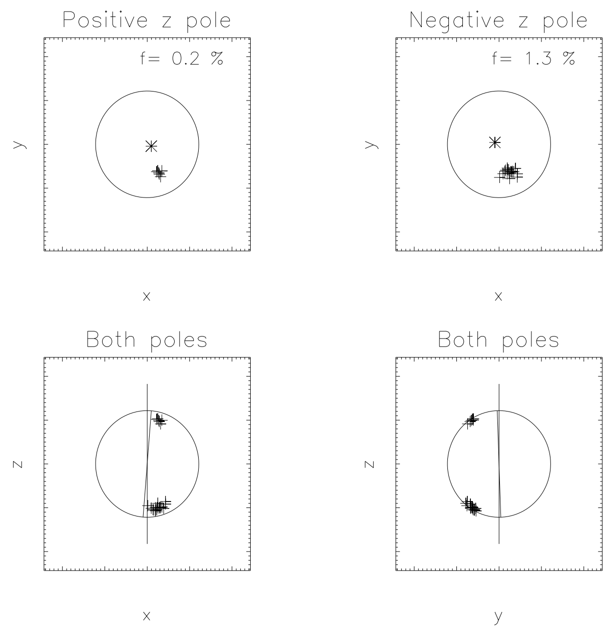

Figure 5.14: Location of the emission points on the surface of the WD from a stream flow with a magnetic co-latitude of 5°. The vertical and near-vertical lines represent the spin and magnetic axis respectively. The values of f in the top plots are estimates of the size of the footprint.

therefore be caused by absorption by the accreting material. This has allowed models where a much smaller footprint is needed and the emission region is placed above the WD surface. Occultation will still have some effect on the emission profiles in certain circumstances.

As noted earlier the accretion flow topology will feed the accretion column from different places for each flow type. The location of the footprint is therefore dependant on the flow type as well as the magnetic co-latitude. To explore this effect the model was run with emission points at a height of 1.05$r_{\rm wd}$ i.e. at a height above the surface of 5% of the WD radius for a variety of m and i for each of the flow types.

The values of m chosen ($0°$, $5°$, $45°$, $85°$ & $90°$) were such that a range of different behaviour was expected to be seen. At $m = 0°$ the magnetic axis should be aligned with the spin axis of the WD. The footprint should therefore fall on the spin axis, this should mean no modulation will be present associated with the WD spin. At $m = 5°$ the slight mis-alignment with the spin axis should result in some modulation, with this effect becoming more profound as m increases. At high m the second magnetic pole should become visible - leading to a double peaked profile at the sidereal period. As accretion will occur at both poles, there is no reason to go above $m = 90°$.

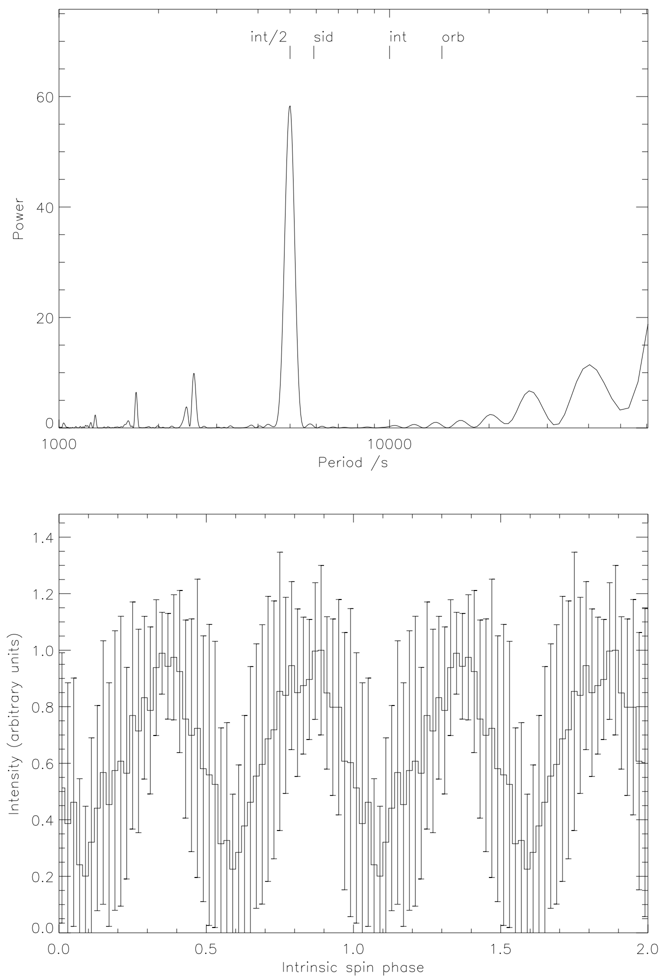

Figure 5.15: Periodogram (top) and intrinsic spin phase binned light curve (bottom) of the emission points defined by the the footprint algorithm with no orbital variation. In this case the accretion flow is a stream. Two spin periods are plotted.

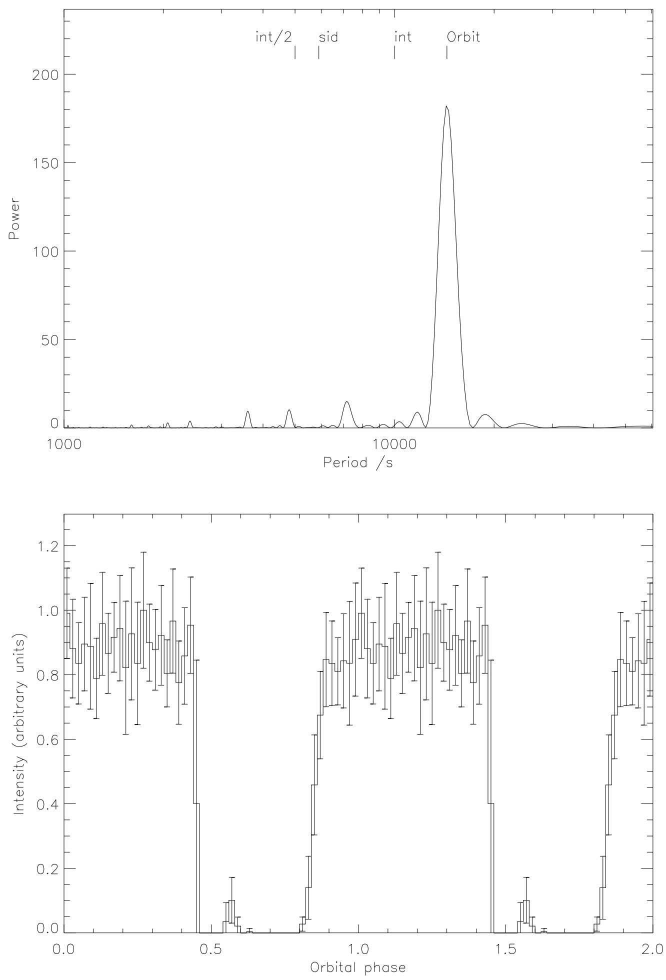

Figure 5.16: Periodogram (top) and orbital phase binned light curve (bottom) of the emission points defined by the the footprint algorithm with no spin modulation. In this case the accretion flow is a stream. Two orbital periods are plotted.

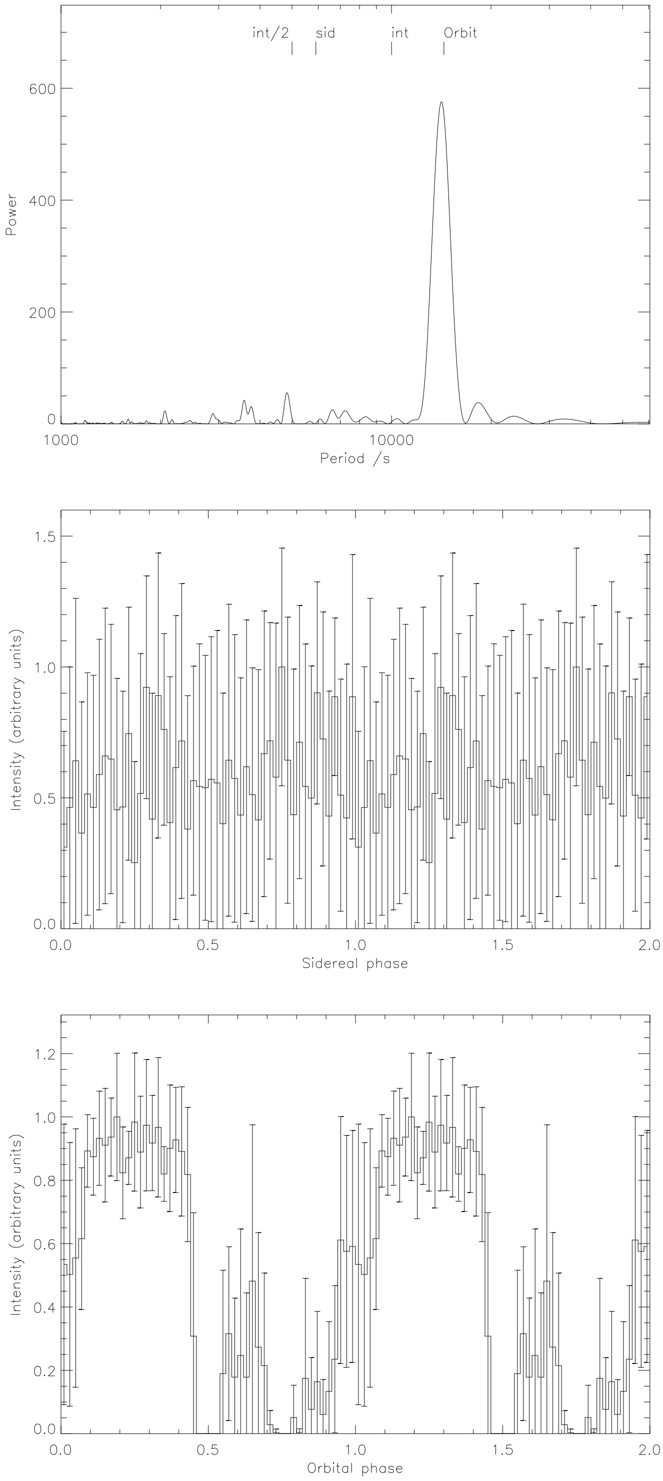

Figure 5.17: Periodogram (top), sidereal phase binned (middle) and orbital phase binned (bottom) light curves of a footprint emission region with spin and orbital modulation. Two periods are plotted.

The values of i chosen ($0°$, $5°$, $45°$, $70°$ & $90°$) were such that the observer is directly above the spin axis ($i = 0°$) and just off it ($i = 5°$), this should show any variation for the high m systems and little to no variation for the low m systems. $i = 90°$ is in the plane of the orbit, therefore occultations by the secondary should be seen, $i = 70°$ is sufficiently out of the plane that modulation caused by the accretion flow should be seen, but not the occultation caused by the secondary.

Disc

The accretion flow of the disc close to the WD is almost symmetrical in the $x - y$ plane (see Figure 5.5), this means that in general the WD can accrete material from the accretion flow at all intrinsic spin phases.

The unabsorbed sidereal modulations for the disc are shown in Figure 5.18. There is very little modulation for most of the i and m combinations. At $m = 90°$ there is a hint of a double peak profile at $i = 45°$ and $70°$. As noted above this is due to both poles becoming visible. This effect would likely also be seen when the inclination was 90°, however the eclipse by the secondary adds extra 'noise' to the folded plot. The presence of *any* double peaked modulation at the sidereal period is an indication of an asymmetry in the accretion flow, since a perfectly symmetric disc would have one pole come into view as the other goes out of view - leading to a flat emission profile. Some asymmetry is to be expected in the disc flows as the material from the secondary has angular momentum as it passes through the L_1 point, and therefore passes to one side of the disc.

The unabsorbed orbital variation of the disc accretion flow is shown in Figure 5.19. As noted above for the sidereal case the disc is a fairly uniform flow for the footprint to accrete material from. This again has the effect of giving a fairly constant emission profile for the range of i and m. When $i = 90°$ the eclipse of the secondary is seen at a phase of 0.5.

Stream

The stream flow is much more asymmetric than the disc flow (see Figure 5.5). This will have the effect that the WD can only accrete material when a magnetic pole is facing part of the flow where material is present.

The model unabsorbed emission profiles from the stream flows folded at the sidereal period, are shown in Figure 5.20. The general trend is that for low inclinations the unabsorbed emission does not exhibit coherent modulation. At higher inclinations more variation is seen, however at an inclination of 90° there is no significant coherency in the folded data (again this is due to the 'noise' introduced by the secondary occultations). The

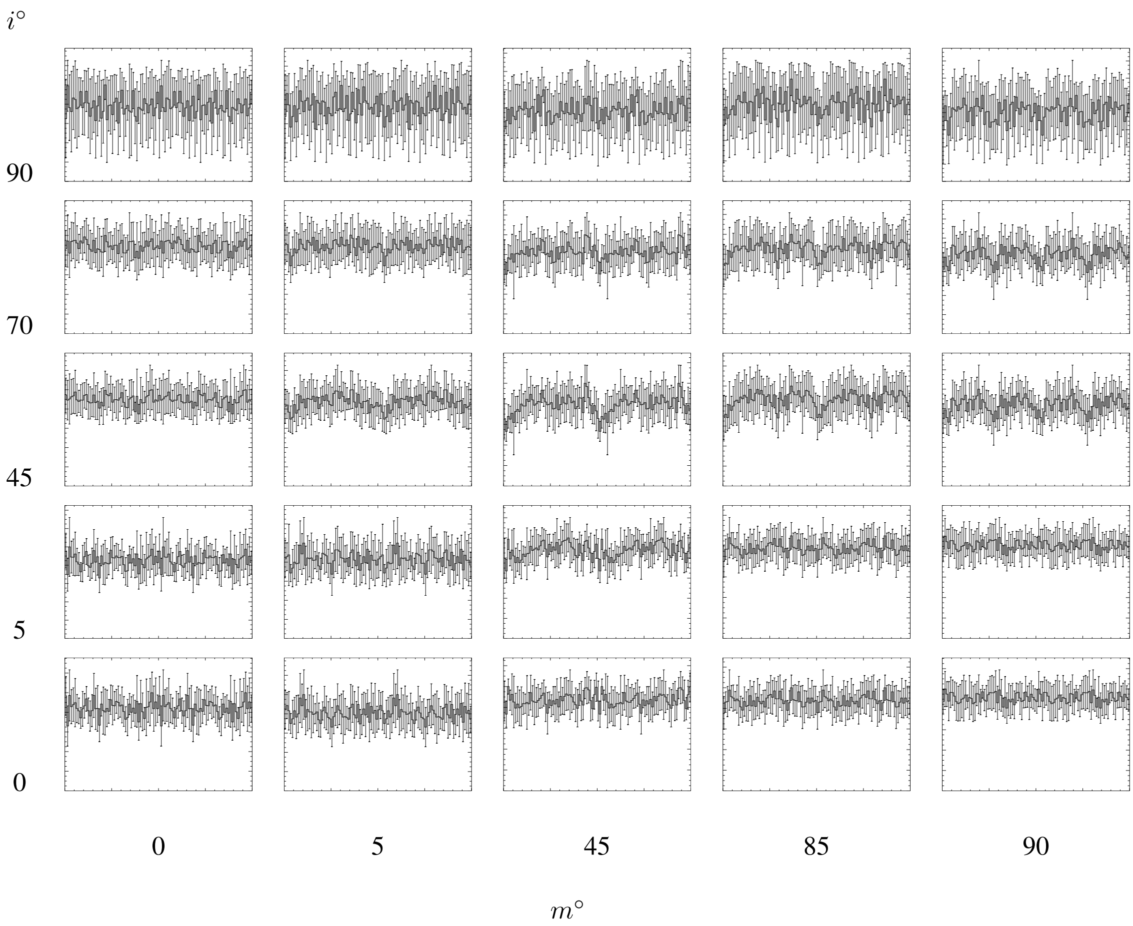

Figure 5.18: Unabsorbed sidereal modulation profiles of a range of magnetic co-latitude and inclination angles for a disc accretion flow. The abscissa is the phase and the ordinate the relative intensity. Two periods are plotted in each case.

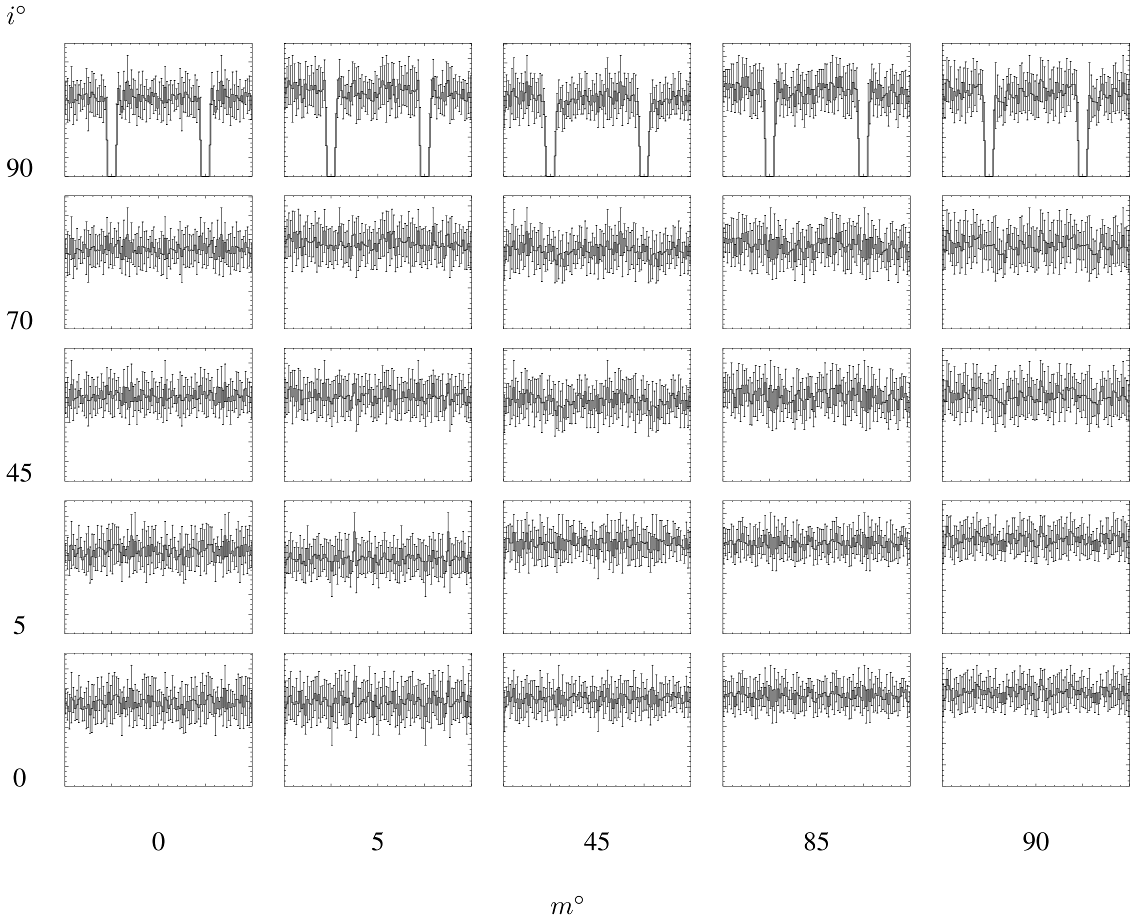

Figure 5.19: Unabsorbed orbital modulation profiles of a range of magnetic co-latitude and inclination angles for a disc accretion flow. The abscissa is the phase and the ordinate the relative intensity. Two periods are plotted in each case.

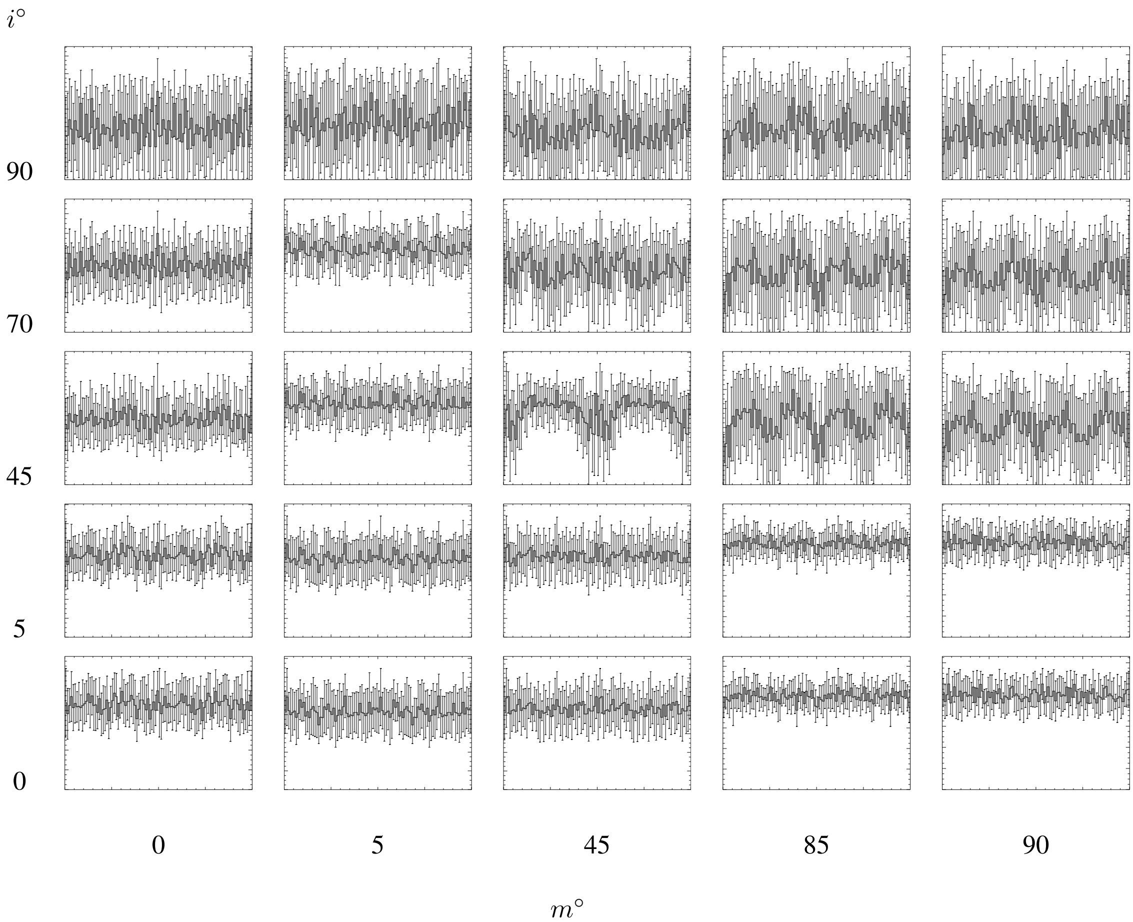

Figure 5.20: Unabsorbed sidereal modulation profiles of a range of magnetic co-latitude and inclination angles for a stream accretion flow. The abscissa is the phase and the ordinate the relative intensity. Two periods are plotted in each case.

double peak profile is more obvious in this case than it was for the disc case above. This is due to the increased asymmetry in the accretion flow.

The model unabsorbed emission folded at the orbital period is shown in Figure 5.21. The emission profiles show much more coherency than for the sidereal period. An obvious feature in the $i = 90°$ plots is the eclipse by the secondary which occurs at an orbital phase of 0.5. After this eclipse the intensity increases but then quickly drops to zero again, this can be explained as the footprint being on side of the WD closest to the stream (and hence occulted from the observer).

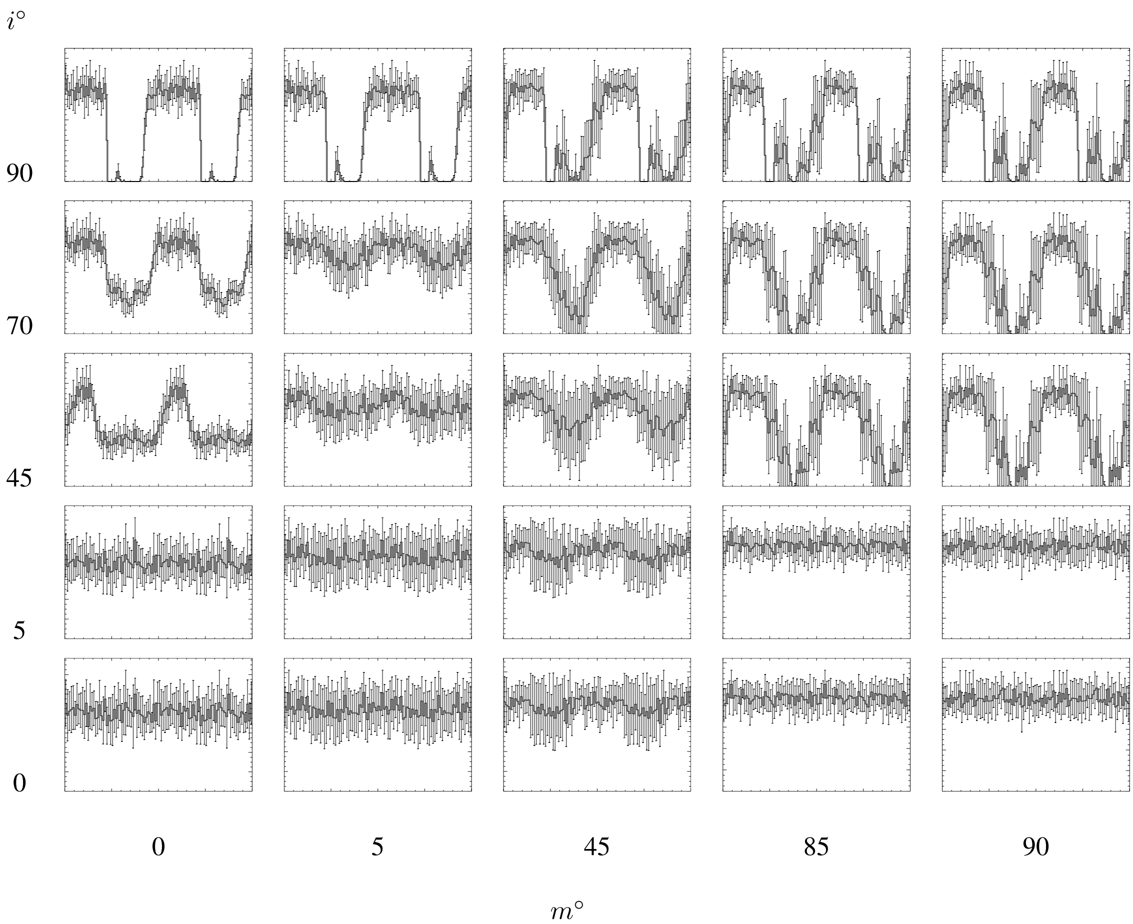

Figure 5.21: Unabsorbed orbital modulation profiles of a range of magnetic co-latitude and inclination angles for a stream accretion flow. The abscissa is the phase and the ordinate the relative intensity. Two periods are plotted in each case.

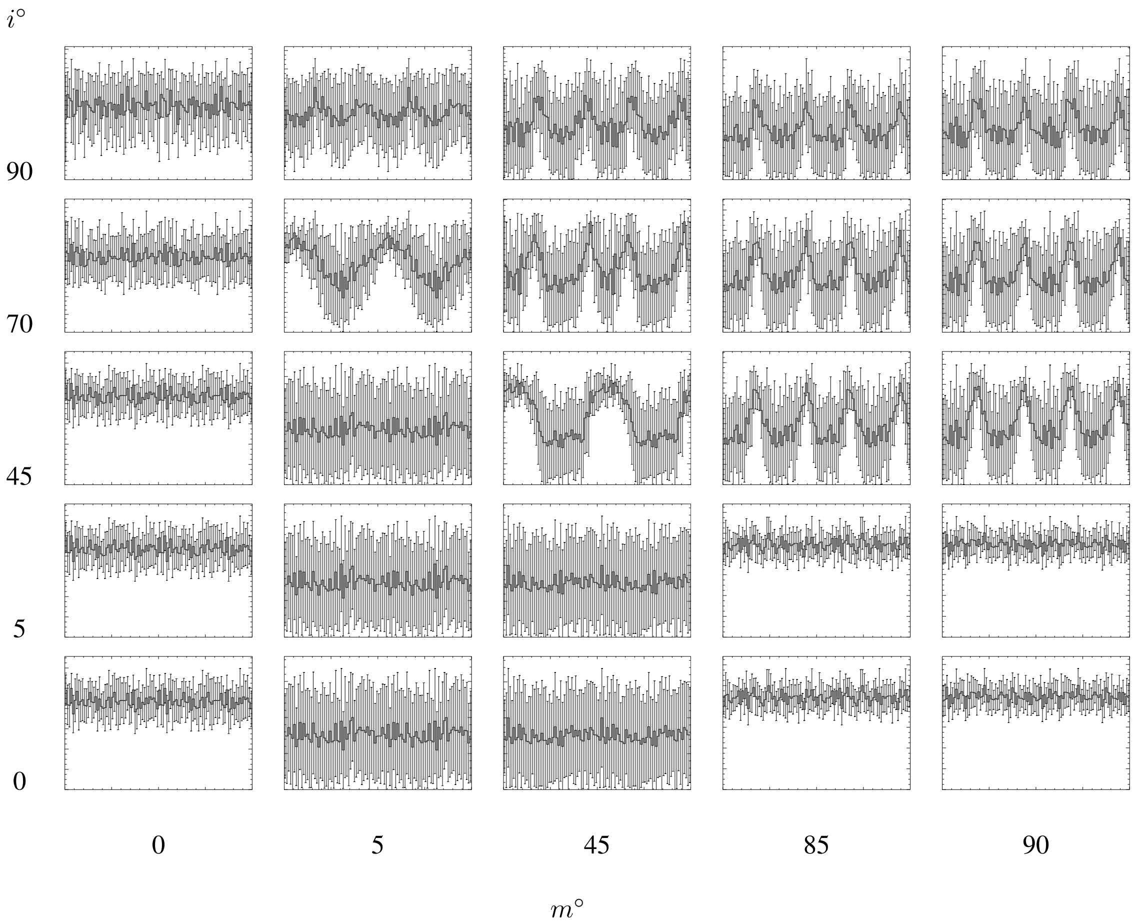

Figure 5.22: Unabsorbed sidereal modulation profiles of a range of magnetic co-latitude and inclination angles for a propeller accretion flow. The abscissa is the phase and the ordinate the relative intensity. Two periods are plotted in each case.

Propeller

The propeller is similar to the stream in that it is not symmetric (see Figure 5.5). This will again have the effect that the WD can only accrete material when the magnetic pole is facing part of the accretion flow.

The unabsorbed sidereal variation of the propellers is shown in Figure 5.22. There is no coherent modulation at the sidereal period for most of the i and m combinations. At high i and m values a double peaked structure is seen.

The unabsorbed orbital variation of the propellers is shown in Figure 5.23. Similar to the stream emission profiles, at $i = 90^\circ$ after eclipse from the secondary the intensity increases and then decreases again. This is due to the footprint being on the accretion flow side of the WD and so being obscured from view.

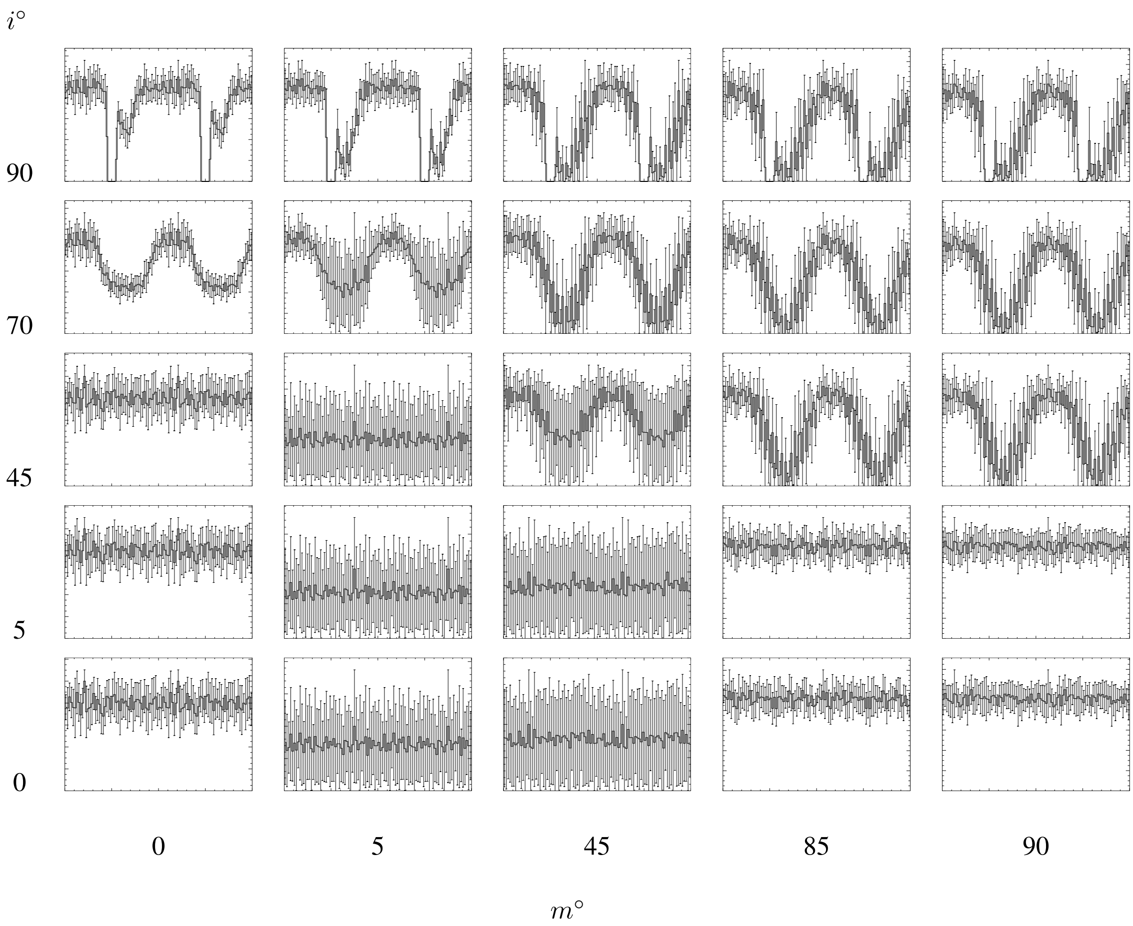

Figure 5.23: Unabsorbed orbital modulation profiles of a range of magnetic co-latitude and inclination angles for a propeller accretion flow. The abscissa is the phase and the ordinate the relative intensity. Two periods are plotted in each case.

Ring

The ring accretion flow is similar to the disc flow in that it is generally quite symmetric at low m (see Figure 5.5), however, the high magnetic field in these systems means that the blobs will generally orbit outside the Roche lobe and reaccreate onto the secondary. This has the effect of having very little material accrete onto the surface of the WD. This greatly effects the statistics used in the error estimates of the relative intensity. As such some extra caution is needed when interpreting these results.

The unabsorbed sidereal variation of the rings is shown in Figure 5.24. For $m = 0°$ there is no coherent modulation for $i \neq 90°$, but at $m = 5°$ modulation is present. This has not been the case for the other flows, and therefore shows that the footprint is very sensitive to changes in inclination for very high B. For higher m there is some hint of a double peaked modulation profile, however, as noted above, the error estimates are uncertain for this flow, and it may not therefore be real.

The unabsorbed orbital variation is shown in Figure 5.25. For low m and $i = 90°$ the emission profile is constant except for the occultations by the secondary. At higher m the emission profiles become noisy, then show a strong coherent modulation. This can be explained by the chaotic flow the ring transitions through at $m = 45$, whereas at higher m the flow is much more steady (and almost stream-like) in the orbital frame and will therefore accrete material onto the same part of the WD.

Unabsorbed emission discussion

The key result from the unabsorbed emission profile modelling is that they can vary - both at the orbital and sidereal periods. Moreover the variation seen is dependent on the accretion flow type. This has the consequence that the observed absorbed emission from IPs is not necessarily due to just photoelectric absorption, but in fact it depends on the flow type as well.

The next section takes this a step further and carries out the full photoelectric absorption expected to occur in IPs.

5.5.2 Absorbed emission profile

The model was then run in a similar way to the previous section, except the mass of the blobs was not set to zero. This allowed the full treatment of the emission profile and thus the best indication of what the true observed emission profile looks like. The ring accretion was not explored as the number of blobs hitting the

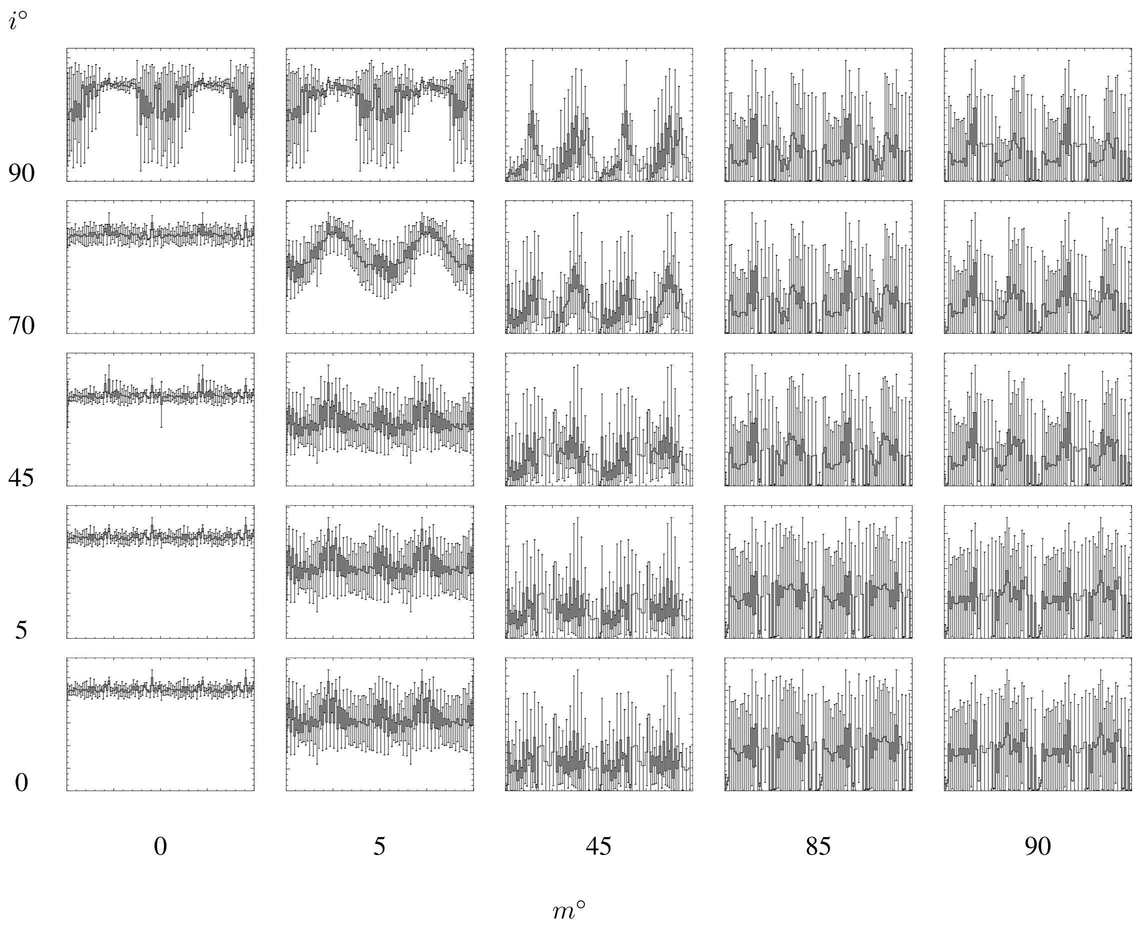

Figure 5.24: Unabsorbed sidereal modulation profiles of a range of magnetic co-latitude and inclination angles for a ring accretion flow. The abscissa is the phase and the ordinate the relative intensity. Two periods are plotted in each case.

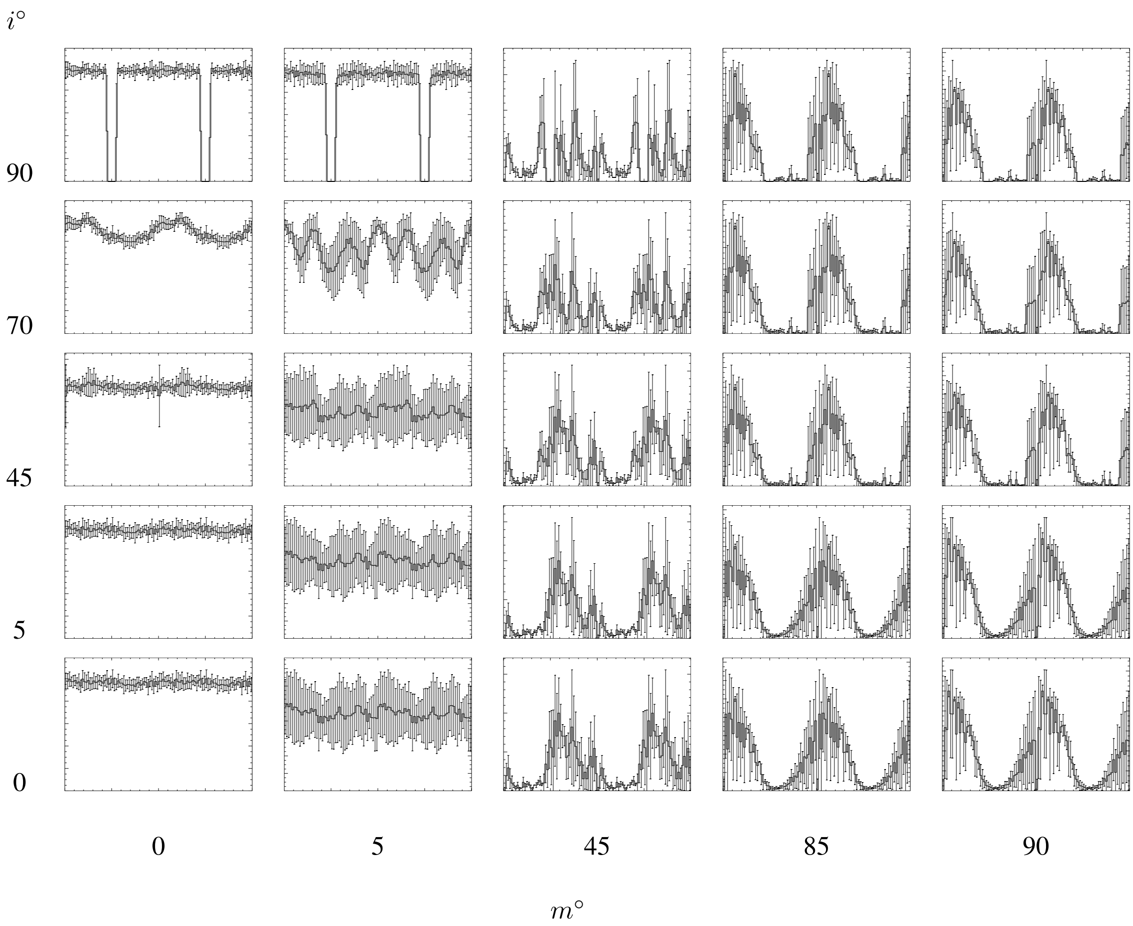

Figure 5.25: Unabsorbed orbital modulation profiles of a range of magnetic co-latitude and inclination angles for a ring accretion flow. The abscissa is the phase and the ordinate the relative intensity. Two periods are plotted in each case.

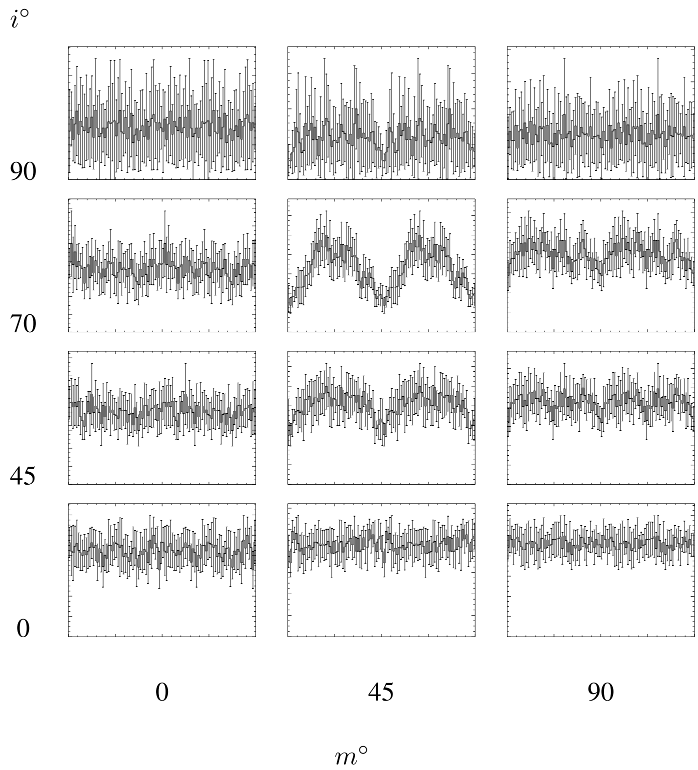

Figure 5.26: Absorbed sidereal modulation profiles of a range of magnetic co-latitude and inclination angles for a disc accretion flow. The abscissa is the phase and the ordinate the relative intensity. Two periods are plotted in each case.

surface of the WD was so low.

Unfortunately the model takes a lot of CPU time to run, and as a consequence not as much of parameter space can be explored as was for the previous section. The values of the inclination looked at were $0°$, $45°$, $70°$ and $90°$. The values of the magnetic co-latitude were $0°$, $45°$ and $90°$.

Disc

The absorbed sidereal emission from the disc flow is shown in Figure 5.26. As in the unabsorbed case (Figure 5.18) there is no coherent modulation for any inclination at $m = 0°$. For $m = 45°$ $i = 45°$ and $i = 70°$ coherent modulation is present. Some modulation was seen in the unabsorbed case for $m = 45°$ $i = 45°$, but here it is seen to a greater extent. The $i = 70°$ case is significantly deeper than the $i = 45°$ case, and must result from photoelectric absorption. There is a hint of a double peaked profile in the $m = 90°$ case, as was seen in the unabsorbed emission profile.

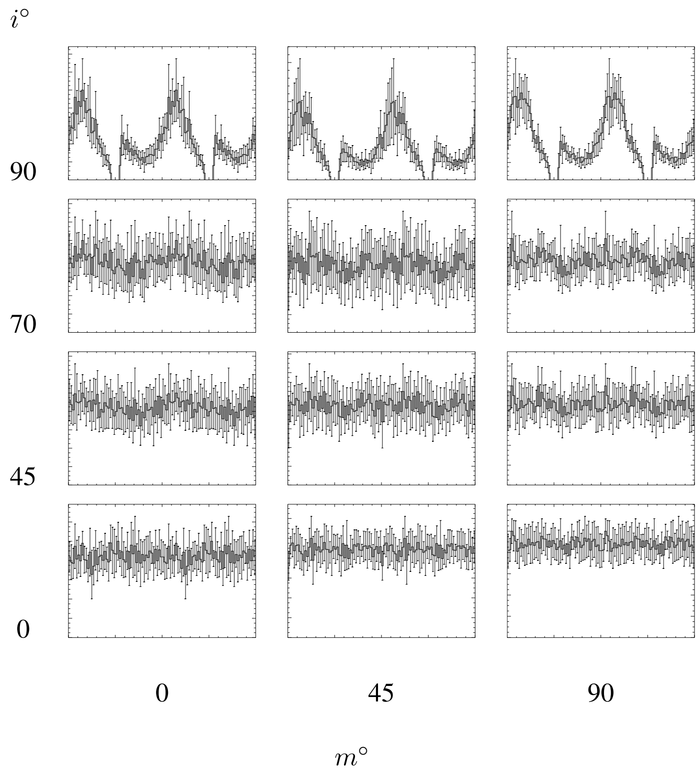

Figure 5.27: Absorbed orbital modulation profiles of a range of magnetic co-latitude and inclination angles for a disc accretion flow. The abscissa is the phase and the ordinate the relative intensity. Two periods are plotted in each case.

The absorbed orbital emission from the disc flow is shown in Figure 5.27. As in the unabsorbed case (Figure 5.19) for low inclination there is little modulation. At $i = 90°$ a complex modulation structure is seen which includes the occultation by the secondary at phase 0.5. Given that the unabsorbed case was constant (other than for the secondary occultation) this modulation is due solely to photoelectric absorption, and therefore is a reflection of the column density of the disc. The unabsorbed case gave an indication of an asymmetric disc from the sidereal modulation seen, this is also seen here in the structure seen in the orbital modulation.

Stream

The absorbed sidereal emission from the stream accretion flow is shown in Figure 5.28. As in the unabsorbed case (Figure 5.20) there is no coherent modulation for any inclination at $m = 0°$. The $m = 45°$ shows some modulation at the sidereal period for $i = 45°$ and $i = 70°$. Also at $m = 45°$ a hint of a double peaked modulation is seen. This modulation is very similar to the unabsorbed case implying that photoelectric

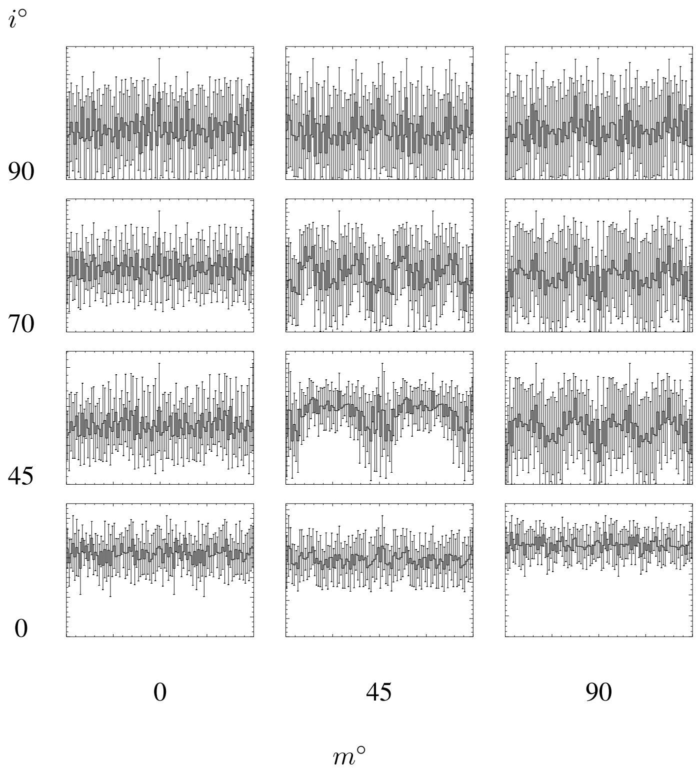

Figure 5.28: Absorbed sidereal modulation profiles of a range of magnetic co-latitude and inclination angles for a stream accretion flow. The abscissa is the phase and the ordinate the relative intensity. Two periods are plotted in each case.

absorption has very little effect on the sidereal modulation in stream flows.

The absorbed orbital emission from the stream flow is shown in Figure 5.29. All of the flows are very similar to the unabsorbed case (Figure 5.21) which further adds to idea of absorption not being a significant factor in the stream flows. One exception to this is for $m = 0°$, $i = 45°$, where at a orbital phase of ~ 0.75 the intensity starts to drop, almost to zero by zero phase. This is due to the accretion stream close to the WD obscuring the line of sight.

Propeller

The absorbed sidereal emission from the propeller accretion flow is shown in Figure 5.30. As in the unabsorbed case (Figure 5.22) there is virtually no modulation at $m = 0°$. At $m = 45°$ $i = 45°$ the absorption is such that the absorbed and unabsorbed cases are anti-phase. This can be explained as the part of the flow which is closest to the WD (and therefore the part accreting onto the WD) is also the densest part of the flow, hence the

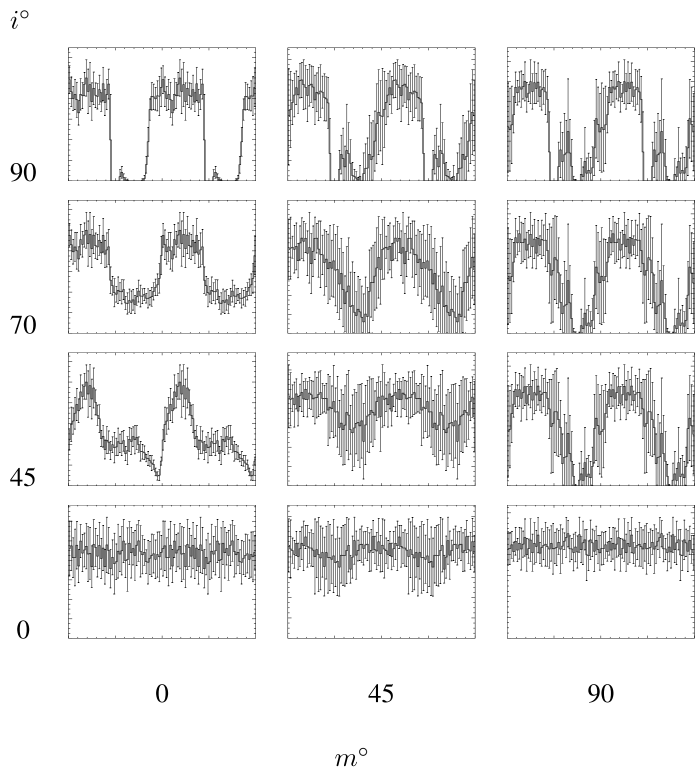

Figure 5.29: Absorbed orbital modulation profiles of a range of magnetic co-latitude and inclination angles for a stream accretion flow. The abscissa is the phase and the ordinate the relative intensity. Two periods are plotted in each case.

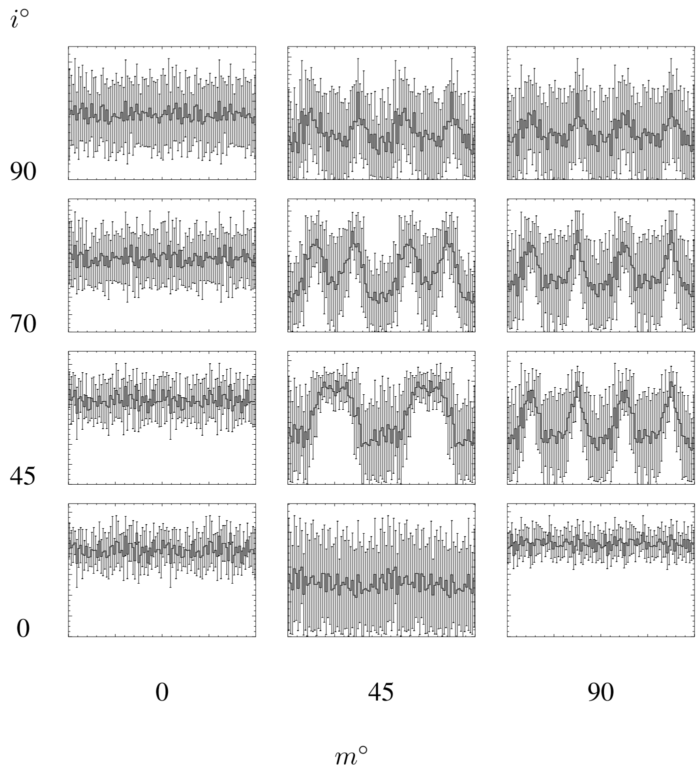

Figure 5.30: Absorbed sidereal modulation profiles of a range of magnetic co-latitude and inclination angles for a propeller accretion flow. The abscissa is the phase and the ordinate the relative intensity. Two periods are plotted in each case.

absorption will be greatest. For $m = 90°$ the modulation is very similar to the unabsorbed case (Figure 5.22), this again implies that absorption plays a minor role at these angles.

The absorbed orbital emission from the propeller flow is shown in Figure 5.31. The $m = 45°$ flows are very similar to the unabsorbed case (Figure 5.23). The $m = 0°$ emission profiles show significantly different features. The $i = 90°$ emission profile has a second dip in it after the secondary occultation at a phase of ~ 0.8, this can be identified as being when the line of sight is along the main arm of the propeller. The $i = 45°$ case shows hints of the secondary dip as in the $i = 90°$ case for $m = 0°$. The $m = 90°$ emission profiles are very similar to the unabsorbed case.

Absorbed emission discussion

The absorbed disc emission profile followed what was expected and showed modulation at the sidereal period arising from photoelectric absorption. This is the traditional picture of accretion around IPs and is used as a

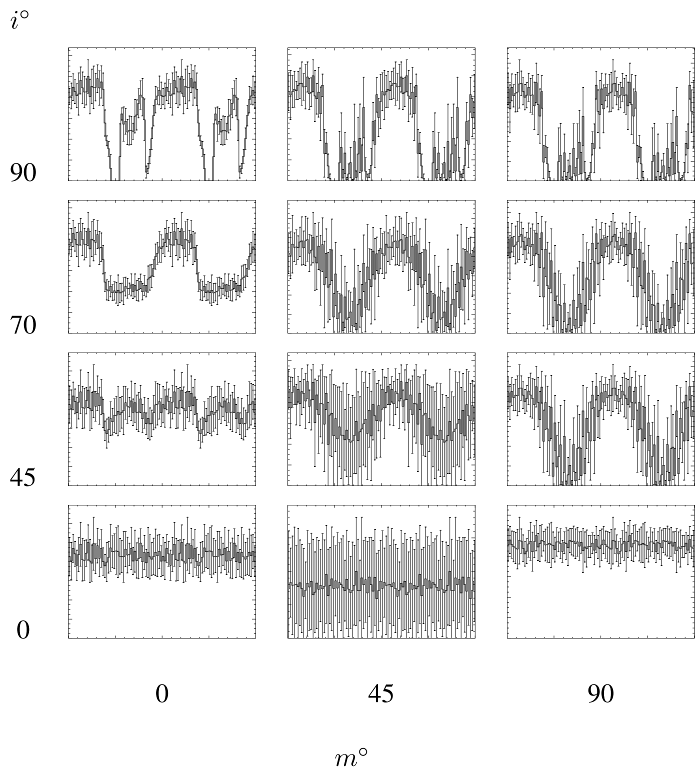

Figure 5.31: Absorbed orbital modulation profiles of a range of magnetic co-latitude and inclination angles for a propeller accretion flow. The abscissa is the phase and the ordinate the relative intensity. Two periods are plotted in each case.

defining feature (via the increasing modulation depths at lower energies) for their classification. The lack of modulation introduced in the stream case by the accreting material was unexpected and indicates that the use of photoelectric absorption as a defining feature may be too stringent. As such the true population of stream-fed IPs may be under-reported. The propeller flows sit somewhere between the disc and stream flows, in that they have some features at some orientations that are caused by photoelectric absorption, and others that are not. This too will likely have the effect of the propeller population of IPs being underestimated due to the lack of photoelectric absorption seen.

The presence of a sidereal modulation may be linked to an asymmetry in the accretion flow, since a completely symmetric flow would give zero modulation in the emission profile. As such it is possible that, with further development work, this effect could be exploited to gauge the nature of the accretion flow.

5.6 Conclusion

The model has shown that the unabsorbed emission profile may vary with both the orbital and sidereal phase in all four accretion flow types. Moreover the characteristics of the variation are dependent on the flow type. This then forms the basis for the absorbed emission profile, which is a result of the unabsorbed emission profile being absorbed by a column density, which itself is dependent on the flow type.

The decoupling of the modulation caused by the location and visibility of the footprint in the unabsorbed case and the modulation caused by absorption has allowed a scenario where modulation is possible without photoelectric absorption. This raises serious questions as to the use of photoelectric absorption (in the form of an increasing modulation depth with decreasing energy) features as a legitimate requirement for IP classification. Certainly the presence of it is a sign of IP-ness, but the lack of it should not necessarily mean the rejection of a candidate.

5.7 Future work

The nascent model is still in its infancy, as such there are numerous developments and studies that would enhance the results produced so far. Assuming the author can find the time, planned enhancements include:

1. An added neutral H absorption based on interstellar absorption.

2. Make the emission region closer to reality by equating the total intensity from the discretized points to an observed amount in order to make the intensity more physical.

3. An investigation of the size of the footprint as a function of m would help explain the unabsorbed emission profile.

4. Analogously the size of the footprint as a function of phase (both orbital and sidereal) may prove useful.

5. Ultimately the model will be used as a way of estimating the unknown/unmeasurable parameters of IPs by matching the observed light curves to those it generates.

6. Couple the accretion flow to the Bremsstrahlung emission to achieve a full multi-temperature, multi-density emission profile.

7. Investigate the effect of a non-uniform density of the blobs.

Chapter 6

Concluding remarks

The aim of this thesis was to explore the nature of intermediate polars in a variety of ways, based on the accretion processes occurring close to the white dwarf. In this study theoretical modelling combined with observational data have been used to achieve this aim.

6.1 The circular polarization observations of IPs

The accretion process is heavily dependent on the magnetic field strength of the white dwarf. The *only* way to directly measure the magnetic field strength is with circular polarization measurements. The circular polarization survey in Chapter 3 began by reviewing the field as it currently stands. This was an important task as the techniques used and the style of reporting the data have changed dramatically over time. This has lead to a situation where there is no consistency in the results from different projects. Moreover the nature of the analysis of some targets essentially renders any conclusions meaningless. This is demonstrated well by the tendency of reporting an average circular polarization value for an observing run. If a target exhibits both positive and negative circular polarization in a given waveband, modulated at the spin period, then the average value may be zero, thus masking all the meaningful data.

The circular polarization survey of intermediate polars initiated here aimed to address this problem by surveying as many targets as possible in a *consistent* way. This survey looked at eight targets in the Northern sky over three nights in 2006 using TurPol at the Nordic Optical Telescope on La Palma.

Two targets showed significant circular polarization which varied at the spin period. These were both relatively newly classified intermediate polars (1RXS J173021.5–055933 and 1RXS J213344.1+510725). Both these targets are also *INTEGRAL* sources, and so hard X-ray emitting systems. This follows a trend found when reviewing previous measurements that the systems which exhibit a large circular polarization also tend to be hard X-ray sources. There also seems to be a trend of the soft X-ray sources tending to be sources of strong circular polarization. We suggest that perhaps the magnetic field is being suppressed by a high accretion rate in the accretion column and that those systems with a soft X-ray component have some of the accreting material bypass the column and therefore the suppression is less.

Five of the remaining six targets showed some degree of circular polarization (DQ Her, V1223 Sgr, V2306 Cyg, FO Aqr and AO Psc), with the last (AE Aqr) showing none. Overall these measurements compare well to the previous measurements (where they have been done in a way which allows comparison with this data), in that a low level of circular polarization is generally present, with a minority showing a much larger degree of of it.

6.2 X-ray observations of IPs

RXTE time was granted for six hard X-ray selected candidates that had been seen with either *INTEGRAL* or *Swift*. Each target had suitable optical properties to be classified as an intermediate polar, but was lacking an X-ray modulation that would confirm this classification. Hard X-ray selected candidates were chosen as the current population is generally soft X-ray selected, and this may lead to a bias in the population.

Each target was searched for periodic variation in multiple energy bands. Where variation was found the characteristics of photoelectric absorption were looked for. Spectral models were also fitted to the data to see if it corresponded to a intermediate polar like emission process.

Of the six targets three were confirmed as intermediate polars showing coherent modulation at a period that could be reconciled with the spin period of the system (SWIFT J0732.5–1331, XSS J00564+4548 and IGR J15094–6649). Two were classified as likely intermediate polars, but were missing some of the characteristics required to confirm them (XSS J12270–4859 and IGR J17195–4100). The final one was classified as a likely polar (IGR J14536–5522).

The three confirmed intermediate polars do not appear to be significantly different than the existing population. Based on this very small sample this indicates that the hard X-ray selected population is no different than the soft X-ray selected one.

6.3 Accretion flow topology simulation

Using the magnetic field strength typical of systems that produce the levels of circular polarization seen in Chapter 3, the *HyDisc* simulation was used to investigate the accretion flow topology seen around IPs.

HyDisc is a magneto-hydro-dynamical code written to simulate the accretion flow in intermediate polars. By varying the inputs, parameter space was explored and accretion flow topologies characterized. There are four main types of accretion topology - a disc, a stream, a ring and a propeller. The stream is a net accretor of material, and so the angular momentum increases (therefore the white dwarf spins up) over time. The propeller does the opposite and centrifugally ejects material, the white dwarf therefore spins down. The disc and ring flows can sit in the middle and have a net angular momentum change of zero, and so can maintain the white dwarf spin rates. The distribution of these flow topologies is such that there exist points where disc, stream, and propeller flows can be located in very close proximity in parameter space. The same is also true for the disc, propeller and ring flows. These regions were dubbed ‘triple points’, the disc one being labelled as the lower triple point and the ring as the upper.

These triple points were found to vary as a function of the mass ratio of the system, moreover the lower triple point was well described by setting the co-rotation radius equal to the circularization radius. This is consistent with the equilibrium condition suggested by King & Wynn (1999). King & Wynn (1999) also suggested a second equilibrium condition when the co-rotation radius equals the distance to the inner Lagrange point. The upper triple point here was found to be 1.2 times the distance to the inner Lagrange point.

Consideration of the spin and orbital periods of known IPs indicated that most systems lie close to the lower triple point in the spin-orbital plane of parameter space. Those which deviate from this tend to be systems which are known to be out of equilibrium - such as AE Aqr.

6.4 Light curve simulation

The modelling in Chapter 4 was taken a step further in Chapter 5, with the development of a new program that takes the output from *HyDisc* (i.e. the accretion flow topologies) and simulates light curve from it. The ultimate aim of this being to take a measured light curve, then using the known systemic parameters, explore free parameter space to create synthetic light curves that match the measured one. By doing this, the free (potentially unmeasurable) parameters of the system may be constrained.

The model is still in the early stages of development, but has already yielded some interesting results. The model runs in two main steps, firstly it calculates the emission location and profile of the accreting material close to the white dwarf, based on the accretion flow topology. Then the emission profile is absorbed along a line of sight to a fictional observer outside of the system, the column density along this line of sight being used to calculate the absorption.

By approaching the modelling in this two stage process the dependence of the emission profile on the accretion flow topology was explored. The different accretion flow types seed the accretion column from different regions e.g. the disc can accrete material at all spin phases, but the propeller can only accrete material when the WD is facing part of the flow close in. The overall trend here was that the more symmetric accretion flows (i.e. the disc and ring), which can seed the accretion column from all phases do not produce much variability in the unabsorbed emission profile. The less symmetric ones (i.e. the stream and propeller), do show significant variability phased at the spin and orbital periods of the system. It is this modulation that would be present if no absorption occurred from the accreting material.

In the case where absorption by the accreting material does occur, the disc and ring flows show significantly more modulation than in the unabsorbed case. The stream and propeller flows do not show a great deal more than from the unabsorbed case. This implies that disc and ring systems would show the photoelectric absorption characteristic that is seen as an essential aspect in the classification of intermediate polars. The stream and propeller showing little extra variation from the absorption would not show this photoelectric absorption characteristic. This has a significant consequence on how intermediate polars are classified, it is likely that many streams and propellers are being wrongly disregarded at legitimate intermediate polars based on the lack of photoelectric absorption. Given that ring accretion flows tend to be from the very high end of the magnetic field strength scale, this means that disc accretion flow intermediate polars are much more likely to be classified as legitimate members and the whole population is therefore very likely biased towards this.

6.5 Future work

This thesis has begun the task of unravelling the true nature of intermediate polars, but there is still scope for continued investigation.

The optical circular polarization survey needs to be extended to cover more systems, so a more complete picture of the magnetic field strengths can be gained. This process is ongoing with the successful procurement of data of new targets that extend the work presented here.

Spectro-polarimetry is also a route that should be explored. The new X-Shooter instrument on the VLT is powerful enough that cyclotron harmonics should be observable. This would allow unambiguous fitting of the cyclotron emission to a magnetic field strength.

The *RXTE* classification program has been extended and eight targets were granted time in cycle 13. Seven of these have been taken and analysed and one so far shows strong signs of being classified as an intermediate polar. It is likely that this particular investigation will stop here, as most of the hard X-ray candidate intermediate polars have now been investigated.

The light curve modelling is in its early stages of development, but future work will allow it to investigate how the footprint varies in size and location for different parameters for each accretion flow type. This could give a much better general understanding of how the accretion column forms on the white dwarf.

The ultimate aim of the light curve model is still to be able to constrain some of the unknown parameters in existing intermediate polars. This requires a significant time investment as *HyDisc* (the input to the model) is time consuming to run for an exploration of parameter space.

Whilst all of the assumptions used in *HyDisc* are still valid today, the program itself is ageing. As such it would benefit from a major rewrite to use some more modern computing techniques. The underlying way it treats each blob is a pseudo N-body type simulation that could be highly parallelized to run on a cluster. This speed up would allow a much greater number of blobs per run, and thus a much finer detail in the accretion flows. Alternatively, if the code were sped up and coupled to the light curve modelling program written here, then the two could be used as an *automatic* light curve fitting suite. This would allow an X-ray light curve to be input to the program, along with the known parameters, and then the program allowed to explore parameter space in such a way as to fit a simulated light curve to the measured light curve. Obviously there is a significant amount of work involved in getting to this stage.

With the continuation of this observational and theoretical modelling work the true nature of intermediate polars is being unveiled, and a much deeper understanding is finally within grasp.

The End.

Appendix A

Energy resolved light curves

This appendix shows the energy resolved light curves of each of the energy bands used in Chapter 2 for the modulation depth profiling.

A.1 J0056

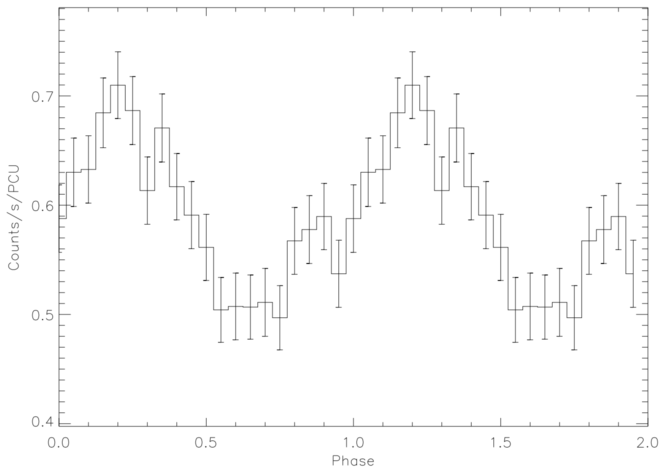

Figure A.1: 2–4 keV light curve of J0056 folded at the 465.68 s pulse period with an arbitrary zero point. Two cycles shown for clarity.

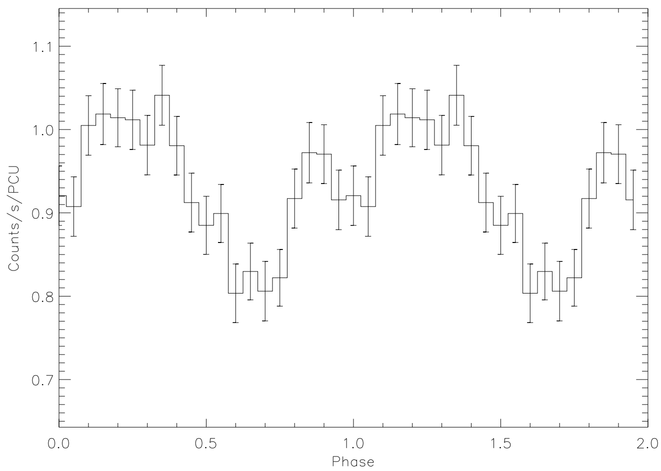

Figure A.2: 4–6 keV light curve of J0056 folded at the 465.68 s pulse period with an arbitrary zero point. Two cycles shown for clarity.

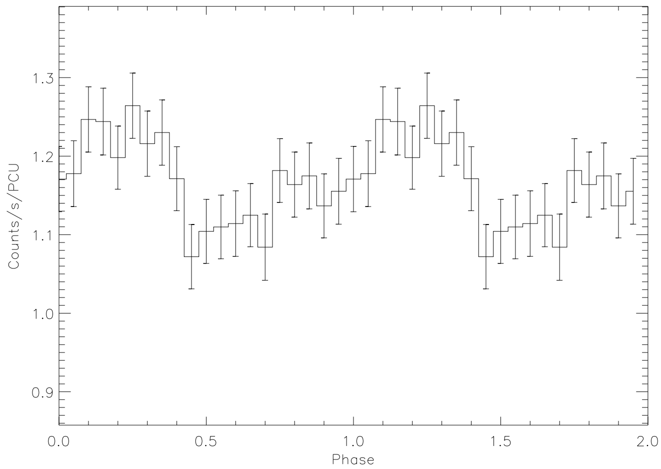

Figure A.3: 6–10 keV light curve of J0056 folded at the 465.68 s pulse period with an arbitrary zero point. Two cycles shown for clarity.

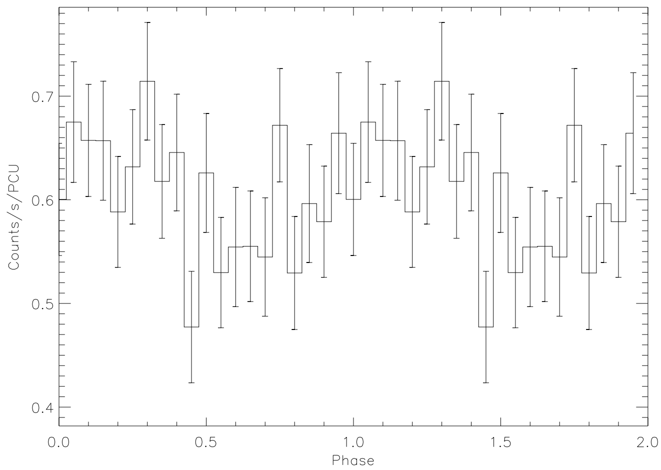

Figure A.4: 10–20 keV light curve of J0056 folded at the 465.68 s pulse period with an arbitrary zero point. Two cycles shown for clarity.

A.2 J0732

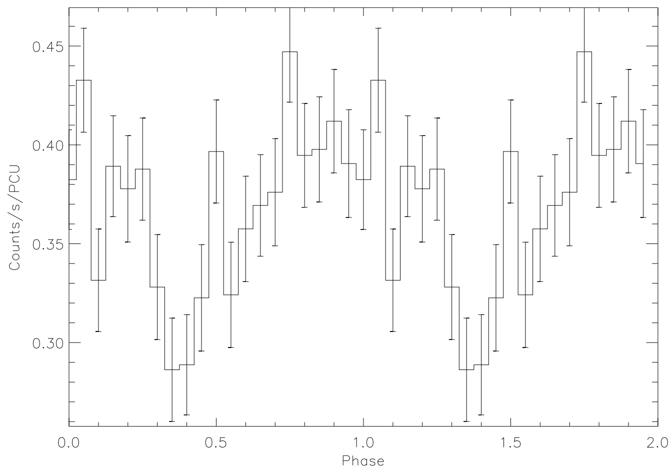

Figure A.5: 2–4 keV light curve of J0732 folded at the 512.4 s pulse period with an arbitrary zero point. Two cycles shown for clarity.

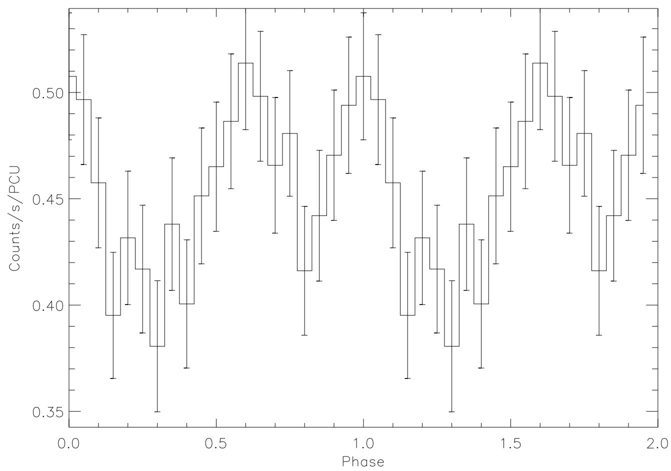

Figure A.6: 4–6 keV light curve of J0732 folded at the 512.4 s pulse period with an arbitrary zero point. Two cycles shown for clarity.

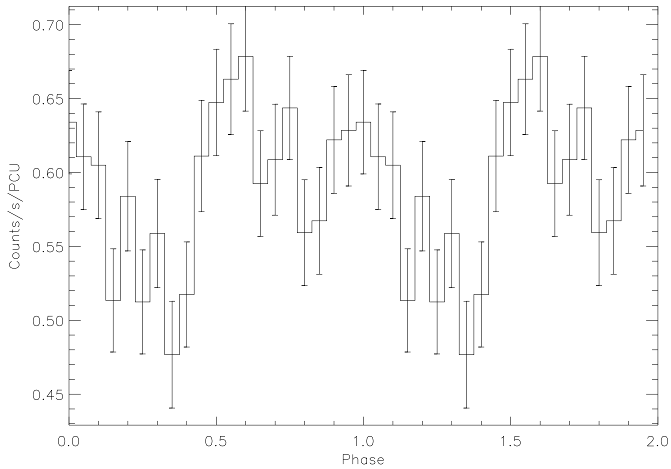

Figure A.7: 6–10 keV light curve of J0732 folded at the 512.4 s pulse period with an arbitrary zero point. Two cycles shown for clarity.

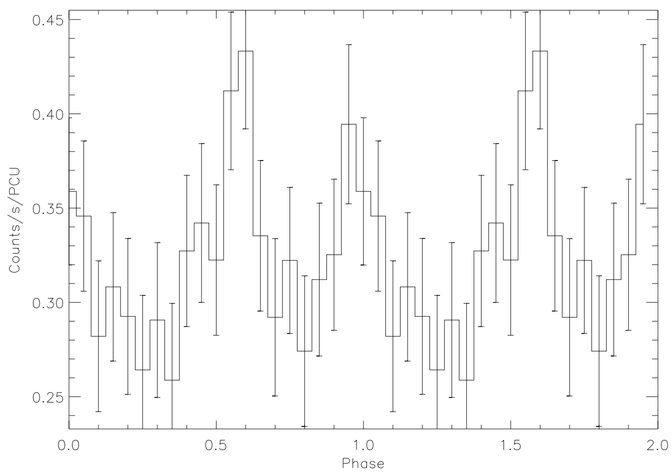

Figure A.8: 10–20 keV light curve of J0732 folded at the 512.4 s pulse period with an arbitrary zero point. Two cycles shown for clarity.

A.3 J1227

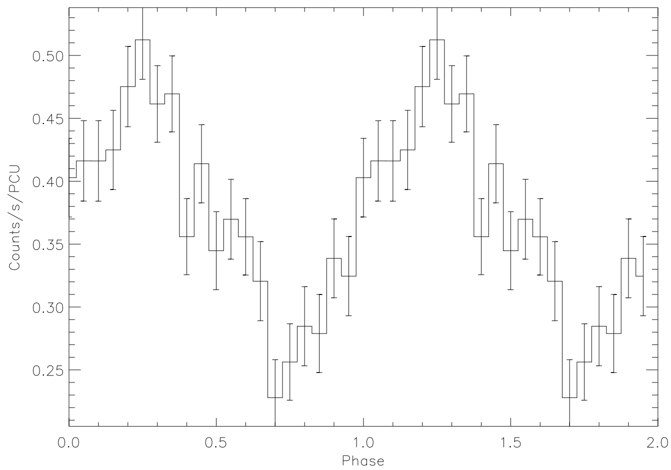

Figure A.9: 2–4 keV light curve of J1227 folded at the 859.57 s pulse period with an arbitrary zero point. Two cycles shown for clarity.

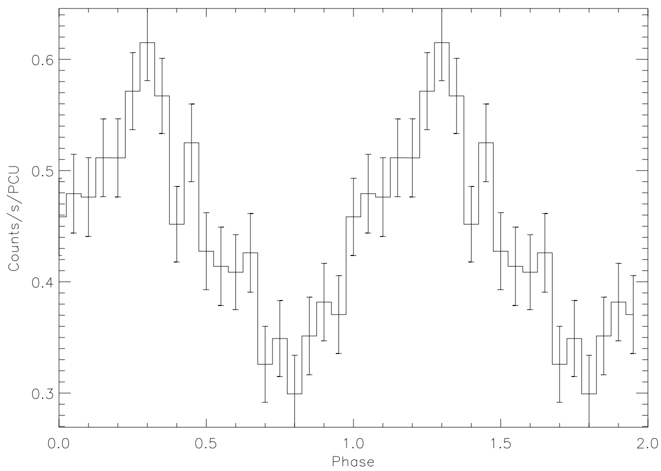

Figure A.10: 4–6 keV light curve of J1227 folded at the 859.57 s pulse period with an arbitrary zero point. Two cycles shown for clarity.

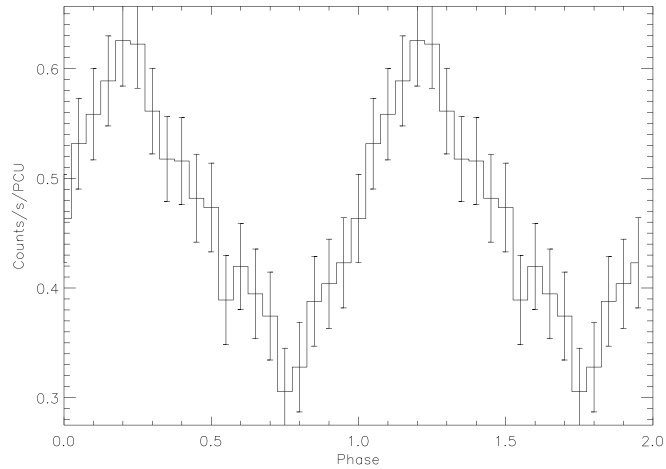

Figure A.11: 6–10 keV light curve of J1227 folded at the 859.57 s pulse period with an arbitrary zero point. Two cycles shown for clarity.

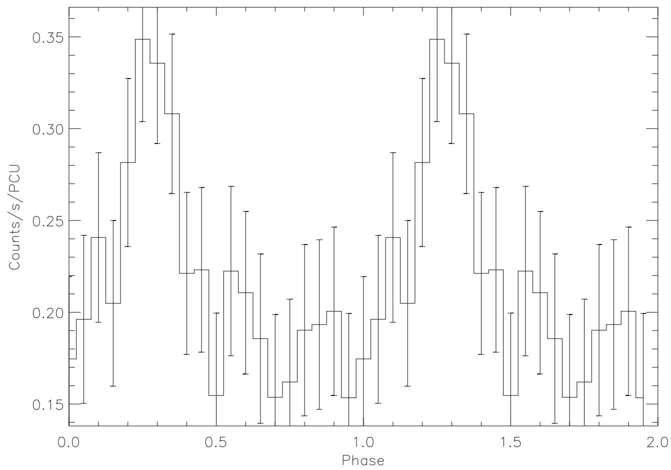

Figure A.12: 10–20 keV light curve of J1227 folded at the 859.57 s pulse period with an arbitrary zero point. Two cycles shown for clarity.

A.4 J1453

A.4.1 3746 s period

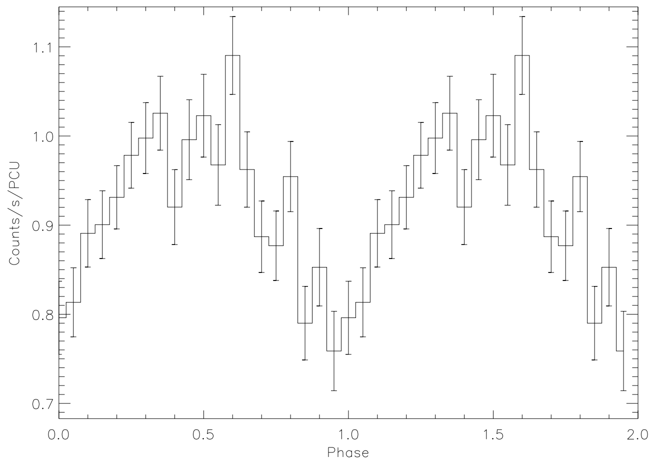

Figure A.13: 2–4 keV light curve of J1453 folded at the 3746 s pulse period with an arbitrary zero point. Two cycles shown for clarity.

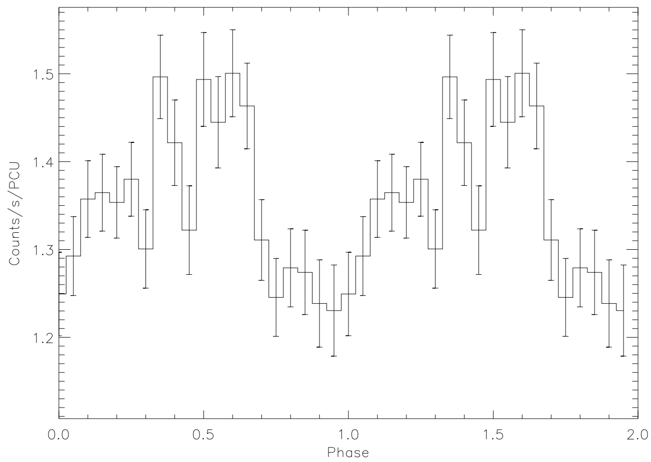

Figure A.14: 4–6 keV light curve of J1453 folded at the 3746 s pulse period with an arbitrary zero point. Two cycles shown for clarity.

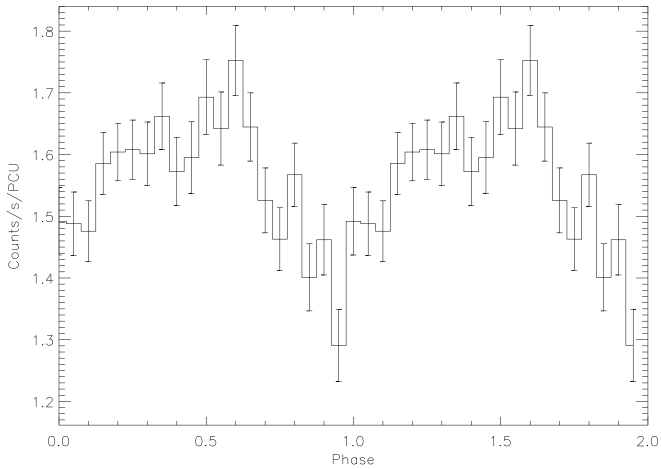

Figure A.15: 6–10 keV light curve of J1453 folded at the 3746 s pulse period with an arbitrary zero point. Two cycles shown for clarity.

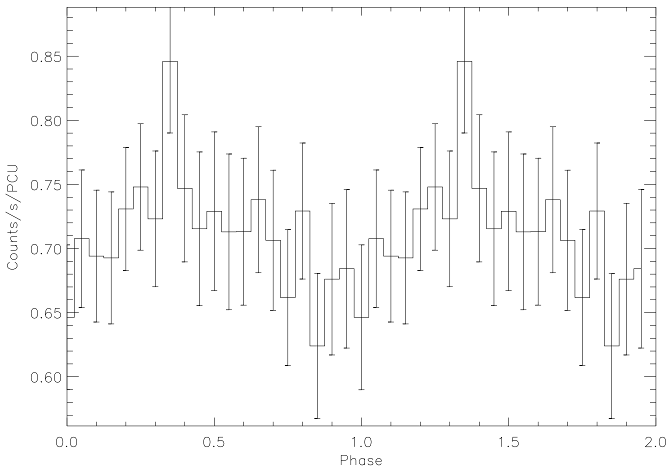

Figure A.16: 10–20 keV light curve of J1453 folded at the 3746 s pulse period with an arbitrary zero point. Two cycles shown for clarity.

A.4.2 7202 s period

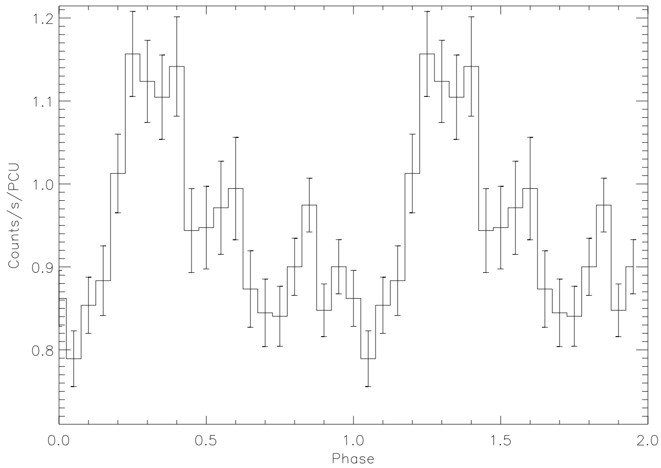

Figure A.17: 2–4 keV light curve of J1453 folded at the 7202 s pulse period with an arbitrary zero point. Two cycles shown for clarity.

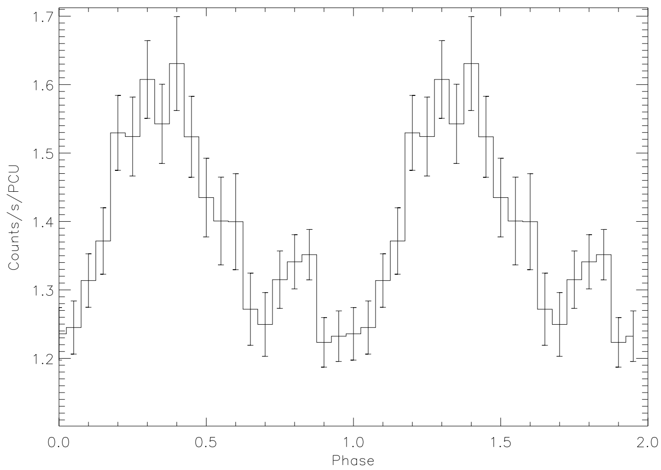

Figure A.18: 4–6 keV light curve of J1453 folded at the 7202 s pulse period with an arbitrary zero point. Two cycles shown for clarity.

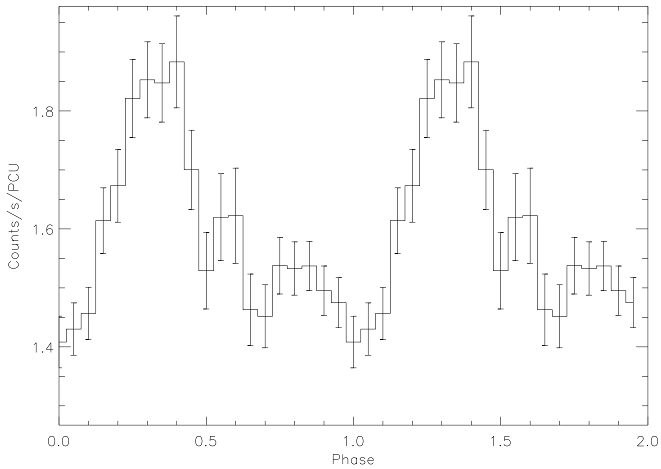

Figure A.19: 6–10 keV light curve of J1453 folded at the 7202 s pulse period with an arbitrary zero point. Two cycles shown for clarity.

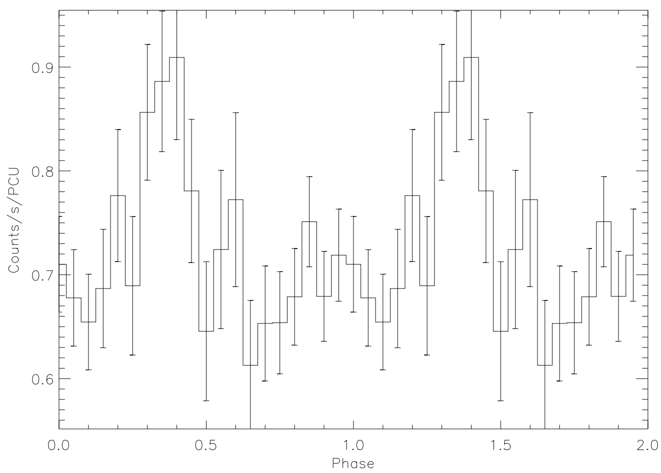

Figure A.20: 10–20 keV light curve of J1453 folded at the 7202 s pulse period with an arbitrary zero point. Two cycles shown for clarity.

A.4.3 11 363 s period

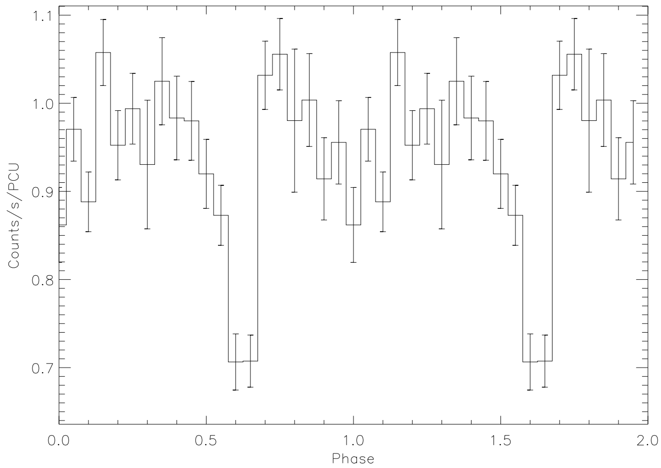

Figure A.21: 2–4 keV light curve of J1453 folded at the 11 363 s pulse period with an arbitrary zero point. Two cycles shown for clarity.

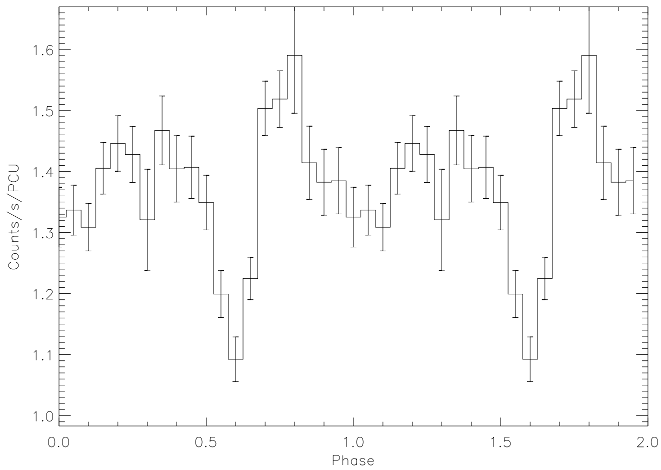

Figure A.22: 4–6 keV light curve of J1453 folded at the 11 363 s pulse period with an arbitrary zero point. Two cycles shown for clarity.

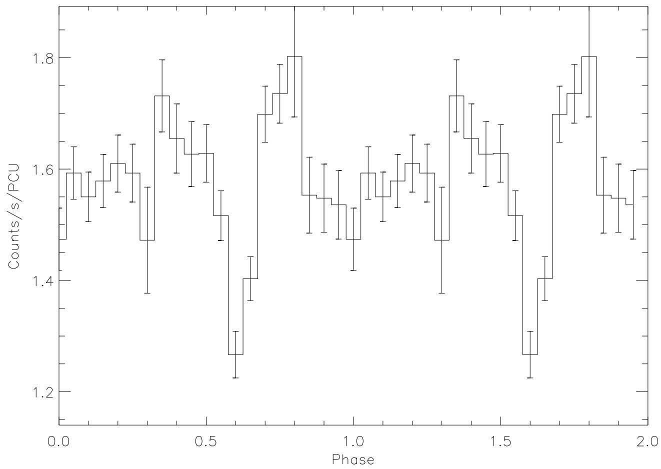

Figure A.23: 6–10 keV light curve of J1453 folded at the 11 363 s pulse period with an arbitrary zero point. Two cycles shown for clarity.

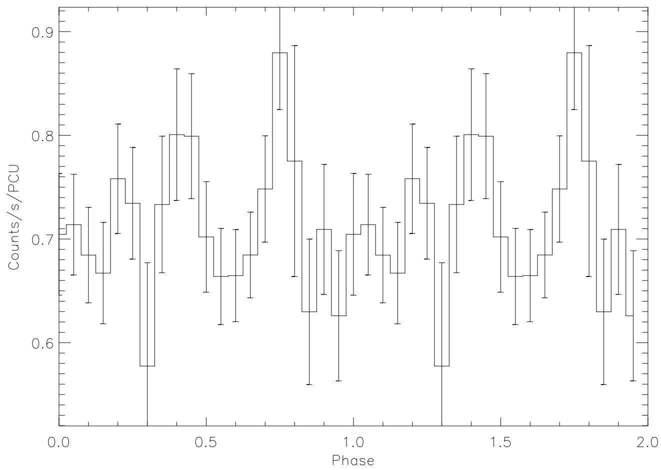

Figure A.24: 10–20 keV light curve of J1453 folded at the 11 363 s pulse period with an arbitrary zero point. Two cycles shown for clarity.

A.4.4 15 594 s period

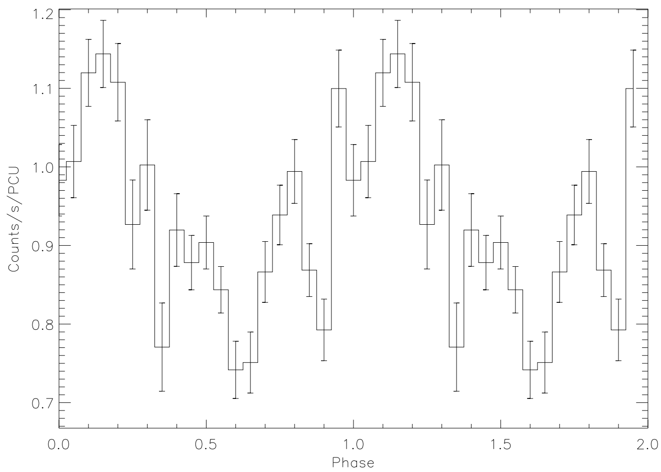

Figure A.25: 2–4 keV light curve of J1453 folded at the 15 594 s pulse period with an arbitrary zero point. Two cycles shown for clarity.

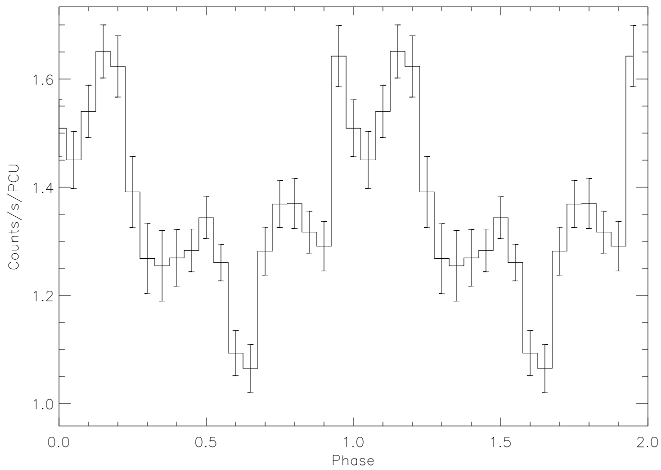

Figure A.26: 4–6 keV light curve of J1453 folded at the 15 594 s pulse period with an arbitrary zero point. Two cycles shown for clarity.

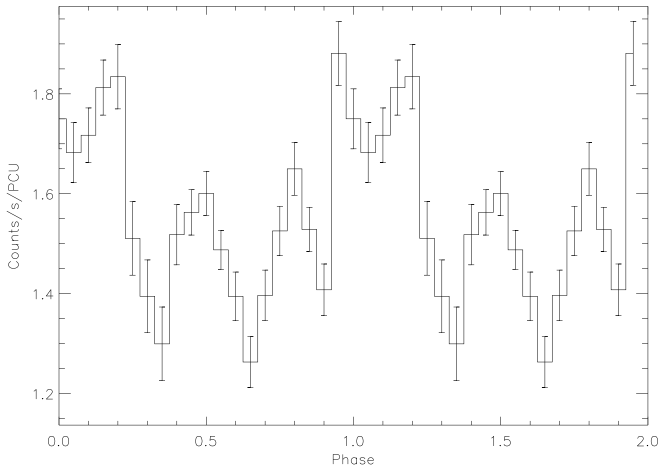

Figure A.27: 6–10 keV light curve of J1453 folded at the 15 594 s pulse period with an arbitrary zero point. Two cycles shown for clarity.

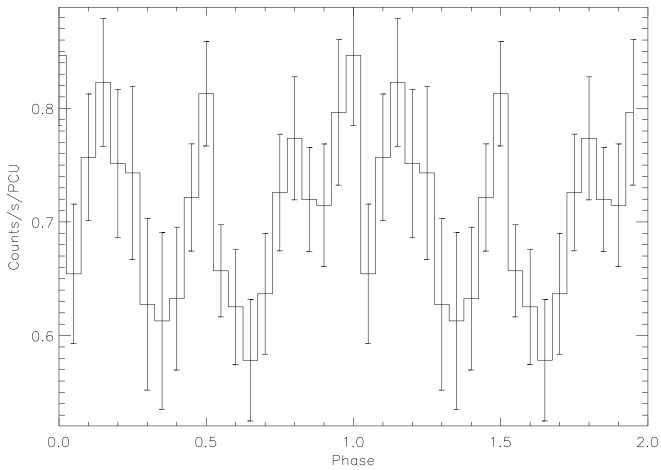

Figure A.28: 10–20 keV light curve of J1453 folded at the 15 594 s pulse period with an arbitrary zero point. Two cycles shown for clarity.

A.5 J1509

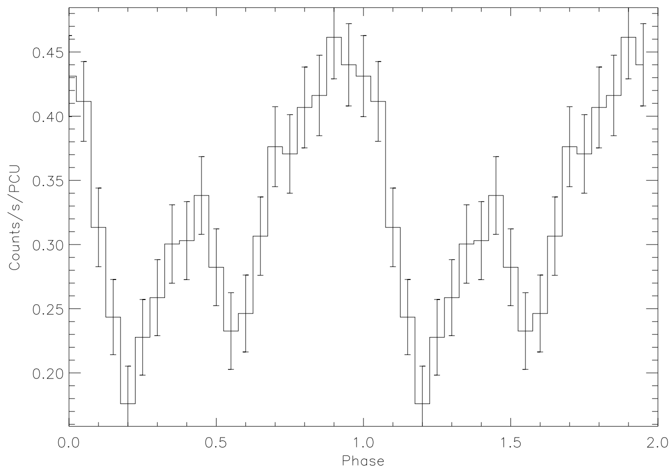

Figure A.29: 2–4 keV light curve of J1509 folded at the 809.7 s pulse period with an arbitrary zero point. Two cycles shown for clarity.

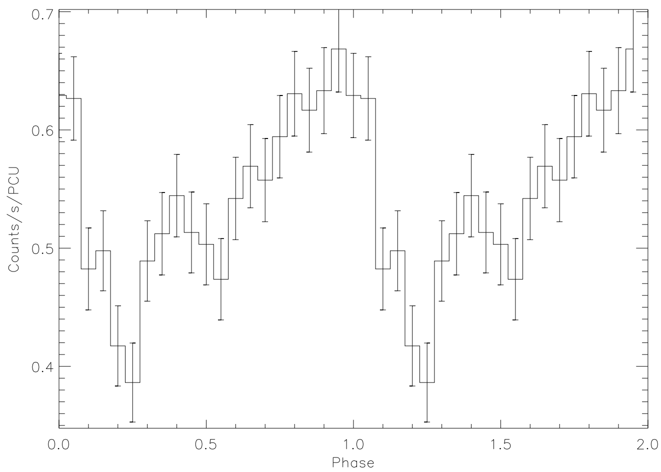

Figure A.30: 4–6 keV light curve of J1509 folded at the 809.7 s pulse period with an arbitrary zero point. Two cycles shown for clarity.

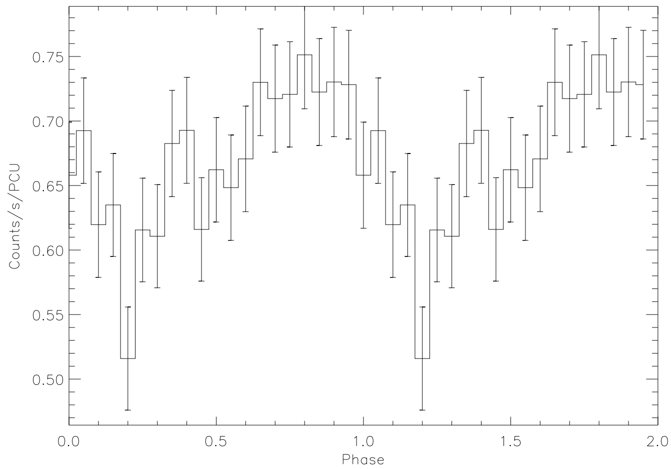

Figure A.31: 6–10 keV light curve of J1509 folded at the 809.7 s pulse period with an arbitrary zero point. Two cycles shown for clarity.

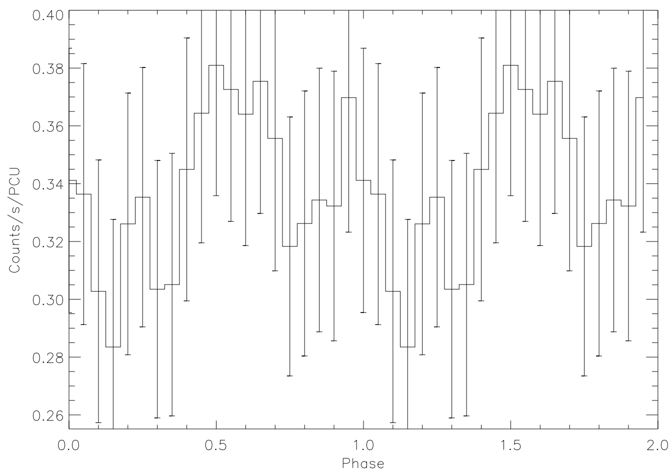

Figure A.32: 10–20 keV light curve of J1509 folded at the 809.7 s pulse period with an arbitrary zero point. Two cycles shown for clarity.

A.6 J1719

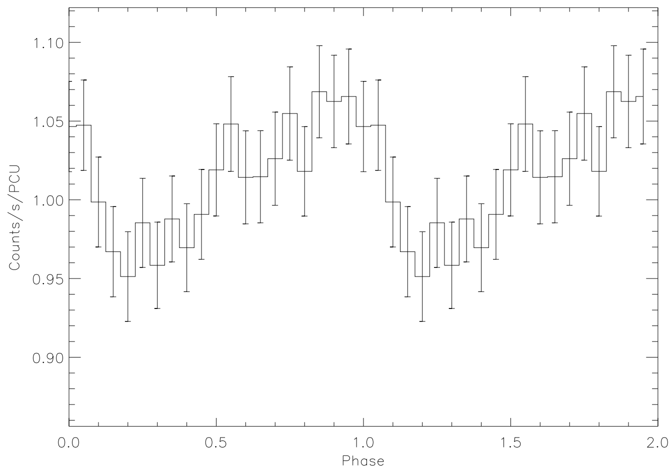

Figure A.33: 2–4 keV light curve of J1719 folded at the 1842.4 s pulse period with an arbitrary zero point. Two cycles shown for clarity.

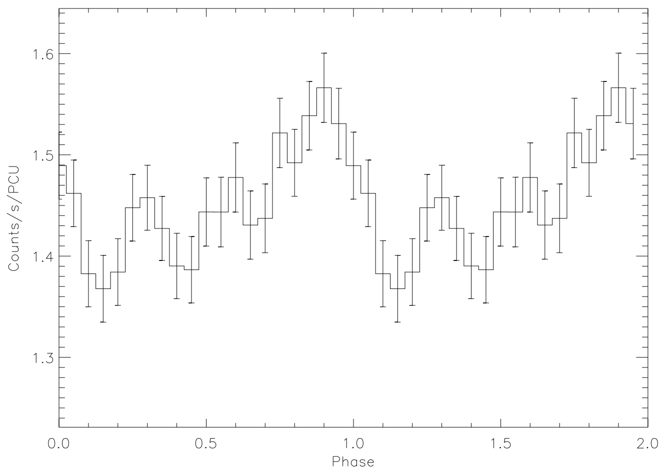

Figure A.34: 4–6 keV light curve of J1719 folded at the 1842.4 s pulse period with an arbitrary zero point. Two cycles shown for clarity.

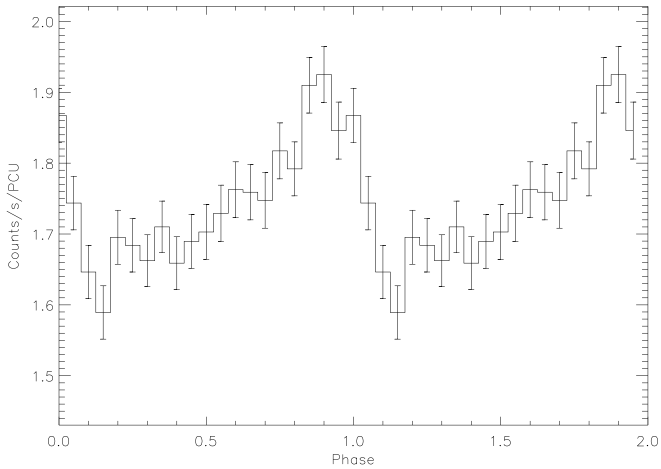

Figure A.35: 6–10 keV light curve of J1719 folded at the 1842.4 s pulse period with an arbitrary zero point. Two cycles shown for clarity.

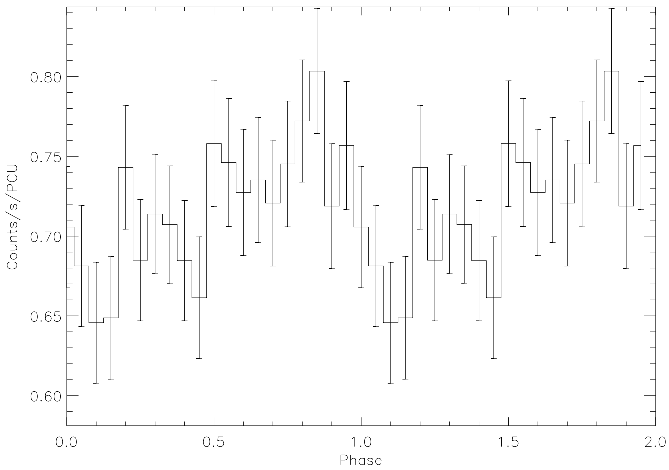

Figure A.36: 10–20 keV light curve of J1719 folded at the 1842.4 s pulse period with an arbitrary zero point. Two cycles shown for clarity.

Appendix B

Model overview

This appendix gives a more technical outline of the structure of the model presented in Chapter 5.

B.1 Overview

The model is a three stage process as outlined in Figure B.1. Firstly a script runs in which the free parameters are defined (these are the parameters which are not defined in *HyDisc* and therefore are user defined), the file tree is also built at this stage. Secondly this script then launches the main program, this is a large program that works on each snapshot file independently, allowing a very large degree of parallelization. In Figure B.1 this corresponds to the dashed box. Finally, when each snapshot has been processed all of the outputs are processed and reduced.

The main program calculates discrete emission points close to the WD, based upon the accretion structure. The line of sight from each emission point to an external observer is calculated, taking account of the inclinations, spin and orbital phases of the system. This line of sight then has its column density calculated based upon the density of material along its path. The emission profile is then absorbed accordingly for each individual emission point.

B.2 The program

The main body of the model is written in C++, with various aspects/functionality spread over thirteen main source files (see Table B.1). In total the model is over ten thousand lines of code.

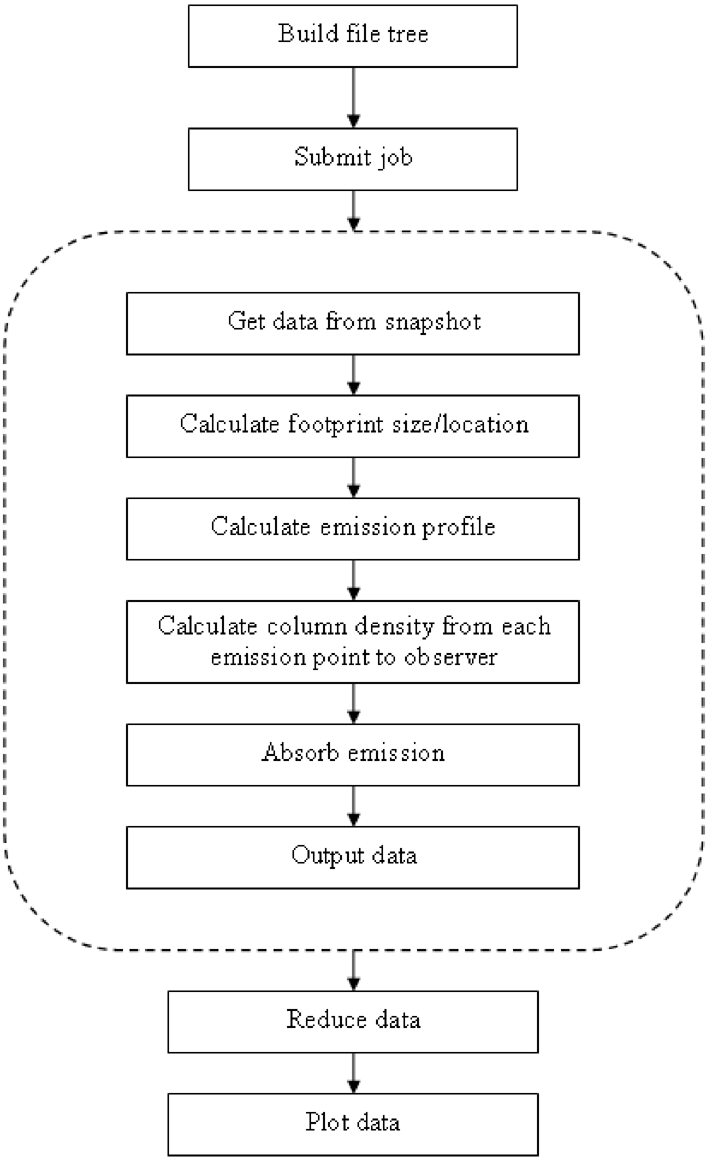

Figure B.1: Flow chart of the basic structure of the program. The dashed line corresponds to the main program which operates on each snapshot file independently, and therefore can run in parallel.

The model is controlled with a master script in which all the parameters are defined and then passed to the main program. All of the housekeeping is done by this script - including the building of file trees etc. Once all the initial housekeeping has been done, the main program is started. If it is running locally then it iterates through the snapshot files produced by *HyDisc* (typically ∼1000) one at a time. If it is run on a cluster then it submits all the tasks at once, allowing them to be run in parallel. When all the snapshot files have been analysed, a reduction program is called which amalgamates all of the separate files together and phase bins them. The master script then calls a series of IDL routines to further reduce and plot the data, finishing with a set of post script files. Finally the master script finishes with some error checking of the output files, then deletes any unnecessary intermediary files.

The length of time it takes to run the model is very strongly dependent on the number of blobs in the accretion stream and the number of blobs that hit the surface (since it scales as a multiple of the two). Running the full model can take up to a day running in parallel on 128 nodes.

B.2.1 File structure

Everything is located relative to a root directory, under which the directories called `absorption` and `hydisc` are assumed to exist. The `absorption` directory is where all of the synthetic light curve modelling source files and data are located (see Table B.1), and the `hydisc` directory is where the snapshot files from *HyDisc* are located.

Table B.1: Overview of the location and function of each of the source files used in the synthetic light curve modelling

FOLDERS:	
source_code/	Where the source code is.
idl_routines/	Where the IDL routines are.
running/error/	Where the error files from the grid engine go.
running/output/	Where the standard output data goes.
data/	Where all the data is stored.

Continued on the next page ...

Continued from the previous page

SOURCE CODE:	
column_density.cpp	Calculates the column density.
data_reduction.cpp	Post processing step to reduce all the output files to one single file.
emission_points.cpp	Calculates where the emission points are for the structured emission column.
filenames.cpp	Creates all the file names.
footprint.cpp	Calculates where the blobs hit the surface.
get_sorted_density.cpp	Get all the data from the snapshot files and sort it.
main.cpp	Gets the inputs and controls everything.
mymaths.cpp	Tweaked maths functions.
optical_properties.cpp	Calculates the optical depth.
ray_tracing.cpp	Does the main ray tracing algorithm.
radiation.cpp	Initialise and absorb the emission profile.
transformations.cpp	Frame transformation routines.
phasebin.cpp	Phase bins all the data.
column_density.h	
defines.h	All physical constants, verbosity level.
emission_points.h	
filenames.h	
footprint.h	
get_sorted_density.h	
grid_disc_properties.h	
mymaths.h	
optical_properties.h	
radiation.h	

Continued on the next page ...

Continued from the previous page	
ray_tracing.h	
SCRIPTS:	
master	Runs the WHOLE thing.
dave_launcher	Called by master, this is passed to the cluster.
makefile	Makes all the above. make clean tidies up.
EXECUTABLES:	
dave	Made by make, used by dave_launcher.
reduce	Made by hand, used by master.
phasebin	Made by hand, used by master.
IDL routines:	
abs_spin_unbinned.pro	Plots the unbinned spin data.
abs_spin_binned.pro	Plots the spin binned data.
abs_spin_binned_one_energy.pro	Plots the spin binned data at one energy.
abs_orb_unbinned.pro	Plots the orbitally unbinned data.
abs_orb_binned.pro	Plots the orbitally binned data.
abs_period_search.pro	Plots the Lomb-Scargle periodogram of the data.
abs_footprint.pro	Plots the location of the footprints, and calculates their sizes.
MISC:	
exitstatus.txt	Output file of qsub giving error codes. Should always be 0.

Appendix C

Published papers

This appendix contains copies of each of the refereed publications which contain some of the work presented in this thesis.

- *RXTE* confirmation of the intermediate polar status of *Swift* J0732.5–1331

  ***O. W. Butters**, E. J. Barlow, A. J. Norton and K. Mukai.*

  A&A 475,L29-L32 (2007) DOI:10.1051/0004-6361:20078700

- *RXTE* determination of the intermediate polar status of XSS J00564+4548, IGR J17195–4100, and XSS J12270–4859

  ***O. W. Butters**, A. J. Norton, P. Hakala, K. Mukai and E. J. Barlow.*

  A&A 487,271-276 (2008) DOI:10.1051/0004-6361:200809942

- *RXTE* confirmation of the intermediate polar status of IGR J15094-6649

  ***O. W. Butters**, A. J. Norton, K. Mukai and E. J. Barlow.*

  A&A 498,L17-L19 (2009) DOI:10.1051/0004-6361:200911725

- The accretion flows and evolution of magnetic cataclysmic variables

  *A. J. Norton, **O. W. Butters**, T. L. Parker and G. A. Wynn*

  The Astrophysical Journal, 672:524-530 (2008) DOI:10.1086/523932

- Discovery of polarized emission from the long period intermediate polar RX J2133.7+5107

*S. Katajainen, **O. W. Butters**, A. J. Norton, H. J. Lehto and V. Piirola*

A&A 475,1011-1018 (2007) DOI: 10.1051/0004-6361:20077618

- Circular polarization survey of intermediate polars I. Northern targets in the range 17h<R.A.<23h

  ***O. W. Butters**, S. Katajainen, A. J. Norton, H. J. Lehto and V. Piirola*

  A&A 496,891-902 (2009) DOI: 10.1051/0004-6361/200811058

C.1 Paper I – *RXTE* confirmation of the intermediate polar status of *Swift* J0732.5–1331

This paper (Butters et al. 2007) reported the first findings of a project to observe hard X-ray selected intermediate polar candidates. The data was proprietary *RXTE* (cycle 12) data. The findings of this paper are also presented in Chapter 2.

A&A 475, L29–L32 (2007)
DOI: 10.1051/0004-6361:20078700

Astronomy & Astrophysics

LETTER TO THE EDITOR

RXTE confirmation of the intermediate polar status of Swift J0732.5–1331

O. W. Butters[1], E. J. Barlow[1], A. J. Norton[1], and K. Mukai[2]

[1] Department of Physics and Astronomy, The Open University, Walton Hall, Milton Keynes MK7 6AA, UK
e-mail: o.w.butters@open.ac.uk
[2] CRESST and X-ray Astrophysics Laboratory NASA/GSFC, Greenbelt, MD 20771, USA; Department of Physics, University of Maryland, Baltimore county, 1000 Hilltop Circle, Baltimore, MD 21250, USA

Accepted 18 September 2007 / Received 11 October 2007

ABSTRACT

Aims. We intend to establish the X-ray properties of Swift J0732.5–1331 and therefore confirm its status as an intermediate polar.
Methods. We analysed 36 240 s of X-ray data from *RXTE*. Frequency analysis was used to constrain temporal variations and spectral analysis used to characterise the emission and absorption properties.
Results. The X-ray spin period is confirmed to be 512.4(3) s with a strong first harmonic. No modulation is detected at the candidate orbital period of 5.6 h, but a coherent modulation is present at the candidate 11.3 h period. The spectrum is consistent with a 37 keV bremsstrahlung continuum with an iron line at 6.4 keV absorbed by an equivalent hydrogen column density of around 10^{22} atoms cm^{-2}.
Conclusions. Swift J0732–1331 is confirmed to be an intermediate polar.

Key words. stars: binaries: general – stars: novae, cataclysmic variables – stars: individual: Swift J0732.5–1331 – X-rays: binaries

1. Introduction to magnetic cataclysmic variables

Intermediate polars (IPs) are a sub-class of cataclysmic variables (CVs). They fill the phase space, in terms of magnetic field strength, and spin and orbital periods, between non-magnetic CVs and the strongly magnetic synchronously rotating polars. The magnetic field strength is believed to be in the range of a few MG to tens of MG at the white dwarf surface. This is large enough to dramatically alter the accretion flow, yet not large enough to synchronize the spin and orbital periods. This magnetic field gives rise to the defining characteristic of the sub-class, that of X-ray variation pulsed at the spin period of the white dwarf. For an exhaustive review of CVs see e.g. Warner (1995).

There are between twenty six[1] and fifty IPs currently known (depending on the selection criteria used). The hard X-ray selected object, Swift J0732.5–1331 (hereafter J0732), is a suspected IP in need of confirmation. The circumstance of its discovery makes J0732 similar to the host of candidate IPs that have been discovered to be powerful emitters of hard X-rays/soft gamma-rays in the 20−100 keV range in the *INTEGRAL*/IBIS survey (Barlow et al. 2006). We have embarked on a campaign of pointed *RXTE* observations of these hard X-ray discovered candidate IPs. Here we present the first results of our campaign on J0732.

2. Previous observations of Swift J0732.5-1331

There is to date no peer-reviewed analysis of J0732 published in the literature. There are however several mentions of it in Astronomical Telegrams, which we summarise below. These were all published over the course of a couple of months in early 2006.

J0732 was first detected by Ajello et al. (2006) with the *Swift* Burst Alert Telescope and *Swift* X-ray telescope (XRT). With the XRT 600 counts in 3400 s were recorded, coincident with the *ROSAT* source 1RXS J073237.6−133113. This is also coincident with the 2MASS source J073237.64−133109.4, a proposed K main-sequence star 400 pc away. Based on its X-ray luminosity and colours, Ajello et al. (2006) suggested a CV identification for the object.

Masetti et al. (2006) used the BFOSC instrument on the G.D. Cassini 1.5 m telescope to obtain the optical spectrum of the counterpart to J0732. Two objects were found close to the reported position, a normal G/K type Galactic star (the 2MASS source) and a fainter one deemed to be the true optical counterpart. The spectral signature of the system was concluded to be that of an accretion disc in a low mass X-ray binary.

Patterson et al. (2006) also obtained low resolution spectra, this time on the MDM 2.4 m telescope, of the 2MASS optical counterpart proposed by Ajello et al. (2006) (i.e. the field star), concluding that it was indeed a normal G star. In the same telegram Patterson et al. (2006) also reported optical photometry (obtained by the small telescope network of the Center for Backyard Astrophysics[2]) which revealed a stable pulsation period of 512.42(3) s with most of the power in the first harmonic. This was deemed to be the spin period of a rotating white dwarf and Patterson et al. (2006) consequently suggested an IP classification for the object. A possible 11.3 h orbital signal was also suggested, but owing to its low amplitude, this required the binary to be close to face on, as any variation in brightness due to the projected Roche lobe filling secondary was small.

[1] http://asd.gsfc.nasa.gov/Koji.Mukai/iphome/iphome.html as of 23/8/7.

[2] http://cba.phys.columbia.edu/

Article published by EDP Sciences and available at http://www.aanda.org or http://dx.doi.org/10.1051/0004-6361:20078700

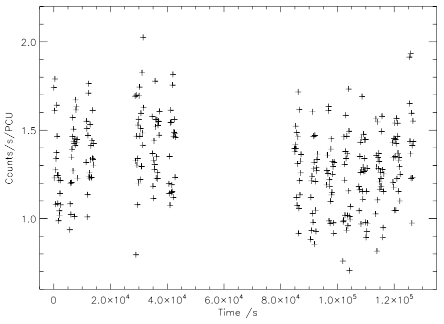

Fig. 1. 2−10 keV background subtracted light curve of J0732.5−1331. The zero time corresponds to the start of the observations at JD 2 454 295.30035. The data is binned into bins of 128 s width. The typical error on each point is ±0.2.

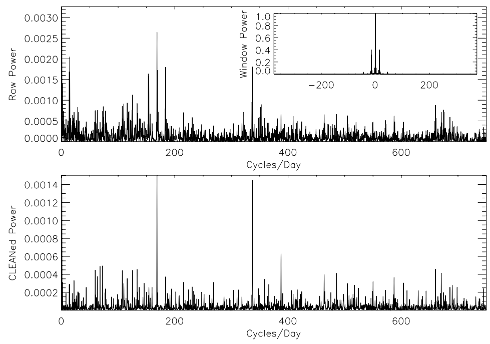

Fig. 2. CLEANed periodogram. The upper plot shows the raw periodogram, with the window function inset; the lower plot shows the deconvolved (CLEANed) periodogram.

Marsh et al. (2006) subsequently used *ULTRACAM* mounted on the William Herschel Telescope to observe the optical counterpart of J0732. The spin pulsation detected by Patterson et al. (2006) was seen. The counterpart and the non-associated field star were found to be approximately 1.8″ apart.

Torres et al. (2006) performed spectral analysis of the optical counterpart at the Mt. Hopkins 1.5 m telescope. Balmer emission lines from Hα to at least Hγ were found. This reinforced its classification as a probable IP. However, despite seeing a variation in the radial velocities of the various emission lines, they were unable to determine an orbital period.

Wheatley et al. (2006) later reanalysed the original *Swift* data reported in Ajello et al. (2006) and found an X-ray pulsation at the proposed spin period. The modulation was found to be single peaked and only present below 2 keV. Reanalysis of the spectral data suggested a temperature typical of intermediate polars ($kT \sim 20$ keV). This data set is, however, short and suffers from severe aliasing effects.

Thorstensen et al. (2006) carried out time series spectroscopy at the MDM Observatory on the optical counterpart. The radial velocities of the Hα emission lines were found to vary periodically with a period of 0.2335(8) days (5.60(2) h), which was interpreted as the orbital period of the system. We note this is close to half the photometric period suggested by Patterson et al. (2006).

Given all this information, J0732 is strongly suspected to be an intermediate polar, but the only way to confirm this is the unambiguous detection of pulsed hard X-ray emission at the spin period.

3. Observations and data reduction

Data were obtained from the *RXTE* satellite (Bradt et al. 1993) with the PCA instrument over two consecutive days, from 13th−15th July 2007. The total time on target was 36 240 s, comprising fourteen approximately equal segments of one satellite orbit each. Initial data reduction was done with the standard FTOOLS, and the flux was normalised according to the number of correctly functioning PCUs. For the light curve analysis PCUs 2, 3, and 4 were used; whilst for the spectral analysis only PCU 2 was used as the other PCUs were only turned on infrequently. Only the top layer of each PCU was included in the measurements and the time resolution of the data was 16 s. Background subtracted light curves were constructed in four energy bands: 2−4 keV, 4−6 keV, 6−10 keV and 10−20 keV, as well as a combined 2−10 keV band for maximum signal-to-noise. A mean X-ray spectrum was also extracted.

Table 1. Modulation depths of the pulse profile in different energy bands. Modulation depth is defined here as the semi-amplitude of a fitted sinusoid divided by the fitted mean.

Energy band (keV)	Modulation depth (%)	Uncertainty (%)	Fitted mean (ct s^{-1} PCU^{-1})
2–10	8	1	1.31
2–4	16	3	0.25
4–6	7	2	0.46
6–10	7	2	0.56
10–20	10	4	0.28

3.1. Light curve analysis

The raw count rate varied between 3.9 and 5.4 count s^{-1} PCU^{-1}. The background count rate, generated from the calibration files, varied between 2.9 and 3.8 count s^{-1} PCU^{-1}. The background subtracted 2−10 keV light curve is shown in Fig. 1. The data were subsequently analysed with a variable gain implementation of the CLEAN algorithm (Lehto 1997) to discover any periodicities and discount any aliasing effects. The results of this are shown in Fig. 2.

3.1.1. Spin period

Strong peaks are evident in the CLEANed periodogram at 168 cycles day^{-1} (512 s) and at its first harmonic, in the 2−10 keV energy band. Similar signals are seen in each energy band. Analysis of the peaks yields a pulsation period of 512.4(3) s. The data in each of the energy resolved light curves were then folded at the 512.4 s period, and Fig. 3 shows the result in the 2−10 keV energy band. The modulation depths of the pulse profile were then estimated by fitting a sinusoid to the folded data in each energy band and dividing the semi-amplitude by the fitted mean. The results of this are shown in Table 1.

3.1.2. Orbital period

The windowing of the data is such that no reliable signal can be extracted for periods of a few hours from the periodogram,

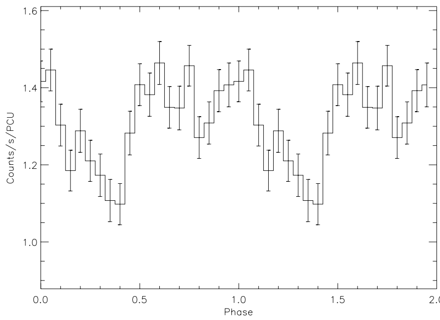

Fig. 3. 2–10 keV light curve folded at the 512.4 s pulse period with an arbitrary zero point. Two cycles are shown for clarity.

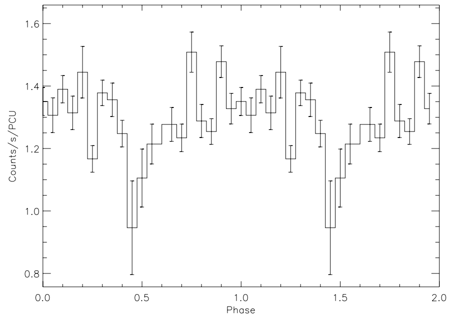

Fig. 4. 2–10 keV light curve folded at the 11.3 h photometric period suggested by Patterson et al. (2006) with an arbitrary zero point. Two cycles are shown for clarity.

therefore no reliable orbital period can be found. Folding the X-ray data at the 5.6 h spectroscopic period (Thorstensen et al. 2006) yields no coherent modulation, but folding it at the 11.3 h photometric period suggested by Patterson et al. (2006) gives a plausible signal (see Fig. 4).

3.2. Spectral analysis

Analysis of the X-ray spectrum was carried out with the XSPEC package. The best fit for a simple photoelectrically absorbed bremsstrahlung model had the parameters $kT = 37 \pm 7$ keV and $n_{\rm H} = (2.0 \pm 0.5) \times 10^{22}$ cm^{-2} (reduced $\chi^2 = 3.0$). The residuals of this plot indicate the presence of an excess at approximately 6.5 keV. Keeping the temperature and column density fixed and fitting a Gaussian to this region indicates an iron line at 6.4 ± 0.1 keV with a width of $\sigma = 0.3 \pm 0.1$ keV (reduced $\chi^2 = 1.0$), as shown in Fig. 5.

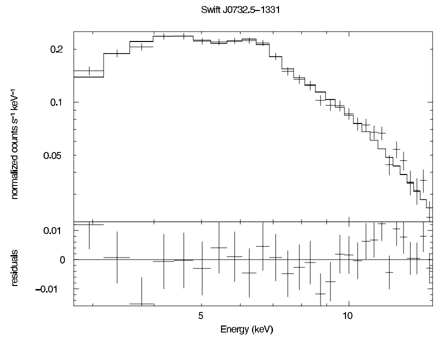

Fig. 5. 2.5–15 keV mean spectrum fitted with a photoelectrically absorbed bremsstrahlung plus iron line profile. Fitting parameters are $kT = 37 \pm 7$ keV, $n_{\rm H} = (2.0 \pm 0.5) \times 10^{22}$ cm^{-2}, iron line fitted with a Gaussian centred on 6.4 ± 0.1 keV with $\sigma = 0.3 \pm 0.1$ keV. Reduced $\chi^2 = 1.0$.

4. Discussion

The strong X-ray signal at the 512.4(3) s pulse period seen at all energies is characteristic of IPs and confirms the nature of the object. Patterson et al. (2006) found a much stronger peak at the first harmonic in their frequency analysis of the optical photometry data. This is characteristic of a double-peaked pulse profile and indicates that two emission regions can be seen. The X-ray data reported here exhibit the same periodicity, but a somewhat different profile. The first harmonic in the X-ray data is still present, and the pulse profile consequently shows a second minimum superimposed on the pulse maximum, but the overall profile is only marginally double-peaked. The most likely geometry of this system is therefore such that one magnetic pole can always be seen, the other being behind the WD for most of the cycle. If the heights of the accretion columns are such that a fraction of the hidden pole's column can be seen at certain phases then the X-ray profile may be explained. If the optical emission arises from reprocessed X-rays (i.e. further up the accretion column) then it may be seen from both poles and this would explain the optical signal of Patterson et al. (2006).

The modulation depth of the X-ray pulse profile is approximately constant above 4 keV, implying that the dominant effect shaping the profile is geometric, probably self-occultation by the white dwarf. At the lowest energies (2–4 keV) the modulation depth is higher, which implies that phase-varying photoelectric absorption (as well as occultation) is the process which causes the modulation. The spectral fitting also indicates the presence of a significant local absorbing column, and has parameters that are typical of other IPs.

There is still some ambiguity about the orbital period of this system. The chance of it being the 11.3 h period suggested by Patterson et al. (2006) is now increased, given the X-ray signal seen here, but the possibility of aliasing in this data set means that it cannot be definitively said to be so and we cannot rule out the 5.6 h spectroscopic period found by Thorstensen et al. (2006). The absence of a beat period in the frequency analysis of the optical data does suggest that the true orbital period may be long, since no reprocessed radiation is seen from the face of the secondary star and therefore the bodies are likely to be far apart.

The lack of an X-ray beat signal in these *RXTE* data indicates that there is no significant stream-fed component to the flow. This suggests a relatively weak magnetic field strength and is consistent with the small $P_{\rm spin}/P_{\rm orb}$ ratio of the system (Norton et al. 2004), namely 0.025 or 0.013 depending on which is the correct orbital period.

The high temperature bremsstrahlung continuum and the presence of an iron line at 6.4 keV reinforce the case for J0732 to be an IP since these are both features often seen in other IPs (Hellier & Mukai 2004).

Finally, we note that the average *RXTE* count rate (1.3 ct s^{-1} PCU^{-1} in the $2-10$ keV band) is consistent[3] with the value obtained with the *Swift* satellite, indicating that the system has not changed significantly in brightness since its discovery.

5. Conclusion

The unambiguous X-ray spin period detection at 512.4(3) s, along with the spectral fit to an absorbed 37 keV bremsstrahlung model with an iron line, confirm the intermediate polar status of Swift J0732.5−1331. We are unable to determine the orbital period from these *RXTE* data although there is some indication of modulation at the previously suggested photometric period of 11.3 h and none at the spectroscopic period of 5.6 h. To conclude we note that this system is similar, in terms of its small $P_{\rm spin}/P_{\rm orb}$ value, to the IPs RX J2133.7+5107 and NY Lup (IGR J15479–4529). Both of these are *INTEGRAL* hard X-ray sources and both also have soft X-ray components. We might therefore expect that Swift J0732.5−1331 would also display such characteristics upon further study.

References

Ajello, M., Greiner, J., Rau, A., et al. 2006, The Astronomer's Telegram, 697, 1
Barlow, E. J., Knigge, C., Bird, A. J., et al. 2006, MNRAS, 372, 224
Bradt, H. V., Rothschild, R. E., & Swank, J. H. 1993, A&AS, 97, 355
Hellier, C., & Mukai, K. 2004, MNRAS, 352, 1037
Lehto, H. J. 1997, in Applications of time series analysis in astronomy and meteorology, ed. T. Subba Rao, M. B. Priestley, & O. Lessi (London Chapman and Hall)
Marsh, T., Littlefair, S., & Dhillon, V. 2006, The Astronomer's Telegram, 760, 1
Masetti, N., Bassani, L., Dean, A. J., Ubertini, P., & Walter, R. 2006, The Astronomer's Telegram, 735, 1
Norton, A. J., Wynn, G. A., & Somerscales, R. V. 2004, ApJ, 614, 349
Patterson, J., Halpern, J., Mirabal, N., et al. 2006, The Astronomer's Telegram, 757, 1
Thorstensen, J. R., Patterson, J., Halpern, J., & Mirabal, N. 2006, The Astronomer's Telegram, 767, 1
Torres, M. A. P., Steeghs, D., Garcia, M. R., et al. 2006, The Astronomer's Telegram, 763, 1
Warner, B. 1995, Cataclysmic variable stars, Cambridge Astrophysics Series (Cambridge, New York: Cambridge University Press)
Wheatley, P. J., Marsh, T. R., & Clarkson, W. 2006, The Astronomer's Telegram, 765, 1

[3] Using webpimms:
`http://heasarc.gsfc.nasa.gov/Tools/w3pimms.html`

C.2 Paper II – *RXTE* determination of the intermediate polar status of XSS J00564+4548, IGR J17195–4100, and XSS J12270–4859

This paper (Butters et al. 2008) is a continuation of the observations of the hard X-ray selected intermediate polar candidates. The findings of this paper are also presented in Chapter 2.

A&A 487, 271–276 (2008)
DOI: 10.1051/0004-6361:200809942

Astronomy & Astrophysics

RXTE determination of the intermediate polar status of XSS J00564+4548, IGR J17195–4100, and XSS J12270–4859

O. W. Butters[1], A. J. Norton[1], P. Hakala[2], K. Mukai[3], and E. J. Barlow[1]

[1] Department of Physics and Astronomy, The Open University, Walton Hall, Milton Keynes MK7 6AA, UK
e-mail: o.w.butters@open.ac.uk
[2] Tuorla Observatory, University of Turku, 21500 Piikkiö, Finland
[3] CRESST and X-ray Astrophysics Laboratory NASA/GSFC, Greenbelt, MD 20771, USA

Received 10 April 2008 / Accepted 24 May 2008

ABSTRACT

Aims. We determine the nature of the intermediate polar candidates XSS J00564+4548, IGR J17195–4100, and XSS J12270–4859.
Methods. Pointed *RXTE* observations searched for intermediate polar characteristics in these candidate systems.
Results. XSS J00564+4548 exhibits a period of 465.68 ± 0.07 s, which we interpret as the spin period, an energy dependent modulation depth, and a spectrum that is fit by a 22 keV photoelectrically absorbed bremsstrahlung with an iron line profile. IGR J17195–4100 shows several candidate periodicities and a spectrum that is fit by a power law with an iron line. XSS J12270–4859 exhibits a candidate spin period of 859.57 ± 0.64 s and a spectrum that is fit by a power law with no evidence of an iron line.
Conclusions. XSS J00564+4548 is confirmed to be an intermediate polar. IGR J17195–4100 and XSS J12270–4859 both show some properties of intermediate polars, but cannot be confirmed as definite members of the class here.

Key words. binaries: close – stars: novae, cataclysmic variables – X-rays: binaries

1. Introduction to magnetic cataclysmic variables

Intermediate polars (IPs) belong to the class of systems known as cataclysmic variables (CVs). They occupy the phase space, in terms of magnetic field strength, between the polars and the non-magnetic CVs. This intermediate strength magnetic field alters the accretion flow from the main sequence donor star to the white dwarf (WD). Eventually, most of the accreting material is channelled to accretion curtains above the WD magnetic poles. The temperature and density of this region causes the emission of bremsstrahlung radiation, which varies at the spin period of the WD. It is this variation that most consider to be the defining characteristics of IPs. For a review of IPs see e.g. Warner (1995). There are at least 30 confirmed IPs[1]. Ramsay et al. (2008), however, have recently pointed out that the commonly used criteria to certify CVs as IPs may be too restrictive. It is possible that many of the 84 candidates[1] are indeed IPs, and if classes such as SW Sex systems are in fact IPs then the true number may be several hundred.

In recent years there have been 16 IPs found to emit in the hard X-ray/soft gamma-ray part of the spectrum, with the *INTEGRAL*/IBIS survey (Barlow et al. 2006; Bird et al. 2007). With this in mind we have embarked on a campaign to observe some hard X-ray sources and determine their credentials as potential IPs. In the first paper in this campaign, SWIFT J0732.5–1331 was confirmed as an IP (Butters et al. 2007). Here the results of pointed *RXTE* observations of XSS J00564+4548 (hereafter J0056), IGR J17195–4100 (hereafter J1719) and XSS J12270–4859 (hereafter J1227) are presented.

[1] `asd.gsfc.nasa.gov/Koji.Mukai/iphome/iphome.html` as at 30/04/08.

2. Previous observations

J0056 was associated with the *ROSAT* source 1RXS J005528.0+461143, and catalogued as an unidentified object in the *RXTE* all sky survey (Revnivtsev et al. 2004). It was found to have a count rate of 0.71 ± 0.04 ct s^{-1} PCU^{-1} in the 3–8 keV energy band and a photon index of 1.77 ± 0.23. Analysis by Bikmaev et al. (2006) using *SWIFT*/XRT archive data revealed two X-ray sources in the *ROSAT* error circle. One source was present at low energy, which they presumed to be a chromospherically active star. The other source showed a typical spectrum of a CV, with an emission feature close to 6.7 keV. Bikmaev et al. (2006) also carried out optical observations with the 1.5 m Russian-Turkish Telescope. Their photometric data indicated a period of approximately 480 s to be present.

J1719 was detected as an *INTEGRAL* object by Bird et al. (2004); Pandey et al. (2006) found radio galaxies coincident with its error circle and suggested it was extragalactic. Tomsick et al. (2006) confirmed a tentative association of J1719 with the softer X-ray target 1RXS J171935.6–410054 using pointed *Chandra* data. They also reported variability of J1719 in the 0.3–10 keV band and a flux of $2.5^{+0.9}_{-0.4} \times 10^{-11}$ erg cm^{-2} s^{-1}. In calculating this flux they used a power law model and a galactic column density of 0.77×10^{22} cm^{-2} (derived from Dickey & Lockman 1990). Tomsick et al. (2006) also reported the spectral properties of J1719 using public *INTEGRAL* data, finding a flux of 1.9×10^{-11} erg cm^{-2} s^{-1} in the 20–50 keV energy band. Masetti et al. (2006) classified J1719 as a CV based upon its optical spectrum, they also speculated that it may be an IP.

J1227 was found in the *RXTE* all sky survey (Revnivtsev et al. 2004). It was classified as a CV and suggested to be an IP

Article published by EDP Sciences

by Masetti et al. (2006), using optical spectroscopy. Bird et al. (2007) later found J1227 to be an *INTEGRAL* source.

3. Observations and data reduction

Data were obtained from the *RXTE* satellite (Bradt et al. 1993) with the PCA instrument.

In each case initial data reduction was done with the standard FTOOLS, and the flux was normalised according to the number of correctly functioning PCUs. For the lightcurve analysis PCUs 2, 3, and 4 were used; whilst for the spectral analysis only PCU 2 was used. Only the top layer of each PCU was included in the measurements and the time resolution of the data was 16 s. Background subtracted light curves were constructed in four energy bands: 2–4 keV, 4–6 keV, 6–10 keV and 10–20 keV, as well as a combined 2–10 keV band for maximum signal-to-noise.

In the presence of white noise in the data, the power values in the power spectrum are expected to follow an exponential distribution. However, any correlated noise e.g. red noise, will mean the distribution becomes frequency dependent. This makes estimating the significance limits in the power spectra non-trivial. As accreting systems usually show flickering in their lightcurves, it is feasible to believe that there may be a significant red noise component in the data. In order to take this into account in the analysis, the technique introduced in Hakala et al. (2004) was used. The data were equally spaced (apart from the large gaps in between different orbits), so the red noise component was modelled by fitting a second order autoregressive process model to the lightcurves. This model was then used to generate 50 000 synthetic lightcurves with similar red and white noise properties, as well as observing window, to the original datasets. The 95.2%, 99.72% and 99.954% (2, 3 and 4σ respectively) significance limits (as a function of frequency) were then calculated.

To estimate the error on the measured periods we folded the raw data at the period found from the period analysis. We then fitted a curve to this folded data. This curve (repeated over the whole data set) was then subtracted from the raw data leaving residual values. These were then shuffled and added to the fitted curve, yielding a new synthetic raw data set. This synthetic data was then analysed as before. This whole process was repeated ~200 times and the resulting periods were then used to calculate a standard deviation of periods, which was then used as the error estimate.

A mean X-ray spectrum was also extracted for each source, and two spectral models applied to find the best fit, using the XSPEC package. The models considered were a photoelectrically absorbed single temperature bremsstrahlung with a Gaussian at the iron line emission energy (model A), and a photoelectrically absorbed power law with a similar Gaussian (model B).

Table 1. Observing log.

Target	Start time (UTC)	End time (UTC)	Time on target (s)	Good time[a] (s)
J0056	05:27 20/12/07	00:31 22/12/07	84 672	37 800
J1719	18:45 07/01/08	11:16 09/01/08	69 636	35 936
J1227	16:13 28/11/07	16:20 29/11/07	58 183	26 814

[a] Good time is defined as the time that met our selection criteria.

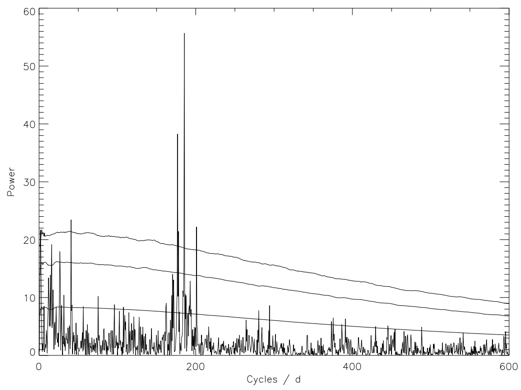

Fig. 1. 2–10 keV periodogram of J0056. Three significance levels, 95.2, 99.7 and 99.954% (2, 3 and 4σ respectively), are superimposed.

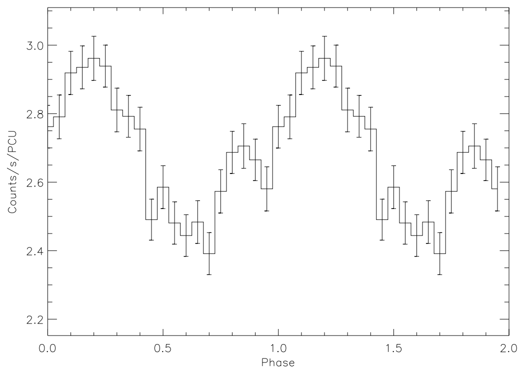

Fig. 2. 2–10 keV lightcurve of J0056 folded at the 465.68 s pulse period with an arbitrary zero point. Two cycles are shown for clarity.

3.1. XSS J00564+4548

J0056 was observed over two consecutive days (see Table 1). The total good time on target (37 800 s) comprised fourteen approximately equal segments of one satellite orbit each. In the 2–10 keV energy band the raw count rate varied between 3.9 and 9.1 ct s^{-1} PCU^{-1}. The background count rate, generated from the calibration files, varied between 2.9 and 4.1 ct s^{-1} PCU^{-1}.

A significant (>4σ) peak was present in the periodogram at ~185 cycles day^{-1} in the 2–10 keV energy band (see Fig. 1). Analysis of the peak gave a pulsation period of 465.68 ± 0.07 s. The data were then folded in each energy band at this period, Fig. 2 shows the result of the 2–10 keV energy band. In each energy band a sinusoid was fitted to the folded data to estimate the modulation depth of the variation (see Table 2). There is a clear decreasing trend in the modulation depth with increasing energy. Clustered around the 185 cycles day^{-1} peak were a series of smaller peaks, spaced apart by ~8 cycles day^{-1}, the largest of which was at 489.0 ± 0.7 s. There was also one other peak detected at above the 4σ level at ~41 cycles day^{-1} (2109 s).

The best spectral fit was a simple photoelectrically absorbed bremsstrahlung model with a Gaussian added. This fit had the parameters kT = 22 ± 2 keV, $n_{\rm H}$ = (0.6 ± 0.4) × 10^{22} cm^{-2} and a Gaussian at 6.5 ± 0.1 keV with a width of 0.3 ± 0.1 keV,

Table 2. Modulation depths of the pulse profile in different energy bands. Modulation depth is defined here as the semi-amplitude of a fitted sinusoid compared to the fitted mean.

	J0056[a]		J1719[b]		J1227[c]	
Energy band (keV)	Modulation depth (%)	Fitted mean (ct s^{-1} PCU^{-1})	Modulation depth (%)	Fitted mean (ct s^{-1} PCU^{-1})	Modulation depth (%)	Fitted mean (ct s^{-1} PCU^{-1})
2–10	8 ± 1	2.69	5 ± 1	4.22	26 ± 2	1.29
2–4	14 ± 2	0.59	4 ± 1	1.01	27 ± 3	0.37
4–6	9 ± 1	0.93	4 ± 1	1.45	25 ± 3	0.45
6–10	5 ± 1	1.17	6 ± 1	1.75	27 ± 3	0.47
10–20	8 ± 3	0.60	5 ± 2	0.72	28 ± 7	0.22

[a] Folded at the 465.68 s period; [b] folded at the possible period of 1 842.4 s; [c] folded at the 859.57 s period.

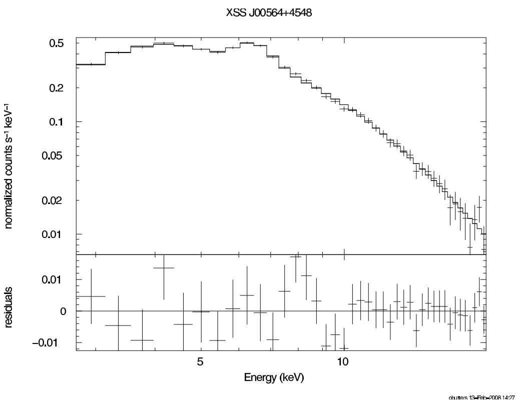

Fig. 3. 2.5–20 keV mean spectrum of J0056 fitted with a photoelectrically absorbed bremsstrahlung plus iron line profile.

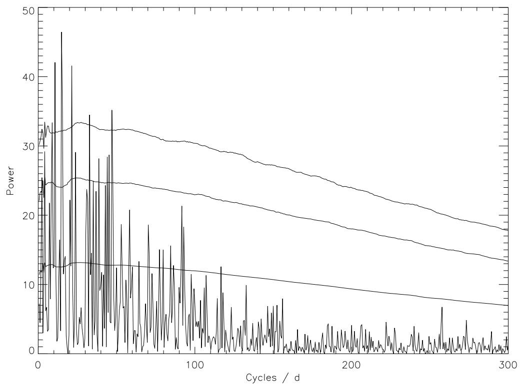

Fig. 4. 2–10 keV periodogram of J1719. Three significance levels, 95.2, 99.7 and 99.954% (2, 3 and 4σ respectively), are superimposed.

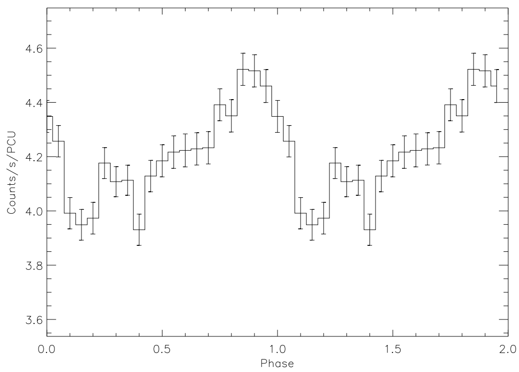

Fig. 5. 2–10 keV folded lightcurve of J1719. Folded at 1 842.4 s with an arbitrary zero point. Two periods are shown for clarity.

which was interpreted as a iron feature ($\chi^2_{\rm reduced} = 0.8$), as shown in Fig. 3 and summarised in Table 3. The table also shows the Galactic column density to the object as derived from the HEASARC $n_{\rm H}$ tool[2].

3.2. IGR J17195–4100

Data were taken over two consecutive days (see Table 1). The total good time on target (35 936 s) was split over twelve approximately equal segments. The raw target flux varied from 5.4–11.3 ct s^{-1} PCU^{-1} and the generated background varied from 2.8–3.9 ct s^{-1} PCU^{-1}.

The periodogram of J1719 had six potential periods that were over 4σ, see Fig. 4. To discount any artifacts arising from the windowing of the raw data we also used the CLEAN algorithm of Lehto (1997). This was a necessary step as the raw data was rather fragmented. This iteratively deconvolved the window function from any signals present in the lightcurve itself. The four peaks between 8 and 22 cycles day^{-1} were found to have a much lower significance in the CLEANed analysis and were thus discounted as an artifact of the windowing. Both remaining peaks above the 4σ level (1 842.4 ± 1.5 s and 2 645.0 ± 4.0 s) were equally viable periods. We selected the 1 842.4 s period to fold the data at, but we stress that the other period was an equally likely candidate period, see Fig. 5. Folding the data in each energy band at this period showed that the modulation depth is constant across them all (see Table 2). We also note that there is a further peak (at just below 3σ significance) at 941 s, whose period is close to half that of the 1842.4 s candidate period, and may therefore represent a first harmonic.

Spectral analysis showed the presence of an iron line in a photoelectrically absorbed bremsstrahlung profile, however the fit was poor with $\chi^2_{\rm reduced} = 3.0$. A better fit was achieved with a power law model as shown in Fig. 6 and Table 3, however

[2] http://heasarc.nasa.gov/cgi-bin/Tools/w3nh/w3nh.pl

Table 3. Spectral fits.

Target	n_H(Galactic) ($\times 10^{22}$ cm^{-2})	Model	n_H ($\times 10^{22}$ cm^{-2})	kT (keV)	Γ	Fe (keV)	σ_{Fe} (keV)	EW (keV)	$\chi^2_{reduced}$	Flux (2–10 keV) ($\times 10^{-11}$ erg cm^{-2} s^{-1})
J0056	0.1	A	0.6 ± 0.3	22 ± 3	–	6.5 ± 0.1	0.3 ± 0.1	0.8	0.8	2.8
J0056	0.1	B	1.9 ± 0.7	–	1.7 ± 0.1	6.5 ± 0.1	0.3 ± 0.1	0.9	1.1	2.9
J1719	0.7	A	0.7 ± 0.1	17 ± 1	–	6.5 ± 0.1	0.1 ± 0.1	0.5	3.0	4.4
J1719	0.7	B	0.7[a]	–	1.8 ± 0.1	6.5 ± 0.1	0.3 ± 0.1	0.7	1.1	4.7
J1227	0.1	A	0.1[a]	14 ± 1	–	6.5[b]	0.1[b]	<0.08	1.3	1.5
J1227	0.1	B	0.1[a]	–	1.8 ± 0.1	6.5[b]	0.1[b]	<0.17	0.8	1.5

[a] Pegged to a lower limit of this value to reflect the Galactic column density; [b] no error as this value was imposed. See notes in the text.

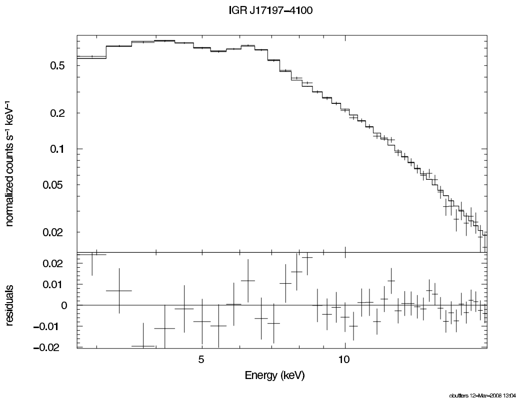

Fig. 6. 2.5–20 keV mean spectrum of J1719 fitted with a photoelectrically absorbed power law plus iron line profile.

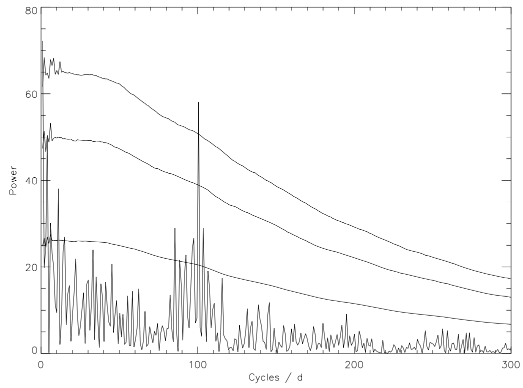

Fig. 7. 2–10 keV periodogram of J1227. Three significance levels, 95.2, 99.7 and 99.954% (2, 3 and 4σ respectively), are superimposed.

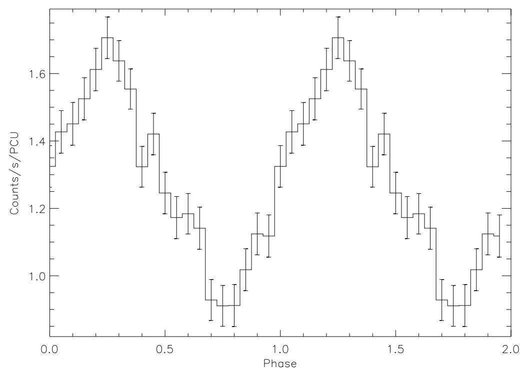

Fig. 8. 2–10 keV lightcurve of J1227 folded at the 859.57 s pulse period with an arbitrary zero point. Two cycles are shown for clarity.

this fit had the column density pegged to a lower limit of 0.7 $\times$ 10^{22} cm^{-2} to reflect the galactic column density.

3.3. XSS J12270–4859

Data were collected over the course of just over one day (see Table 1). Total good time on target (26 814 s) was split over nine segments. The raw target count rate varied between 2.4–10.9 ct s^{-1} PCU^{-1}, the generated background count rate varied between 2.8–3.9 ct s^{-1} PCU^{-1}.

Analysis of the lightcurve showed significant (>4σ) structure at ~100 cycles day^{-1} (see Fig. 7). The peak of this structure was at 859.57 ± 0.64 s. Folding the data at this period showed a clear modulation in the 2–10 keV energy band (see Fig. 8), with approximately the same percentage depth in each energy band (see Table 2). There was also a peak at approximately one cycle day^{-1} in the periodogram; we discounted this peak as it was of the order of the length of the observing run, and was probably a feature of the window function.

In fitting the spectrum, the column density was again pegged to the lower limit of the galactic column density for both the models. The best fit was the power law model, giving $\chi^2_{reduced}$ = 0.8 (see Table 3). There is no significant sign of an excess at the iron line energy (see Fig. 9). A Gaussian was fitted to the expected position of the iron emission feature, but in each case only a small upper limit to the equivalent width was found (<0.08 and <0.17 keV for models A and B respectively).

4. Discussion

4.1. XSS J00564+4548

We interpret the period found here (465.68 ± 0.07 s) as the spin period of the WD in J0056. Bikmaev et al. (2006) gave an approximate value of 480 s from their analysis. To obtain an estimate of the error in their period we consider the *FWHM* of their Lomb-Scargle plot, which gives 480 ± 20 s. Our period determination therefore is in agreement with their optical data. If

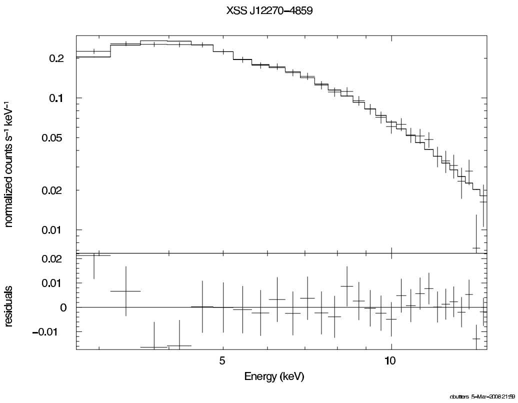

Fig. 9. 2–15 keV mean spectrum of J1227 fitted with a photoelectrically absorbed power law plus Gaussian.

we interpret the second strongest peak in our periodogram as a beat period, this implies the orbital period must be ~2.7 h. This places it in the 2–3 h CV period gap, but we note that there are now several CVs in this range and some mCVs too. This interpretation would also explain the cluster of peaks around the spin period as being various harmonics of the beat period. We are unsure of the origin of the 41 cycles day^{-1} peak as it is too short to be interpreted as an orbital period of a typical IP. The energy dependant modulation depth of the folded lightcurves is common among IPs and indicates an accretion column absorbing structure (Norton & Watson 1989). We also note that the pulse profile of J0056 is very similar in shape to that of FO Aqr (Beardmore et al. 1998).

The spectral fits indicate that the emission process is more likely to be a photoelectrically absorbed single temperature bremsstrahlung process rather than a power law, as is common in IPs. The power law spectral fit is however in agreement with Revnivtsev et al. (2004). The Gaussian at 6.5 keV is identifiable with an iron feature which is also a common aspect of IPs, and agrees with the feature found by Bikmaev et al. (2006).

The *ROSAT* bright source catalogue has no other sources in the *RXTE* PCA field of view of J0056. Bikmaev et al. (2006) showed that there was a source in the error circle of *ROSAT* but it was only present at low energies, and so will not affect this measurement. There is therefore very little contamination from other near by sources. We note that J0056 is significantly brighter now than was reported in the *RXTE* all sky survey (Revnivtsev et al. 2004).

4.2. IGR J17195–4100

The peaks in the periodogram of J1719 (1 842.4 ± 1.5 s and 2 645.0 ± 4.0 s) are typical for a spin period length in IPs. The small peak at 941 s is close to being half the 1 842.4 period, and therefore may be a first harmonic, however, the significance of this peak is below 3σ. We note that if the two longer periods above correspond to the spin and beat periods respectively then this implies an orbital period of approximately 1.7 h. The small, almost constant, modulation depth seen in the lightcurves in each energy band is not present among any other confirmed IPs and implies that the modulation is caused by obscuration as opposed to absorption.

The presence of an iron feature at 6.5 keV is a strong indicator of an IP classification. A significantly better spectral fit is obtained from a power law instead of a bremsstrahlung model. The 2–10 keV fluxes obtained from each of the spectral models are also considerably larger than the value reported by Tomsick et al. (2006) in the 0.3–10 keV energy band. This may be indicative of the simplistic single temperature bremsstrahlung model used here; multi-temperature fits are often needed to model the post-shock flow (see e.g. Ezuka & Ishida 1999). However, the signal to noise and the spectral resolution of the data is such that a complex model may yield non-unique or degenerate results.

There are several X-ray sources near by in the PCA field of view which may contribute to the count rate. We used the *ROSAT* count rate of each source to estimate an *RXTE* count rate using the on line tool webPIMMS[3] (for each source we assume a power law with a photon index of 1.7), we then scaled this value by the response of the PCAs based upon the distance from the source. For this source the contribution is up to 1.1 ct s^{-1} PCU^{-1} in the 2–20 keV energy band, i.e. $\lesssim$20% of the measured count rate. These extra sources will have the effect of decreasing the percentage modulation depth. Moreover, since it is likely that these sources are softer than the target, the contamination will have a greater effect at lower energies. The modulation depth will therefore be reduced more at lower energies. This could make a decreasing modulation depth with energy look like a constant modulation depth with energy. The spectral fitting is likely to be affected by these other sources and they may be the cause of the poor bremsstrahlung model fit. It is also possible these other sources may skew the model fit in such a way that the calculated flux is then overestimated, this may explain why the flux reported here is larger than the Tomsick et al. (2006) value. We emphasise that this is only an estimate of the contamination; the other sources may differ markedly from the assumed spectral shape.

4.3. XSS J12270–4859

J1227 exhibits a structure in the periodogram that indicates it has a period close to 100 cycles day^{-1}. This is consistent with being interpreted as a spin period. It shows an approximately constant modulation in each energy band at the 859.57 ± 0.64 s period, which implies that the process causing this effect must be a geometrical effect causing obscuration instead of absorption.

The upper limit placed on the equivalent width of a potential iron line is small, and goes against the classification of this as an IP, since all IPs exhibit some kind of iron emission features. We do note however that Masetti et al. (2006) did see significant iron features in their optical spectra. The best spectral fit is obtained from a power law profile, the parameters of which are in good agreement with Revnivtsev et al. (2004). Again we note that a multi-temperature bremsstrahlung fit may be more accurate, but beyond the scope of this study. The count rate has not changed significantly since the measurements of Revnivtsev et al. (2004).

This source also has nearby X-ray sources that may contribute to the count rate. Using the same procedure as outlined above we estimate that they may have contributed up to 0.26 ct s^{-1} PCU^{-1} in the 2–20 keV energy band, i.e. $\lesssim$20% of the total count rate. It is again possible that these extra sources would alter the modulation depths, and that the spectral fits are also skewed.

[3] http://heasarc.nasa.gov/Tools/w3pimms.html

5. Conclusion

The unambiguous detection of an X-ray spin period of 465.68 ± 0.07 s in J0056 and its decreasing modulation depth with increasing energy, along with its spectral properties, confirm its inclusion into the IP class. Both J1719 and J1227 clearly exhibit some properties seen in IPs, but not to an extent for us to definitively classify them as such. We do note that it is likely these latter two are IPs, and that their true nature is being masked by the presence of contamination from other sources. X-ray imaging of these sources will definitively decide their fate, allowing their true spectral characteristics to be revealed. All three sources would benefit from long base line optical campaigns to determine their orbital periods and ratify the validity of the periods in J1719 and J1227. If J1227 does turn out to be an IP, then the presence of an X-ray iron feature will have to be reconsidered as a defining characteristic of IPs, since it is not present here.

References

Barlow, E. J., Knigge, C., Bird, A. J., et al. 2006, MNRAS, 372, 224
Beardmore, A. P., Mukai, K., Norton, A. J., Osborne, J. P., & Hellier, C. 1998, MNRAS, 297, 337
Bikmaev, I. F., Revnivtsev, M. G., Burenin, R. A., & Sunyaev, R. A. 2006, Astron. Lett., 32, 588
Bird, A. J., Barlow, E. J., Bassani, L., et al. 2004, ApJ, 607, L33
Bird, A. J., Malizia, A., Bazzano, A., et al. 2007, ApJS, 170, 175
Bradt, H. V., Rothschild, R. E., & Swank, J. H. 1993, A&AS, 97, 355
Butters, O. W., Barlow, E. J., Norton, A. J., & Mukai, K. 2007, A&A, 475, L29
Dickey, J. M., & Lockman, F. J. 1990, ARA&A, 28, 215
Ezuka, H., & Ishida, M. 1999, ApJS, 120, 277
Hakala, P., Ramsay, G., Wheatley, P., Harlaftis, E. T., & Papadimitriou, C. 2004, A&A, 420, 273
Lehto, H. J. 1997, in Applications of time series analysis in astronomy and meteorology, ed. T. Subba Rao, M. B. Priestley, & O. Lessi (London: Chapman and Hall)
Masetti, N., Morelli, L., Palazzi, E., et al. 2006, A&A, 459, 21
Norton, A. J., & Watson, M. G. 1989, MNRAS, 237, 853
Pandey, M., Rao, A. P., Manchanda, R., Durouchoux, P., & Ishwara-Chandra, C. H. 2006, A&A, 453, 83
Ramsay, G., Wheatley, P. J., Norton, A. J., Hakala, P., & Baskill, D. 2008, ArXiv e-prints, 804
Revnivtsev, M., Sazonov, S., Jahoda, K., & Gilfanov, M. 2004, A&A, 418, 927
Tomsick, J. A., Chaty, S., Rodriguez, J., et al. 2006, ApJ, 647, 1309
Warner, B. 1995, Cataclysmic variable stars, Cambridge Astrophysics Series (Cambridge, New York: Cambridge University Press)

C.3 Paper III – *RXTE* confirmation of the intermediate polar status of IGR J15094-6649

This paper (Butters et al. 2009b) gives the results of *RXTE* observations of the hard X-ray target IGR J15094-6649. The results of this paper are also presented in Chapter 2.

A&A 498, L17–L19 (2009)
DOI: 10.1051/0004-6361/200911725

Astronomy & Astrophysics

Letter to the Editor

RXTE confirmation of the intermediate polar status of IGR J15094–6649

O. W. Butters[1,2], A. J. Norton[2], K. Mukai[3,4], and E. J. Barlow[2]

[1] Department of Physics and Astronomy, University of Leicester, Leicester LE1 7RH, UK
e-mail: oliver.butters@star.le.ac.uk
[2] Department of Physics and Astronomy, The Open University, Walton Hall, Milton Keynes MK7 6AA, UK
[3] CRESST and X-ray Astrophysics Laboratory NASA/GSFC, Greenbelt, MD 20771, USA
[4] Department of Physics, University of Maryland, Baltimore County, 1000 Hilltop Circle, Baltimore, MD 21250, USA

Received 26 January 2009 / Accepted 13 March 2009

ABSTRACT

Aims. We aim to establish the X-ray properties of the intermediate polar candidate IGR J15094–6649 and therefore confirm its inclusion into the class.
Methods. 42 856 s of X-ray data from *RXTE* was analysed. Frequency analysis was used to constrain temporal variations and spectral analysis used to characterise the emission and absorption properties.
Results. A spin period of 809.7 ± 0.6 s is present, revealed as a complex pulse profile whose modulation depth decreases with increasing X-ray energy. The spectrum is well fitted by either a 17 ± 4 keV Bremsstrahlung or $\Gamma = 1.8 \pm 0.1$ power law, with an iron emission line feature and significant absorption in each case.
Conclusions. IGR J15094–6649 is confirmed to be an intermediate polar.

Key words. stars: binaries: general – stars: novae, cataclysmic variables – stars: individual: IGR J15094-6649 – X-rays: binaries

1. Introduction

Intermediate polars (IPs) are members of the cataclysmic variables class. They are thought to harbour a magnetic field strong enough to greatly influence the accretion from the main sequence star to the white dwarf, but not strong enough to synchronise the system. For this situation to occur the magnetic field is believed to be in the range of a few MG to tens of MG at the white dwarf surface. This has the effect of channelling the accreting material onto the magnetic poles of the white dwarf and causes a hot dense accretion column to form, which emits high energy X-rays. As the white dwarf spins, the absorbing column density in the line of sight varies; this gives rise to one of the defining characteristics of IPs – X-ray modulation at the spin period with a modulation depth which decreases as the X-ray energy increases. For an exhaustive review of CVs see e.g. Warner (1995).

The exact number of IPs is heavily dependent on the selection criteria used, but the lower end estimate is currently taken to be thirty three[1].

In recent years hard X-ray telescopes (*INTEGRAL* and Swift) have unexpectedly found many known IPs and discovered several candidate systems. This has raised the question of whether a sample of hard X-ray selected candidate IPs would be different from the current soft X-ray selected population. With this in mind the candidate IGR J15094–6649 (hereafter J1509) is studied. This forms part of an ongoing survey to classify hard X-ray selected IPs (Butters et al. 2007, 2008).

[1] http://asd.gsfc.nasa.gov/Koji.Mukai/iphome/iphome.html (IP catalogue version 2008b).

2. Previous observations of J1509

J1509 was discovered in the *INTEGRAL*/IBIS survey as an unclassified object in the 17−60 keV energy band (Revnivtsev et al. 2006).

Masetti et al. (2006) classified J1509 as an IP based upon optical spectra taken at the 1.5 m Cerro Tololo Interamerican Observatory (CTIO) in Chile.

Barlow et al. (2006) also reported *INTEGRAL* data, but in the 20−100 keV energy range this time. Both a Bremsstrahlung and a power law were fitted to the data in order to determine an identification. In both cases a good fit was found; Bremsstrahlung with $kT = 13.8 \pm 5.1$ keV and power law with $\Gamma = 3.6 \pm 0.8$. The flux was given as 1.38×10^{-11} erg s^{-1} cm^{-2} in the 20−100 keV band.

Very recently Pretorius (2009) published optical photometry and spectroscopy of J1509, along with four other candidate IPs from the *INTEGRAL* sample. She detected a clear radial velocity signal at a period of 5.89 ± 0.01 h which was identified as the orbital period of the system, as well as a photometric modulation at 809.42 ± 0.02 s which was taken to be the spin period of the magnetic white dwarf. These results provided very strong indications that J1509 is an IP, and detection of a commensurate pulse period in X-ray data would absolutely confirm its classification.

3. Observations and data reduction

Data were obtained from the *RXTE* satellite (Bradt et al. 1993) with the PCA instrument over two consecutive days, from 30th−31st December 2008. The total time on target was 42 856 s. Initial data reduction was done with the standard FTOOLS. Only the top layer of PCU2 was included in the measurements and we

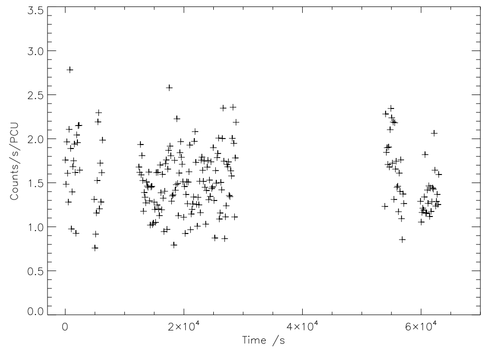

Fig. 1. 2−10 keV background subtracted light curve of J1509. The zero time corresponds to the start of the observations at JD 2 454 830.77312937984. The data is binned into bins of 128 s width. The typical error on each point is 0.26 counts s^{-1} PCU^{-1}.

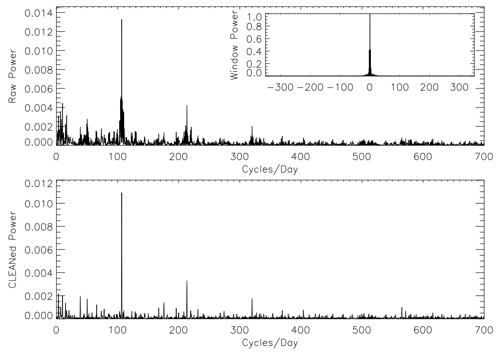

Fig. 2. 2−10 keV CLEANed periodogram. The upper plot shows the raw periodogram, with the window function inset; the lower plot shows the deconvolved (CLEANed) periodogram.

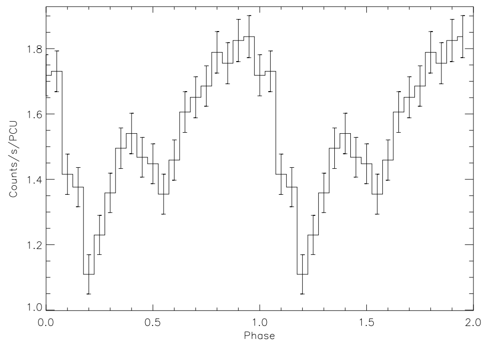

Fig. 3. 2−10 keV light curve folded at the 809.7 s period with an arbitrary zero point. Two cycles are shown for clarity.

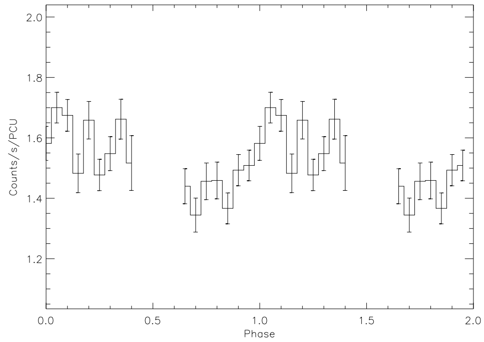

Fig. 4. 2−10 keV light curve folded at the 21 204 s period of Pretorius (2009) with an arbitrary zero point. Two cycles are shown for clarity.

Table 1. Modulation depths of the pulse profile in different energy bands.

Energy band (keV)	Modulation depth (%)	Fitted mean (ct s^{-1} PCU^{-1})
2–10	15 ± 1	1.54
2–4	27 ± 3	0.33
4–6	16 ± 2	0.54
6–10	9 ± 2	0.67
10–20	7 ± 4	0.34

used the standard 2 mode data with a time resolution of 16 s. Background subtracted light curves were constructed in four energy bands: 2–4 keV, 4–6 keV, 6–10 keV and 10–20 keV, as well as a combined 2–10 keV band for maximum signal-to-noise. A mean X-ray spectrum was also extracted.

3.1. Light curve analysis

In the 2−10 keV energy band the raw count rate varied between 2.5 and 6.9 count s^{-1} PCU^{-1}. The background count rate, generated using the faint source background model, varied between 2.9 and 4.1 count s^{-1} PCU^{-1}. The background subtracted 2−10 keV light curve is shown in Fig. 1. The data were subsequently analysed with a variable gain implementation of the CLEAN algorithm (Lehto 1997) to discover any periodicities and discount any aliasing effects. The results of this are shown in Fig. 2.

A strong peak is evident in the CLEANed periodogram at approximately 107 cycles day^{-1}, in the 2−10 keV energy band. Also present are its first and second harmonics at ∼214 and ∼321 cycles day^{-1} respectively. Analysis of the second harmonic peak yields a fundamental pulsation period of 809.7 ± 0.6 s (based on a Gaussian fit to the periodogram). This is in excellent agreement with the optical photometric period detected by Pretorius (2009). Each of the energy resolved light curves were folded at the 809.7 s period, and Fig. 3 shows the result in the 2−10 keV energy band. The modulation depths of the pulse profile were then estimated by fitting a sinusoid to the folded data in each energy band and dividing the semi-amplitude by the fitted mean. The results of this are shown in Table 1.

There is no indication in the power spectrum of the spectroscopic orbital period previously reported by Pretorius (2009). Folding the X-ray light curve at the proposed orbital period yields a profile with no significant coherent modulation (see Fig. 4).

Table 2. Bremsstrahlung (top) and power law (bottom) spectral fitting parameters of J1509. n_{H}(Galactic) = 0.2×10^{22} cm^{-2}.

n_{H} 10^{22} cm^{-2}	kT keV	Γ	Fe keV	σ_{Fe} keV	EW keV	$\chi^2_{\mathrm{reduced}}$	Flux (2–10 keV) 10^{-11} erg cm^{-2} s^{-1}
1.6 ± 1.0	17 ± 4	–	6.4 ± 0.1	0.4 ± 0.1	0.8	0.7	1.5
3.0 ± 1.3	–	1.8 ± 0.1	6.4 ± 0.1	0.4 ± 0.1	0.9	0.8	1.5

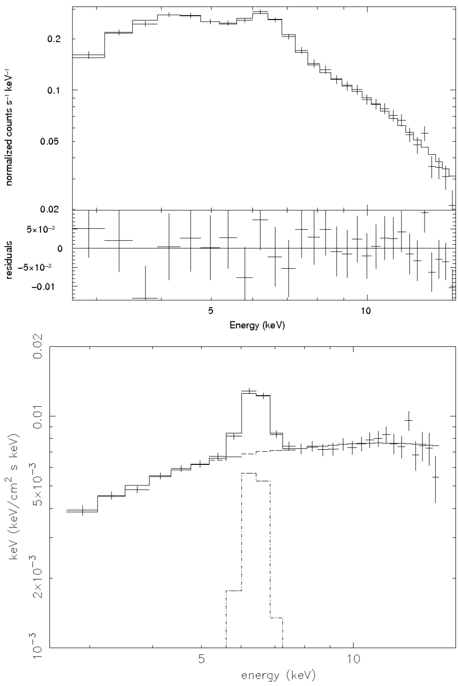

Fig. 5. Folded (*top*) and unfolded (in νF_ν representation, *bottom*) 2.5−15 keV mean spectrum fitted with a photoelectrically absorbed Bremsstrahlung plus iron line profile.

3.2. Spectral analysis

Analysis of the X-ray spectrum was carried out with the XSPEC package. Two models were used for fitting; a photoelectrically absorbed Bremsstrahlung, and a photoelectrically absorbed power law. Both models had an excess at approximately 6.4 keV, so a Gaussian was added to account for the iron line emission. Both models gave a good fit to the data (see Fig. 5 and Table 2).

4. Discussion

The X-ray period found here (809.7 s) is in agreement with the photometric pulsation period found by Pretorius (2009) and is typical of a white dwarf spin period in an IP. Furthermore, the increasing modulation depth with decreasing energy in the folded pulse profiles is an indication that an accretion column absorbing structure is present (Norton & Watson 1989). The complex pulse profile and presence of strong harmonics in the power spectrum are reminiscent of the canonical IP FO Aqr (Beardmore et al. 1998), although unlike that system, there is here no evidence for an additional X-ray modulation at the beat period (841.5 s), which would be indicative of a stream-fed component to the accretion. We note that whilst some IPs exhibit the white dwarf spin period in their X-ray flux, they may show the beat period in optical photometry (for example, AO Psc). This arises due to reprocessing of the X-ray signal, probably from the face of the donor star. In the case of J1509 we can be confident that we are seeing the spin period of the white dwarf in both the optical and X-ray light curves. The length of the X-ray data set probably precludes the detection of the orbital period, or may indicate that the system is seen at relatively low inclination angle (Parker et al. 2005), so no such modulation is present.

Both spectral fits are good and the Bremsstrahlung model in particular is in agreement with that seen in the *INTEGRAL* data at higher energies (Barlow et al. 2006). The fit parameters are typical of those seen in other IPs. The column density is greater than the Galactic column density (as given by the HEASARC n_{H} estimator[1]). This too is typical of IPs and is likely due to absorption by material within the accretion flow. The *ROSAT* Bright Source Catalogue has one other source in the *RXTE* field of view. A count rate for it was estimated using the webPIMMS[2] tool and scaled according to the response of the detector. The count rate of this additional source was small (∼0.04 counts s^{-1} PCU^{-1}) and therefore does not affect our result.

5. Conclusion

IGR J15094–6649 is confirmed as an IP and adds to the growing list of hard X-ray selected magnetic CVs discovered by *INTEGRAL*.

References

Barlow, E. J., Knigge, C., Bird, A. J., et al. 2006, MNRAS, 372, 224
Beardmore, A. P., Mukai, K., Norton, A. J., Osborne, J. P., & Hellier, C. 1998, MNRAS, 297, 337
Bradt, H. V., Rothschild, R. E., & Swank, J. H. 1993, A&AS, 97, 355
Butters, O. W., Barlow, E. J., Norton, A. J., & Mukai, K. 2007, A&A, 475, L29
Butters, O. W., Norton, A. J., Hakala, P., Mukai, K., & Barlow, E. J. 2008, A&A, 487, 271
Lehto, H. J. 1997, in Applications of time series analysis in astronomy and meteorology, ed. T. Subba Rao, M. B. Priestley, & O. Lessi (London: Chapman and Hall)
Masetti, N., Morelli, L., Palazzi, E., et al. 2006, A&A, 459, 21
Norton, A. J., & Watson, M. G. 1989, MNRAS, 237, 853
Parker, T. L., Norton, A. J., & Mukai, K. 2005, A&A, 439, 213
Pretorius, M. L. 2009, MNRAS, in press [arXiv:0901.2841]
Revnivtsev, M. G., Sazonov, S. Y., Molkov, S. V., et al. 2006, Astron. Lett., 32, 145
Warner, B. 1995, Cataclysmic variable stars, Cambridge Astrophys. Ser. (Cambridge, New York: Cambridge University Press)

[1] http://heasarc.nasa.gov/cgi-bin/Tools/w3nh/w3nh.pl
[2] http://www.ledas.ac.uk/pimms/w3p/w3pimms.html

C.4 Paper IV – The accretion flows and evolution of magnetic cataclysmic variables

This paper (Norton et al. 2008) is a continuation of theoretical modelling by Norton et al. (2004). My contributions to this paper are also presented in Chapter 4.

The Astrophysical Journal, 672:524–530, 2008 January 1

THE ACCRETION FLOWS AND EVOLUTION OF MAGNETIC CATACLYSMIC VARIABLES

A. J. Norton and O. W. Butters
Department of Physics and Astronomy, The Open University, Walton Hall, Milton Keynes, MK7 6AA, UK; A.J.Norton@open.ac.uk, O.W.Butters@open.ac.uk

T. L. Parker
Department of Physics and Astronomy, University of Leicester, Leicester, LE1 7RH, UK; tp57@le.ac.uk

and

G. A. Wynn
Astronomy Group, University of Leicester, Leicester, LE1 7RH, UK; gaw@astro.le.ac.uk
Received 2007 July 10; accepted 2007 September 25

ABSTRACT

We have used a model of magnetic accretion to investigate the accretion flows of magnetic cataclysmic variables (mCVs). Numerical simulations demonstrate that four types of flow are possible: disks, streams, rings, and propellers. The fundamental observable determining the accretion flow, for a given mass ratio, is the spin-to-orbital–period ratio of the system. If intermediate polars (IPs) are accreting at their equilibrium spin rates, then for a mass ratio of 0.5, those with $P_{\rm spin}/P_{\rm orb} \lesssim 0.1$ will be disklike, those with $0.1 \lesssim P_{\rm spin}/P_{\rm orb} \lesssim 0.6$ will be streamlike, and those with $P_{\rm spin}/P_{\rm orb} \sim 0.6$ will be ringlike. The spin-to-orbital–period ratio at which the systems transition between these flow types increases as the mass ratio of the stellar components decreases. For the first time we present evolutionary tracks of mCVs, which make it possible to investigate how their accretion flow changes with time. As systems evolve to shorter orbital periods and smaller mass ratios, in order to maintain spin equilibrium their spin-to-orbital–period ratio will generally increase. As a result, the relative occurrence of ringlike flows will increase, and the occurrence of disklike flows will decrease, at short orbital periods. The growing number of systems observed at high spin-to-orbital–period ratios with orbital periods below 2 hr and the observational evidence for ringlike accretion in EX Hya are fully consistent with this picture.

Subject headings: accretion, accretion disks — binaries: close — stars: magnetic fields

1. INTRODUCTION

Magnetic cataclysmic variable stars (mCVs) provide an excellent probe of the accretion process under extreme astrophysical conditions. They are interacting binary stars in which a magnetic white dwarf (WD) accretes material from a late-type companion star via Roche lobe overflow. The WD has a large magnetic moment ($\mu_1 \sim 10^{32}$–10^{35} G cm^3), which has a wide-ranging influence on the dynamics of the accretion flow. The mCVs fall into two distinct classes: the AM Herculis stars (or polars) and the intermediate polars (IPs, or DQ Herculis stars); a comprehensive review may be found in Warner (1995). The rotational periods of the WDs ($P_{\rm spin}$) in polars are generally locked to the orbital period ($P_{\rm orb}$), whereas the WDs in IPs are asynchronous with $P_{\rm spin}/P_{\rm orb} \approx 0.01$–$0.6$. Polars contain the most strongly magnetic WDs, and their synchronism is thought to come about due to the interaction between the magnetic fields of the two stars, which is able to overcome the spin-up torque of the accreting matter (see, e.g., King et al. 1991). IPs fill the parameter space between the strongly magnetic polars and the nonmagnetic CVs. The accretion flows within IPs are known to take on a wide variety of forms, from magnetically confined accretion streams to extended accretion disks, similar to nonmagnetic CVs. This variety has constantly perplexed efforts to understand these objects and is the subject of this work.

In an earlier paper (Norton et al. 2004; hereafter Paper I) we used a model of magnetic accretion to investigate the rotational equilibria of mCVs. We showed that there is a range of parameter space in the $P_{\rm spin}/P_{\rm orb}$ versus μ_1 plane at which rotational equilibrium occurs. This finding allowed us to infer approximate values for the magnetic moments of all known intermediate polars. As a result we established that the number of systems as a function of the WD magnetic moment is distributed approximately according to $N(\mu_1)d\mu_1 \propto \mu_1^{-1}d\mu_1$. In that paper we noted that the spin equilibria correspond to a variety of different types of accretion flow, including disklike accretion at small $P_{\rm spin}/P_{\rm orb}$ values, streamlike accretion at intermediate $P_{\rm spin}/P_{\rm orb}$ values, and accretion fed from a ring at the outer edge of the WD Roche lobe at higher $P_{\rm spin}/P_{\rm orb}$ values. In this paper we investigate these flows in a more systematic manner and examine how the accretion flow varies as a system evolves. In particular, for the first time we determine the evolutionary tracks of IPs at a range of magnetic field strengths and compare these with the observed distribution of IPs.

2. MAGNETIC ACCRETION FLOWS AND THE MAGNETIC MODEL

Full details of how the magnetic accretion flow may be characterized and how we model this may be found in Paper I. Briefly, we assume that material moving within the binary system interacts with the local WD magnetic field via a shear velocity-dependent acceleration. This is analogous to the assumption that the magnetic stresses are dominated by the magnetic tension rather than the magnetic pressure, which will be valid in all but the innermost regions of the flow, close to the WD surface. We thus write the magnetic acceleration as a coefficient (k) multiplied by the difference in velocity between the accreting material and the field lines ($\boldsymbol{v}_\perp$):

$$k(r)\boldsymbol{v}_\perp = \frac{1}{\rho(r)R_c(r)}\frac{B^2(r)}{4\pi}\hat{\boldsymbol{n}}, \qquad (1)$$

where the unit vector $\hat{\boldsymbol{n}}$ is perpendicular to field lines, $\rho(r)$ is the local density of plasma, and $R_c(r)$ is the local radius of curvature

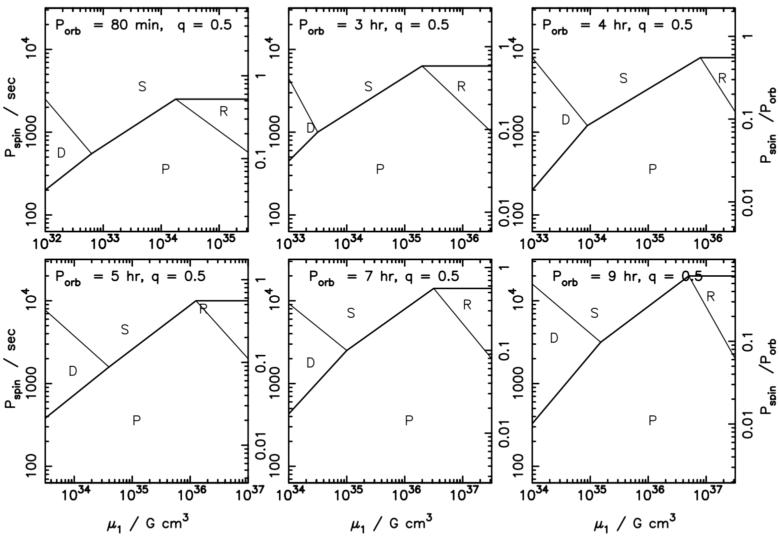

Fig. 1.—Distribution of accretion flow types as a function of orbital period, in the spin period vs. magnetic moment plane, at a mass ratio of $q = 0.5$. The right-hand axes show the spin-to-orbital–period ratio in each case. Approximate regions within which each type of flow is seen are delineated as shown, where "D" stands for disk accretion, "S" for stream accretion, "R" for ring accretion, and "P" for propeller flow. The thick line shows the approximate locus of the equilibrium spin period in each case and marks the boundary between accretion flows that spin up the WD and those that cause it to spin down. Note that the horizontal scale shifts between the panels to enable us to plot the parameter space investigated at each orbital period.

of the field lines. The coefficient k therefore contains the details of the plasma-magnetic field interaction and, as shown in Paper I, it scales as

$$k(r) = k_0 \left(\frac{r}{r_{\rm WD}} \right)^{-3}, \tag{2}$$

where k_0 is the parameter that is input to the modeling code and encodes both the magnetic field strength at the WD surface and the plasma density at the L1 point. A Gaussian distribution of k_0 is used in the model, with typically a standard deviation of 1% around the mean value to represent the range of plasma densities in the flow. Larger values of this Gaussian width result in more "blurred" boundaries between regions displaying different accretion flows (see below) but do not alter the WD equilibrium spin period for a given k_0.

The results we present here were obtained with a three-dimensional particle hydrodynamics code known as HyDisc, using an implementation of the model described fully in Paper I. The calculations are carried out in the full binary potential and include a simple treatment of the gas viscosity. Previous results obtained with HyDisc are described in King & Wynn (1999), Wynn et al. (1997), and Wynn & King (1995). The HyDisc code uses "packets" of plasma injected at the L1 point. The density and size scale of these packets change as they travel toward the white dwarf and they interact individually with the magnetic field lines. This structure mimics the "blobby" accretion seen in (e.g.) AM Her (Heise et al. 1985; Hameury & King 1988), which gives rise to large variations in the density of the flow at the WD surface.

3. FLOW RESULTS

3.1. *Triple Points in the $P_{\rm spin}/P_{\rm orb}$ versus Magnetic Moment Plane*

In Paper I we reported the accretion flows corresponding only to the equilibrium spin periods as a function of orbital period and magnetic field strength. Although mCVs are expected to remain close to equilibrium when considered on long timescales, at a given instant a particular system may be spinning up or spinning down. Indeed, Patterson (1994) predicted that the period derivative of an IP in equilibrium will not be steady. The observed spin-up and spin-down rates in IPs typically correspond to much longer timescales ($\sim 10^9$ yr) than the timescale to reach spin equilibrium ($\sim 10^7$ yr), indicating that systems are only exhibiting random excursions away from equilibrium, probably driven by mass transfer fluctuations.

In order to explore the accretion flows corresponding to the full range of mCV parameter space, including behavior away from spin equilibrium, the magnetic model was run for each combination of parameters in a grid defined by the orbital period ($P_{\rm orb} =$ 80 minutes to 9 hr), spin period ($P_{\rm spin} = 100$ s to 5 hr), magnetic field strength [$k = (10^2\text{–}10^7)(2\pi/P_{\rm orb})$ s^{-1}], and the mass ratio of the two stellar components ($q = M_2/M_1 = 0.2,\ 0.5,\ 0.9$). This corresponds to a range of WD magnetic moments from about 10^{32} to 10^{36} G cm^3. The secular mass transfer rate appropriate to the particular orbital period was assumed in each case. A model based on each combination of parameters was allowed to run to steady state

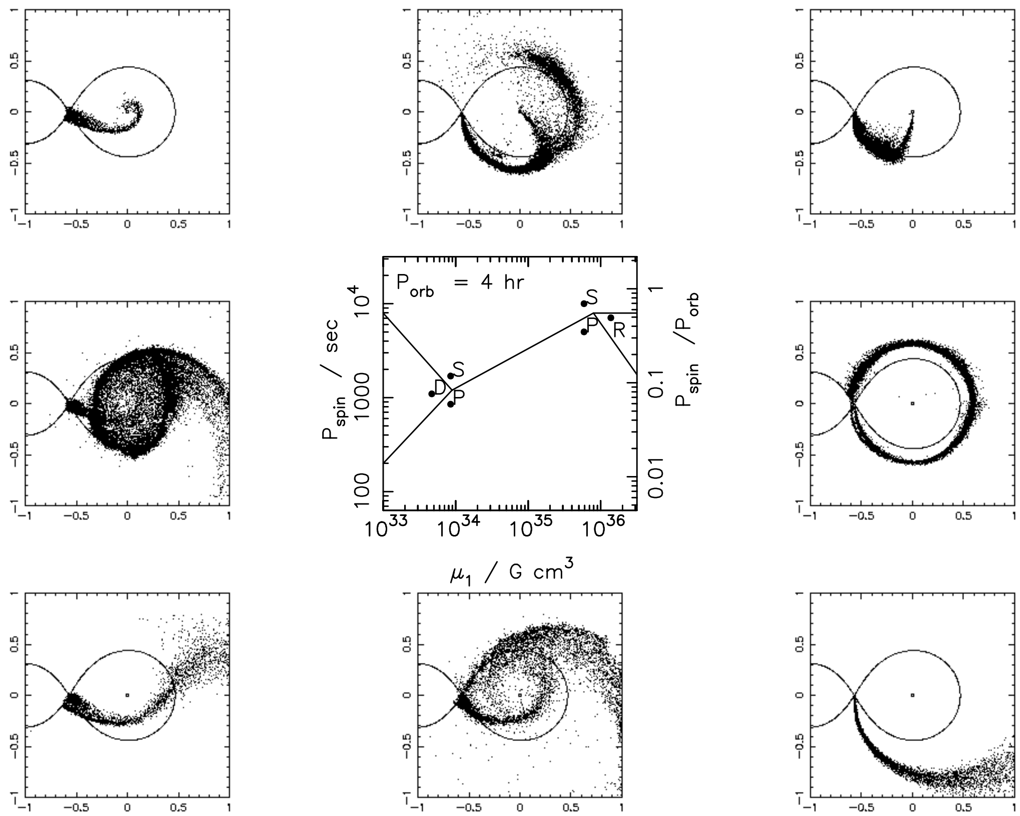

FIG. 2.— Variation of the accretion flow in the vicinity of the boundaries between the different flow types. The models shown are all for $P_{\rm orb}$ = 4 hr and $q = 0.5$. The panels on the left show flows in the vicinity of the stream-disk-propeller triple point, indicated by "S," "D," and "P" on the central panel, while the panels on the right show flows in the vicinity of the stream-ring-propeller triple point, indicated by "S," "R," and "P" on the central panel. The panel at the bottom, center is the accretion flow *at* the stream-disk-propeller triple point and shows characteristics of all three flows at an equilibrium spin period of $\sim$1200 s for $\mu_1 \sim 10^{34}$ G cm^3. The panel at the top center is the accretion flow *at* the stream-ring-propeller triple point and shows characteristics of all three flows at an equilibrium spin period of $\sim$8000 s for $\mu_1 \sim 5 \times 10^{35}$ G cm^3.

before the nature of the resulting accretion was examined. An atlas of these flows may be found in the Ph.D. thesis by Parker (2005). Broadly speaking, each of the flows may be characterized as one of the following:

1. *propellers*: in which most of the material transferred from the secondary star is magnetically propelled away from the system by the rapidly spinning magnetosphere of the WD;

2. *disks*: in which most of the material forms a circulating flattened structure around the WD, truncated at its inner edge by the WD magnetosphere where material attaches to the magnetic field lines before accreting on the WD surface;

3. *streams*: in which most of the material latches onto the field lines immediately and follows these on a direct path down to the WD;

4. *rings*: in which most of the material forms a narrow annulus circling the WD at the outer edge of its Roche lobe, with material stripped from its inner edge by the magnetic field lines before being channeled down to the WD surface.

We show in Figure 1 the results of analyzing where the various flow types occur for systems with a mass ratio of $q = 0.5$. Each panel is for a particular orbital period, and the $P_{\rm spin}$ versus μ_1 plane is divided according to where each flow pattern is observed. We emphasize that the boundaries between the flow types are generally rather blurred, and this blurring increases a little as the Gaussian spread of input k_0 values is increased. Nonetheless, the plane divides into the regions shown, with the bold line marking roughly the locus of the equilibrium spin period in each case, as derived in Paper I. Clearly this marks the boundary between accretion flow types that will generally spin up the WD (streams) and accretion flow types that will generally spin down the WD (propellers). Broadly speaking, if an asynchronous mCV finds itself in a region of parameter space where it is fed by a stream, this will spin up the white dwarf and so shift it downward in the plane of Figure 1 toward the equilibrium line. Similarly, if an asynchronous mCV finds itself in a region of parameter space where the flow takes the form of a propeller, this will spin down the white dwarf and so shift it upward in the plane of Figure 1, again toward

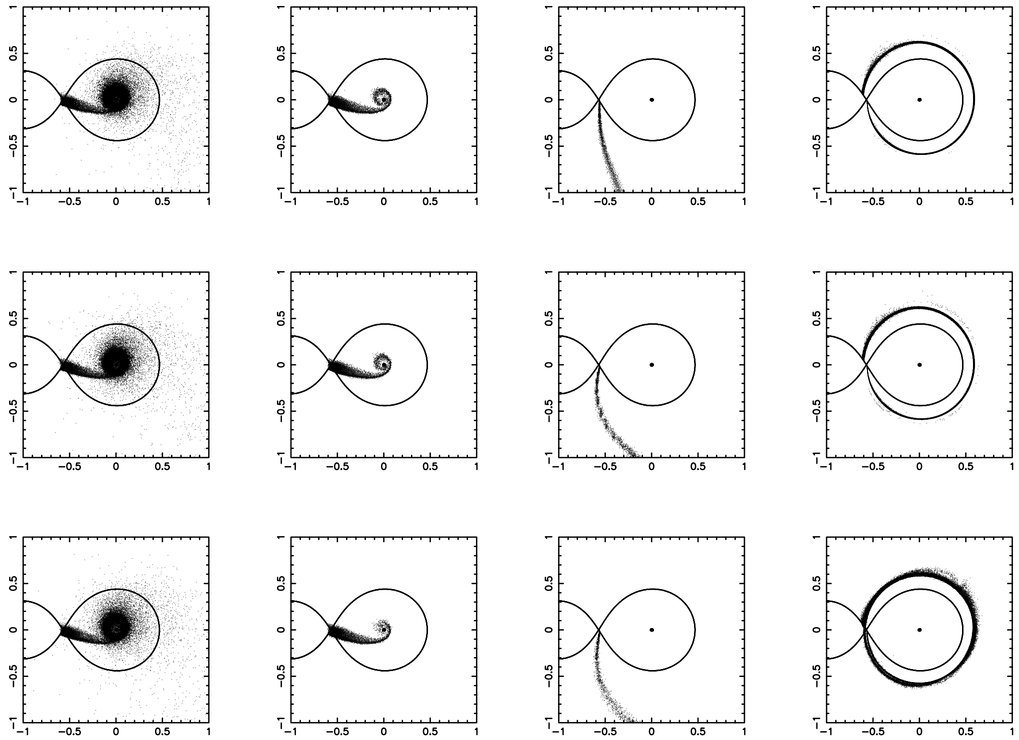

FIG. 3.— Accretion flows for different ranges of plasma density. All the flows shown here are for an orbital period of $P_{\rm orb} = 4$ hr and a mass ratio of $q = 0.5$. In the top row the standard deviation of the Gaussian distribution of k_0 values is 1% of the mean value, in the second row it is 10%, and in the third row 100%. The disklike flows (*first column*) are for a magnetic moment of $\mu_1 \sim 10^{33}$ G cm^3 and a spin period of $P_{\rm spin} = 1000$ s, the streamlike flows (*second column*) are for $\sim 10^{34}$ G cm^3 and 5000 s, the propeller-like flows (*third column*) are for $\sim 10^{35}$ G cm^3 and 1000 s, and the ringlike flows (*fourth column*) are for $\sim 2 \times 10^{36}$ G cm^3 and 5000 s.

the equilibrium line. We note that the accretion flow in the (possibly) magnetic system WZ Sge was modeled by Matthews et al. (2007) who derived a ringlike flow with a strong magnetic propeller in that case. This system contains a rapidly spinning white dwarf ($P_{\rm spin} = 28$ s) and shows that other solutions are possible in non-equilibrium situations such as this.

We note that the disk- and ringlike flows we see can each maintain the white dwarf close to spin equilibrium through a combination of accretion and ejection of material. As noted in Paper I, at equilibrium in the disk- and ringlike flows, angular momentum from the WD is passed back to the accreting material, some of which is lost from the outer edge of the ring or disk to maintain equilibrium. Elsewhere in the parameter space at equilibrium, a stream-propeller combination is seen, which we have previously referred to as a "weak propeller." As shown in Figure 2, close to the stream-disk-propeller triple point and the stream-ring-propeller triple point, the equilibrium flows are a combination of the various flow types. In each case at equilibrium the angular momentum accreted by the WD is balanced by an equal amount lost from the system via material that is magnetically propelled away from the WD. This, after all, is the definition of the equilibrium spin period. Hence, if real IPs sit at their equilibria they will exhibit accretion flows that are disk-, stream-, or ringlike, each with a component of the flow that is propelled away.

As can be seen in Figure 1, both triple points move to smaller magnetic moments as the orbital period decreases. However, for this mass ratio, the triple points occur at the *same* spin-to-orbital–period ratio at all orbital periods. In particular, the lower triple point is always close to $P_{\rm spin}/P_{\rm orb} \sim 0.1$, while the upper triple point is always close to $P_{\rm spin}/P_{\rm orb} \sim 0.6$. Hence, for a mass ratio of 0.5, if IPs are accreting at their equilibrium spin rates, those with $P_{\rm spin}/P_{\rm orb} \lesssim 0.1$ will be disklike, those with $0.1 \lesssim P_{\rm spin}/P_{\rm orb} \lesssim 0.6$ will be streamlike, and those with $P_{\rm spin}/P_{\rm orb} \sim 0.6$ will be ringlike. Equilibrium is not possible for $P_{\rm spin}/P_{\rm orb} \gtrsim 0.6$, until a system reaches synchronism (and is therefore a polar, exhibiting stream-fed accretion once more). Details of the synchronization condition are given in Paper I.

3.2. *Changing the Range of Plasma Density*

Changing the spread in the input k_0 value mimics changing the range of plasma density throughout the flow. For the simulations described above, the k_0 values had a Gaussian distribution with a standard deviation of 1% of the mean value. Increasing this width to 10% or 100% results in the changes to the flow shown in Figure 3. These simulations each correspond to a system with $P_{\rm orb} = 4$ hr and $q = 0.5$ and sit in the four regions of the $P_{\rm spin}/P_{\rm orb}$ versus μ_1 plane identified above. In this case, the disklike flow corresponds to a magnetic moment of $\sim 10^{33}$ G cm^3

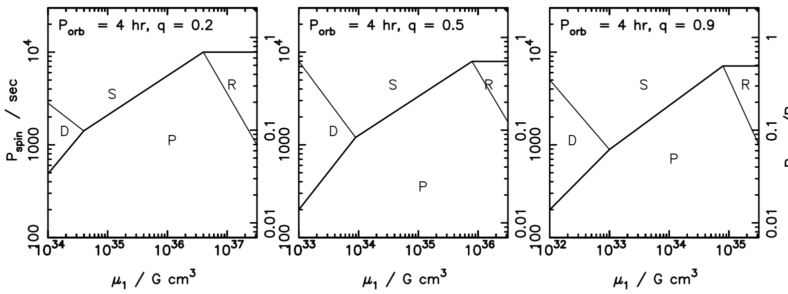

FIG. 4.— Distribution of accretion flow types for mass ratios of $q = 0.2$, 0.5, and 0.9 at an orbital period of $P_{orb} = 4$ hr, in the spin period vs. magnetic moment plane. The right-hand axes show the spin-to-orbital–period ratio in each case. "D" stands for disk accretion, "S" for stream accretion, "R" for ring accretion, and "P" for propeller flow. The thick line shows the approximate locus of the equilibrium spin period in each case and marks the boundary between accretion flows that spin up the WD and those that cause it to spin down.

and a spin period of 1000 s, the streamlike flow to $\sim 10^{34}$ G cm^3 and 5000 s, the propeller-like flow to $\sim 10^{35}$ G cm^3 and 1000 s, and the ringlike flow to $\sim 2 \times 10^{36}$ G cm^3 and 5000 s. As can be seen, the four types of flow are still readily classified, and the effect of broadening the range of plasma densities in each model is minimal.

3.3. *Changing the Mass Ratio*

Changing the mass ratio of the stars in the system changes where the equilibrium spin period occurs. Figure 4 shows representative diagrams for mass ratios of $q = 0.2$, 0.5, and 0.9 for the case of a 4 hr orbital period. The same pattern of accretion flow behaviors is seen, but the triple points move to larger P_{spin}/P_{orb} ratios and larger WD magnetic moments as the mass ratio decreases.

King & Wynn (1999) noted that mCVs have an equilibrium condition specified by $R_{co} \sim R_{circ}$. Here R_{co} is the corotation radius, namely, that at which matter in local Keplerian rotation corotates with the magnetic field of the white dwarf, and R_{circ} is the circularization radius, namely, that at which the specific angular momentum equals that of matter at the inner Lagrangian point. This, in turn, yields the condition

$$\frac{P_{spin}}{P_{orb}} \sim (1+q)^2(0.500 - 0.227 \log q)^6. \quad (3)$$

We identify this equilibrium with the lower triple point in Figures 1 and 4. For the three mass ratios examined here (i.e., $q =$ 0.2, 0.5, and 0.9), equation (3) predicts spin-to-orbital–period ratios of 0.118, 0.076, and 0.064, respectively. From our simulations, the triple points are at spin-to-orbital–period ratios of 0.097, 0.083, and 0.063, in good agreement with the predictions.

King & Wynn (1999) also noted another possible equilibrium, where $R_{co} \sim b$, i.e., the distance from the white dwarf to the inner Lagrangian point. This yields the condition

$$\frac{P_{spin}}{P_{orb}} \sim (0.500 - 0.227 \log q)^{3/2}. \quad (4)$$

We identify this equilibrium with the upper triple point in Figures 1 and 4, as it indicates ringlike accretion flow confined to the outer edge of the WD's Roche lobe. For the three mass ratios examined here (i.e., $q = 0.2$, 0.5, and 0.9), equation (4) predicts spin-to-orbital–period ratios of 0.53, 0.43, and 0.36, respectively. From our simulations, the triple points are at spin-to-orbital–period ratios of 0.69, 0.56, and 0.49. The slightly higher ratios observed probably reflect the fact that we observe ringlike structures to form just outside the WD's Roche lobe, rather than at the edge of the lobe itself.

4. DISCUSSION

4.1. *The Observed Distribution of Intermediate Polars*

Figure 5 shows the distribution of currently known mCVs in the P_{spin} versus P_{orb} plane. The diagonal lines represent loci of constant spin-to-orbital–period ratio corresponding to the triple points at each of three mass ratio values. They therefore divide the plane into regions where different accretion flows may be expected to occur. Regions below any of the three lines corresponding to the stream-disk-propeller triple points for mass ratios of 0.2, 0.5, and 0.9 indicate where disklike flows can occur; regions between any of these three lines and the three lines corresponding to the stream-ring-propeller triple points for mass ratios of 0.2, 0.5, and 0.9 indicate where streamlike flows can occur; and the region around these upper three lines indicate where ringlike flows will be most likely to occur.

As can be seen, at least half of the IPs cluster around the region where the spin-to-orbit–period ratio is in the range $0.05 \lesssim P_{spin}/P_{orb} \lesssim 0.15$, which characterizes the stream-disk-propeller triple point for plausible mass ratios. Assuming these systems are accreting close to their equilibrium spin period, they are all therefore likely to exhibit accretion flows that resemble the combination disk-stream-propeller–like flow shown in the bottom center panel of Figure 2.

There is a growing number of "EX Hya–like" systems below a 2 hr orbital period. Many of these (e.g., SDSS J023322.61+005059.5 [Southworth et al. 2006], SDSS J233325.92+152222.1 [Southworth et al. 2007], DW Cnc [Patterson et al. 2004], V1025 Cen [Hellier et al. 2002], as well as EX Hya itself) have high P_{spin}/P_{orb} ratios in the range 0.4–0.7. As noted in Paper I, they are likely to be characterized by ringlike accretion if they are at equilibrium. We note that this suggestion has recently received considerable support from the spectroscopic observations of EX Hya presented by Mhlahlo et al. (2007). The velocities they observed (in the range 500–600 km s^{-1}) suggested that in this system material circulates the WD near to its Roche lobe and that accretion curtains are fed from a ring at this radius. This is exactly as predicted by our simulations.

Finally, the systems at very small P_{spin}/P_{orb} ratios ($\lesssim 0.01$) are likely to be either disklike accretors or, if they are out of equilibrium like AE Aqr, strong magnetic propellers.

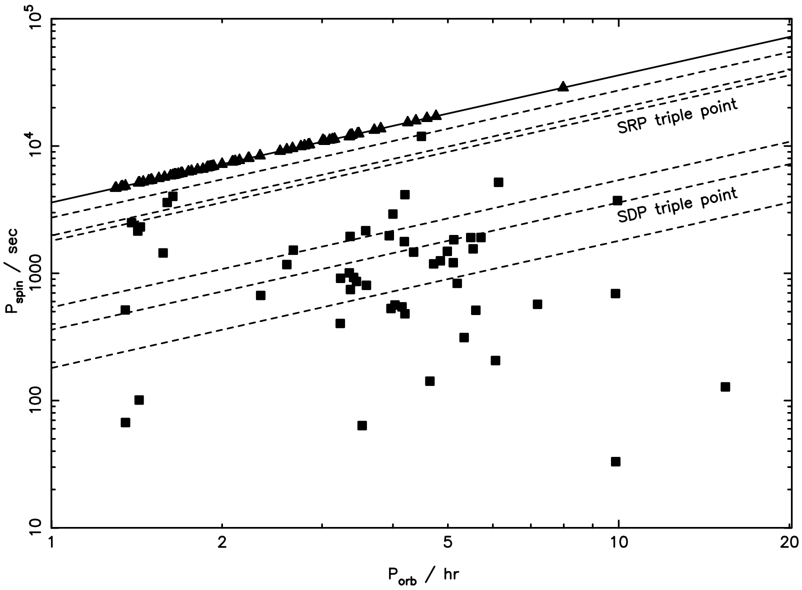

FIG. 5.—Known mCVs distributed throughout $P_{\rm spin}$ vs. $P_{\rm orb}$ parameter space. Polars are indicated by triangles, and IPs by squares. The lower set of three diagonal lines corresponds to the spin-to-orbital–period ratio of the stream-disk-propeller triple point at mass ratios of 0.2, 0.5, and 0.9 (*top to bottom*). The top set of three diagonal lines corresponds to the stream-ring-propeller triple point for the same mass ratios.

Given that there are likely to be roughly equal numbers of magnetic CVs per decade of magnetic field strength (as derived in Paper I), we can comment on the expected distribution of accretion flows among the observed population of IPs. Examining the distribution of accretion flow types in Figure 1, and assuming that all IPs are close to their spin equilibria at all times, we can expect there to be relatively more disklike accretors at long orbital periods and relatively more ringlike accretors at short orbital periods. The number of streamlike accretors is likely to be roughly constant at all orbital periods, as the region between the two triple points occupies about one and a half decades of magnetic moment in each panel of Figure 1.

4.2. *The Evolution of Intermediate Polars*

The observed distribution of IPs in the spin-period–orbital-period plane is a result of observing systems with a range of magnetic field strengths at different stages in their evolution. Assuming that they remain close to their equilibrium spin periods at all times, we can investigate how the observed distribution may be understood in terms of our results.

As IPs evolve, like all CVs, their mass ratio ($q = M_2/M_1$) will decrease and they will move to shorter orbital periods as they lose angular momentum via a combination of magnetic braking and gravitational radiation. As a system evolves in this way, if the magnetic locking torque ($\propto \mu_1\mu_2/a^3$) exceeds the accretion torque, it may synchronize and emerge as a polar. As noted in Paper I, the reason we see several intermediate polars at short orbital periods may be because their secondary stars have weak magnetic field strengths and so the magnetic locking torque is ineffective. Alternatively, the magnetic fields of the two stars may be misaligned in some way so as to minimize the effectiveness of this mechanism.

In order to investigate the variation in spin period and accretion flow as intermediate polars evolve, we took a typical theoretical evolutionary track of a cataclysmic variable, and followed this as it evolves to the orbital period minimum. In this evolutionary track, the WD had a constant mass of 1 $M_\odot$ and the mass ratio decreased from $q = 1.18$ at $P_{\rm orb} = 9$ hr to $q = 0.11$ at $P_{\rm orb} = 80$ minutes. The mass accretion rate at each instant was determined from the evolutionary model. We ran accretion flow simulations for three different WD magnetic moments, namely, $\mu_1 = 10^{32}$ G cm^3 (i.e., $B_{\rm WD} = 0.6$ MG), $\mu_1 = 10^{33}$ G cm^3 (i.e., $B_{\rm WD} = 6$ MG), and $\mu_1 = 10^{34}$ G cm^3 (i.e., $B_{\rm WD} = 60$ MG). For each field value, we determined the equilibrium spin period of the white dwarf, following the same method as the one used in Paper I, at a range of orbital periods along the evolutionary track.

The results of this, assuming that the systems under study do not synchronize, are shown in Figure 6. In order to maintain spin equilibrium as a system evolves to shorter orbital periods, the WD spin period will generally change in the manner shown. Note that since both the mass ratio and orbital period of the system vary continuously as the system evolves, the progress of the system cannot be easily tracked across the panels of Figure 1 or 4. In particular, since a decrease in orbital period causes the triple points to move to smaller magnetic moments, while a decrease in mass ratio causes the triple points to move to larger magnetic moments, the behavior of a given system is not easy to predict. Nevertheless, it is apparent from our simulations that as systems evolve, their spin-to-orbital–period ratios will generally increase and their accretion flows will become less disklike and more streamlike. By the time they have crossed the period gap, the accretion flows are likely to be ringlike, and systems (if not synchronized) will appear similar to EX Hya with a large spin-to-orbital–period ratio. As noted above, this has

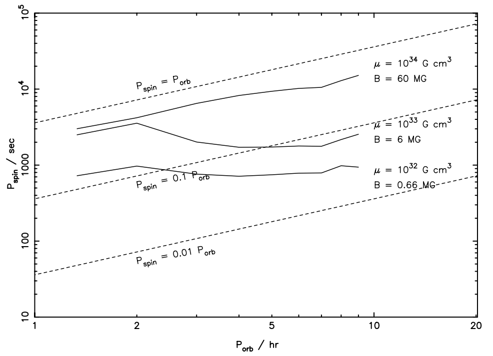

FIG. 6.— Evolution of a magnetic CV with a solar-mass WD whose magnetic moment is 10^{34}, 10^{33}, or 10^{32} G cm^3, assuming that it does not synchronize. Evolution proceeds from right to left in each case. Diagonal dashed lines indicate tracks of constant spin-to-orbital–period ratio.

been supported by the recent observations of EX Hya presented by Mhlahlo et al. (2007), which show evidence for a ringlike accretion flow. Furthermore, the growing number of systems discovered with high spin-to-orbital–period ratios at short orbital periods, as noted earlier, provides additional support for the picture we have outlined.

We also note that Cumming (2002) has suggested that the relatively high accretion rates in IPs may overcome ohmic diffusion, such that magnetic flux is advected into the interior of the white dwarf, reducing the surface magnetic field strength. This effective burying of the WD magnetic field would make IPs appear less magnetic than they really are. Under this scenario, when IPs emerge below the period gap after magnetic braking has presumably turned off, their accretion rates will be substantially lower, and their "true" magnetic field strengths might be expected to emerge. With a higher effective magnetic moment, at a shorter orbital period, systems will be in spin equilibrium farther to the right along the tracks in Figure 1 or 4, thus making a ringlike accretion flow even more likely for those systems that have not synchronized to become polars. In terms of Figure 6, one can imagine a system jumping from a lower magnetic field track to one corresponding to a higher magnetic field strength, as it emerges below an orbital period of 2 hr. However, we also note that Cumming's suggestion, which was extrapolated from the case of accreting neutron stars, must be treated with caution, as the timescale of the Rayleigh-Taylor instability in the upper layers of an accreting WD differs substantially from that in neutron stars (Romani 1990). This may mean that the flows in WDs are not so easily buried after all. Furthermore, nova outbursts in accreting WDs will clear away much of the accreted layer, thus helping to restore the field of the WD.

5. CONCLUSIONS

Using a three-dimensional particle hydrodynamical model of magnetic accretion, we have demonstrated that broadly four types of accretion flow are possible in mCVs: disks, streams, rings, and propellers. We have shown that the equilibrium spin periods in asynchronous mCVs, for a given orbital period and magnetic moment, occur where the flow changes from a type characterized by spin up (i.e., streamlike) to one characterized by spin down (i.e., propeller-like). As a result, the plane of WD spin period versus WD magnetic moment divides into four regions, one for each type of accretion flow, and contains a pair of triple points at which stream-disk-propeller and stream-ring-propeller flows coexist. The first of these corresponds to when the corotation radius is equal to the circularization radius, and the second is when the corotation radius is equal to the distance from white dwarf to the L1 point. Changing the orbital period does not alter the spin-to-orbital–period ratios at which these triple points occur, although they do move to smaller WD magnetic moments as the orbital period decreases. If IPs are accreting at their equilibrium spin rates, then for a mass ratio of 0.5, those with $P_{\rm spin}/P_{\rm orb} \lesssim 0.1$ will be disklike, those with $0.1 \lesssim P_{\rm spin}/P_{\rm orb} \lesssim 0.6$ will be streamlike, and those with $P_{\rm spin}/P_{\rm orb} \sim 0.6$ will be ringlike. In each case, at equilibrium some material is also propelled away from the system to maintain angular momentum balance. Decreasing the mass ratio increases the $P_{\rm spin}/P_{\rm orb}$ ratio at the stream-disk-propeller and stream-ring-propeller triple points and also increases the WD magnetic moments at which they occur.

At long orbital periods disklike accretion flows are likely to be predominant, while at short orbital periods the number of systems displaying ringlike accretion flows will increase. The relative number of systems displaying streamlike accretion flows is predicted to be roughly constant at all orbital periods. As IPs evolve to shorter orbital periods and smaller mass ratios, in order to maintain spin equilibrium their spin-to-orbital–period ratios will generally increase. Those systems at short orbital periods that avoid synchronization are likely to appear similar to EX Hya, with a large spin-to-orbital–period ratio and a ringlike accretion flow, as recently seen by Mhlahlo et al. (2007).

REFERENCES

Cumming, A. 2002, MNRAS, 333, 589
Hameury, J.-M., & King, A. R. 1988, MNRAS, 235, 433
Heise, J., Brinkman, A. C., Gronenschild, E., Watson, M. G., King, A. R., Stella, L., & Kieboom, K. 1985, A&A, 148, L14
Hellier, C., Wynn, G. A., & Buckley, D. A. H. 2002, MNRAS, 333, 84
King, A. R., Frank, J., & Whitehurst, R. 1991, MNRAS, 250, 152
King, A. R., & Wynn, G. A. 1999, MNRAS, 310, 203
Matthews, O. M., Speith, R., Wynn, G. A., & West, R. G. 2007, MNRAS, 375, 105
Mhlahlo, N., Buckley, D. A. H., Dhillon, V. S., Potter, S. B., Warner, B., & Woudt, P. 2007, MNRAS, 378, 211
Norton, A. J., Wynn, G. A., & Somerscales, R. V. 2004, ApJ, 614, 349 (Paper I)
Patterson, J. 1994, PASP, 106, 209
Patterson, J., et al. 2004, PASP, 116, 516
Parker, T. L. 2005, Ph.D. thesis, Open Univ.
Romani, R. W. 1990, Nature, 347, 741
Southworth, J., Gaensicke, B. T., Marsh, T. R., de Martino, D., & Aungwerojwit, A. 2007, MNRAS, 378, 635
Southworth, J., Gaensicke, B. T., Marsh, T. R., de Martino, D., Hakala, P., Littlefair, S., Rodriguez-Gil, P., & Szkody, P. 2006, MNRAS, 373, 687
Warner, B. 1995, Cataclysmic Variable Stars (Cambridge: Cambridge Univ. Press)
Wynn, G. A., & King, A. R. 1995, MNRAS, 275, 9
Wynn, G. A., King, A. R., & Horne, K. D. 1997, MNRAS, 286, 436

C.5 Paper V – Discovery of polarized emission from the long period intermediate polar RX J2133.7+5107

This paper (Katajainen et al. 2007) is the first of a series of papers looking at circular polarization in intermediate polars. This data set is based on an observing run of mine in La Palma in July and August 2006. The data presented here is also presented in Chapter 3.

A&A 475, 1011–1018 (2007)
DOI: 10.1051/0004-6361:20077618

Astronomy & Astrophysics

Discovery of polarized emission from the long period intermediate polar RX J2133.7+5107*

S. Katajainen[1], O. W. Butters[2], A. J. Norton[2], H. J. Lehto[1,3], and V. Piirola[1,4]

[1] Tuorla Observatory, University of Turku, Väisäläntie 20 21500, Piikkiö, Finland
e-mail: [sekataja;hlehto;piirola]@utu.fi
[2] Department of Physics and Astronomy, The Open University, Walton Hall, Milton Keynes MK7 6AA, UK
e-mail: [o.w.butters;A.J.Norton]@open.ac.uk
[3] Department of Physics, 20014 University of Turku, Finland
[4] Vatican Observatory, 00120 Cittá del Vaticano

Received 6 April 2007 / Accepted 18 September 2007

ABSTRACT

Aims. We intended to investigate the magnetic field properties of the recently identified intermediate polar RX J2133.7+5107.
Methods. We carried out UBVRI photopolarimetric observations of the target using TURPOL on the Nordic Optical Telescope over 2 nights in July/August 2006.
Results. We found that RX J2133.7+5107 emits circularly polarized light in all UBVRI bands (up to 3%). This is the first detection of circular polarization in this object. The circular polarization modulations and flux variations give hints of cyclotron beaming effects and suggest that the field strength in RX J2133.7+5107 is possibly one of the highest found amongst the IPs.
Conclusions. The highly asynchronous rotation of RX J2133.7+5107 (the spin to orbital period ratio is ~0.022), suggests that it has only recently come into contact and although it is likely to evolve into a polar, it is currently a long way from doing so. We suggest a possible link between the detection of a soft X-ray blackbody component and polarized optical emission in intermediate polars.

Key words. stars: binaries: close – stars: magnetic fields – polarization – stars: novae, cataclysmic variables – stars: individual: RX J2133.7+5107

1. Introduction to magnetic cataclysmic variables

Cataclysmic Variables (CVs) are binary stars where a low mass main sequence star (the secondary) transfers matter via Roche lobe overflow onto a compact white dwarf (WD) primary. One group of CVs, among their many subclasses, is the magnetic CVs (mCVs) (Cropper 1990). In these systems the WD has a strong enough magnetic field to channel the accreting matter along the magnetic field lines toward the magnetic poles near the surface of the WD. Just above the magnetic poles the accretion flow forms a strong shock, as accreted matter is decelerated from supersonic to subsonic speeds. This matter then cools, emitting hard X-rays ($kT \sim 10$–30 keV) as bremsstrahlung radiation and cyclotron radiation in the optical and infrared (Cropper 1990; Warner 1995).

In mCVs where the magnetic field strength is of the order tens or even hundreds of MG, ranging from 7 MG (V2301 Oph, Ferrario et al. 1995) to 230 MG (AR UMa, Schmidt et al. 1996), the strong magnetic field prevents the formation of an accretion disc, and the matter follows the field lines from the inner Lagrange point down to the surface of the WD. In addition, the magnetic locking torque balances the accretion torque and the spin of the WD is synchronized with the orbital period (typically $\lesssim 2$ h). These systems are known as polars.

Those mCVs with a slightly weaker magnetic field ($B \leq 10$ MG is generally assumed, see Warner 1995) do generally possess an accretion disc. In these systems, known as intermediate polars (IPs), the WDs typically have spin periods of the order of ~1000 s and are asynchronous with the orbit, which typically has a period of a few hours. The subclass of rapidly spinning IPs, with spin periods from 31 s (AE Aqr) to of order a hundred seconds (DQ Her: 142 s) are occasionally referred to as DQ Her stars, but often in the literature *all* IPs are referred to as DQ Her stars (for a comprehensive review of intermediate polars see Patterson 1994).

Many IPs have a WD spin period which is about one tenth of the orbital period of the binary system and this has long been suspected to be the case in IPs in general. If IPs are in spin equilibrium, a period ratio of about 0.1 is expected for typical mass ratios, as long as the co-rotation radius (i.e. that at which material in a local Keplerian orbit co-rotates with the magnetic field of the white dwarf) is at the circularization radius (i.e. that at which the specific angular momentum equals that of matter at the inner Lagrangian point). However, in the last 5 years, several IPs with rather different spin/orbital period ratios have been found, e.g 1RXS J173021.5–055933 ($P_{\rm spin}/P_{\rm orb} = 0.0023$, Gaensicke et al. 2005); HS2331+3905 ($P_{\rm spin}/P_{\rm orb} = 0.0138$, Araujo-Betancor et al. 2005); 1RXS J1548–4528 (NY Lup) ($P_{\rm spin}/P_{\rm orb} = 0.0195$, Haberl et al. 2002; de Martino et al. 2006a); Swift J0732.5–1331 ($P_{\rm spin}/P_{\rm orb} = 0.0254$, Patterson et al. 2006); 1RXS J070407.9+262501 ($P_{\rm spin}/P_{\rm orb} = 0.0320$, Gaensicke et al. 2005); HS0943+1404 ($P_{\rm spin}/P_{\rm orb} = 0.276$, Rodrigues-Gil et al. 2005); DW Cnc ($P_{\rm spin}/P_{\rm orb} = 0.448$, Patterson et al. 2004); SDSS J233325.92+152222.1 ($P_{\rm spin}/P_{\rm orb} = 0.501$, Southworth et al. 2007) and SDSS J023322.61+005059.5 ($P_{\rm spin}/P_{\rm orb} = 0.625$, Southworth et al. 2006). In the most

* Based on observations obtained at the Nordic Optical Telescope at the Roque de los Muchachos Observatory in La Palma.

Article published by EDP Sciences and available at http://www.aanda.org or http://dx.doi.org/10.1051/0004-6361:20077618

extreme cases, such as AE Aqr, the spin to orbital period ratio is as small as ~0.001.

On the other hand, some polars are known to have a WD spin period which differs by a few percent from their orbital period: V1500 Cyg (Stockman et al. 1988), BY Cam (Silber et al. 1992), V1432 Aql (RX J19402–1025) (Patterson et al. 1995; Geckeler & Staubert 1997), CD Ind (RX J2115–58) (Schwope et al. 1997), and RX J0524+42 (Schwarz et al. 2004). The polar RX J0524+42 is a key target for studies in mCV evolution as it could be the first transition object between the IPs and polars where the white dwarf is currently in the process of synchronization. In addition to this, the polars WW Hor and DP Leo have shown secular shifts in their accretion regions, which may be due to small asynchronisms in these binaries (Bailey et al. 1993). One of these asynchronous polars has signs of a recent nova outburst (V1500 Cyg), which may explain the unsynchronized nature of the WD spin period in that case. Although a similar cause might be postulated in the other asynchronous polars, none of them have direct evidence of recent nova explosions.

Polars are predominantly soft X-ray emitters, whilst almost all IPs show quite a hard X-ray spectrum. This has been reinforced by the recent discovery that IPs form a significant population amongst the catalogue of *INTEGRAL* sources (Barlow et al. 2006). Recently, however, Evans & Hellier (2007) have argued that most IPs show a soft blackbody component too. Whilst the soft component in Polars is believed to be due to blobby accretion from the stream directly heating the WD surface, Evans & Hellier (2007) suggest that in IPs this component arises from reprocessing of hard X-rays and its visibility depends on geometric factors in a given system.

Only five IPs have been found to emit polarized light, whereas in all polars the emitted light is both linearly and circularly polarized, due to cyclotron emission processes near the surface of the WD. Those IPs where circular polarization has been found so far are: BG CMi (Penning et al. 1986; West et al. 1987), PQ Gem (RE 0751+14) (Rosen et al. 1993; Piirola et al. 1993; Potter et al. 1997), V2400 Oph (RX J1712.6–2414) (Buckley et al. 1997), V405 Aur (RX J0558.0+5353) (Shakhovskoj & Kolesnikov 1997) and V2306 Cyg (1WGA J1958.2+3232) (Uslenghi et al. 2001; Norton et al. 2002).

As the weakest magnetic fields found in polars have been estimated to be ~7 MG (V2301 Oph, i.e. 1H1752+08, Ferrario et al. 1995), and the strongest magnetic field strengths in IPs have been estimated as more than 10 MG (i.e. PQ Gem: 8–18 MG (Piirola et al. 1993) or 9–21 MG (Vaeth et al. 1996; Potter et al. 1997) and V2400 Oph: 9–20 MG (Vaeth 1997)), there is likely to be some overlap between the magnetic field strengths in these two subclasses. It is not clear though how the evolution of IPs and polars is connected. Polars are predominantly seen at shorter orbital periods ($P_{\rm orb} < 2$ h) and intermediate polars at longer orbital periods ($P_{\rm orb} > 3$ h). However, there are several examples of each type of system outside these ranges, and the period distribution of mCVs as a whole may not exhibit the ~2–3 h period gap, as seen in non-magnetic systems Wickramasinghe & Wu (1994).

All CVs will evolve towards shorter orbital periods as they lose angular momentum via magnetic wind braking and gravitational radiation. In mCVs, the magnetic white dwarfs are also expected to spin down on long timescales, under the effect of the magnetic locking torque. Chanmugam & Ray (1984) consequently suggested that polars evolve from IPs, but this idea has not generally been accepted, mostly because very few IPs are found to emit circularly polarized radiation. Polarization surveys, such as that by Cropper (1986), have shown that upper limits to the fractional circular polarization in many IPs are around 0.1–0.2 per cent. It is therefore generally believed that the magnetic field strength in IPs is about 10–100 times lower than that found in polars, so evolving one subclass into the other may not be feasible. Cumming (2004) suggested a possible solution whereby the relatively high accretion rates in IPs may overcome ohmic diffusion, such that magnetic flux is advected into the interior of the white dwarf, reducing the surface magnetic field strength. This effective burying of the WD magnetic field would make them appear less magnetic than they really are. In this case there is also so much unpolarized light (due to the high accretion rate) that polarized emission is not seen. Under his suggestion, once accretion turns off below an orbital period of ~3 h, the magnetic field resurfaces, so that when accretion resumes below an orbital period of ~2 h, the system will synchronize and emerge as a polar.

The magnetic moment of the WD, μ_1, seems to determine whether a mCV will appear as an IP, a polar, or just as a non-magnetic (i.e. "normal") CV. According to Norton et al. (2004), there exists a difference in the observed magnetic moments of polars and IPs, with virtually all IPs having $\mu_1 \leq 5 \times 10^{33}$ G cm^3 and all polars having $\mu_1 \geq 5 \times 10^{33}$ G cm^3. It is estimated (King et al. 1985; Lamb & Melia 1987; Norton et al. 2004) that if $\mu_1 \leq 10^{31}$ G cm^3, the magnetic field of the WD is not able to funnel the accretion flow, and we do not then observe any evidence for magnetic fields. If 10^{31} G cm$^3 \leq \mu_1 \leq 5 \times 10^{33}$ G cm^3 and $P_{\rm orb} > 3$ h, a magnetic CV will be seen as an IP, which may evolve eventually into a low magnetic field polar or if their magnetic field is stronger than supposed (under the model of Cumming (2004) mentioned above), they could evolve into polars below the ~2–3 h period gap. Finally, if $\mu_1 \geq 5 \times 10^{33}$ G cm^3 and $P_{\rm orb} > 3$ h, an IP will rapidly evolve into a polar in the conventional manner.

2. The intermediate polar RX J2133.7+5107

In this paper we discuss our recent *UBVRI* photopolarimetric observations of the long period intermediate polar RX J2133.7+5107. This target was discovered from the *ROSAT* Galactic Plane survey by Motch et al. (1998), and identified as a $B \sim 16$ mag star, which they classified as a CV. Recent observations with *XMM-Newton* showed that the X-ray data from RX J2133.7+5107 require a multi-temperature bremsstrahlung *and* a blackbody component with a temperature $kT_{\rm bb} \sim 100$ eV in order to fit the detailed spectrum obtained (de Martino et al. 2006b). It is therefore similar to other IPs with a strong soft X-ray spectral component such as PQ Gem (RE 0751+14, Duck et al. 1994), V405 Aur (RX J0558.0+5353, Haberl & Motch 1995), UU Col (RX J0512.2–3241, Burwitz et al. 1996), NY Lup (RX J154814.5–452845, Haberl et al. 2002) and MU Cam (RX J062518.2+733433, Staude et al. 2003).

Like the soft intermediate polar NY Lup, but unlike most other IPs, RX J2133.7+5107 has an unusually long orbital period, which in this case is $P_{\rm orb} = 7.193 \pm 0.016$ h (Bonnet-Bidaud et al. 2006). Only a few IPs are known to have a longer orbital period than this, and thus RX J2133.7+5107 is among the widest IP binaries. The spin period of the WD in RX J2133.7+5107 is relatively short, $P_{\rm spin} = 570.823 \pm 0.013$ s, and its $P_{\rm spin}/P_{\rm orb}$ ratio (a measure of the degree of asynchronism) is therefore 0.022, which is one of the smallest amongst all IPs: Norton et al. (2004) Table 1 lists only 7 IPs and IP candidates which have smaller $P_{\rm spin}/P_{\rm orb}$ ratio (WZ Sge, AE Aqr, GK Per, V533 Her, DQ Her, XY Ari and V709 Cas), to which may now be added also HS2331+3905

Table 1. The observing log of RX J2133.7+5107.

Date of obs. (start of night)	HJD of first obs. (+2453000.0)	Durations (h)	Cycles $P_{\rm orb}$	$P_{\rm spin}$(full)	Filter(s)	Exp. Time (s)	(V) (mag)
2006 July 31	948.57384	2.01	0.28	12	*UBVRI*	10	15.1–15.5
2006 August 2	950.64636	1.81	0.25	11	*UBVRI*	10	14.9–15.4

(Araujo-Betancor et al. 2005) and 1RXS J154814.5–452845 (NY Lup, de Martino et al. 2006a). On this basis, the magnetic field in RX J2133.7+5107 is expected to be weak (Bonnet-Bidaud et al. 2006). We also note that RX J2133.7+5107 was one of the intermediate polars detected by the *INTEGRAL*/IBIS survey Barlow et al. (2006) as a hard X-ray (20–100 keV) source.

3. Observations

Our observations were made on the nights of 2006 July 31/August 1, and 2006 August 2/August 3 at the 2.56 m Nordic Optical Telescope (NOT) on La Palma, using *TURPOL*. This is the Double Image Chopping Polarimeter (Piirola 1973, 1988; Korhonen et al. 1984), which is able to perform simultaneous photopolarimetry in all *UBVRI* bands by using four dichroic filters (which split the light into five spectral pass-bands). The diaphragm in the instrument has two apertures, one passing the star's light plus the sky background, while the other one passes background light through the aperture. A chopper opens and closes apertures, illuminating the photo-cathode of the photomultiplier tube consecutively. By inserting a plane parallel calcite plate into the beam before the focal plane, polarization measurements are possible. The calcite splits the incoming light into two components, the ordinary and extra-ordinary, which are orthogonally linearly polarized. By measuring the relative intensities of these rays, after a wave-plate, the degree of polarization of the light entering from the star can be measured.

TURPOL was used in its circular-mode, in which intensities are measured in 90.0° steps of the $\lambda/4$-plate. For each step, both polarized beams are integrated with a chopping frequency of 25 Hz for the required integration time. The sky background polarization is directly eliminated using a calcite plate as a polarizing beam splitter. For every orientation of the $\lambda/4$-plate, a 10 s integration for each beam is taken. Taking into account some dead time involved in the *TURPOL* mechanism, integrations take 24 s. One complete polarization observation consists of four different orientation of the $\lambda/4$-plate (a full 360° cycle) and the final time resolution is ~1.5 min.

The instrumental polarization and the correct sign of the positive and negative circular polarization were determined through observations of the zero polarization standard star BD +28 4211 and the high circular polarization standard star GRW+70 8247. Instrumental polarization was found to be negligible (<0.1 percent) in *TURPOL*. Sky intensity was measured at ~15 min intervals. The zero-points of the *UBVRI*-magnitude scale were determined by using observations of several Landolt standard stars (109 954, 111 250, 111 2093 and 114 637; Landolt (1992)) during each night.

4. Results

We detected circular polarization from RX J2133.7+5107 in all of the *UBVRI* wavebands on both observation nights, of order a few percent. Furthermore, there is a modulation at the white dwarf spin period clearly present in both the photometric light curves and in the circular polarization curves. In the following subsections, we first present the *UBVRI* light curves and colour indices, followed by the results of the Fourier analysis of the light curves and polarization curves. Finally we present the light curves and polarization curves folded at the white dwarf spin period, using the updated ephemeris which we here define.

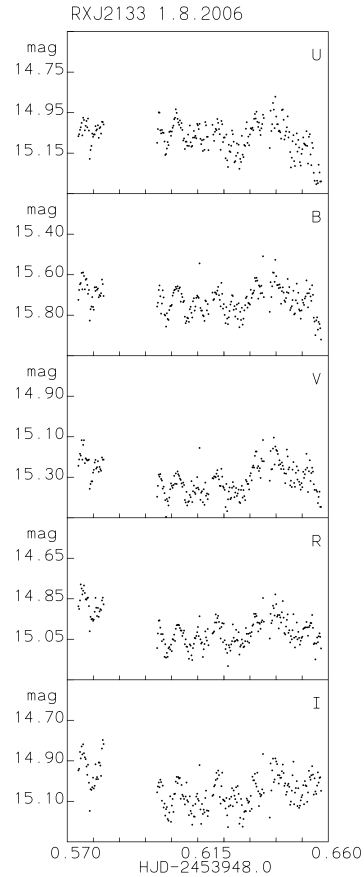

Fig. 1. *UBVRI* light curves of RX J2133.7 + 5107, obtained on 2006 July 31/August 1. Each point presents a single photometric measurement, with 24 s time resolution.

4.1. UBVRI light curves and colour indices

RX J2133.7+5107 was observed for a total of 3.82 hours over the two nights (see the observing log in Table 1). Figures 1 and 2 show the *UBVRI* photometry of RX J2133.7+5107 from both

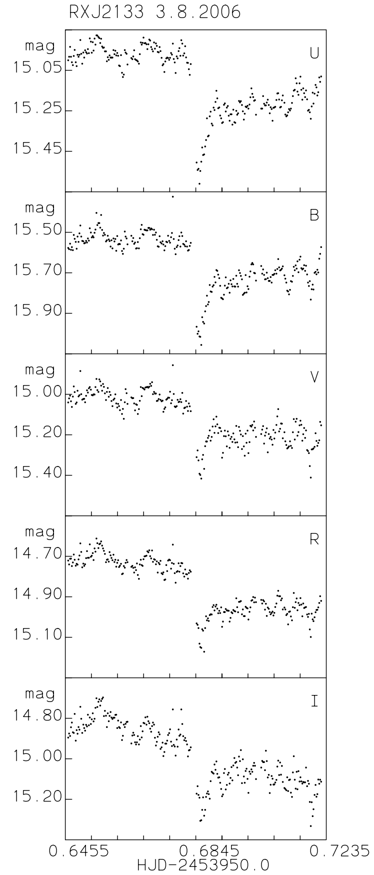

Fig. 2. *UBVRI* light curves of RX J2133.7 + 5107, obtained on 2006 August 2/August 3. Each point presents a single photometric measurement, with 24 s time resolution.

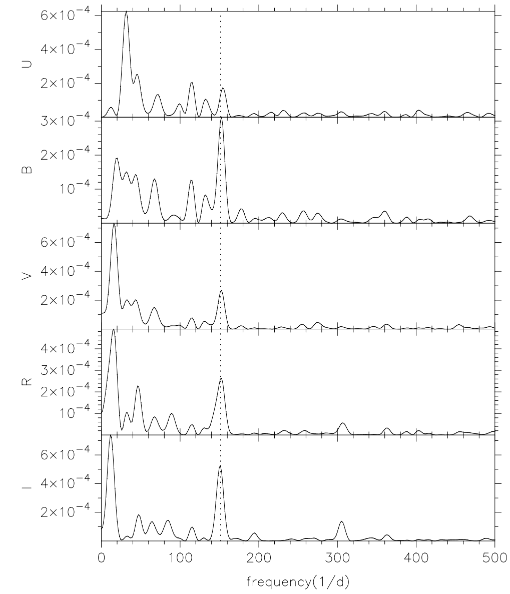

Fig. 3. CLEANed periodogram of the light curves of RX J2133.7+5107 observed during the night of 2006 July 31/August 1. The spin frequency of the white dwarf is ~152 cycles per day. The units of pseudopower on the ordinate axis are mag^2 . A sinusoid with an amplitude of A = 0.04 mag would produce a peak with power $\sim 4 \times 10^{-4}$.

of the observing nights. Each data point corresponds to a single measurement with 24 s time resolution. This consists of 10 s integration time on the target, 10 s integration time on the sky, and 4 s lost time due to the instrument mechanics. A "saw-tooth" shape with an amplitude of ~0.1 mag is seen in the light curves, which represents the pulsed modulation at the white dwarf spin period.

On the second night (HJD 2453950.0) a significant dip was observed in all *UBVRI* bands near the epoch HJD 2453950.685, when the brightness of the target dropped suddenly by approximately 0.5 in the U-band, and 0.4 in the *BVRI*-bands. Unfortunately we observed the sky background at the same time as the start of this dip, and therefore missed most of its ingress. Later analysis showed that we were observing RX J2133.7+5107 around same orbital phase as this dip on the first night, but unfortunately no data was taken exactly at the same phase. Bonnet-Bidaud et al. (2006) presented light curves from three separate nights (their Fig. 1) covering almost the whole orbital period (7.2 h) in each. There is no such dip seen in any of their light curves, and thus the dip seen in our data from 2006 August 2/3, is unlikely to be an eclipse, and its cause still remains a puzzle.

The colours of RX J2133.7+5107 for $U-B$, $B-V$ and $V-R$, show some small flickering, and these too exhibit the "saw tooth" profile reflecting the white dwarf pulse period. This is most apparent in the $U-B$ colour.

The average magnitudes in each of the *UBVRI* bands are 15.1, 15.7, 15.2, 14.9 and 15.0 respectively. This is consistent with the B band value of 15.8 reported by Motch et al. (1998), indicating that the brightness of the system has not changed significantly.

4.2. Period analysis of the polarization and light curves

We performed a CLEAN periodogram analysis for the *UBVRI* light curves. We selected CLEAN in favour of a more direct, simple power spectrum because in addition to measuring the temporal frequency of the variability, this enabled us to get a good measure of the phases of each component of this variability. On July 31/Aug 1 the single consistent large peak occurred at a frequency of ~ 152 d^{-1}, which corresponds to the spin period of the white dwarf (Fig. 3).

The details of the analysis are shown in Table 2. The average frequency of the spin modulation is 152.48 ± 0.66 periods per day. This equates to a period of 566.6 ± 2.5 s, which is within 2σ of the value in Bonnet-Bidaud et al. (2006). From our CLEAN analysis, phase zero is defined at the maximum magnitude value of the modulation, and the average phase at the reference time of HJD 2 453 948.621 873 is -150.75 ± 7.64 degrees. This provides

Table 2. White dwarf spin peaks in the power spectra of RX J2133.7+5107.

	Band	Frequency day^{-1}	Zero point of time HJD -2 453 000
Night 1	U	154.5	948.62419
	B	152.5	948.62453
	V	152.4	948.62458
	R	152.2	948.62481
	I	150.8	948.62499
	average	152.48	948.62462
	uncertainty	0.66	0.00015
Night 2	U	163.0	950.70601
	B	155.7	950.70596
	V	156.3	950.70594
	R	158.3	950.70614
	I	154.5	950.70655
	average	157.56	950.70612
	uncertainty	1.67	0.00013

us with a new zero point for the epoch of maximum magnitude, which takes place at HJD 2 453 948.62462 ± 0.00015. Adopting the more accurate Bonnet-Bidaud et al. (2006) value for the period, we revise the ephemeris by updating only the zero-point to:

$$\text{Minimum flux} = \text{HJD } 2\,453\,948.62462(15) + 0.0066067(2) \cdot E.$$

A second spectral peak in the periodogram is also present at approximately 45 d^{-1}. This corresponds to a period of roughly 0.0222 days or about 32 min. This is roughly the length of the brightening episode seen between 0.628 d and 0.660 d in Fig. 1.

On the night Aug 2/Aug 3, a modulation is also found in all wavebands. The average frequency of 157.56 ± 1.67 periods per day can be identified as the spin period of the white dwarf. However, this value is not very trustworthy because it is affected by the very deep dip in the light curve. This dip is also the cause of a consistent feature seen in the power spectra at 253 cycles per day, or a timescale of about 0.004 days.

The time difference between the zeropoints of the two nights equals 315.06 periods, which is consistent with 315 periods, but our data alone cannot exclude other nearby integer numbers of periods. This is the main reason for adopting the Bonnet-Bidaud et al. (2006) period for our ephemeris. Our light curves do not cover the full orbital cycle, so no inference about the orbital period can be made from these data.

An identical analysis was performed for the raw polarization curves. The white dwarf spin frequency is detected clearly in the polarization curves of *RVI* and only marginally in *UB* (Fig. 4).

4.3. UBVRI spin folded circular polarization and light curves

Figure 5 shows the circular polarimetry obtained at the NOT on the two nights observing, folded at the previously known WD spin period of 570.823 s and then phase binned into 20 equal bins. Stokes parameters have been calculated for polarization from the integrations made in different orientations of the quarter-wave retarder (rotated in 90.0° steps). Uncertainties are then calculated both from the photon statistics and from the least square fit to the integrations; whichever is greater has been taken as an uncertainty estimate. The error bars correspond to $\pm 1\sigma$ uncertainties.

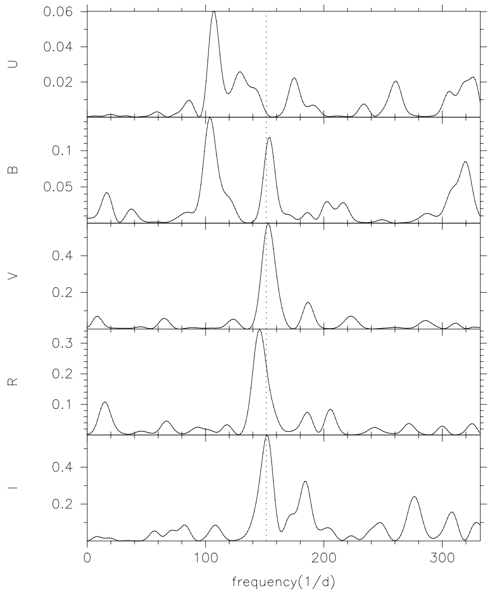

Fig. 4. CLEANed periodogram of the polarization curves of RX J2133.7+5107 observed during the night of 2006 July 31/August 1. The spin frequency of the white dwarf is ~152 cycles per day. The units of pseudopower on the ordinate axis are %^{2}. A sinusoid with an amplitude of $A = 1\%$ would produce a peak with power ~0.25.

Significant circular polarization is seen in all *UBVRI* bands from RX J2133.7+5107, and polarization variations are modulated at the WD spin period. Polarization is near to zero at phase $\Phi = 0.5$, and it increases smoothly until relative phase $\Phi = 0.0$. After that epoch there is a small dip in the polarization curves in the blue part of the spectrum, near phase $\Phi = 0.1$–0.2 (possibly due to cyclotron beaming effects), whilst from phase $\Phi = 0.2$ the polarization decreases until $\Phi \sim 0.5$. Polarization is positive over the whole WD spin period, and it has a colour dependence; the peak polarization values in the *UBVRI* bands are: +1.5, +2.5, +3.5, +3, and +2.5 percent, respectively.

Figure 6 shows the photometry from the two observing nights, similarly folded and phase binned. Bonnet-Bidaud et al. (2006) observed RX J2133.7+5107 in a broad band (between 300–600 nm) filter with a peak at ~380 nm. Reconstructing a broad band filter by combining our corresponding filters allows a direct comparison to be made between our Fig. 7 and their Fig. 4.

5. Discussion

5.1. Magnetic field strength and cyclotron emission

Known polarized IPs so far have shown polarization predominantly in the red part of their spectrum, for example in PQ Gem, circular polarization is seen only in the *R*- and *I*-bands in the *UBVRI* observations of Piirola et al. (1993). Similarly in BG CMi, polarization was found in the red part of the optical and particularly in the infrared region (Penning et al. 1986; West et al. 1987), whilst it was seen in the red part of the spectrum in V405 Aur (Shakhovskoj & Kolesnikov 1997).

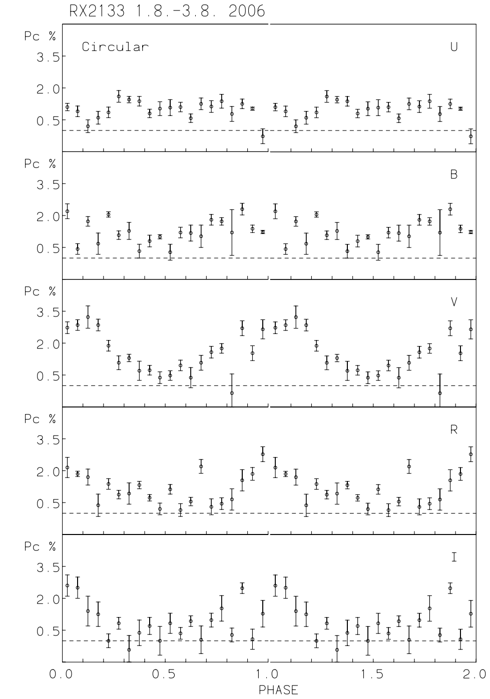

Fig. 5. *UBVRI* polarization curves of RX J2133.7+5107 observed at the NOT between 2006 July 31 and August 3, folded at the white dwarf spin period of 0.0066067d and averaged into 20 phase bins.

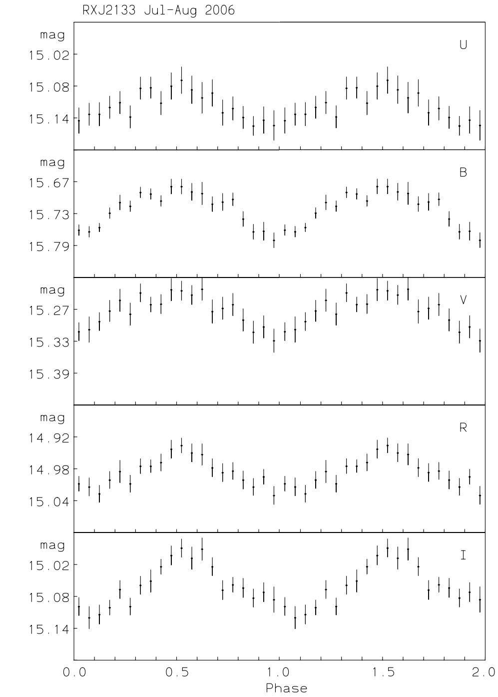

Fig. 6. *UBVRI* light curves of RX J2133.7+5107 observed at the NOT between 2006 July 31 and August 3, folded at the white dwarf spin period 0.0066067d and averaged into 20 phase bins.

Norton et al. (2002) reported optical polarization found in V2306 Cyg, where circular polarization was seen to be negative at the several percent level in the *R*-band, but positive around one percent in the *B*-band. In V2400 Oph, Buckley et al. (1995) found optical polarization which was highest in the *I*-band. RX J2133.7+5107 seems to be quite different in that sense, and this may be an indicator that the inferred magnetic field is stronger than found in other polarized IPs.

In RX J2133.7+5107 circular polarization is positive throughout the spin cycle (Fig. 5), which indicates that one pole is dominant. There is no sign of cyclotron emission from the other (negative) pole. Circular polarization is close to zero near phase 0.5, which suggests that our line of sight is nearly perpendicular to the magnetic field lines at that phase, i.e. the emission region is at the stellar limb. In terms of the colatitude of the emission region, β, and the inclination of the WD spin axis, i, this can be written as $\beta \sim 90° - i$. Circular polarization increases smoothly from phase 0.5 towards 0.0, when the emission region moves away from the limb to the position where the field lines point closest to us (phase 0.0).

At small viewing angles cyclotron emission *intensity* approaches zero (due to the cyclotron beaming effect), and the diluting effect of unpolarized thermal emission decreases the observed degree of polarization. The peak observed in the *R* band at phase 0.0 (Fig. 5) becomes flatter in the *V* band, and a polarization dip is seen in the *B* and *U* bands, due to the cyclotron beaming effect, which is strongest at high harmonics (shorter

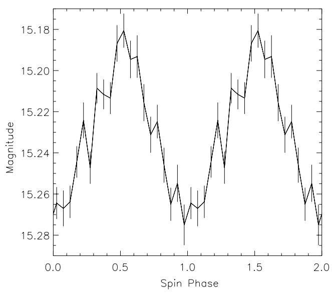

Fig. 7. Reconstructed broad band photometry of RX J2133.7+5107 folded at the 571s spin period.

wavelengths). The minimum in the light curves (Fig. 6) takes place near phase 0.0, in accordance with the proposed cyclotron beaming geometry.

Circular polarization does not go to zero at phase 0.0, which means that viewing angles are $\gg 0°$ even when looking closest along the field lines. Simple geometric considerations then imply that either $i - \beta \gg 0°$ or $\beta - i \gg 0°$. For a high inclination system the emission region has to be closer to the rotation pole, and for a low inclination system it must be closer to the equator, to fulfil also the relation $\beta \sim 90° - i$ (see above). However, without

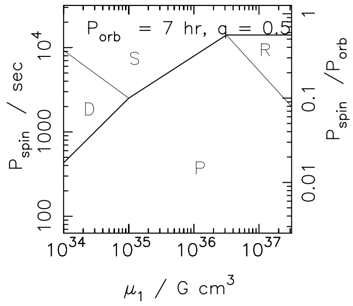

Fig. 8. Spin period vs. magnetic moment diagram for a mass ratio of 0.5 and an orbital period of 7 h (adapted from Norton et al. (2007). The letters "S", "P", "D" and "R" indicates regions of the parameter space in which a stream-like, propeller-like, disc-like and ring-like flow respectively may be seen. In spin equilibrium, systems tend toward the line which divides disc-like and stream-like flows from propeller-like and ring-like flows.

linear polarization measurements we cannot fix the value of i. The absence of eclipses by the companion star requires that i is smaller than about 75°.

Circular polarization variations of RX J2133.7+5107 can be compared with systems where the magnetic field strength is estimated to be about 25MG, such as the polars V834 Cen (Piirola 1995) and BY Cam (Piirola et al. 1994). The observed circular polarization variations in those stars resemble (in their colour dependence) those seen in RX J2133.7+5107. Naturally the circular polarization level is higher in polars, for example in BY Cam or in V834 Cen the circular polarization peak values are almost 30 percent, as there is much less unpolarized light diluting the observed polarization in those systems. In IPs there is more unpolarized light due to their higher accretion rates and larger accretion stream compared to polars. More accurate estimates of the magnetic field of RX J2133.7+5107 could be obtained in the future by using phase resolved circular spectropolarimetry and modelling of such data. Also, high signal-to-noise linear polarimetry of RX J2133.7+5107 to find out the orbital inclination would be very useful.

5.2. The magnetic moment of RX J2133.7+5107

Theoretical modelling of IPs by Norton et al. (2004) has begun to explain equilibrium values of the magnetic moment in these systems. They determined the equilibrium spin periods at which systems would lie, with a given orbital period and magnetic moment, assuming the white dwarf not to be spinning up or down on long timescales. This theoretical work has since been extended so that the position of a system in the $P_{\rm spin}/P_{\rm orb}$ vs. magnetic moment plane can indicate the structure of the accretion flow in the system (Norton et al. 2007). The key result from this study is that the spin-to-orbital period ratio vs. magnetic moment plane can be divided into regions where the system will display either a disc-like, stream-like, propeller-like or ring-like accretion flow (Fig. 8). Furthermore, the "triple point" positions (at which stream, disc and propeller or stream, ring and propeller flows can co-exist) on the $P_{\rm spin}/P_{\rm orb}$ axis are a function of mass ratio and not orbital period. The magnetic moments at which these transitions occur are, however, a function of orbital period.

The mass ratio of RX J2133.7+5107 is uncertain, but likely to be in the range $q \sim 0.3$–0.6 (Bonnet-Bidaud et al. 2006). For a typical mass ratio of 0.5, the results of Norton et al. (2007) show that, if RX J2133.7+5107 is in equilibrium with $P_{\rm spin}$ = 571 s and $P_{\rm orb} \sim 7$ h, its magnetic moment is of order $\sim 10^{34}$ G cm^3; a larger value of magnetic moment for a system with these periods and mass ratio would indicate a propeller-type flow subject to a spin-down of the white dwarf, and a smaller value of the magnetic moment would indicate a disc-like flow which is spinning up the white dwarf (see Fig. 8). For a smaller mass ratio, the magnetic moment corresponding to the equilibrium may be significantly smaller, and for a larger mass ratio, the magnetic moment may be somewhat higher. Hence, for a mass ratio in the range $q \sim 0.3$–0.6, if RX J2133.7+5107 is accreting at close to its equilibrium spin rate, the magnetic moment is likely to be in the range 3×10^{33}–3×10^{34} G cm^3. This magnetic moment is consistent with a relatively high magnetic field strength, as implied by the polarization results presented earlier.

5.3. The evolutionary status of RX J2133.7+5107

RX J2133.7+5107 is apparently a high magnetic field strength intermediate polar (possibly μ_1 is about 10^{34} G cm^3), yet it is a long way from synchronism ($P_{\rm spin}/P_{\rm orb} \sim 0.022$). A magnetic CV with a field this strong would be expected to synchronize on a relatively short timescale and emerge as a polar with a period of less than about 4 h. However, to become synchronized at the present orbital period it would require an even stronger magnetic field, and in fact very few polars have an orbital period this long: V1309 Ori has the longest known period amongst the polars at P = 7.98 h (Staude et al. 2001). So we suggest that RX J2133.7+5107 is a relatively young system that has only recently come into contact and begun mass transfer, and has not yet had time to evolve to a shorter orbital period and approach synchronism. Nonetheless we believe it will eventually synchronize and emerge as a polar.

It is also interesting to note a possible link between the presence of significant soft X-ray emission in intermediate polars and the presence of polarized emission, as these two features are also seen in polars. Indeed, Beuermann & Schwope (1994) demonstrated an anti-correlation between magnetic field strength and the ratio of the strength of the hard X-ray emission to that of the soft X-ray emission in polars. Hence, the polars with stronger magnetic fields have a stronger blackbody component and/or a weaker bremsstrahlung component. In both polars and intermediate polars, a soft X-ray component may arise as accreting material impacts the white dwarf directly, resulting in blackbody radiation with a temperature of $kT_{\rm bb} \sim$ 50–100 eV being emitted from the heated white dwarf surface. Although we note the recent suggestion of Evans & Hellier (2007) that the visibility of a soft component in IPs is a geometrical effect and arises from reprocessing of hard X-rays. In either case, it has a different origin to the multi-temperature X-ray bremsstrahlung emission, whereas the cyclotron emission arises in the cooling plasma as it settles slowly onto the white dwarf surface below a shock. Amongst the soft X-ray emitting IPs, there are two objects which have also been seen to display polarized emission (PQ Gem and V405 Aur) to which may now be added RX J2133.7+5107 as a third example.

We recall the suggestion of Cumming (2004) that the high accretion rates in intermediate polars might overcome ohmic diffusion and significantly affect the magnetic field structure. In this regime, magnetic flux is advected into the interior of the white dwarf, dramatically reducing the surface field. Hence, intermediate polars would appear to have a weaker field than they actually have. Now, it is apparent that in some intermediate polars, the accretion flow and magnetic field geometry are such that some of the accreting material directly, or indirectly, heats the white dwarf surface, giving rise to a soft X-ray component. If direct heating occurs, less of the accreting material interacts with the shock, and we suggest this may lead to a less significant "burying" of the white dwarf magnetic field. Hence we might expect those intermediate polars with soft X-ray spectral components to preferentially exhibit signs of stronger magnetic fields, such as enhanced polarized emission.

The intermediate polars with polarized emission that have yet to show evidence for a soft X-ray component (e.g. BG CMi, V2306 Cyg, V2400 Oph) may simply suffer from less significant magnetic field burying for various reasons. Both BG CMi and V2400 Oph show evidence for stream-fed accretion (Norton et al. 1992; Buckley et al. 1997) and V2306 Cyg shows evidence for an asymmetric magnetic field at the two poles (Norton et al. 2002). Both of these differences could conceivably reduce the magnetic field burial, allowing detection of polarized emission from accretion under the influence of the inherent (stronger) magnetic field. We suggest that the soft X-ray emitting intermediate polars that are so far without detected polarized emission (e.g. UU Col, MU Cam, NY Lup) would make ideal targets to search for such a component. In particular, the system parameters of NY Lup ($P_{\rm spin} = 693$ s, $P_{\rm orb} = 9.87$ h) (Haberl et al. 2002; de Martino et al. 2006a) make it appear a close twin of RX J2133.7+5107, and it too may be a young intermediate polar which will eventually evolve into a polar.

6. Conclusion

We have found that RX J2133.7+5107 emits circularly polarized light in all *UBVRI* bands (up to 3%). The variation of this light gives hints of cyclotron beaming effects. To explain this level of polarization and its colour dependence, a strong magnetic field is needed, (possibly $\mu_1 \sim 10^{34}$ G cm^3), which would make RX J2133.7+5107 one of the most magnetic IPs so far discovered. Due to its highly asynchronous degree of rotation (spin-to-orbital period ratio of 0.022) these results suggest that it may be a young system, which has only recently come into contact. This asynchronism coupled with the inferred magnetic field strength suggests that the system may eventually evolve into a polar.

We propose that there may be a link between the emission of a soft X-ray spectral component due to direct heating of the white dwarf surface and the detection of polarized emission in intermediate polars. Possibly the direct heating means that magnetic field burial below the accretion shock is less effective, so allowing the intrinsic field to produce a stronger polarization signal. If this link is confirmed it would argue that the soft X-ray component in IPs is indeed due to direct heating (as in polars) and not due to reprocessing of the hard X-rays.

Acknowledgements. The Nordic Optical Telescope is operated on the island of La Palma jointly by Denmark, Finland, Iceland, Norway, and Sweden, in the Spanish Observatorio del Roque de los Muchachos of the Instituto de Astrofisíca de Canarias. This work has been supported by the Academy of Finland and "Societas Scientiarum Fennica – Suomen Tiedeseura" and its Magnus Ehrnrooth foundation.

References

Araujo-Betancor, S., Gaensicke, B. T., Hagen, H.-J., et al. 2005, A&A, 430, 629
Bailey, J., Wickramasinghe, D. T., Ferrario, L., Hough, J., & Cropper, M. 1993, MNRAS, 261, L31
Barlow, E. J., Knigge, C., Bird, A. J., et al. 2006, MNRAS, 372, 224
Beuermann, K., & Schwope, A. D. 1994, in ASP Conf. Ser., 56, Interacting Binary Stars, ed. A. W. Shafter, 119
Bonnet-Bidaud, J. M., Mouchet, M., de Martino, D., Silvotti, R., & Motch, C. 2006, A&A, 445, 1037
Buckley, D. A. H., Sekiguchi, K., Motch, C., et al. 1995, MNRAS, 275, 1028
Buckley, D. A. H., Haberl, F., Motch, C., et al. 1997, MNRAS, 287, 117
Burwitz, V., Reinsch, K., Beuermann, K., & Thomas, H.-C. 1996, A&A, 310, L25
Chanmugam, G., & Ray, A. 1984, ApJ, 285, 252
Cropper, M. 1986, MNRAS, 222, 225
Cropper, M. 1990, Space Sci. Rev., 54, 195
Cumming, A. 2004, in IAU Coll., 190, Magnetic Cataclysmic Variables, ed. S. Vrielmann, & M. Cropper, ASP Conf. Ser., 315, 58
de Martino, D., Bonnet-Bidaud, J.-M., Mouchet, M., et al. 2006a, A&A, 449, 1151
de Martino, D., Matt, G., Mukai, K., et al. 2006b, in ESA SP-604: The X-ray Universe 2005, ed. A. Wilson, 261
Duck, S. R., Rosen, S. R., Ponman, T. J., et al. 1994, MNRAS, 271, 372
Evans, P. A., & Hellier, C. 2007, ApJ, 663, 1277
Ferrario, L., Wickramasinghe, D. T., Bailey, J., & Buckley, D. 1995, MNRAS, 273, 17
Gaensicke, B. T., Marsh, T., Edge, A., et al. 2005, MNRAS, 361, 141
Geckeler, R. D., & Staubert, R. 1997, A&A, 325, 1070
Haberl, F., & Motch, C. 1995, A&A, 297, L37
Haberl, F., Motch, C., & Zickgraf, F.-J. 2002, A&A, 387, 201
King, A. R., Frank, J., & Ritter, H. 1985, MNRAS, 213, 181
Korhonen, T., Piirola, V., & Reiz, A. 1984, The Messenger, 38, 20
Lamb, D. Q., & Melia, F. 1987, Ap&SS, 131, 511
Landolt, A. U. 1992, AJ, 104, 340
Motch, C., Guillout, P., Haberl, F., et al. 1998, A&AS, 132, 341
Norton, A. J., Butters, O. W., Parker, T. L., & Wynn, G. A. 2007, ApJ, in press
Norton, A. J., McHardy, I. M., Lehto, H. J., & Watson, M. G. 1992, MNRAS, 258, 697
Norton, A. J., Quaintrell, H., Katajainen, S., et al. 2002, A&A, 384, 195
Norton, A. J., Wynn, G. A., & Somerscales, R. V. 2004, ApJ, 614, 349
Patterson, J. 1994, PASP, 106, 209
Patterson, J., Skillman, D. R., Thorstensen, J., & Hellier, C. 1995, PASP, 107, 307
Patterson, J., Thorstensen, J. R., Vanmunster, T., et al. 2004, PASP, 116, 516
Patterson, J., Halpern, J., Mirabal, N., et al. 2006, The Astronomers Telegram, 757, 1
Penning, W. R., Schmidt, G. D., & Liebert, J. 1986, ApJ, 301, 881
Piirola, V. 1973, A&A, 27, 383
Piirola, V. 1988, Simultaneous five-colour (UBVRI) photopolarimeter (Polarized Radiation of Circumstellar Origin), 735
Piirola, V. 1995, in Magnetic Cataclysmic Variables, ed. D. A. H. Buckley, & B. Warner, ASP Conf. Ser., 85, 31
Piirola, V., Hakala, P., & Coyne, G. V. 1993, ApJ, 410, L107
Piirola, V., Coyne, G. V., Takalo, S. J., et al. 1994, A&A, 283, 163
Potter, S. B., Cropper, M., Mason, K. O., Hough, J. H., & Bailey, J. A. 1997, MNRAS, 285, 82
Rodrigues-Gil, P., Gaensicke, B. T., Hagen, H.-J., et al. 2005, A&A, 440, 701
Rosen, S. R., Mittaz, J. P. D., & Hakala, P. J. 1993, MNRAS, 264, 171
Schmidt, G. D., Szkody, P., Smith, P. S., et al. 1996, ApJ, 473, 483
Schwarz, R., Schwope, A. D., Staude, A., et al. 2004, ASPC, 315, 230
Schwope, A., Buckley, D. A. H., O'Donoghue, D., Hasinger, G., & Truemper, J. 1997, A&A, 326, 195
Shakhovskoj, N. M., & Kolesnikov, S. V. 1997, IAUCirc, 6760, 2
Silber, A., Bradt, H. V., Ishida, M., Ohashi, T., & Remillard, R. A. 1992, ApJ, 389, 704
Southworth, J., Gaensicke, B. T., Marsh, T., et al. 2006, MNRAS, 373, 687
Southworth, J., Gaensicke, B. T., Marsh, T., de martino, D., & Aungwerojwit, A. 2007, MNRAS, 378, 635
Staude, A., Schwope, A. D., & Schwarz, R. 2001, A&A, 374, 588
Staude, A., Schwope, A. D., Krumpe, M., Hambaryan, V., & Schwarz, R. 2003, A&A, 406, 253
Stockman, H. S., Schmidt, G. D., & Lamb, D. Q. 1988, ApJ, 332, 282
Uslenghi, M., Tommasi, L., Treves, A., Piirola, V., & Reig, P. 2001, A&A, 372, L1
Vaeth, H. 1997, A&A, 317, 476
Vaeth, H., Chanmugam, G., & Frank, J. 1996, ApJ, 457, 407
Warner, B. 1995, Cataclysmic Variable stars (Cambridge University Press), 572
West, S. C., Berriman, G., & Schmidt, G. D. 1987, ApJ, 322, L35
Wickramasinghe, D., & Wu, K. 1994, MNRAS, 266, L1

C.6 Paper VI – Circular polarization survey of intermediate polars I. Northern targets in the range 17h<R.A.<23h

This paper (Butters et al. 2009a) is the second in a series focusing on circular polarization in intermediate polars. It gives an overview of the field as it stands in order to put this work in context. The data is based on an observing run in La Palma during July and August 2006. The work in this chapter is also presented in Chapter 3.

A&A 496, 891–902 (2009)
DOI: 10.1051/0004-6361/200811058

Astronomy & Astrophysics

Circular polarization survey of intermediate polars I. Northern targets in the range 17 h < RA < 23 h*

O. W. Butters[1,2], S. Katajainen[3], A. J. Norton[1], H. J. Lehto[3], and V. Piirola[3]

[1] Department of Physics and Astronomy, The Open University, Walton Hall, Milton Keynes MK7 6AA, UK
[2] Department of Physics and Astronomy, University of Leicester, Leicester, LE1 7RH, UK
e-mail: oliver.butters@star.le.ac.uk
[3] Tuorla Observatory, Department of Physics and Astronomy, University of Turku, Väisäläntie 20, 21500 Piikkiö, Finland
e-mail: sekataja@utu.fi

Received 30 September 2008 / Accepted 14 January 2009

ABSTRACT

Context. The origin, evolution, and ultimate fate of magnetic cataclysmic variables are poorly understood. It is largely the nature of the magnetic fields in these systems that leads to this poor understanding. Fundamental properties, such as the field strength and the axis alignment, are unknown in a majority of these systems.

Aims. We undertake to put all the previous circular polarization measurements into context and systematically survey intermediate polars for signs of circular polarization, hence to get an indication of their true magnetic field strengths and try to understand the evolution of magnetic cataclysmic variables.

Methods. We used the TurPol instrument at the Nordic Optical Telescope to obtain simultaneous *UBVRI* photo-polarimetric observations of a set of intermediate polars, during the epoch 2006 July 31–August 2.

Results. Of this set of eight systems two (1RXS J213344.1+510725 and 1RXS J173021.5–055933) were found to show significant levels of circular polarization, varying with spin phase. Five others (V2306 Cyg, AO Psc, DQ Her, FO Aqr, and V1223 Sgr) show some evidence for circular polarization and variation of this with spin phase, whilst AE Aqr shows little evidence for polarized emission. We also report the first simultaneous UBVRI photometry of the newly identified intermediate polar 1RXS J173021.5–055933.

Conclusions. Circular polarization may be ubiquitous in intermediate polars, albeit at a low level of one or two percent or less. It is stronger at longer wavelengths in the visible spectrum. Our results lend further support to the possible link between the presence of soft X-ray components and the detectability of circular polarization in intermediate polars.

Key words. infrared: stars – polarization – stars: binaries: general – stars: magnetic fields

1. Introduction to magnetic cataclysmic variables

Cataclysmic variables (CVs) are a class of binary system in which a main sequence star (the secondary) transfers matter to its white dwarf (WD) companion (the primary), via Roche lobe overflow. Within this class there is a division of systems based upon the magnetic field strength of the WD, the non-magnetic (or only very slightly magnetic) CVs and the magnetic systems (mCVs). This is an important distinction, as the presence of a magnetic field on the WD has a profound effect on the structure and evolution of the system, since the accreting material is a plasma, its motion is subject to the field. In mCVs the accreting material typically attaches itself to the magnetic field lines close to the magnetospheric radius and is funnelled toward the WD surface. If the WD has a dipole magnetic field structure then this has the effect of concentrating the accreting material into small regions above the magnetic poles. The material reaches supersonic speeds as it is accelerated toward the surface under the influence of gravity. It then goes through a shock as it decelerates to subsonic speeds. This matter then cools as it falls to the surface, emitting hard X-rays ($kT \sim$ 10–60 keV) via bremsstrahlung radiation and optical/infrared cyclotron radiation. Many mCVs also exhibit a soft X-ray component, which is thought to occur due to either some of the accreting material somehow avoiding the shock and directly impacting the surface of the WD (see e.g. Motch et al. 1996), or from the reprocessing of hard X-rays (see e.g. Lamb & Masters 1979). Recently Evans & Hellier 2007 have suggested that this component is in fact present in all mCVs, and that its detection depends on whether geometric factors allow it to be seen or not.

The mCVs are themselves divided into two groups based upon their periodicities, which are in turn assumed to imply different magnetic field strengths. The polars contain synchronously rotating WDs, whilst in intermediate polars (IPs) the WDs rotate asynchronously with respect to the binary orbit.

The polars typically have a magnetic field strength of the order 10–100 MG. This has the effect of channelling the accreting material onto the WD surface before an accretion disc can form. Furthermore, the magnetic field of the WD extends to the body of the secondary and will act to synchronize the spin and orbital periods of the system. Typically the polars are found to have an orbital and spin period of less than two hours. For an overview of polars see e.g. Cropper (1990).

IPs are asynchronous systems, generally *believed* to have a magnetic field strength of approximately 1–10 MG. This smaller field means that matter falls inward toward the WD in much the same way as in non-magnetic CVs. However, at some critical distance from the WD, the magnetic field will begin to dominate,

* Based on observations obtained at the Nordic Optical Telescope at the Roque de los Muchachos Observatory in La Palma.

Article published by EDP Sciences

and the accretion process is altered. It then carries on in much the same way as in the polars. For a comprehensive review of IPs see e.g. Warner (1995) or Patterson (1994).

Non-magnetic CVs evolve from long orbital periods (a few hours) to short orbital periods (just over an hour). The proposed explanation for this evolution is magnetic braking and gravitational radiation (King 1988). Both these processes should also be present in mCVs and since IPs generally have a longer orbital period than the polars it was suggested that IPs evolve into polars (Chanmugam & Ray 1984). This hypothesis has not been widely accepted as there is little evidence of strong magnetic fields in IPs. There are however some IPs with a similar magnetic field strength to the polars, up to 30 MG in the case of V405 Aur (Piirola et al. 2008).

Cumming (2004) suggested that the relatively high accretion rate in IPs may suppress the magnetic field by overcoming ohmic diffusion, such that magnetic flux is advected into the interior of the WD. This would cause the surface magnetic field to appear less than it really is. Considering the evolution of non-magnetic CVs, i.e. the orbital period decreases until $\sim$3 h when the accretion effectively "turns off" then it resumes at $\sim$2 h, allows a regime where an IP may have its "true" magnetic field resurface when the accretion turns off, allow synchronization, then reappear as a polar when the accretion resumes at a lower rate. This theory also ties in with studies of isolated WDs, where peak magnetic fields of $\sim 10^9$ G are seen, whereas in binaries the field strength is typically an order of magnitude smaller (the maximum seen is 230 MG in AR UMa Schmidt et al. 1996) (Wickramasinghe & Ferrario 2000).

In order to test any evolutionary hypotheses an accurate determination of the magnetic fields present in IPs is needed. The best way of doing this is via circular polarization measurements.

Here we report the first paper in our survey of circular polarization emission from IPs. Initially we summarise the field as it stands, in order to put our survey in context (Sect. 2). Then we outline the method we use and the style of reporting our data (Sect. 3). Then we report the results of each of the targets (Sect. 4), followed by a discussion of each (Sect. 5). We have further data in hand for some of the Southern Hemisphere targets that we will be reporting in the near future.

2. Circular polarization

2.1. mCVs

In an accretion column in a mCV there will be material accreting onto the magnetic poles of the WD. The electrons in this material will spiral along the magnetic field lines as they fall to the surface, emitting circularly polarized radiation. The inhomogeneity of the magnetic field structure, the velocity of the electrons, and their varying temperature will have the effect of causing the electrons to emit a broad harmonic structure. By modelling the polarized radiation given off (i.e. simulating the harmonic structure) it is possible to estimate the magnetic field strength of the WD. Wickramasinghe & Meggitt (1985) did this for a range of magnetic field strengths in polars. Their models take into account the magnetic field strength, the temperature, the plasma parameter, and the viewing angle. These four variables cause the modelling to give non-unique solutions for the fitting of the harmonic curve. Their model has been used extensively in estimating the magnetic field strength in polars by measuring the level of circular polarization in different wave-bands (see e.g. Piirola et al. 1987a,b; Katajainen et al. 2003) and has also been used in IPs (see e.g. Piirola et al. 1993).

The polarized light measured in mCVs is generally quoted as a fraction of the total incoming radiation. In polars the source of the unpolarized and polarized radiation should vary at the same period – the orbital period. In IPs however, the situation is more complex. The presence of an accretion disc, that emits at optical frequencies, will dilute the measured polarization. If the flux from the accretion disc varies at any period other than the spin period then this will dilute the signal in a complex fashion. Added to this are the possible presence of a hot spot and the emission from the secondary which will vary at the orbital period.

The geometry of the accretion column is also an issue, since the circular polarization is not given off in all directions (see e.g. Norton et al. 2002). The specific size/shape of the accretion column will therefore affect the emission.

Another likely complexity is that the magnetic field structure of the WD may not be dipole-like. This could lead to multiple accretion columns at multiple magnetic poles. If the magnetic field is close to being a dipole it is also possible that it could be offset from the centre, leading to one pole appearing to be stronger than the other and not at diametrically opposed poles. This complexity is further confounded by the very fact that the accreting material does not come from infinity, in which case even an ideal dipole would not form an accretion column at exactly the position of the magnetic poles.

Given all these complications we cannot be certain what the average magnetic field strength *really* is in IPs, it is possible that estimates of the field strength are over an order of magnitude understated. What we are then assuming to be low number harmonics of a low magnetic field may be high number harmonics of a much larger field.

2.2. Method of circular polarization detections

Assuming circular polarization in IPs can be measured in a similar way to polars and that IPs are of a comparable field strength, implies that harmonics will be present in the UV-IR. The optimal method to reveal these harmonics would be spin phase resolved circular spectro-polarimetry. This requires very large telescopes with very specialised instrumentation allowing high time resolution data collection. This is beyond the scope of this study, therefore we concentrate on the more readily available technique of circular photo-polarimetry.

The general principle of circular photo-polarimetry is to measure the fraction of polarized radiation after a $\lambda/4$ wave plate, which converts circular polarization into linear polarization. This process introduces biases however, for example, incomplete 90° retardation by the wave plate. These biases may cause so called "Stokes parameters cross talks", particularly in the case of targets with non-negligible linear polarization. These cross talks can effectively be eliminated by rotating the wave plate to at least two different wave plate angles and then calculating a single measurement of the circular polarization by using flux values from both positions. This process has an important effect on the temporal resolution of the data, since enough time must be spent integrating on the target to get a good signal to noise value, and if this has to be done multiple times then the temporal resolution will suffer.

By taking simultaneous circular polarization measurements in different pass-bands a clearer understanding of the harmonic structure may be gained. If the pass-bands are defined to have a range comparable to the expected width of the harmonics then comparison of the circular polarization in each band gives an indication of the magnetic field strength.

The method of reporting the level of circular polarization is rather ambiguous, some authors quote the average level throughout their observing run (e.g. Stockman et al. 1992), some give orbitally binned data, but most report data phase binned at the spin period. Each method may have the effect of giving a different interpretation of the magnetic field (see e.g. Uslenghi et al. 2001 where the data is presented in mean, spin binned and orbitally binned format). The average value approach could potentially smooth a sinusoidal-like variation, with an arbitrary amplitude and zero offset, to an average of zero. Phase binning at the orbital period may be severely affected by the variation in orbitally varying unpolarized light. Phase binning over the spin period can reduce both these effects, and since the circular polarization is thought to originate from the accretion column (emission from which varies at the spin period) this is therefore the most desirable approach. The base line chosen needs to be sympathetic to the orbital variation, i.e. either be short in relation to the orbital period, or considered in chunks, and the integration time short compared to the spin period.

2.3. Previous circular polarization detections in IPs

DQ Her was the first IP (although not classified as an IP at the time) to have circular polarization detected (Swedlund et al. 1974). This white light detection was carried out over the course of three months allowing many measurements over the entire 4.6 h orbital period. The level of circular polarization was found to vary periodically over the spin period (142 s) and to be both positive and negative. This variation was found to have a different profile over the orbital period also. The maximum amplitude of variation was found to be approximately 0.6%. Stockman et al. (1992) also measured the level of circular polarization on DQ Her, they found a mean level of $+0.01 \pm 0.01\%$, however, they remark that short period systems will have their levels of reported circular polarization reduced due to the long measurement times.

The next detection of circular polarization in an IP was BG CMi (Penning et al. 1986; West et al. 1987). Measurements were taken in five different pass bands at various times over four months. This allowed the measurements to be plotted over the orbital period (3.75 h). In the 1.10–1.38 μm band the data were distributed randomly about the mean of $-1.74 \pm 0.26\%$ indicating no orbital modulation. Phase binning the data at the spin period (15.9 mn) showed a coherent modulation, however the variation was within two sigma of being zero. West et al. (1987) also considered the variation of the circular polarization with the passband, they found that the amplitude detected increased with wavelength, ranging from $-0.053 \pm 0.051\%$ at 0.32–0.86 μm to $-4.24 \pm 1.78\%$ at 1.40–1.65 μm.

PQ Gem (RE 0751+14) was found in the early 1990's to exhibit significant circular polarization which was modulated at the spin period (Rosen et al. 1993; Piirola et al. 1993; Potter et al. 1997).

Since then, several IPs have been found to exhibit similar behaviour, or have had upper limits placed on their circular polarization (see Table 1 for a summary of all measurements).

V2306 Cyg is the only reported IP to show significant positive polarization in one band and negative in another (Norton et al. 2002), this requires two opposite poles to be seen and for them to be in different states (i.e. one or more of the temperature, geometry, accretion rate etc must be different at the two poles). In all the other cases the polarization has the same sign across the different wave bands.

Each significant (non-zero) measurement of circular polarization has had an estimate of the magnetic field present on the WD attributed to it. Different approaches to modelling the emission have lead to differing inferred values however (see Table 2).

Given the rather disparate nature of previous studies, which generally tend to have information lost in the style of reporting, we have initiated a survey to conclusively measure the degree of circular polarization and comprehensively characterise its nature in IPs.

3. Observations

Observations were carried out at the 2.56 m Nordic Optical Telescope (NOT) on the island of La Palma over three consecutive nights starting 2006 July 31. The telescope was fitted with the TurPol instrument. This is the double image chopping polarimeter (Piirola 1973, 1988; Korhonen et al. 1984), which is able to perform simultaneous photo-polarimetric measurements in all *UBVRI* bands, by using four dichroic filters (which split the light into five spectral pass-bands). The pass-bands are defined as having an effective wavelength of 360, 440, 530, 690, and 830 nm for each of *UBVRI* respectively. By inserting a plane parallel calcite plate into the beam before the focal plane, polarization measurements are possible. The calcite splits the incoming light into two components, the ordinary and the extra-ordinary, which are orthogonally linearly polarized. A diaphragm in the instrument has two apertures, one passes the star's ordinary component, the other passes the extra-ordinary component. A chopper opens and closes the apertures alternately, illuminating the photo-cathode of the photomultiplier tube. By measuring the relative intensities of components after a wave-plate, (which may be rotated in 90° steps) the degree of circular polarization of the light entering from the star can be calculated. Both components of the sky background pass both diaphragms, and the polarization of the sky is thus directly eliminated. In addition, measurements of empty sky are also done at 10 mn intervals, as this sky value is needed in calibration of the photometry.

For one polarization data point, normally at least four multiples of the integration time plus mechanical dead-time (few seconds) generated from rotation of the wave plate is needed, assuming that the circular polarization is measured from two different wave plate positions. This will have the effect of "smearing" out the data on some very short period objects, and therefore may under report their true polarization value. In this study, as some of the targets show remarkable variability within a short timescale, we have chosen in those cases to use only one wave plate position measurement, instead of two. The reduction software was altered in such a way that it could take a circular polarization measurement from only one position of the wave plate. This single position polarization measurement improves the temporal resolution of the data, but at the cost of increasing the uncertainty on the measurement as the biases are not cancelled out.

The targets chosen for this northern hemisphere survey are those in Table 3, and the observing log in Table 4. Note the very short period systems (AE Aqr (33 s), DQ Her (142 s), and RX1730 (128 s)) have one orientation of the wave-plate per measurement, and the other targets have two.

The instrumental polarization was small in all bands (see Table 5). The circular polarization standard star GRW+70 8247 (West 1989) was used to check the calibration, the values reported here are consistent with previous measurements of the standard. The uncertainties quoted on each circular polarization measurement are based on photon noise and are one sigma.

Table 1. Summary of previously measured circular polarization in IPs.

Name	Wavelength range[a] (nm)	Mean (%)	Min (%)	Max (%)	Integration time (s)	Total time	Ref.[1]
AE Aqr	350–920	−0.03 ± 0.02			15	140 min	1
	I	−0.06 ± 0.03			15	150 min	1
	350–570	−0.06 ± 0.02			5	390 min	1
	320–860	+0.01 ± 0.02			$8\times I$[c]	×2	2
	590–860	−0.01 ± 0.01			1[d]	34 min	2
	320–860	−0.13 ± 0.03			$8\times I$[c]	×5	2
	320–860	+0.01 ± 0.01			$8\times I$[c]	×3	2
	1150–1350	+0.06 ± 0.08				4 min	2
	1450–1650	−0.80 ± 0.60				7 min	2
	500–750	+0.07 ± 0.02			5	255 min	3
	(550)	+0.06 ± 0.01			5	323 min	3
AO Psc	570–920	+0.03 ± 0.03			240	180 min	1
	I				240	180 min	1
	320–860	−0.05 ± 0.06			$8\times I$[c]	×1	2
	660–860	+0.00 ± 0.07			$8\times I$[c]	×3	2
	320–860	+0.03 ± 0.03			$8\times I$[c]	×2	2
BG CMi	640–860	−0.24 ± 0.03			2 × ∼ 30		4
	320–860	−0.05 ± 0.05					5
	720–860	−0.25 ± 0.06					5
	1110–1380(1250)	−1.74 ± 0.26					5
	1400–1650(1500)	−4.24 ± 1.78					5
DQ Her	370–580		−0.6[b]	+0.6[b]	14.2	∼1980 min	6
	320–860	+0.01 ± 0.01				250 min	2
EX Hya	570–920	−0.02 ± 0.04			240	200 min	1
	590–860	+0.01 ± 0.02			2[d]	68 min	2
FO Aqr	640–860	+0.06 ± 0.02					4
	330–920	−0.01 ± 0.02			120	200 min	1
	I	+0.11 ± 0.07			240	200 min	1
	320–860	−0.06 ± 0.04			$8\times I$[c]	×2	2
	320–860	+0.01 ± 0.04			$8\times I$[c]	×6	2
	720–860	−0.01 ± 0.17			$8\times I$[c]	×5	2
	1150–1350	+0.19 ± 0.13				51 min	2
	1150–1350	+1.09 ± 0.31				141 min	2
	Visual	+0.11 ± 0.13	−0.2[b]	+0.3[b]	28	270 min	7
	IR	−0.01 ± 0.55	−1.3[b]	+0.8[b]	28	270 min	7
GK Per	1150–1350	+0.03 ± 0.10				45 min	2
PQ Gem	*U*	+0.0 ± 0.6				80 min	8
	B	+0.0 ± 0.6				80 min	8
	V	+0.0 ± 0.9				80 min	8
	R		−1.1	+0.6		80 min	8
	U		−0.4[b]	+0.3[b]	8 × 5	162 min	9
	B		−0.3[b]	+0.4[b]	8 × 5	162 min	9
	V		−0.7[b]	+0.7[b]	8 × 5	162 min	9
	R		−1.5[b]	+0.7[b]	8 × 5	162 min	9
	I		−2.7	+1.5	8 × 5	162 min	9
	U		−0.5[b]	+0.3[b]		∼730 min	10
	B		−0.2[b]	+0.3[b]		∼730 min	10
	V		−0.6[b]	+0.4[b]		∼730 min	10
	R		−1.0[b]	+0.2[b]		∼730 min	10
	I		−1.3[b]	+1.3[b]		∼730 min	10
	J		−1.2[b]	+1.0[b]		∼270 min	10
	K		−2.0[b]	+1.3[b]		∼460 min	10
RXJ2133	(360)	+0.90 ± 0.06	−0.2[b]	+1.5	4 × 24	229 min	11
	(440)	+1.12 ± 0.05	+0.2[b]	+2.5	4 × 24	229 min	11
	(530)	+1.17 ± 0.09	−0.3[b]	+3.5	4 × 24	229 min	11
	(690)	+0.85 ± 0.07	+0.2[b]	+3	4 × 24	229 min	11
	(830)	+0.89 ± 0.08	−0.4[b]	+2.5	4 × 24	229 mn	11
TV Col	640–860	−0.03 ± 0.04					4
	320–860	−0.13 ± 0.09			$8\times I$[c]	×1	2
	320–860	−0.07 ± 0.07			$8\times I$[c]	×3	2
	320–860	−0.08 ± 0.10			$8\times I$[c]	×1	2
V1223 Sgr	350–920	−0.06 ± 0.03			240	144 min	1

Table 1. continued.

Name	Wavelength range[a] (nm)	Mean (%)	Min (%)	Max (%)	Integration time (s)	Total time	Ref.[1]
	I+ *R*	−0.04 ± 0.07			240	563 min	1
	V	−0.48 ± 0.62	≳−2	≲+2	14		12
	R	+0.03 ± 0.13	≳ −0.5	≲+0.5	14		12
	J	−0.36 ± 0.13	≳ −1	≲ +0.5	14		12
	K	+1.14 ± 1.26	≳−8	≲+8	14		12
V2306 Cyg	(360)	+0.04 ± 0.06			8 × 10 (210)	872 min	13
	(440)	+0.16 ± 0.08			8 × 10 (210)	872 min	13
	(530)	+0.18 ± 0.11			8 × 10 (210)	872 min	13
	(690)	−0.55 ± 0.08	−1.3[b]	+1[b]	8 × 10 (210)	872 min	13
	(830)	−0.91 ± 0.14	−1.7[b]	+0.4[b]	8 × 10 (210)	872 min	13
	B	+0.32 ± 0.10	−0.3[b]	+0.7[b]	58	52 min	14
	R	−1.99 ± 0.11	−5.2[b]	−0.6[b]	45	55 min	14
V2400 Oph	WL		−2.9[b]	−1.0[b]	120 & 180	∼900 min	15
	V	∼−1.8[b]	−4.8[b]	−1.0[b]	120	∼33 min	15
	R	∼−2.3[b]	−5.1[b]	−0.5[b]	120	∼71 min	15
	I	∼−3.3[b]	−6.0[b]	−1.0[b]	120	∼32 min	15
	320–700 (470)	−0.90 ± 0.03			50		16
	560–900 (700)	−2.82 ± 0.04			50		16
V405 Aur	500–750	1.8 (Semi-amp)					17
	U		−2	+2	8 × 12 (96)	1328 min	18
	B		−3	+3	8 × 12 (96)	1328 min	18
	V		−3	+3	8 × 12 (96)	1328 min	18
	R		−2	+2	8 × 12 (96)	1328 min	18
	I		−1	+1	8 × 12 (96)	1328 min	18
YY Dra	320–860	+0.09 ± 0.10			8 × *I*[c]	×1	2

[a] Numbers in parentheses indicate the effective wavelength of the filter; [b] estimated from plots; [c] *I* corresponds to an unspecified time between 0.5–1 mn; [d] constant polarimeter position.

[1] References – (1) Cropper (1986); (2) Stockman et al. (1992); (3) Beskrovnaya et al. (1996); (4) Penning et al. (1986); (5) West et al. (1987); (6) Swedlund et al. (1974); (7) Berriman et al. (1986); (8) Rosen et al. (1993); (9) Piirola et al. (1993); (10) Potter et al. (1997); (11) Katajainen et al. (2007); (12) Watts et al. (1985); (13) Uslenghi et al. (2001); (14) Norton et al. (2002); (15) Buckley et al. (1995); (16) Buckley et al. (1997); (17) Shakhovskoj & Kolesnikov (1997); (18) Piirola et al. (2008).

The zero points of the *UBVRI* magnitude scale were determined by observations of Landolt standards (109 954, 111 250, 111 2093 and 114 637; Landolt 1992) during each night.

4. Results

Successful measurements are outlined for seven of the targets below. The results of RXJ2133 are reported separately in Katajainen et al. (2007).

Given the ambiguity in the previously reported results, we give our data in multiple formats. The average value over the run will show any large unmodulated polarization (like that in BG CMi) and allow comparison with most of the previous measurements. The peak amplitude (of the spin folded and phase binned data) gives an idea of how modulated the system is. The peak to peak value shows whether or not both magnetic poles can be seen, and gives the best indication of the presence of modulation.

4.1. AE Aqr

AE Aqr has the shortest spin period of all the known IPs (∼33 s), and a relatively long orbital period of 9.88 h. Observed over two nights it was at an orbital phase of 0.6 and 0.3 from superior conjunction of the WD with respect to the secondary on the two nights respectively (Welsh et al. 1993). We used a spin period of 0.000382833 d, calculated for July/August 2006 from the ephemeris of de Jager et al. (1994). The zero spin phase point used here is arbitrarily set to the midnight epoch at HJD 2 453 949.5.

Over the two nights this system showed a marked difference in its behaviour. During the first night the *U* band exhibited significant flickering and a general trend of an increase in magnitude (see Fig. 1). This was mirrored in the raw *U* band circular polarization where the magnitude increased as the run went on. On the second night the *U* band exhibited significantly less flickering. This was a trend that was seen in all bands to some extent (see Fig. 1). This flickering is a well known feature of AE Aqr (see e.g. Beskrovnaya et al. 1996). With this in mind the data from the two nights is presented separately.

The short period of the system is such that the temporal resolution must be as small as possible to search for any periodic variations. In order to satisfy this only one position of the wave

Table 2. Inferred magnetic field strengths from the measured circular polarization in IPs.

Name	Inferred magnetic field strength (MG)	Reference
BG CMi	5–10	West et al. (1987)
	3–10	Chanmugam et al. (1990)
PQ Gem	8–18	Piirola et al. (1993)
	9–21	Vaeth et al. (1996)
	9–21	Potter et al. (1997)
V2400 Oph	>8	Buckley et al. (1995)
	9–27	Vaeth (1997)
V405 Aur	∼30	Piirola et al. (2008)

Table 3. Target list.

Name	α2000	δ2000	V (mag)	$P_{\rm spin}$ (s)	$P_{\rm orb}$ (h)
RXJ1730	17:30:21	−05:59:32	15.8	128.0	15.42
DQ Her	18:07:30	+45:51:32	13	142.1	4.65
V1223 Sgr	18:55:02	−31:09:48	13.2	745.6	3.37
V2306 Cyg	19:58:14	+32:32:42	16	1466.7	4.35
AE Aqr	20:40:09	−00:52:16	12	33.1	9.88
RXJ2133	21:33:44	+51:07:24	15.3	570.8	7.19
FO Aqr	22:15:55	−08:21:05	13.5	1254.5	4.85
AO Psc	22:55:17	−03:10:39	13.3	805.2	3.59

RXJ1730 = 1RXS J173021.5−055933;
RXJ2133 = 1RXS J213344.1+510725.

plate was used for each polarization measurement. On the first night an integration time of ∼3 s was used, this gave an overall temporal resolution of ∼8.5 s. On the second night an integration time of ∼1 s was used, giving a temporal resolution of ∼4.5 s for a full polarization measurement. Even at this short time scale the measurements will be smoothed to some extent. The data was folded and binned into 10 bins over the spin cycle (see Figs. 2 and 3). Both nights show a very small amplitude circular polarization. However in the raw data, values with an amplitude of over 2% (with a typical error of 0.6%) are not uncommon.

The mean values in each band (over each of the nights) are all within three sigma of zero. The peak amplitude is 0.80 ± 0.39% and the maximum peak to peak value is 1.22 ± 0.48% (see Table 6). The short spin period means that this data set covers many spin periods, and therefore the signal to noise is good.

4.2. AO Psc

AO Psc is a typical IP with a spin and orbital period of 805.2 s and 3.59 h respectively. Using the orbital ephemeris of Kaluzny & Semeniuk (1988), AO Psc was at an orbital phase of 0.14 from the maximum optical light. We note that the error in the calculation of this phase is small, but the ephemeris is old (20 years) so it may be somewhat out of date. The spin ephemeris has an accumulated uncertainty of greater than one spin, so we have used a zero point of HJD 2 453 949.5. The spin period from Kaluzny & Semeniuk (1988) of 0.0009319484 d was used.

Each polarization measurement consisted of two positions of the wave plate at 10 s each. The polarization data was then binned into eight bins across the spin cycle. The mean values in each band were within three sigma of being zero. The maximum amplitude in the binned data was 0.86 ± 0.37%, with a maximum peak to peak variation of 1.30 ± 0.50%, see Fig. 4 and Table 6. This peak to peak variation is less than three sigma, so we cannot claim this as a reliable detection of variable polarization.

4.3. DQ Her

DQ Her has an orbital period of 4.65 h and a spin period of 142 s. Using the ephemerids of Zhang et al. (1995) DQ Her was at an orbital phase of 0.23 from the optical eclipse. We used an arbitrary zero point of phase as HJD 2 453 948.5. A spin value of 0.00164504 d was used.

Due to the short period, a single wave plate position was used for an integration time of 10 s. The data was binned into ten bins over the spin period. All of the mean polarization values are less than three sigma from zero. The maximum amplitude seen is 0.64 ± 0.31% and the maximum peak to peak value was 1.00 ± 0.39% (see Table 6), this is less than a three sigma detection of variation (see Fig. 5).

4.4. FO Aqr

FO Aqr has an orbital period of 4.85 h and a spin period of 1254.5 s. Using the ephemeris of Patterson et al. (1998), FO Aqr was at an orbital phase of 0.98 from the dip in the optical light curve at the start of this observation. It was also at a spin phase of approximately 0.6 from pulse maximum, but we note that FO Aqr is rather erratic and this value may be some way off now, so zero phase was arbitrarily set to HJD 2 453 948.5. Here a spin value of 0.014519035 d from Patterson et al. (1998) was used.

Each polarization measurement was taken with two positions of the wave plate with an integration time of 10 s in each. The data was binned into four bins over the spin cycle. The mean circular polarization was within two sigma of being zero in each band. A peak amplitude of 1.15 ± 0.65% is present in the I band (see Fig. 6). The peak to peak values had a maximum of 1.43 ± 0.80% (see Table 6).

4.5. 1RXS J173021.5–055933

1RXS J173021.5–055933 (RXJ1730) is a relatively newly classified IP. It has a reported orbital period of 15.42 h and spin period of 128.0 s (Gänsicke et al. 2005). This short period (and therefore large number of spin cycles) has rendered the spin ephemeris of de Martino et al. (2008) out of date, and there is no published orbital ephemeris. Zero spin phase was set to HJD 2 453 950.5. A spin period of 0.001481481 d (Gänsicke et al. 2005) was used.

Here the first simultaneous *UBVRI* photometry of this object is presented (see Fig. 7). The photometry exhibits a double peak profile with equal maxima and unequal minima in each band. The photometric CLEANed (Lehto 1997) periodograms of each individual band are shown in Fig. 8. The spin period is seen at a value of 128.1 ± 0.7 s and the first harmonic at 64.0 ± 0.2 s (uncertainties based on a one sigma Gaussian fit to the periodogram). The spin peak is seen strongest in the V band.

The wave plate was positioned in one orientation for each circular polarization measurement for 10 s. The data were binned into 15 bins over the spin cycle. In each band the mean circular polarization was within two sigma of being zero. The biggest amplitude modulation was 4.26 ± 1.09% and the greatest peak to peak value was 8.26 ± 1.56% (see Table 6). The spin period was recovered from a period search of the B band circular polarization also. The short spin period means that many spin cycles (69) were completed, this leads to a high confidence in this data set.

4.6. V1223 Sgr

V1223 Sgr has a spin and orbital period of 745.6 s and 3.37 h respectively. Using the orbital ephemeris of Jablonski & Steiner (1987) V1223 Sgr is at an orbital phase of 0.83 from the maximum light, again this phase is valid with respect to the ephemeris, but the ephemeris is over 20 years old. The spin ephemeris has accumulated too much uncertainty to be useful here, so zero phase was arbitrarily set to HJD 2 453 950.5. A spin value of 0.00863 d from Osborne et al. (1985) was used.

The polarization measurements consisted of two positions of the wave plate, each of 10 s. The data was binned into ten bins across the spin cycle. The mean values of the circular

Table 4. Observing log.

Name	Start time (HJD[a])	End time (HJD[a])	Duration (mins)	No. of P_{orb}	No. of P_{spin}	Filters	Exposure time[b] (s)	Resolution[c] (s)	V^d (mag)
DQ Her	13 948.4240	13 948.5349	159.7	0.57	67.4	*UBVRI*	1 × 10	~24	14.5
RXJ2133	13 948.5732	13 948.6542	116.6	0.27	12.3	*UBVRI*	4 × 10	~96	15.3
FO Aqr	13 948.6933	13 948.7091	22.8	0.08	1.1[e]	*UBVRI*	2 × 10	~48	13.9
AE Aqr	13 949.5103	13 949.5704	86.5	0.15	156.8	*UBVRI*	1 × 3	~8.5	11.4
V2306 Cyg	13 949.5794	13 949.6528	105.7	0.40	4.3	*UBVRI*	2 × 10	~48	14.7
AO Psc	13 949.7047	13 949.7194	21.2	0.10	1.6[e]	*UBVRI*	2 × 10	~48	13.2
RXJ1730	13 950.4112	13 950.5134	147.2	0.16	69.0	*UBVRI*	1 × 10	~24	16.3
V1223 Sgr	13 950.5298	13 950.5871	82.5	0.41	6.6	*UBVRI*	2 × 10	~48	13.7
AE Aqr	13 950.6224	13 950.6366	20.4	0.03	37.0	*UBVRI*	1 × 1	~4.5	11.6
RXJ2133	13 950.6455	13 950.7187	105.4	0.24	11.1	*UBVRI*	4 × 10	~96	15.2

[a] +2 440 000; [b] the number of orientations of the wave plate, and the time spent at each orientation; [c] the resolution is roughly the number of orientations of the wave plate multiplied by the exposure time multiplied by two (to account for the ordinary and extraordinary measurements) plus some mechanical dead time; [d] measured; [e] these data sets are short and therefore the reported uncertainties are probably underestimated.

Table 5. Calibration data (taken on the first night).

Band	Instrumental polarization Value (%)	uncertainty (%)	Measured standard polarization Value (%)	uncertainty (%)
U	−0.005	0.030	+0.126	0.103
B	−0.064	0.024	−3.607	0.112
V	−0.017	0.028	−3.959	0.166
R	−0.011	0.024	−4.064	0.156
I	−0.059	0.029	−2.647	0.226

polarization are all within three sigma of being zero. The maximum amplitude variation was 1.30 ± 1.12% in the *U* band and the maximum peak to peak value was 2.16 ± 1.22% (see Fig. 9). The peak to peak values are all within three sigma of being zero (see Table 6).

4.7. V2306 Cyg

V2306 Cyg has an orbital period of 4.35 h and a spin period of 1466.7 s (Norton et al. 2002; Zharikov et al. 2002). The spin ephemeris of Norton et al. (2002) was used to phase the spin variations here.

Each polarization measurement consisted of two positions of the wave plate, each position being 10 s. The data were binned into 15 bins over the spin cycle. The maximum amplitude circular polarization was 1.06 ± 0.41% in the *I* band. The mean circular polarization in each band is consistent with zero (see Table 6). The maximum peak to peak value (1.95 ± 0.66% in the *I* band) indicates that variation is present (see Fig. 10 and Table 6).

4.8. Summary of results

Table 6 summarises the results obtained, this should now be used in conjunction with the results in Table 1. As noted earlier, our results on RXJ2133 have been reported separately in Katajainen et al. (2007).

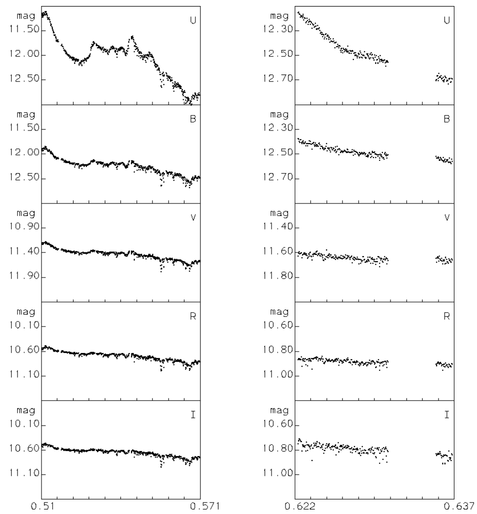

Fig. 1. Raw *UBVRI* photometry of AE Aqr taken on the two nights. The abscissa is in left plot is HJD – 2 453 949, in the right plot it is HJD – 2 453 950.

5. Discussion

5.1. AE Aqr

This is the first simultaneous *UBVRI* polarimetry measurement of AE Aqr. In most previous measurements a broad band filter and/or a much too long integration time has been used (see Table 1). This will have had the effect of smearing any polarization out to almost zero. In the cases where a short integration time has been used only a mean value has been reported, except for Cropper (1986) where a maximum semi-amplitude of ~0.1% was given.

The data reported here broadly agrees with the previous mean measurements of close to zero. The small peak to peak values are also in agreement with this. We do note that there is a hint of circular polarization in the raw data (over 2% in places – with a typical error of 0.6%).

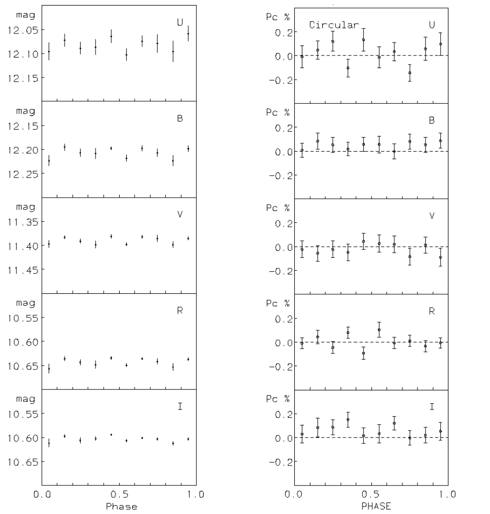

Fig. 2. Spin folded and phase binned simultaneous *UBVRI* photometry (*left*) and circular polarization (*right*) plots of AE Aqr, taken on the first night (HJD 2 453 949). Zero phase corresponds to HJD 2 453 949.5. A spin period of 0.000382833 d was used.

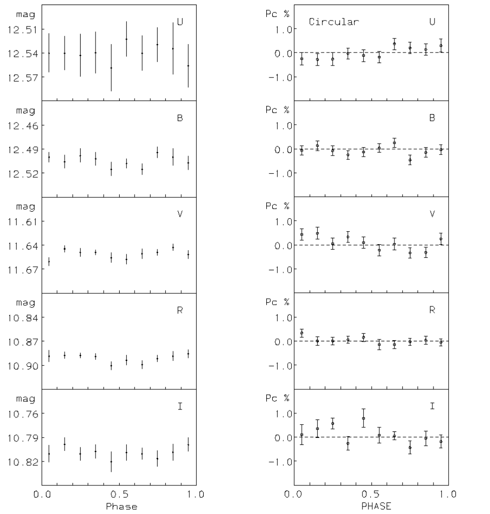

Fig. 3. Spin folded and phase binned simultaneous *UBVRI* photometry (*left*) and circular polarization (*right*) plots of AE Aqr, taken on the second night (HJD 2 453 950). Zero phase corresponds to HJD 2 453 949.5. A spin period of 0.000382833 d was used.

Given the generally accepted view that AE Aqr is a propeller system it seems intuitive to assume that it would have a large magnetic field to power this regime. Norton et al. (2008) have shown in their theoretical modelling that propellers can exist at low magnetic field strengths when they are spinning sufficiently fast. So a large magnetic field in AE Aqr is not necessarily required.

5.2. AO Psc

This is the first simultaneous *UBVRI* polarimetric observation of this target. All previous measurements have had a long integration time ($\gtrsim$240 s) when compared to the spin period (805.2 s) (see Table 1), so any variations shorter than this will have been smeared out effectively.

The mean measured circular polarization values are consistent with previous measurements (all of which were within one sigma of zero) (see Table 1).

The peak to peak values show hints of variation, (1.30 ± 0.50%) in the *I* band, but the detection is not conclusive. The short data set (1.6 spin periods) means that the uncertainties in this observation are large. This, coupled with the non-zero peak to peak values and a tentative detection in the *I* band may warrant further investigation.

5.3. DQ Her

This is the first simultaneous *UBVRI* polarimetric observation of DQ Her. The maximum level of circular polarization seen here (0.64 ± 0.31%) is consistent with the plots of Swedlund et al. (1974) who illustrate a variation with a max/min of $\gtrsim$0.5%. They found that the polarization was also variable on the orbital period, our data was just under 0.6 of a complete orbital period so we cannot bin our data as they did, and we see no overall trend in our data. Their pass band was approximately equal to our *UBV* bands combined.

The only other measurement of circular polarization in DQ Her was that of Stockman et al. (1992). They give a broadband integrated result close to zero, this is likely consistent with Swedlund et al. (1974) who see both positive and negative polarization values. As such, this is the first published result of time-resolved *R* and *I* band (as well as the first simultaneous *UBVRI*) data. The largest departure from zero polarization is seen in the *I* band here, and the raw data show up to 6 ± 1%.

Although by itself this data cannot claim a significant circular polarization detection, when considered with the results of Swedlund et al. (1974), it seems likely that DQ Her does exhibit variable circular polarization. To make a definite conclusion, more measurements are needed, particularly in the *I* band.

5.4. FO Aqr

This is the first simultaneous *UBVRI* polarimetry of FO Aqr. All previous measurements report a mean value close to zero, except for in the 1.15–1.35 μm range where +1.1 ± 0.3% polarization has been detected (see Table 1). The mean circular polarization seen here is within two sigma of all the previous measurements where there is an overlap in pass band (see Table 1). Since the large value of the circular polarization in the *I* band has such a large uncertainty we cannot claim this as a detection, although it is possible that circular polarization is present at the level of around 1%.

The short data set (1.1 spin periods) means that the uncertainties are probably much higher than quoted. This system also perhaps warrants further investigation, particularly in the *I* band.

5.5. RXJ1730

RXJ1730's short spin period (128.0 s) and long orbital period (15.4 h) make it a close sibling to the enigmatic AE Aqr (spin and orbital periods of 33.1 s and 9.88 h respectively).

Table 6. Summary of results. Min and max correspond to the phase binned data.

Target	Filter	Mean (%)	Min (%)	Max (%)	Peak-Peak (%)
AE Aqr[a]	*U*	+0.02 ± 0.02	−0.14 ± 0.07	+0.13 ± 0.10	0.27 ± 0.12
	B	+0.05 ± 0.02	−0.00 ± 0.06	+0.09 ± 0.06	0.09 ± 0.08
	V	−0.02 ± 0.02	−0.09 ± 0.08	+0.04 ± 0.07	0.13 ± 0.11
	R	+0.01 ± 0.01	−0.09 ± 0.05	+0.11 ± 0.06	0.20 ± 0.08
	I	+0.06 ± 0.02	−0.00 ± 0.06	+0.15 ± 0.07	0.15 ± 0.09
AE Aqr[b]	*U*	+0.00 ± 0.08	−0.27 ± 0.26	+0.38 ± 0.23	0.65 ± 0.35
	B	−0.07 ± 0.07	−0.46 ± 0.21	+0.26 ± 0.21	0.72 ± 0.30
	V	+0.08 ± 0.07	−0.33 ± 0.23	+0.50 ± 0.26	0.83 ± 0.35
	R	+0.02 ± 0.04	−0.14 ± 0.18	+0.34 ± 0.18	0.48 ± 0.25
	I	+0.10 ± 0.07	−0.42 ± 0.28	+0.80 ± 0.39	1.22 ± 0.48
AO Psc	*U*	+0.07 ± 0.05	−0.06 ± 0.14	+0.48 ± 0.16	0.54 ± 0.21
	B	+0.07 ± 0.06	−0.08 ± 0.20	+0.20 ± 0.28	0.28 ± 0.34
	V	+0.05 ± 0.09	−0.55 ± 0.33	+0.43 ± 0.25	0.98 ± 0.41
	R	−0.02 ± 0.08	−0.44 ± 0.29	+0.19 ± 0.21	0.63 ± 0.36
	I	+0.29 ± 0.10	−0.44 ± 0.35	+0.86 ± 0.37	1.30 ± 0.50
DQ Her	*U*	+0.00 ± 0.04	−0.16 ± 0.14	+0.19 ± 0.13	0.35 ± 0.19
	B	+0.14 ± 0.05	−0.05 ± 0.17	+0.47 ± 0.16	0.53 ± 0.23
	V	+0.12 ± 0.07	−0.08 ± 0.25	+0.35 ± 0.29	0.43 ± 0.39
	R	+0.03 ± 0.06	−0.22 ± 0.20	+0.40 ± 0.23	0.61 ± 0.31
	I	+0.04 ± 0.07	−0.64 ± 0.31	+0.35 ± 0.25	1.00 ± 0.39
FO Aqr	*U*	+0.16 ± 0.10	−0.00 ± 0.24	+0.56 ± 0.53	0.60 ± 0.58
	B	+0.07 ± 0.10	−0.27 ± 0.20	+0.47 ± 0.28	0.74 ± 0.34
	V	+0.17 ± 0.15	−0.38 ± 0.36	+0.40 ± 0.36	0.78 ± 0.51
	R	+0.11 ± 0.12	−0.01 ± 0.60	+0.42 ± 0.30	0.43 ± 0.67
	I	+0.27 ± 0.20	−0.28 ± 0.47	+1.15 ± 0.65	1.43 ± 0.80
RXJ1730	*U*	−0.23 ± 0.18	−1.48 ± 0.72	+1.02 ± 0.84	2.50 ± 1.11
	B	+0.00 ± 0.21	−4.00 ± 1.11	+4.26 ± 1.09	8.26 ± 1.56
	V	−0.39 ± 0.21	−1.79 ± 1.45	+1.38 ± 1.19	3.17 ± 1.88
	R	−0.07 ± 0.13	−1.55 ± 0.79	+1.80 ± 0.67	3.35 ± 1.07
	I	−0.12 ± 0.19	−1.95 ± 0.93	+1.82 ± 0.75	3.77 ± 1.19
V1223 Sgr	*U*	−0.01 ± 0.20	−1.30 ± 1.12	+0.86 ± 0.48	2.16 ± 1.22
	B	−0.00 ± 0.08	−0.40 ± 0.34	+0.36 ± 0.38	0.77 ± 0.51
	V	−0.04 ± 0.09	−0.45 ± 0.25	+0.55 ± 0.41	1.00 ± 0.48
	R	−0.05 ± 0.09	−0.40 ± 0.36	+0.32 ± 0.55	0.71 ± 0.65
	I	−0.27 ± 0.11	−0.92 ± 0.43	+0.50 ± 0.46	1.42 ± 0.63
V2306 Cyg	*U*	+0.06 ± 0.08	−0.61 ± 0.45	+0.61 ± 0.33	1.23 ± 0.56
	B	−0.00 ± 0.07	−0.47 ± 0.51	+0.46 ± 0.29	0.92 ± 0.59
	V	−0.07 ± 0.08	−0.86 ± 0.29	+0.51 ± 0.37	1.36 ± 0.48
	R	−0.08 ± 0.06	−0.78 ± 0.26	+0.45 ± 0.26	1.23 ± 0.37
	I	−0.11 ± 0.10	−1.06 ± 0.41	+0.89 ± 0.52	1.95 ± 0.66

[a] First night; [b] second night.

The photometric data shows a double peaked profile with equal maxima and unequal minima (see Fig. 7). Period analysis yields a spin period of 128.1 ± 0.7 with the first harmonic visible at 64.0 ± 0.2 s. This is in good agreement with Gänsicke et al. (2005) who concluded that both poles could be seen.

de Martino et al. (2008) report simultaneous optical Sloan filter data from the u', g' and r' bands. The u' filter is approximately the same as our U band, g' covers all our B and the upper half of V, and r' covers the lower half of V as well as R. In each of their u', g' and r' band observations the fundamental and the first harmonic were seen, with the first harmonic, on average, being strongest. This is in contrast to what we see (see Fig. 8), i.e. the fundamental being dominant. However, de Martino et al. (2008) show their r' band power spectra obtained on each of six consecutive nights. This shows a marked change in the relative strengths of the first harmonic and fundamental over time, the last night exhibiting a similar structure to ours. de Martino et al. (2008) see the strongest signal in their g' and u' bands, our U band has very little power, but our V band is the strongest, and since this contributes to what is their g' band this tallies up.

The level of polarization, 8.26 ± 1.56% peak to peak in the B band, makes this one of the most variable circularly polarized IPs, and therfore likely one of the most magnetic, measured to date. The variation of the circular polarization in the B band, showing both positive and negative values is indicative of both magnetic poles being visible (since each pole may only emit either positive or negative circular polarization). We note that the raw circular polarization data is somewhat noisy, with individual measurements of over 15%, we are unsure of the origin of these values, but we speculate that they may arise from short epochs when the diluting light is randomly lower due to flickering.

In the B band the photometry and circular polarization are coincident; the peaks in the photometry align with the peak and trough in the circular polarization. This strengthens the assertion that both poles are seen and they are both emitting circular polarization.

Like many of the other IPs for which circular polarization has been detected, RXJ1730 is also an *INTEGRAL* source (Barlow et al. 2006). We discuss this further in Sect. 5.8.

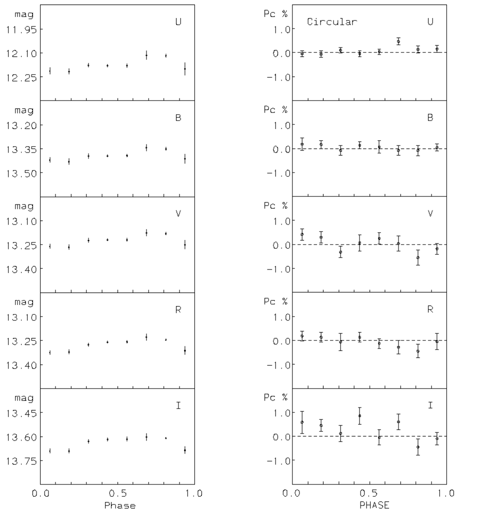

Fig. 4. Spin folded and phase binned simultaneous *UBVRI* photometry (*left*) and circular polarization (*right*) plots of AO Psc. Circular polarization measurements have an 23 s resolution. Zero phase corresponds to HJD 2 453 949.5. A spin period of 0.009319484 d was used.

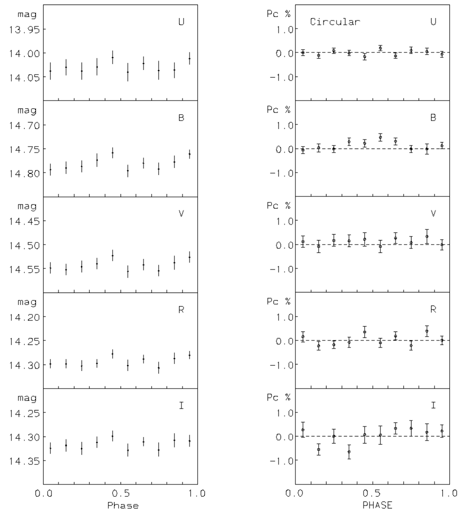

Fig. 5. Spin folded and phase binned simultaneous *UBVRI* photometry (*left*) and circular polarization (*right*) plots of DQ Her. Zero phase corresponds to HJD 2 453 948.5. A spin value of 0.00164504 d was used.

The variable nature of this object over the course of several days (de Martino et al. 2008) makes this an ideal target for a long base line follow up. Monitoring how the circular polarization varies as the accretion column structure changes over time and linking this to the photometry may reveal more about the magnetic nature of this source and IPs in general. Phase resolved circular spectro-polarimetry would be the ideal tool in revealing the magnetic field strength of RXJ1730, but taking into account the extremely short spin period (128 s), and relative faintness ($V \sim 17$) there are very few telescope and instrument combinations available where these kind of observations are possible.

5.6. V1223 Sgr

The mean circular polarization in V1223 Sgr is within four sigma of the previously reported values, and zero (see Tables 1 & 6). The maximum peak to peak variation of 2.16 ± 1.22% in the *U* band is not constrained enough for this to be considered a definite detection, but when considered with the results of Watts et al. (1985) it is likely that V1223 Sgr is strongly polarized.

There is a clear hint of a double peaked structure in the *UVRI* circular polarization curves, indicating that two magnetic poles can be seen. This is an effect seen in the photometry also, with hints of a double peaked profile in each band. This is in contrast to previous results which show a single peaked structure.

The raw circular polarization measurements are stable in all bands at the start of the run, but the *U* band begins to fluctuate as the run goes on, sometimes, quite randomly, up to 20%.

V1223 Sgr has a similar spin and orbital period to V405 Aur which was recently found to be very magnetic (Piirola et al. 2008) and has its circular polarization peak in the blue part of the spectrum. If the level of polarization seen here is confirmed then V1223 Sgr would be a close twin of V405 Aur. We also note that V1223 Sgr is an *INTEGRAL* source (Barlow et al. 2006).

5.7. V2306 Cyg

V2306 Cyg has had significant levels of circular polarization reported previously; Uslenghi et al. (2001) first reported it after using the TurPol instrument at the NOT (results summarised in Table 1). The mean results reported here are within the bounds given by uncertainties (two sigma) in their *UBV* bands, however in *R* and *I* Uslenghi et al. (2001) find a much higher amplitude mean value. Norton et al. (2002) also reported *B* and *R* band polarization at the NOT, this time using the ALFOSC instrument, they obtained mean values of $+0.32 \pm 0.10\%$ and $-1.99 \pm 0.11\%$ in each band respectively. Here we see significantly lower values than theirs also.

The shape of the circular polarization variation seen here is one of two minima per spin cycle in the *B* and *I* bands (see Fig. 10). The *B* band of Norton et al. (2002) has an indication of a two peaked profile, our results confirm this.

The discrepancy between our results and those reported previously can be explained in a variety of ways. The orbital phase may be different during each of the observations, Uslenghi et al. (2001) showed the circular polarization varied significantly over the orbital period, unfortunately the orbital ephemeris has accumulated too much uncertainty for this to be calculated. Another consideration is the brightness of the source, Uslenghi et al. (2001) did not quote a magnitude, but Norton et al. (2002) measured *UBVRI* magnitudes which are significantly fainter than ours. Since circular polarization is calculated as a fraction of the total incoming light this may have had the effect of seriously diluting our result.

5.8. Implications of our results

Generally each of the definite or potential circular polarization detections reported here have been most prominent towards the red end of the spectrum. This is in agreement with what has been seen before, and reinforces the notion of IPs being less magnetic

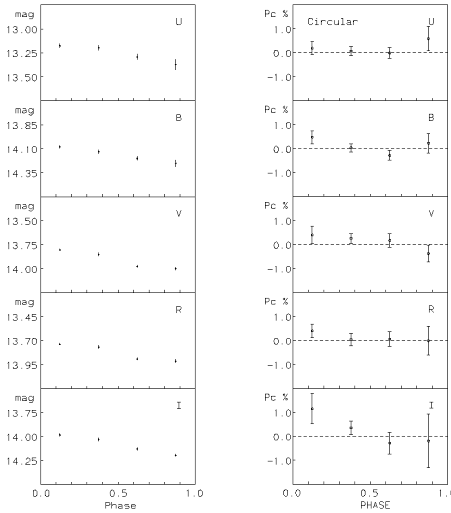

Fig. 6. Spin folded and phase binned simultaneous *UBVRI* photometry (*left*) and circular polarization (*right*) plots of FO Aqr. Zero phase corresponds to HJD 2 453 948.5. A spin period of 0.0014519035 d was used.

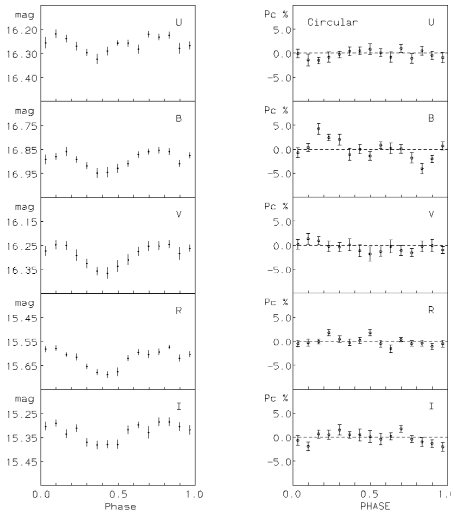

Fig. 7. Spin folded and phase binned simultaneous *UBVRI* photometry (*left*) and circular polarization (*right*) plots of RXJ1730. Zero phase corresponds to HJD 2 453 950.5. A spin period of 0.001481481 d was used.

than polars, as weaker fields will give rise to polarization appearing at longer wavelengths.

Amongst the IPs detected by *INTEGRAL* (Barlow et al. 2006; Bird et al. 2007) RXJ2133 and V2400 Oph have previously been found to display a large degree of circular polarization (Katajainen et al. 2007; Buckley et al. 1995, 1997), whilst RXJ1730, V2306 Cyg, DQ Her, V1223 Sgr and FO Aqr are

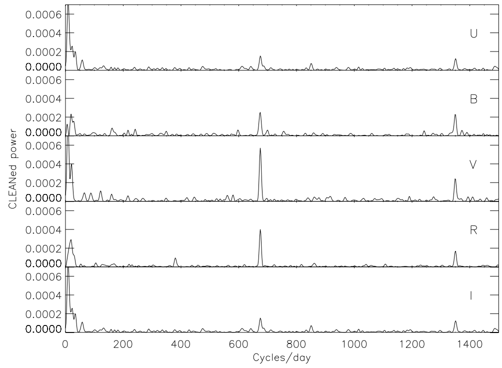

Fig. 8. *UBVRI* CLEANed photometric periodograms of RXJ1730.

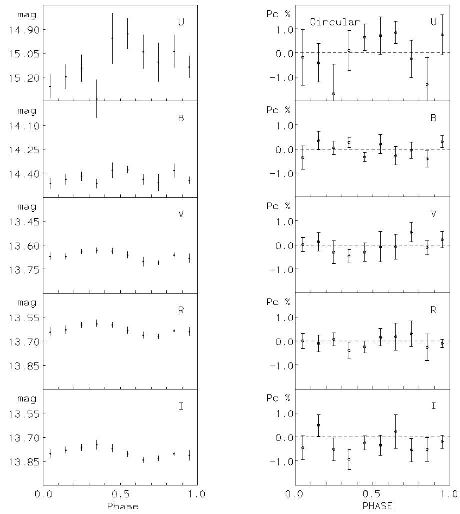

Fig. 9. Spin folded and phase binned simultaneous *UBVRI* photometry (*left*) and circular polarization (*right*) plots of V1223 Sgr. Zero phase corresponds to HJD 2 453 950.5. A spin period of 0.00863 d was used.

shown here to have some degree of circular polarization or at least strong hints of it. The only other *INTEGRAL*-detected IP to have its circular polarization measured is GK Per (Stockman et al. 1992). This was reported as having a mean value of 0.03 ± 0.10%, but as noted earlier, the practice of reporting mean values may seriously under report the true magnetic nature. In light of this, it would be productive to look for circular polarization in the rest of the *INTEGRAL* IP sources, namely V709 Cas, IGR000234+6141, NY Lup, and MU Cam. As noted by Katajainen et al. (2007), NY Lup may well be a close twin of the strongly polarized IP RXJ2133.

It has also been noted that the presence of a soft X-ray component may be related to the presence of a large magnetic field (Katajainen et al. 2007). The circular polarization seen in RXJ1730 further adds to this trend as it is also a soft X-ray source (de Martino et al. 2008). This brings the total of soft

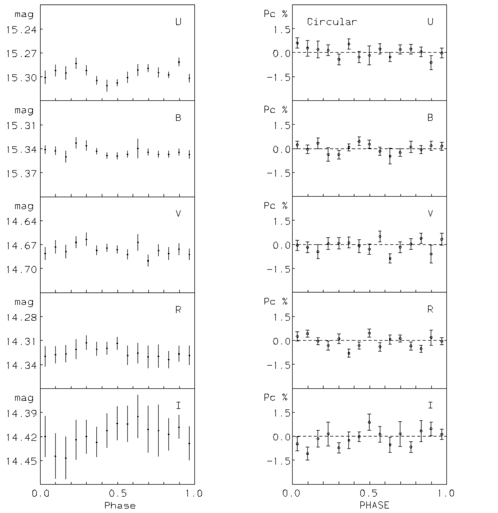

Fig. 10. Spin folded and phase binned simultaneous *UBVRI* photometry (*left*) and circular polarization (*right*) plots of V2306 Cyg. The spin ephemeris of Norton et al. (2002) was used to phase the spin variations.

X-ray emitting, circularly polarized IPs to four, namely PQ Gem, V405 Aur, RXJ2133 and RXJ1730. Perhaps the same geometry which allows the soft X-ray component to be seen in some IPs but not others, as suggested by Evans & Hellier (2007), may also allow the efficient detection of circular polarization. Indeed Evans & Hellier (2007) suggested that the reason some IPs show polarization and the others do not, is mostly due to different accretion geometry and hiding effects of the accretion curtains. This may tie in with the suggestion by Norton et al. (2002) with regard to V2306 Cyg, that cancellation of polarized emission between the two magnetic poles may hide significant polarization in some systems. Futhermore, it may be that only those systems which show an asymmetry between the poles (in terms of temperature etc or accretion curtain structure) or have an offset or non-dipole magnetic field structure, emit a detectable signal.

6. Conclusion

We have detected temporal variation in the circular polarization emission in RXJ1730, with possible emission (and in some cases variation) in V2306 Cyg, DQ Her, V1223 Sgr, AO Psc and FO Aqr; AE Aqr had none detected at a significant level. Broadly speaking this is in agreement with previous results, and adds to the observational trend of IPs having less polarization than polars; and hence likely smaller effective magnetic field strength.

There are indications of a correlation between the detection of circular polarization in IPs and their detection as hard X-ray sources by *INTEGRAL*. We therefore suggest that other *INTEGRAL* sources should be tested for circular polarization. Where such objects also exhibit soft X-ray components (i.e. NY Lup and MU Cam), we predict there is a very good chance of detecting significant circular polarization.

Acknowledgements. The Nordic Optical Telescope is operated on the island of La Palma jointly by Denmark, Finland, Iceland, Norway, and Sweden, in the Spanish Observatorio del Roque de los Muchachos of the Instituto de Astrofisíca de Canarias. This work has been supported by the "Societas Scientiarum Fennica – Suomen Tiedeseura" and its Magnus Ehrnrooth foundation, and the Academy of Finland (SK).

References

Barlow, E. J., Knigge, C., Bird, A. J., et al. 2006, MNRAS, 372, 224
Berriman, G., Bailey, J., Axon, D. J., & Hough, J. H. 1986, MNRAS, 223, 449
Beskrovnaya, N. G., Ikhsanov, N. R., Bruch, A., & Shakhovskoy, N. M. 1996, A&A, 307, 840
Bird, A. J., Malizia, A., Bazzano, A., et al. 2007, VizieR Online Data Catalog, 217, 175
Buckley, D. A. H., Sekiguchi, K., Motch, C., et al. 1995, MNRAS, 275, 1028
Buckley, D. A. H., Haberl, F., Motch, C., et al. 1997, MNRAS, 287, 117
Chanmugam, G., & Ray, A. 1984, ApJ, 285, 252
Chanmugam, G., Frank, J., King, A. R., & Lasota, J.-P. 1990, ApJ, 350, L13
Cropper, M. 1986, MNRAS, 222, 225
Cropper, M. 1990, Space Sci. Rev., 54, 195
Cumming, A. 2004, in Magnetic Cataclysmic Variables, ed. S. Vrielmann, & M. Cropper, ASP Conf. Ser. 315: IAU Colloq. 190: 58
de Jager, O. C., Meintjes, P. J., O'Donoghue, D., & Robinson, E. L. 1994, MNRAS, 267, 577
de Martino, D., Matt, G., Mukai, K., et al. 2008, A&A, 481, 149
Evans, P. A., & Hellier, C. 2007, ApJ, 663, 1277
Gänsicke, B. T., Marsh, T. R., Edge, A., et al. 2005, MNRAS, 361, 141
Jablonski, F., & Steiner, J. E. 1987, ApJ, 323, 672
Kaluzny, J., & Semeniuk, I. 1988, Inf. Bull. Variable Stars, 3145, 1
Katajainen, S., Piirola, V., Ramsay, G., et al. 2003, MNRAS, 340, 1
Katajainen, S., Butters, O. W., Norton, A. J., Lehto, H. J., & Piirola, V. 2007, A&A, 475, 1011
King, A. R. 1988, QJRAS, 29, 1
Korhonen, T., Piirola, V., & Reiz, A. 1984, The Messenger, 38, 20
Lamb, D. Q., & Masters, A. R. 1979, ApJ, 234, L117
Landolt, A. U. 1992, AJ, 104, 340
Lehto, H. J. 1997, in Applications of time series analysis in astronomy and meteorology, ed. T. Subba Rao, M. B. Priestley, & O. Lessi (London: Chapman and Hall)
Motch, C., Haberl, F., Guillout, P., et al. 1996, A&A, 307, 459
Norton, A. J., Quaintrell, H., Katajainen, S., et al. 2002, A&A, 384, 195
Norton, A. J., Butters, O. W., Parker, T. L., & Wynn, G. A. 2008, ApJ, 672, 524
Osborne, J. P., Rosen, R., Mason, K. O., & Beuermann, K. 1985, SSRv, 40, 143
Patterson, J. 1994, PASP, 106, 209
Patterson, J., Kemp, J., Richman, H. R., et al. 1998, PASP, 110, 415
Penning, W. R., Schmidt, G. D., & Liebert, J. 1986, ApJ, 301, 881
Piirola, V. 1973, A&A, 27, 383
Piirola, V. 1988, Simultaneous five-colour (*UBVRI*) photopolarimeter in Polarized Radiation of Circumstellar Origin (Vatican Observatory/University of Arizona Press), 735
Piirola, V., Coyne, G. V., & Reiz, A. 1987a, A&A, 185, 189
Piirola, V., Coyne, G. V., & Reiz, A. 1987b, A&A, 186, 120
Piirola, V., Hakala, P., & Coyne, G. V. 1993, ApJ, 410, L107
Piirola, V., Vornanen, T., Berdyugin, A., & Coyne, G. V., S. J. 2008, ApJ, 684, 558
Potter, S. B., Cropper, M., Mason, K. O., Hough, J. H., & Bailey, J. A. 1997, MNRAS, 285, 82
Rosen, S. R., Mittaz, J. P. D., & Hakala, P. J. 1993, MNRAS, 264, 171
Schmidt, G. D., Szkody, P., Smith, P. S., et al. 1996, ApJ, 473, 483
Shakhovskoj, N. M., & Kolesnikov, S. V. 1997, IAUCirc, 6760, 2
Stockman, H. S., Schmidt, G. D., Berriman, G., et al. 1992, ApJ, 401, 628
Swedlund, J. B., Kemp, J. C., & Wolstencroft, R. D. 1974, ApJ, 193, L11
Uslenghi, M., Tommasi, L., Treves, A., Piirola, V., & Reig, P. 2001, A&A, 372, L1
Vaeth, H. 1997, A&A, 317, 476
Vaeth, H., Chanmugam, G., & Frank, J. 1996, ApJ, 457, 407
Warner, B. 1995, Cataclysmic Variable Stars (Cambridge University Press)
Watts, D. J., Giles, A. B., Greenhill, J. G., Hill, K., & Bailey, J. 1985, MNRAS, 215, 83
Welsh, W. F., Horne, K., & Gomer, R. 1993, ApJ, 410, L39
West, S. C. 1989, ApJ, 345, 511
West, S. C., Berriman, G., & Schmidt, G. D. 1987, ApJ, 322, L35
Wickramasinghe, D. T., & Ferrario, L. 2000, PASP, 112, 873
Wickramasinghe, D. T., & Meggitt, S. M. A. 1985, MNRAS, 214, 605
Zhang, E., Robinson, E. L., Stiening, R. F., & Horne, K. 1995, ApJ, 454, 447
Zharikov, S. V., Tovmassian, G. H., & Echevarría, J. 2002, A&A, 390, L23

Bibliography

Ajello, M., Greiner, J., Rau, A., et al. 2006, The Astronomer's Telegram, 697, 1

Arons, J. & Lea, S. M. 1980, ApJ, 235, 1016

Barlow, E. J., Knigge, C., Bird, A. J., et al. 2006, MNRAS, 372, 224

Beardmore, A. P., Done, C., Osborne, J. P., & Ishida, M. 1995, MNRAS, 272, 749

Beardmore, A. P., Mukai, K., Norton, A. J., Osborne, J. P., & Hellier, C. 1998, MNRAS, 297, 337

Berriman, G., Bailey, J., Axon, D. J., & Hough, J. H. 1986, MNRAS, 223, 449

Beskrovnaya, N. G., Ikhsanov, N. R., Bruch, A., & Shakhovskoy, N. M. 1996, A&A, 307, 840

Beuermann, K., Euchner, F., Reinsch, K., Jordan, S., & Gänsicke, B. T. 2007, A&A, 463, 647

Beuermann, K. & Schwope, A. D. 1994, in ASP Conf. Ser. 56: Interacting Binary Stars, ed. A. W. Shafter, 119

Bikmaev, I. F., Revnivtsev, M. G., Burenin, R. A., & Sunyaev, R. A. 2006, Astronomy Letters, 32, 588

Bird, A. J., Barlow, E. J., Bassani, L., et al. 2004, ApJL, 607, L33

Bird, A. J., Malizia, A., Bazzano, A., et al. 2007, ApJS, 170, 175

Bonnet-Bidaud, J. M., Mouchet, M., de Martino, D., Silvotti, R., & Motch, C. 2006, A&A, 445, 1037

Bradt, H. V., Rothschild, R. E., & Swank, J. H. 1993, A&AS, 97, 355

Buckley, D. A. H., Haberl, F., Motch, C., et al. 1997, MNRAS, 287, 117

Buckley, D. A. H., Sekiguchi, K., Motch, C., et al. 1995, MNRAS, 275, 1028

Burwitz, V., Reinsch, K., Beuermann, K., & Thomas, H.-C. 1996, A&A, 310, L25

Butters, O. W., Barlow, E. J., Norton, A. J., & Mukai, K. 2007, A&A, 475, L29

Butters, O. W., Katajainen, S., Norton, A. J., Lehto, H. J., & Piirola, V. 2009a, A&A, 496, 891

Butters, O. W., Norton, A. J., Hakala, P., Mukai, K., & Barlow, E. J. 2008, A&A, 487, 271

Butters, O. W., Norton, A. J., Mukai, K., & Barlow, E. J. 2009b, A&A, 498, L17

Chanmugam, G., Frank, J., King, A. R., & Lasota, J.-P. 1990, ApJl, 350, L13

Chanmugam, G. & Ray, A. 1984, ApJ, 285, 252

Chevalier, R. A. & Imamura, J. N. 1982, ApJ, 261, 543

Cropper, M. 1986, MNRAS, 222, 225

Cropper, M. 1990, Space Science Reviews, 54, 195

Cumming, A. 2004, in ASP Conf. Ser. 315: IAU Colloq. 190: Magnetic Cataclysmic Variables, ed. S. Vrielmann & M. Cropper, 58

de Jager, O. C., Meintjes, P. J., O'Donoghue, D., & Robinson, E. L. 1994, MNRAS, 267, 577

de Martino, D., Bonnet-Bidaud, J.-M., Mouchet, M., et al. 2006a, A&A, 449, 1151

de Martino, D., Matt, G., Mukai, K., et al. 2006b, in ESA SP-604: The X-ray Universe 2005, ed. A. Wilson, 261

de Martino, D., Matt, G., Mukai, K., et al. 2008, A&A, 481, 149

Dickey, J. M. & Lockman, F. J. 1990, ARAA, 28, 215

Duck, S. R., Rosen, S. R., Ponman, T. J., et al. 1994, MNRAS, 271, 372

Evans, P. A. & Hellier, C. 2007, ApJ, 663, 1277

Ezuka, H. & Ishida, M. 1999, ApJS, 120, 277

Fischer, A. & Beuermann, K. 2001, A&A, 373, 211

Frank, J., King, A., & Raine, D. 2002, Accretion power in astrophysics, 3rd edn. (Cambridge university press)

Fujimoto, R. & Ishida, M. 1997, ApJ, 474, 774

Gänsicke, B. T. 2005, in ASP Conf. Ser. 330: The Astrophysics of Cataclysmic Variables and Related Objects, ed. J.-M. Hameury & J.-P. Lasota, 3

Gänsicke, B. T., Dillon, M., Southworth, J., et al. 2009, MNRAS, 397, 2170

Gänsicke, B. T., Marsh, T. R., Edge, A., et al. 2005, MNRAS, 361, 141

Gonzalez, J. F., Hubrig, S., Nesvacil, N., & North, P. 2005, AO Velorum: a young quadruple system with a ZAMS eclipsing BpSi primary

Haberl, F. & Motch, C. 1995, A&A, 297, L37

Haberl, F., Motch, C., & Zickgraf, F.-J. 2002, A&A, 387, 201

Hakala, P., Ramsay, G., Wheatley, P., Harlaftis, E. T., & Papadimitriou, C. 2004, A&A, 420, 273

Harlaftis, E. T. & Horne, K. 1999, MNRAS, 305, 437

Hellier, C. 1997, MNRAS, 291, 71

Hellier, C. 2001, Cataclysmic Variable Stars (Springer)

Hellier, C. & Mukai, K. 2004, MNRAS, 352, 1037

Imamura, J. N., Wolff, M. T., & Durisen, R. H. 1984, ApJ, 276, 667

Jablonski, F. & Steiner, J. E. 1987, ApJ, 323, 672

Kaluzny, J. & Semeniuk, I. 1988, Informational Bulletin on Variable Stars, 3145, 1

Katajainen, S., Butters, O. W., Norton, A. J., Lehto, H. J., & Piirola, V. 2007, A&A, 475, 1011

Katajainen, S., Piirola, V., Ramsay, G., et al. 2003, MNRAS, 340, 1

King, A. R. 1988, QJRAS, 29, 1

King, A. R. 1993, MNRAS, 261, 144

King, A. R. 1995, in ASP Conf. Ser. 85: Magnetic Cataclysmic Variables, 21

King, A. R. & Shaviv, G. 1984, MNRAS, 211, 883

King, A. R. & Wynn, G. A. 1999, MNRAS, 310, 203

Kolb, U. 2002, Interacting Binary Stars, 1st edn. (The Open University)

Korhonen, T., Piirola, V., & Reiz, A. 1984, The Messenger, 38, 20

Kuijpers, J. & Pringle, J. E. 1982, AAP, 114, L4

Kuiper, L., Keek, S., Hermsen, W., Jonker, P. G., & Steeghs, D. 2006, The Astronomer's Telegram, 684, 1

Landolt, A. U. 1992, AJ, 104, 340

Langer, S. H., Chanmugam, C., & Shaviv, G. 1982, ApJ, 258, 289

Lehto, H. J. 1997, in Applications of time series analysis in astronomy and meteorology, ed. T. Subba Rao, M. B. Priestley, & O. Lessi (London Chapman and Hall)

Li, J. 1999, in ASP Conf. Ser. 157: Annapolis Workshop on Magnetic Cataclysmic Variables, 235

Marsh, T., Littlefair, S., & Dhillon, V. 2006, The Astronomer's Telegram, 760, 1

Masetti, N., Bassani, L., Dean, A. J., Ubertini, P., & Walter, R. 2006a, The Astronomer's Telegram, 735, 1

Masetti, N., Morelli, L., Palazzi, E., et al. 2006b, A&A, 459, 21

Masetti, N., Morelli, L., Palazzi, E., et al. 2006c, The Astronomer's Telegram, 783, 1

Mhlahlo, N., Buckley, D. A. H., Dhillon, V. S., et al. 2007, MNRAS, 378, 211

Motch, C., Guillout, P., Haberl, F., et al. 1998, A&AS, 132, 341

Mukai, K. 2008, The Catalog of IPs and IP Candidates by Right Ascension Version 2008a with 89 objects, http://asd.gsfc.nasa.gov/Koji.Mukai/iphome/catalog/alpha.html

Mukai, K., Markwardt, C. B., Tueller, J., et al. 2006, The Astronomer's Telegram, 686, 1

Mukai, K., Wood, J. H., Naylor, T., Schlegel, E. M., & Swank, J. H. 1997, ApJ, 475, 812

Norton, A. J. 1988, PhD thesis, University of Leicester

Norton, A. J., Butters, O. W., Parker, T. L., & Wynn, G. A. 2008, ApJ, 672, 524

Norton, A. J., McHardy, I. M., Lehto, H. J., & Watson, M. G. 1992, MNRAS, 258, 697

Norton, A. J., Quaintrell, H., Katajainen, S., et al. 2002, A&AS, 384, 195

Norton, A. J. & Watson, M. G. 1989, MNRAS, 237, 853

Norton, A. J., Wynn, G. A., & Somerscales, R. V. 2004, ApJ, 614, 349

Osborne, J. P., Rosen, R., Mason, K. O., & Beuermann, K. 1985, SSRv, 40, 143

Paczynski, B. 1976, in IAU Symp. 73: Structure and Evolution of Close Binary Systems, ed. P. Eggleton, S. Mitton, & J. Whelan, 75

Pandey, M., Rao, A. P., Manchanda, R., Durouchoux, P., & Ishwara-Chandra, C. H. 2006, A&A, 453, 83

Paradijs, J. & Bleeker, J. 1997, Lecture notes in physics, Vol. 520, X-Ray Spectroscopy in Astrophysics (Springer)

Parker, T. L. 2005, PhD thesis, The Open University

Parker, T. L., Norton, A. J., & Mukai, K. 2005, A&A, 439, 213

Patterson, J. 1994, PASP, 106, 209

Patterson, J., Halpern, J., Mirabal, N., et al. 2006, The Astronomer's Telegram, 757, 1

Patterson, J., Kemp, J., Richman, H. R., et al. 1998, PASP, 110, 415

Penning, W. R., Schmidt, G. D., & Liebert, J. 1986, ApJ, 301, 881

Piirola, V. 1973, A&A, 27, 383

Piirola, V. 1988, Simultaneous five-colour (UBVRI) photopolarimeter (Polarized Radiation of Circumstellar Origin), 735–746

Piirola, V. 1995, in ASP Conf. Ser. 85: Magnetic Cataclysmic Variables, ed. D. A. H. Buckley & B. Warner, 31

Piirola, V., Coyne, G. V., & Reiz, A. 1987a, A&A, 185, 189

Piirola, V., Coyne, G. V., & Reiz, A. 1987b, A&A, 186, 120

Piirola, V., Coyne, G. V., Takalo, S. J., et al. 1994, A&A, 283, 163

Piirola, V., Hakala, P., & Coyne, G. V. 1993, ApJL, 410, L107

Piirola, V., Vornanen, T., Berdyugin, A., & Coyne, G. V., S. J. 2008, ApJ, 684, 558

Potter, S., Buckley, D., O'Donoghue, D., et al. 2008, in Society of Photo-Optical Instrumentation Engineers (SPIE) Conference Series, Vol. 7014, Society of Photo-Optical Instrumentation Engineers (SPIE) Conference Series

Potter, S. B., Cropper, M., Mason, K. O., Hough, J. H., & Bailey, J. A. 1997, MNRAS, 285, 82

Pretorius, M. L. 2009, MNRAS, 395, 386

Priest, E. & Forbes, T. 2000, Magnetic reconnection, 1st edn. (Cambridge university press)

Pringle, J. E. & Wade, R. A. 1985, Interacting binary stars (Cambridge University Press)

Ramsay, G., Wheatley, P. J., Norton, A. J., Hakala, P., & Baskill, D. 2008, MNRAS, 387, 1157

Rapaport, D. 2004, The art of molecular dynamics simulation, 2nd edn. (CUP)

Revnivtsev, M., Sazonov, S., Jahoda, K., & Gilfanov, M. 2004, A&A, 418, 927

Ritter, H. & Kolb, U. 2003, VizieR Online Data Catalog, 5113, 0

Rosen, S. R. 1992, MNRAS, 254, 493

Rosen, S. R., Mittaz, J. P. D., & Hakala, P. J. 1993, MNRAS, 264, 171

Rybicki, G. B. & Lightman, A. P. 1986, Radiative Processes in Astrophysics (Radiative Processes in Astrophysics, by George B. Rybicki, Alan P. Lightman, pp. 400. ISBN 0-471-82759-2. Wiley-VCH , June 1986.)

Saitou, K., Tsujimoto, M., Ebisawa, K., & Ishida, M. 2009, PASJ, 61, L13+

Saxton, C. J., Wu, K., Cropper, M., & Ramsay, G. 2005, MNRAS, 360, 1091

Schenker, K., King, A. R., Kolb, U., Wynn, G. A., & Zhang, Z. 2002, MNRAS, 337, 1105

Schmidt, G. D., Szkody, P., Smith, P. S., et al. 1996, ApJ, 473, 483

Shakhovskoj, N. M. & Kolesnikov, S. V. 1997, IAUCirc, 6760, 2

Shakura, N. I. & Sunyaev, R. A. 1973, A&A, 24, 337

Smith, D. A. & Dhillon, V. S. 1998, MNRAS, 301, 767

Staude, A., Schwope, A. D., Krumpe, M., Hambaryan, V., & Schwarz, R. 2003, A&A, 406, 253

Staude, A., Schwope, A. D., & Schwarz, R. 2001, A&A, 374, 588

Stockman, H. S., Schmidt, G. D., Berriman, G., et al. 1992, ApJ, 401, 628

Swedlund, J. B., Kemp, J. C., & Wolstencroft, R. D. 1974, ApJL, 193, L11

Thorstensen, J. R., Patterson, J., Halpern, J., & Mirabal, N. 2006, The Astronomer's Telegram, 767, 1

Tomsick, J. A., Chaty, S., Rodriguez, J., et al. 2006, ApJ, 647, 1309

Torres, M. A. P., Steeghs, D., Garcia, M. R., et al. 2006, The Astronomer's Telegram, 763, 1

Tout, C. A., Wickramasinghe, D. T., Liebert, J., Ferrario, L., & Pringle, J. E. 2008, MNRAS, 387, 897

Uslenghi, M., Tommasi, L., Treves, A., Piirola, V., & Reig, P. 2001, A&A, 372, L1

Vaeth, H. 1997, A&A, 317, 476

Vaeth, H., Chanmugam, G., & Frank, J. 1996, ApJ, 457, 407

van der Sluys, M. 2006, Roche potential, http://hemel.waarnemen.com/Informatie/Sterren/hoofdstuk6.html

Verbunt, F. 1982, Space Science Reviews, 32, 379

Warner, B. 1976, in IAU Symposium, Vol. 73, Structure and Evolution of Close Binary Systems, ed. P. Eggleton, S. Mitton, & J. Whelan, 85

Warner, B. 1995, Cataclysmic Variable Stars (Cambridge University Press)

Watts, D. J., Giles, A. B., Greenhill, J. G., Hill, K., & Bailey, J. 1985, MNRAS, 215, 83

Webbink, R. F. & Wickramasinghe, D. T. 2002, MNRAS, 335, 1

Welsh, W. F., Horne, K., & Gomer, R. 1993, ApJl, 410, L39

West, S. C. 1989, ApJ, 345, 511

West, S. C., Berriman, G., & Schmidt, G. D. 1987, ApJL, 322, L35

Wheatley, P. J., Marsh, T. R., & Clarkson, W. 2006, The Astronomer's Telegram, 765, 1

Whitehurst, R. 1988a, MNRAS, 233, 529

Whitehurst, R. 1988b, MNRAS, 232, 35

Whitehurst, R. 1994, MNRAS, 266, 35

Wickramasinghe, D. T. & Ferrario, L. 2000, PASP, 112, 873

Wickramasinghe, D. T. & Meggitt, S. M. A. 1985, MNRAS, 214, 605

Wu, K. 2000, Space Science Reviews, 93, 611

Wu, K. & Cropper, M. 2001, MNRAS, 326, 686

Wu, K., Cropper, M., Ramsay, G., Saxton, C., & Bridge, C. 2003, Chinese Journal of Astronony and Astrophysics, 3, 235

Wynn, G. A. & King, A. R. 1995, MNRAS, 275, 9

Wynn, G. A., King, A. R., & Horne, K. 1995, in ASP Conf. Ser. 85: Magnetic Cataclysmic Variables, ed. D. A. H. Buckley & B. Warner, 196

Zhang, E., Robinson, E. L., Stiening, R. F., & Horne, K. 1995, ApJ, 454, 447

Zharikov, S. V., Tovmassian, G. H., & Echevarría, J. 2002, A&A, 390, L23